ETH Library

Electronic Transport and Correlation Phenomena at Improper Ferroelectric Domain Walls

Doctoral Thesis

Author(s):
Schaab, Jakob

Publication date:
2017

Permanent link:
https://doi.org/https://doi.org/10.3929/ethz-b-000172456

Rights / license:
In Copyright - Non-Commercial Use Permitted

This page was generated automatically upon download from the ETH Zurich Research Collection.
For more information, please consult the Terms of use.

DISS. ETH NO. 24207

ELECTRONIC TRANSPORT AND CORRELATION PHENOMENA AT IMPROPER FERROELECTRIC DOMAIN WALLS

A thesis submitted to attain the degree of

DOCTOR OF SCIENCES of ETH ZURICH
(Dr. sc. ETH Zurich)

presented by

JAKOB SCHAAB

Dipl.-Ing., University of Stuttgart

born on 19.12.1985
citizen of Germany

accepted on the recommendation of

Prof. Dr. Manfred Fiebig
Prof. Dr. Nicola A. Spaldin
Prof. Dr. Marty Gregg
Prof. Dr. Dennis Meier

2017

Declaration of originality

I hereby declare that the following submitted thesis is original work, which I alone have authored and which is written in my own words.

Title:	Electronic transport and correlation phenomena at improper ferroelectric domain walls
Author:	Jakob Schaab
Supervisor:	Prof. Dr. Manfred Fiebig

With my signature I declare that I have been informed regarding normal academic citation rules and that I have read and understood the information on "Citation etiquette". The citation conventions usual to the discipline in question here have been respected.

Furthermore, I declare that I have truthfully documented all methods, data, and operational procedures, and not manipulated any data. All persons who have substantially supported me in my work are identified in the text and in the acknowledgments.

The above work may be tested electronically for plagiarism.

Zürich, 20. 07. 2017

Acknowledgments

The results of this thesis would have never progressed this far without the support and contributions from numerous collaborators, colleagues, and friends, whom I would like to acknowledge at this point.

First, I would like to thank **Prof. Manfred Fiebig** for welcoming me to his group and for giving me the great opportunity to conduct my PhD studies in the fascinating field of ferroic materials. To my PhD supervisor and mentor **Prof. Dennis Meier** I express my deepest gratitude for all the unlimited support and optimism during the years of my doctorate. I am really glad that I could work at large-scale research facilities, collaborate with scientists abroad, and attend international conferences. Aside from the scientific work, I enjoyed the recreational activities we had, naming a day of snowboarding off-piste with perfect conditions in Andermatt as one of the highlights. For the disposition to be part of my examination committee I especially would like to thank **Prof. Nicola A. Spaldin** and **Prof. Marty Gregg**.

Among the collaborators, I would like to express my particular thanks to **Prof. Andres Cano** for enlightening theoretical discussions, some mathematical tricks, and the calculations on the domain walls, as well as **Dr. Stephan Krohns** for the dielectric spectroscopy measurements, valuable scientific discussions, and 'last-minute' proofreading. Furthermore, I thank **Prof. Massimiliano Stengel**, **Dr. Yu Kumagai**, and **Prof. Nicola A. Spaldin** for the theoretical calculations together with **Dr. Julia Mundy** for the TEM measurements, which were all necessary to better understand our SPM data. Furthermore, I would like to acknowledge **Dr. Zewu Yan** and **Dr. Edith Bourret–Courchesne** for providing the high quality $ErMnO_3$ single crystals.

Working in the FERROIC group has always been a pleasure due to the many friendly and inspiring people I met there. I thank **Dr. Morgan Trassin** for fruitful discussions, involving me in a side project on YIG thin films, and for creating good vibes in the AFM lab. Any SHG related questions during my time as a tutor were easily solved thanks to **Dr. Naëmi Leo** and **Dr. Thomas Lottermoser**. My knowledge in AFM got a big head start due to the great assistance of **Dr. Martin Lilienblum**, who taught me all the tricks and finesse on the device and how to obtain the 'very best' signals. I also appreciated that there was always time for discussions, which triggered various experimental ideas. For her great work and effort on the AC-cAFM measurements, I have to thank **Xiaoyu Dai**, whom I enjoyed working with during her master thesis.

Among the PhD offices, there is only one place to be, i. e., 'E 482.2'. Thank you **Ehsan Hassanpour Yesaghi** and **Christoph Wetli** for this fascinating and joyful time. The temporary office members **Matthias Hudl** and **Stefan Günther** are of course acknowledged, too. I furthermore thank **Peggy Schönherr** for discussing electronic transport mechanisms and introducing me to the low-temperature AFM, **Dr. Laura Maurel** for letting us characterizing the $SrMnO_3$ samples by CLM, **Josef Hecht** for helping with any electronic issues, and **Christian Tzschaschel** for additional Laue measurements. Last but not least, there are the distinguished members of the 'GLRG': **Sebastian Manz** and **Gabriele De Luca**. Getting to know you during the first year of my PhD was valuable and fun. I really liked our extracurricular activities, of which some were even 'moving'.

The people I encountered at the Forschungszentrum Jülich beamline at BESSY II deserve a special thanks for the exceptional and successful time I experienced during my many day and night shifts. **Dr. Ingo P. Krug** is acknowledged for various scientific discussions and input on the dose-dependent measurements. **Dr. Slavomir Nemšák**, thank you for all the support and advice, the arranged back-up beamtime, and the culinary excursions including an invitation to your place in Köpenick. **Dr. Daniel M. Gottlob**, measuring with you was always efficient and 'easy mobisi'. Thank you for proof reading the CLM experimental section and showing me some 'hip' places in the 'maze' of Berlin. I am looking forward to further 'quadruple K's' in the future. In addition, **Hatice Doğanay**, **Johanna Hackl**, and **Imtiaz Khan** are gratefully acknowledged for their strong support during various measurements and assistance in operating microscope or beamline. A place to stay in Berlin for pre- and post-beamtime relaxation was always accessible at **Arman Hashem Pour Roodsari**'s place. Thank you 'Atzepeng', for this terrific time.

Moreover, I want to express my sincere gratitude to my parents **Ulrike** and **Burkhard** as well as to my sister **Luise** for all their unconditional love and support from day one until today. At last, I have to thank my girlfriend **Maud**. Your tranquility, positive attitude, and inexhaustible optimism are unique and motivating, which became especially valuable during the final stage of writing this thesis.

Abstract

Domain walls are attracting significant interest in the field of (multi-)ferroic materials owing to their intriguing functional properties. The domain walls represent natural interfaces that can exhibit substantially different properties than the surrounding bulk due to their low symmetry and unusual electrostatics. The fact, that these interfaces can be moved, erased, and positioned at will is of strong technological interest and highly relevant for the design of domain-wall based nanoelectronic devices. Charged and neutral domain walls in ferroelectrics are of special interest, as they can show diverse electronic behavior ranging from highly conductive to strongly insulating states. Prior to implementation, however, further knowledge is required to generate walls with controllable output and power in order to emulate electronic nano-components such as diodes, transistors and gates.

The scope of this thesis is to present novel strategies to characterize and manipulate functional domain walls in complex ferroelectric oxides. Advanced microscopy studies are realized by combining state-of-the-art imaging techniques, including scanning probe microscopy (SPM) and cathode-lens microscopy (CLM).

Using hexagonal manganites ($R\mathrm{MnO}_3$) as model system, we demonstrate chemical impurity doping as a promising tool to engineer and improve the properties of functional domain walls. In p-type semiconducting ErMnO_3, chemical doping is applied to increase the current densities at charged domain walls by two orders of magnitude and tune from p-type to n-type dominated screening and transport behavior. Moreover, we demonstrate reversible electric-field control of the electronic transport at the charged domain walls, switching between resistive and conductive domain-wall states.

Aside from the charged walls, we perform a comprehensive analysis of neutral domain walls in ErMnO_3 and their functionality. Under adequate boundary conditions, these walls exhibit currents, which can be influenced by thermal annealing in oxygen atmosphere. We further find that the walls facilitate AC-to-DC conversion, emulating the functionality of classical diodes. The rectifying properties, including the practical frequency regime and magnitude of the output, are controlled via the conductivity of the adjacent domains.

Many of the aforementioned discoveries were enabled by the development of new experimental approaches in terms of SPM, including the application of electrostatic force microscopy (EFM) and frequency-dependent domain-wall measurements, as well as pioneering CLM experiments. In particular, x-ray photoemission electron microscopy (X-PEEM) was applied to access local domain-wall physics contact-free and with reduced data acquisition times, and the potential of low-energy electron microscopy (LEEM) was demonstrated to improve spatial resolution to a few nanometers.

This work thus provides novel insight into the physical properties of functional domain walls, demonstrates new advanced characterization techniques, and highlights novel opportunities for the design of future domain-wall based devices.

Zusammenfassung

Im Feld der (multi-)ferroischen Materialforschung genießen Domänenwände besondere Aufmerksamkeit wegen ihrer faszinierenden funktionalen Eigenschaften. Domänenwände verkörpern natürliche Grenzflächen, deren Eigenschaften sich vom benachbarten Bulkmaterial deutlich unterscheiden. Grund dafür sind reduzierte Symmetrie und eine ungewöhnliche Elektrostatik. Die Tatsache, dass diese Wände nach Bedarf bewegt, entfernt und positioniert werden können, ist von bedeutendem technologischen Interesse und maßgeblich für die Konstruktion Domänenwand basierter Nanoelektronik. Hierbei sind geladene und neutrale Domänenwände in Ferroelektrika besonders interessant, da ihr elektronisches Verhalten von extrem leitfähig bis stark isolierend variieren kann. Vor der Anwendung in elektronischen Komponenten ist jedoch weiteres Fachwissen zur Generierung von Domänenwänden mit kontrollierbarer Ausgabe und Leistung nötig, damit nanoelektrische Komponenten wie Dioden, Transistoren und Steuerelektroden nachgebildet werden können.

Im Rahmen dieser Arbeit werden neue Strategien zur Charakterisierung und Beeinflussung von funktionalen Domänenwänden in komplexen Oxidmaterialien vorgestellt. Fortgeschrittene mikroskopische Studien werden durch eine Kombination modernster Abbildungstechniken wie Rastersonden (SPM) und Kathodenlinsenmikroskopie (CLM) umgesetzt.

Anhand eines geeigneten Modellsystems, den hexagonalen Manganaten $R\mathrm{MnO}_3$, zeigen wir, dass das Dotieren von chemischen Verunreinigungen aussichtsreiche Möglichkeiten bietet Domänenwandeigenschaften zu kreieren und zu verbessern. Angewandtes chemisches Dotieren in p-Typ halbleitendem ErMnO_3 verstärkt die Stromdichte geladener Domänenwände um zwei Größenordnungen und erlaubt das Durchstimmen von p-Typ zu n-Typ dominiertem Abschirmungs- und Transportverhalten. Darüber hinaus wird die reversible Kontrolle über den elektronischen Transport an geladenen Wänden durch elektrische Felder demonstriert, was erlaubt zwischen isolierenden und leitfähigen Domänenwandzuständen zu schalten.

Abgesehen von den geladenen Wänden führen wir eine umfassende Analyse der neutralen Wände in ErMnO_3 und deren Funktionalität durch. Unter geeigneten Rahmenbedingungen weisen diese Wände Ströme auf, die sich durch thermisches Auslagern unter Sauerstoffatmosphäre beeinflussen lassen. Ferner stellen wir fest, dass diese Wände Wechsel- zu Gleichstrom konvertieren und dadurch die Funktionalität von Dioden nachahmen. Die Gleichrichteigenschaften, das heißt der zugängliche Frequenzbereich und die Größe der Ausgangsleistung, sind durch die Leitfähigkeitseigenschaften der angrenzenden Domänen kontrollierbar.

Viele der oben genannten Entdeckungen wurden durch die Erarbeitung neuer experimenteller Herangehensweisen ermöglicht. Auf dem Gebiet der Rasterson-

denmikroskopie sind das elektrostatische Kraftmikroskopie (EFM) und frequenzabhängige Domänenwandmessungen. Ferner wird Pionierarbeit durch Experimente mit Kathodenlinsenmikroskopie geleistet. Dabei wird insbesondere gezeigt, dass Röntgen-Photoemissionselektronenmikroskopie (X-PEEM) kontaktfreien Zugang zur Domänenwandphysik liefert und Datenerfassungszeiten reduziert. Das Potential von niederenergetischer Elektronenmikroskopie (LEEM) in der Domänenwandabbildung ist die räumliche Auflösungen von ein paar Nanometern.

Diese Arbeit liefert somit unerwartete Einblicke in die physikalischen Eigenschaften funktioneller Domänenwände, präsentiert neue fortschrittliche Analyseverfahren und wirft ein Streiflicht auf mögliche Entwürfe für zukünftige Domänenwand basierte Schaltungen.

Contents

1. Introduction **1**

2. Scientific background **3**
2.1. Ferroic materials . . . 3
2.1.1. Ferroelectricity . . . 5
2.1.2. A short review on electronic domain-wall transport . . . 17
2.2. Multiferroic hexagonal $R\mathrm{MnO}_3$ . . . 21
2.2.1. General properties . . . 21
2.2.2. Electronic transport at the domain walls . . . 25
2.2.3. Chemically doped compounds . . . 28

3. Experimental methods **33**
3.1. Atomic force microscopy . . . 33
3.1.1. Basic principle and experimental setup . . . 34
3.1.2. Conductive atomic force microscopy . . . 37
3.1.3. Piezoresponse force microscopy . . . 40
3.1.4. Electrostatic force microscopy . . . 42
3.2. Principles of cathode-lens microscopy . . . 44
3.2.1. Photoemission electron microscopy . . . 45
3.2.2. Low-energy electron microscopy . . . 48
3.3. Sample preparation . . . 49
3.3.1. Single-crystal growth . . . 49
3.3.2. Crystal orientation by back-reflection Laue method . . . 50
3.3.3. Surface treatments . . . 50

4. Electronic transport phenomena at charged domain walls **53**
4.1. Charged domain walls in ErMnO_3 . . . 53
4.1.1. Fundamental transport properties . . . 54
4.1.2. Time-dependent domain-wall currents . . . 55
4.1.3. Possible electronic conduction mechanisms . . . 56
4.2. Macroscopic properties of doped ErMnO_3 . . . 58
4.2.1. Robustness of the ferroelectric domain structure . . . 58
4.2.2. Electronic conductance properties of the bulk . . . 58
4.3. Tuning transport of the p-type screened walls . . . 60
4.3.1. Electrostatic responses at the domain walls . . . 61
4.3.2. Current-voltage characteristics . . . 62
4.3.3. Electronic domain-wall width . . . 64

4.4. Impact of n-type doping on domain-wall transport 66
  4.4.1. Persisting p-type transport 66
  4.4.2. N-type dominated domain-wall transport 67
4.5. Functional electronic inversion layers 69
  4.5.1. Voltage-driven insulating to conducting transition 69
  4.5.2. Manganese valence change at the domain wall 72
  4.5.3. Theoretical explanation 74
  4.5.4. Novel functional properties 76
4.6. Summary 78

5. Manipulating electronic transport at neutral domain walls 79
5.1. Direct-current transport properties 79
5.2. Tuning transport properties by oxygen annealing 82
5.3. Frequency-dependent rectification at domain walls 84
5.4. Contrast diagram of local current responses 90
5.5. Summary 91

6. Cathode-lens microscopy for domain-wall characterization 93
6.1. Motivation and state of the art 93
6.2. X-PEEM studies on hexagonal $ErMnO_3$ 94
  6.2.1. Characterization of charged domain walls 94
  6.2.2. Temperature-dependent conductance mapping 98
6.3. LEEM studies on domain walls 103
  6.3.1. Imaging of neutral domain walls 103
  6.3.2. Highly-resolved charged domain walls 106
6.4. Summary 110

7. Conclusion and outlook 111

A. Appendix 113
A.1. AC-cAFM addendum 113
A.2. List of measurements 115
A.3. List of figures 117
A.4. List of abbreviations 119

Bibliography 121

Curriculum vitae 133

1. Introduction

Our daily life would not be imaginable without the help of nanoscopic electronic circuits, memories, and transistors, enabling modern communication, traffic, and computing. Key requirements for the further development of future electronic building blocks are small size, fast performance, energy efficiency, and sustainability. Consequently, new device paradigms are required, which motivates scientists and engineers to look for alternative materials and concepts aside from semiconductor-based technology.

Strongly correlated oxide materials fulfill many of these requirements and offer fascinating opportunities. They exhibit collective electronic effects involving d and f electrons that are both of academic and technological interest[1]. The idea of all-oxide nanoelectronics gained significant momentum in 2004, when a two-dimensional electron gas was observed at the interface between the insulating oxides $LaAlO_3$ and $SrTiO_3$[2]. First field-effect transistors based on this material system have been realized, exhibiting, e. g., low gate voltage operation[3]. Yet, such heterointerfaces are stationary and their growth requires sophisticated deposition techniques.

A fundamentally different type of functional interface is found in ferroic materials[4]. Here, interfaces with intriguing functional properties occur naturally in form of domain walls, separating homogeneously ferroelastic, ferromagnetic, and/or ferroelectric ordered regions. These walls offer an additional degree of freedom that is not available at artificially grown heterointerfaces; they can be induced, moved, and erased on demand. Because of the different symmetry and structure present at these movable walls, novel functional properties arise including photovoltaic effects[5], enhanced electromechanical response[6], unusual electronic transport behavior[7–14], magnetoresistive properties[15], and more[16].

Charged and neutral domain walls in ferroelectrics are of particular interest, because these walls can exhibit diverse properties ranging from strongly insulating to highly conductive states. First evidence of increased conductance at ferroelectric domain walls dates back to the 1970s[17]. Several decades later, in 2009, the seminal discovery of enhanced conductance at domain walls in thin film $BiFeO_3$ created a boost in the field[7]. In the following years, enhanced domain-wall conductance was observed in other systems including textbook ferroelectrics[13,14], improper[11,12] and hybrid systems[18], which indicates that this phenomenon is general to ferroelectric walls.

Despite the significant progress that has been made in the field of conductive domain walls, major challenges remain to be taken before these entities can be incorporated into nanoelectronic devices. This includes, e. g., realization of controllable domain-wall signals and understanding of the response to alternating voltages.

Asides from that, faster, more practical, and more precise domain-wall characterization tools are required than currently applied state-of-the-art scanning probe (SPM) and transmission electron microscopy (TEM).

My thesis aims to understand the processes involved in electronic conductance at ferroelectric domain walls and to provide novel concepts of domain-wall manipulation and characterization with the emphasis on electronic transport. In order to achieve this, we use improper ferroelectric $ErMnO_3$ as a model system. $ErMnO_3$ is a p-type semiconductor that develops an exotic domain structure with an abundance of neutral and charged domain walls in the as-grown state. We study the walls by advanced scanning probe microscopy and tune their properties by chemical impurity doping, strong and alternating electric fields. In addition, we explore cathode-lens microscopy (CLM) as novel characterization technique, which offers contact-free probing, nanoscale resolution, and fast data acquisition times.

The outline of this thesis is the following. **Chapter 2** contains the general background on ferroelectric materials, domain-wall conduction and the properties of our hexagonal manganite model system. In **chapter 3**, we explain the main experimental techniques used in the framework of this thesis, which are scanning probe and cathode-lens microscopy. The subsequent chapters present the results obtained over the course of this thesis.

Chapter 4 focuses on the electronic transport phenomena at charged domain walls in $ErMnO_3$. After revisiting the fundamental transport properties, we present how chemical doping and strong electric fields affect the domain-wall output and to which extend this can be useful for the implementation of domain walls into future devices. **Chapter 5** is devoted to the properties of the neutral domain walls in $ErMnO_3$. We observe intrinsic changes at the wall and by using a novel scanning probe based technique we find that application of alternating voltages significantly influences the electronic transport performance. **Chapter 6** presents the capability of cathode-lens microscopy as an alternative technique to image and study domain walls. Benefits and limits of this technique are discussed with respect to our findings. Each results chapter ends with a short summary of the respective conclusions. Finally, a complete overview of all results together with an outlook is presented in **Chapter 7**.

2. Scientific background

This chapter gives a brief overview of the scientific background necessary to understand and to discuss the electronic transport phenomena observed at the domain walls of our model system multiferroic $\mathrm{ErMnO_3}$ (Chapters 4, 5, 6). First, we provide the definition of a ferroic material in general (Sec. 2.1). We then focus on ferroelectrics and discuss different types of ferroelectricity, their origin, properties of ferroelectric domain walls, and electronic conduction mechanisms (Sec. 2.1.1). This is followed by a short review on domain-wall conduction in ferroic materials (Sec. 2.1.2). At the end of this section, we present the multiferroic hexagonal manganites $R\mathrm{MnO_3}$[a] with emphasis on ferroelectric properties, electronic domain-wall transport, and possible chemical modifications (Sec. 2.2).

2.1. Ferroic materials

By definition *ferroic* materials need to develop spontaneous order of a macroscopic-measurable property that can be switched by an external conjugate field[19,20]. The technical term ferroic originates from ferromagnets, the longest-known ferroic materials, which were iron-based[b] compounds during their discovery 2500 years ago[21]. In modern context, *ferroic* stands for the uniform alignment of a spontaneous moment over many neighboring unit cells characterized by the order-parameter η of the ferroic phase. Ferri or antiferroic phases exist if differently-oriented sublattices of the same type of spontaneous moment partially or fully compensate their macroscopic-measurable property, respectively[22].

The ferroic state of a material evolves during a so-called ferroic phase transition, i. e., a high-symmetry prototype phase[c] G changes to a low symmetry phase L upon cooling below a critical temperature T_c[4]. A ferroic transition is ‘non-disruptive’, meaning that bonds get systematically distorted, but cannot be broken[4,23]. Consequently the following symmetry relation holds, namely

$$L \subset G, \tag{2.1}$$

which states that the group of symmetry elements of L define a subgroup of the symmetry elements of G[23]. The physical quantity arising in the ferroic phase L, which is fully responsible for the symmetry change from G to L, is called the order parameter η of the transition. The number of possible order-parameter orientations is given by the ratio of symmetry operations of both groups $q = |G|/|F|$[23]. Following Mermin[24], the allowed values of the order parameter span a space, which is the so-called order-parameter space. For example, two possible orientations of an order parameter represent two discrete points in the order parameter space. Any ordered ferroic material can now be described by a function $f(r)$ that assigns an allowed value of η to each point r of the material[24].

---

[a] Since we only consider the hexagonal manganites in this thesis, we omit to write h-$R\mathrm{MnO_3}$.

[b] The word ferroic originates from ferrum, the Latin word for the chemical element iron (Fe).

[c] The non-ferroic phase is often called ’para’-phase.

In the ferroic phase, regions of the material in which the orientation of the order parameter is homogeneously aligned to one state are called *domains*. Since all domain states are equal in energy (degenerate) and thus in probability, an unperturbed crystal[d] will, in general, develop a *domain structure* that contains domains of all allowed states. Interfaces separating two domains of different state are defined as *domain walls*. This zone, in which the order parameter has to reorient, cannot be described by any of the discrete points in order-parameter space. The topology of a given domain structure of an infinite crystal is defined by the number and crossings of domain walls, which in this context represent *topological defects*[22,24]. Domain walls are particularly interesting due to properties different from the bulk attributed to local changes in symmetry and structure.

Today we know four primary[e] types of ferroic order defining the different classes of ferroic materials (see Figure 2.1a). These are strain ϵ (ferroelastics), polarization P (ferroelectrics), magnetization M (ferromagnets), and toroidal moment T (ferrotoroidics), with their respective conjugate fields: stress σ, electric field E, magnetic field H, and toroidal field G[19,20]. Each ferroic order transforms differently under the parity operations of temporal reversal and spatial inversion (Fig. 2.1a). Consequently, ferroic order of a given type is only observed in crystal structures belonging to the same parity group, which is known as Von Neumann's principle[25,26]. For example, ferroelectric crystals have to be non-centrosymmetric as the occurrence of spontaneous polarization breaks spatial inversion symmetry. The concepts of ferromagnets, ferroelectrics, and ferroelastics have been well-established over the last 60 years[19,21,27–30]. However, ferrotoroidic order – which follows as a symmetry consequence – was just recently established[31] and ongoing research aims to advance the theoretical framework[32,33] and experimental characterization[34].

Materials that exhibit more than one primary ferroic order in the same phase have been defined as multiferroics in 1994 by Hans Schmidt[36]. The presence of more than one order can lead to new interactions like the magnetoelectric effect, i. e., changing the polarization P by an external magnetic field H or, vice versa, altering the magnetization M by an external electric field E (see green arrows in Fig. 2.1b). By the definition given above many standard ferroelectric materials would be multiferroics (e. g. $BaTiO_3$, $Pb[Ti_{1-x}Zr_x]O_3$ (PZT)) since they are also partially ferroelastic[23,37]. Due to fundamental and technological aspects, we nowadays speak of multiferroics, if materials combine ferroelectric with antiferro-, ferri-, or ferromagnetic order in

---

[d] Strain, external fields, defects, and geometry can strongly influence the domain structure.

[e] Primary stands for first order coupling of the free-energy to the conjugate field[4] (see Eq. 2.2).

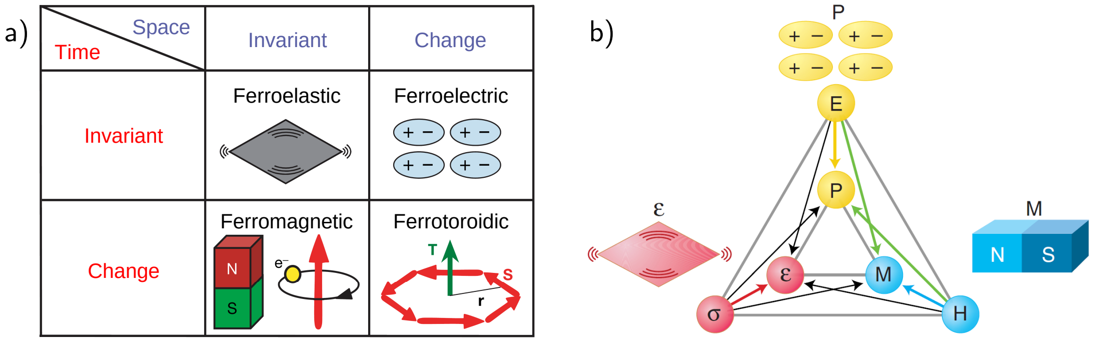

Figure 2.1.: Primary types of ferroic orders and their coupling in multiferroics. a) Ferroic orders and their transformation properties under parity operations[31,33]. b) In primary ferroic materials, electric field E, magnetic field H, and stress σ couple directly to polarization P, magnetization M and strain ϵ, respectively. In materials with more than one ferroic order (multiferroics), new interactions can arise, e. g., switching of magnetization M by an external electric field E or vice versa (green arrows). Graph (a) reprinted by permission from Macmillan Publishers Ltd: Nature, Ref. 31, copyright (2007). Graph (b) republished with permission of AAAS Science, Ref. 35, copyright (2005).

the same phase or multiple constituents of a heterostructure[38]. Among multiferroic materials, one further distinguishes between type I and type II. In the former, magnetic and ferroelectric order emerge individually, whereas in the latter, the magnetic and the ferroelectric transition occur jointly[38,39].

2.1.1. Ferroelectricity

Ferroelectrics define a subclass of ferroic materials, in which the long-range order of microscopic electric dipoles creates a macroscopic spontaneous polarization P_s that can be reversed by an electric field E. The field dependence of the polarization P of the material is typically described by a hysteresis curve (Fig. 2.2a), from which coercive field E_c and spontaneous polarization P_s can be determined as indicated. Once the coercive field is reached, permanent reversal of polarization occurs partially by domain nucleation, but mostly through domain growth involving domain-wall movement.

Ferroelectric materials are classified into proper and improper systems[39,40]. In proper ferroelectrics, the spontaneous polarization is the primary order parameter, directly determining the free energy describing the ferroic phase transition. In contrast, improper ferroelectrics are described by a different primary order to which the spontaneous polarization P_s is coupled. Consequently, P_s represents a secondary order that results as a *byproduct* of the primary oder parameter[40–42].

The ferroic phase transition that creates ferroelectricity can be a first- or second-order phase transition. In second-order transitions the thermodynamically stable phase evolves continuously, whereas first-order transitions are discontinuous, involving nucleation and growth of the stable phase.

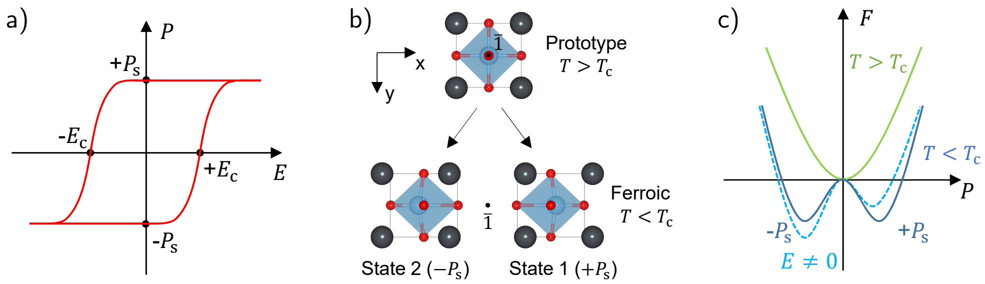

Figure 2.2.: Hysteresis, microscopic mechanism, and free energy of ferroelectrics. a) Ideal hysteresis of a ferroelectric defining spontaneous polarization P_s and coercive field E_c. b) Illustration of a ferroic transition taking the real structure of the perovskite material $\mathrm{PbTiO_3}$[44] as an example. The high-symmetry prototype phase (paraelectric) at $T > T_\mathrm{c}$ is depicted on top. Reducing the temperature ($T < T_\mathrm{c}$) induces the loss of inversion symmetry $\bar{1}$ and the formation two ferroelectric states with distinct orientation. We note that the deformation can also occur along the y- or z-direction, leading to a total of six ferroelectric domain states. c) Free energy as a function of P. One stable state exists in the prototype phase (green curve) and two energy- and displacement-equivalent states are present in the ferroic phase (blue curve). Application of an external field below T_c favors one ferroic state over the other (dashed curve). Atomic structure in (b) rendered with the VESTA software[45].

2.1.1.1. Proper and improper ferroelectricity

In **proper ferroelectrics**, the primary order parameter represents the spontaneous polarization that evolves during the ferroic phase transition (see Sec. 2.1). The top of Figure 2.2b shows a cubic perovskite ($\mathrm{ABO_3}$) structure (a typical prototype for many ferroelectrics, see Sec. 2.1.1.2), which possesses an inversion center $\bar{1}$ as indicated by a black dot in the middle of the unit cell. During the phase transition the loss of inversion operation leads to the formation of two possible ferroic states with distinct orientation. Here, the shift of the metallic cations A/B (black/blue) directly defines the spontaneous polarization P_s. The equal displacement in positive or negative direction along dimension x defines domain state 1 ($+P_\mathrm{s}$) and 2 ($-P_\mathrm{s}$), respectively. From the schematic in Figure 2.2a we see further, that the lost symmetry element $\bar{1}$ transforms one domain state into the other[4,43].

The thermodynamic description of the ferroic phase transition of a proper ferroelectric can be explained in terms of Landau theory[46–48]. Here, we consider a second-order phase transition and include the interaction of the polarization P (primary order parameter) with its conjugate electric field E. Now, the simplest expression of the thermodynamic potential Φ reads[23]

$$\Phi = \Phi_0 + \frac{1}{2}\alpha P^2 + \frac{1}{4}\beta P^4 - PE, \tag{2.2}$$

with $\alpha = \alpha_0(T - T_\mathrm{c})$ and the temperature independent coefficients $\alpha_0 > 0$ and $\beta > 0$.

In order to determine the stable ground states of the homogeneous system, we omit the last term in (2.2) and determine $\partial\Phi/\partial P = 0$, while $\partial^2\Phi/\partial P^2 > 0$. Above the phase transition ($T > T_\mathrm{c}$), only one stable state exists (i. e. $P = 0$), corresponding to the minimum of the green curve shown in Fig. 2.2c. In the ferroelectric phase ($T < T_\mathrm{c}$), we find the two degenerate solutions

$$\pm P_\mathrm{s} = \pm\sqrt{\alpha_0(T_\mathrm{c} - T)/\beta}, \tag{2.3}$$

which leads to the potential distribution described by the blue curve in Fig. 2.2c. Note that the spontaneous polarization in (2.3) shows a square-root dependence on temperature, which is typical for proper ferroelectrics. The application of an external field E lifts the degeneracy of the two ground states due to the linear-coupling term in (2.2). The dashed blue line in Fig. 2.2c shows the resulting potential. In this case, the applied electric field favors the $-P_\mathrm{s}$ state and hence explains why ferroelectrics switch under external fields.

In **improper ferroelectrics**, the spontaneous polarization does not play the role of the primary order parameter. In order to describe the phase transition of an improper ferroelectric, the thermodynamic potential needs to include a primary order parameter of at least two components (η_1, η_2) and a coupling term of order parameter and electric field that is linear in the electric field[42]. Following Ref. 23, we use the improper ferroelectric $\mathrm{Gd_2(MoO_4)_3}$[49] as an example[f], for which the second-order phase transition can be described by the potential

$$\tilde{\Phi} = \tilde{\Phi}_0 + \frac{1}{2}\alpha(\eta_1^2 + \eta_2^2) + \frac{1}{4}\beta_1(\eta_1^4 + \eta_2^4) + \frac{1}{2}\beta_2\eta_1^2\eta_2^2 + \gamma(\eta_1^2 - \eta_2^2)E, \tag{2.4}$$

with $\alpha = \alpha_0(T - T_\mathrm{c})$ and the temperature independent coefficients $\alpha_0 > 0$, $\beta_2 > \beta_1 > 0$, and γ. In case of $\mathrm{Gd_2(MoO_4)_3}$, the primary order parameter (η_1, η_2) describes the amplitude of two waves of atomic shifts that lead to a doubling of the unit cell volume[23,42]. For simplicity, we do not include higher-order electric-field or mechanical cross-terms in (2.4).

Four possible solutions are found for the homogeneous ground state: $(+\eta_\mathrm{s}, 0)$, $(-\eta_\mathrm{s}, 0)$, $(0, +\eta_\mathrm{s})$, $(0, -\eta_\mathrm{s})$ with $\eta_\mathrm{s} = (\alpha_0(T_\mathrm{c} - T)/\beta_1)^{1/2}$. The ground states correspond to four distinct points in the order parameter space and the spontaneous polarization can be obtained from $\partial\tilde{\Phi}/\partial E = -P$, which reads

$$P_\mathrm{s} = -\gamma(\eta_1^2 - \eta_2^2) = \pm\gamma\alpha_0(T_\mathrm{c} - T)/\beta_1. \tag{2.5}$$

This equation has two important consequences for the spontaneous polarization of improper ferroelectrics: (i) P_s exhibits a temperature dependence different from the typical square-root behavior demonstrated by (2.3) for proper ferroelectrics (linear in the particular case here), (ii) P_s is directly defined by the state of the primary order parameter, i. e., the two shifts in the lattice, which hence predetermine the ferroelectric domain structure.

We now have to distinguish the different domain types present in improper ferroelectrics. Domain states that differ only by the sign of the order parameter (e. g.

---

[f] Since the thermodynamic potential of our model system ($R\mathrm{MnO_3}$) is more complex[50], we use $\mathrm{Gd_2(MoO_4)_3}$ to describe the properties of improper ferroelectrics.

$(+\eta_\mathrm{s},0)$ and $(-\eta_\mathrm{s},0)$) show no net change in spontaneous polarization. Since a sign change in the order parameter describes a 180° phase shift in the wave of the atomic shifts, this corresponds to a shift in translation symmetry and hence these domain states represent *translation domains* [23,51]. In contrast, a sign change in the polarization P_s occurs for domain states that differ in the orientation of the order parameter vector $(\eta_1,\ \eta_2)$, e. g., $(+\eta_\mathrm{s},0)$ and $(0,+\eta_\mathrm{s})$. In this case, Eq. (2.5) yields $P_\mathrm{s}=-\gamma\eta_\mathrm{s}^2$ and $P_\mathrm{s}=\gamma\eta_\mathrm{s}^2$, respectively, and these states corresponds to *orientation domains* [23,51].

As a consequence, improper ferroelectrics show a different temperature dependence of the spontaneous polarization P_s, display different dielectric anomalies at the critical temperature T_c [41], usually exhibit smaller values of P_s, and are able to develop exotic domain structures in the as-grown state[18,52–54].

2.1.1.2. Microscopic origin of ferroelectricity

The driving force to develop ferroelectricity can have different microscopic origins. This section explains the microscopic mechanisms facilitating ferroelectricity in proper and improper systems.

Many proper ferroelectrics result from the cubic perovskite structure $\mathrm{ABO_3}$, where two different displacive mechanisms can cause inversion symmetry breaking by the formation of permanent dipoles: i) Covalent bonding between the d^0 orbitals of the B cation ($\mathrm{Ti^{4+}}$, $\mathrm{Zr^{4+}}$, $\mathrm{Nb^{5+}}$) and the $2p$ orbitals of the surrounding oxygen leads to off-centering of the B cation in, e. g., $\mathrm{BaTiO_3}$, $\mathrm{KNbO_3}$. ii) Long-range order of the electron lone pairs of A cations with $6s^2$ configuration ($\mathrm{Bi^{2+}}, \mathrm{Pb^{2+}}$) create polarity for example in $\mathrm{BiFeO_3}$. A combination of both mechanisms can be found in $\mathrm{PbTiO_3}$, where both the Ti $3d^0$ and the Pb $6s^2$ states hybridize with the $2p$ states of oxygen resulting in large displacements of both cations[44,55] (see Fig. 2.2b). Displacive mechanisms result in large polarization values, e. g., $\mathrm{BaTiO_3}$ $P_\mathrm{s}=26\,\mu\mathrm{C\,cm^{-2}}$ [56], $\mathrm{PbTiO_3}$ $P_\mathrm{s}=57\,\mu\mathrm{C\,cm^{-2}}$ [26], $\mathrm{BiFeO_3}$ $P_\mathrm{s}=100\,\mu\mathrm{C\,cm^{-2}}$ [57]. Other proper ferroelectrics result from disorder-order mechanisms. Here, ordering of molecular units with permanent dipoles or the formation of hydrogen bonds create a spontaneous polarization[58].

The ferroelectricity in improper ferroelectrics may be geometrically, charge-order, and magnetically driven[38,40,59]. In geometrically driven ferroelectrics buckling or rotation of atomic polyhedra causes non-polar, but inversion-symmetry-breaking distortions of the lattice often accompanied by a multiplication of the unit-cell volume[42]. Below this transition a spontaneous polarization starts to develop due to a non-linear coupling between the polarization and the lattice distortion (see Eq. 2.5). Prominent examples for geometric ferroelectrics are the hexagonal manganites $R\mathrm{MnO_3}$ [60], which we will explore in more detail in Section 2.2, and the Ruddlesden–Popper compound $\mathrm{(Ca,Sr)_3Ti_2O_7}$ [18]. The latter belongs to the so-called hybrid improper ferroelectrics, in which the combination of two non-polar lattice distortions induces a ferroelectric polarization[61].

In charge-ordered ferroelectrics, the spontaneous polarization is created by low-symmetrical ordering of two or more charge species with different valence[62]. One likely but still questioned[63] candidate for charge-ordering is $LuFe_2O_4$[64,65]. It was observed that layers with different Fe^{2+}: Fe^{3+} ratios form in this compound below $T \lesssim 350\,\mathrm{K}$ giving rise to a net polarization of up to $25\,\mu\mathrm{C\,cm^{-2}}$[64].

Electric-dipole moments can also be induced by acentric spin arrangements in frustrated magnets with complex spin structures[38,40,66,67]. In these systems, the inverse Dzyaloshinskii-Moriya interaction[68–70] or exchange-striction effects[38,71] induce a polar state in the ionic lattice. Representatives of magnetically-driven ferroelectrics are orthorhombic $TbMnO_3$ and $TbMn_2O_5$.

We have discussed the microscopic origins in ferroelectrics and have seen that they can be substantially different. Based on this knowledge, we now want to discuss the domain-wall types that arise in proper and improper ferroelectrics.

2.1.1.3. Domain walls in ferroelectrics

Ferroelectric domain walls separate two adjacent domains with different orientation of the polarization. In the context of this thesis, we distinguish two types of ferroelectric domain walls: charged and neutral walls.

Domain-wall configurations In case of a uniaxial ferroelectric, the left column of Figure 2.3a presents characteristic domain-wall configurations. Uniaxial means that the polarization aligns only along one axis of the crystal, and thus all domain walls are 180° walls[g]. Additional arrangements arise in ferroelectrics that have more than one axis of polarization as illustrated by the right column[59]. We observe neutral, positively charged and negatively charged domain-wall configurations. The bound charge density at the domain wall is given by the divergence in polarization P[72]

$$\mathrm{div}\,P = -\rho_\mathrm{b} \tag{2.6}$$

In the cases presented in Fig. 2.3, positively charged domain walls correspond to head-to-head (→←) configurations, whereas negatively charged domain walls represent tail-to-tail (←→) configurations. For an arbitrary domain wall configuration, the polarization charge density ρ_P located at the wall can be determined by the the difference of the normal components of the polarization vectors of domain 1 and 2 as illustrated in Fig. 2.3b. If n represents the normal vector of the domain wall pointing into domain 2, we can derive whether the domain wall is neutral ($\rho_P = 0$), positively ($\rho_P > 0$) or negatively charged ($\rho_P < 0$) according to[22]

$$\Delta P \cdot n = P_2 \cdot n - P_1 \cdot n = -\rho_P. \tag{2.7}$$

Figure 2.3c shows where the 180° configurations in Fig. 2.3a can be found along a domain wall that meanders arbitrarily through a uniaxial ferroelectric. We clearly see that these cases represent the extremes and between the colored dots we find

---

[g] Here, the angle corresponds to the rotation angle of the polarization from one domain to the next.

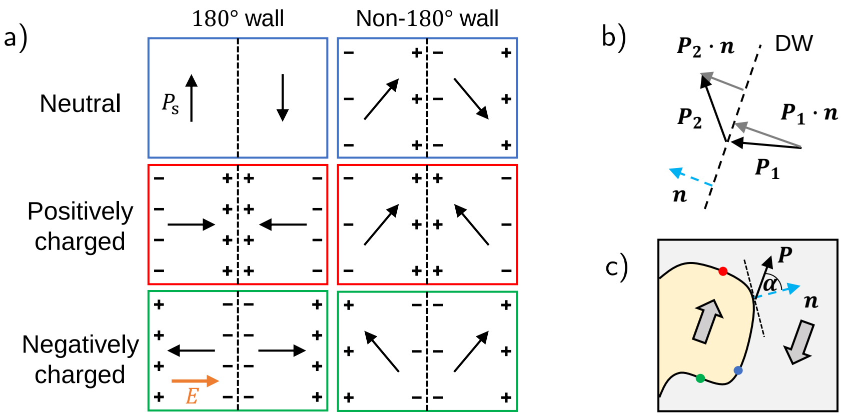

Figure 2.3.: Species of charged and neutral domain walls in ferroelectrics. a) Neutral, positively, and negatively charged domain walls. The left column presents species of domain walls in uniaxial ferroelectrics. Additional domain walls arise in multiaxial ferroelectrics (right column). b) General representation of the polarization charge at the domain wall generated by the difference of the normal components of the polarizations from domain 1 and 2. c) Illustration where the domain walls in (a) can be found along a meandering domain wall of a uniaxial ferroelectric. The polarization lies in the plane as indicated by the arrows. α represents the angle between the polarization and the normal of the domain wall. Graph (a) and (b) partially adapted from Refs. 59 and 22.

inclined[22] domain walls. For the specific domain wall in Fig. 2.3c, we see that the static polarization charge changes continuously with the angle α between the domain wall normal and the polarization; it equals to $2P_\mathrm{s}\cos(\alpha)$. Note that inclined domain-wall configurations are never neutral; they always have a finite charge contribution. Furthermore, they often violate the elastic compatibility condition (see below), giving rise to additional polarization contributions provoked by flexoelectric effects[h] [22].

Domain-wall stability The stable configuration of a domain wall in a crystal is, in general, determined by the minimum of the domain-wall free energy[74] given as

$$F = \int \sigma_{ij}\epsilon_{ij}dV + \int D_i E_i dV + \int \sigma_\mathrm{w} dS. \tag{2.8}$$

The energy includes contributions from external or internal stresses σ_{ij}, from depolarization fields E_i, and from the structural domain-wall energy σ_w. In the following discussion, we will only consider domain walls that fulfill the elastic compatibility criterion stating $\sigma_{ij}\epsilon_{ij} = 0$. Such domain walls meet in an unstressed state along the wall and have been defined as *permissible* domain walls[74]. We note that contributions from internal and external stresses can have significant influence on the domain wall configuration, leading to compromise domain-wall states higher in electric and structural energy than in the unstressed state[75,76].

---

[h] Flexoelectricity denotes the creation of spontaneous polarization by strain gradients[73].

We begin with domain walls of **proper ferroelectrics**. Landau theory allows us to determine the structural domain-wall energy. If (2.2) is expanded with a gradient term $\nabla = (\partial/\partial x, \partial/\partial y, \partial/\partial z)$ in the polarization P, one obtains

$$\Phi = \Phi_0 + \frac{1}{2}\alpha P^2 + \frac{1}{4}\beta P^4 + \frac{1}{2}\delta(\nabla P)^2, \tag{2.9}$$

with the correlation coefficient δ[23]. This coefficient determines the energy cost if the polarization changes from one unit cell to the next ($\delta > 0$). For a neutral (planar) 180° domain wall in an infinite ferroelectric, the following solution for the domain wall profile can be found[23]

$$P = P_\mathrm{s} \tanh\left(\frac{x}{t_\mathrm{th}}\right), \tag{2.10}$$

where t_th is a measure for the structural wall thickness

$$t_\mathrm{w} = 2t_\mathrm{th} = 2\sqrt{-2\delta/\alpha}. \tag{2.11}$$

As $t_\mathrm{w} \propto \sigma_\mathrm{w}$[23], both structural domain-wall width and energy are directly proportional to the correlation coefficient δ and inversely proportional to the leading coefficient α of the Landau expansion (2.9). The latter is usually quite large for proper ferroelectrics and hence neutral 180° walls are almost atomically sharp[77] (width in the order of one unit cell; $\sim 0.5\,\mathrm{nm}$ for PZT[78]) and represent the energetically most stable configuration since only structural domain-wall energy contributes predominantly to (2.8).

At charged domain walls, the divergence in polarization causes a larger structural width that can be in the order of several unit cells[76,78] ($\sim 5\,\mathrm{nm}$ for PZT[78]). Here, additional energy contributions arise due to the emerging depolarization fields between the bound domain wall charges (see orange arrow in Fig. 2.3a). Charged domain walls are thus always unfavored with respect to neutral configurations. The unscreened depolarization field E in Fig. 2.3a, which is opposed to the direction of P_s, can be obtained via $\varepsilon E + P_\mathrm{s} = 0$[72] and hence

$$E = \frac{-P_\mathrm{s}}{\varepsilon}, \tag{2.12}$$

with the dielectric permittivity ε of the ferroelectric material. The magnitude of E can get so large that ferroelectricity is suppressed due to a drop in the critical temperature T_c by several thousand Kelvin[72]. Moreover, the depolarization field can exceed the coercive field E_c, which causes domain-wall movement until a domain structure with neutral walls is established (electrostatic compatibility condition). Consequently, charged domain walls can only be stabilized if the bound charge at the domain wall is sufficiently screened[22,72,74].

Screening of bound domain-wall charge ρ_b can happen via several mechanisms[72]. One would be the creation of an electron-hole pair by exciting an electron over the band gap E_{g} of the ferroelectric. In this case, full screening of the domain wall requires the following energy[72]

$$E_{\mathrm{scr}} = |\rho_{\mathrm{b}}|\, E_{\mathrm{g}} = |\mathrm{div}\, P|\, E_{\mathrm{g}}. \tag{2.13}$$

Due to this energy term also the completely screened domain wall, for which the second term in (2.8) equals to zero, is energetically more costly than any neutral configuration. In proper ferroelectrics, where polarization values are high and bulk properties rather insulating (see Sec. 2.1.1.2), charged domain walls are rarely found, but can be stabilized by means of specialized poling procedures[10,13,14,72], super band-gap illumination[79], defects[13], and strain[76].

For **improper ferroelectrics**, structural domain-wall width and energy can be determined in a similar way as presented above, i. e., via introducing an order-parameter gradient term in the thermodynamic potential[23]. If we turn back to the case discussed before (see Eq. 2.4), where four stable domain states exist, we find two basic domain-wall types: 180° and 90° domain walls[23]. Here, the angle correspond to the respective rotations of the order parameter (η_1, η_2) in the order parameter space. Rotations by 180° and 90° correspond to translation[i] and orientation domain walls; the latter representing an actual ferroelectric (or polarization) domain wall[23] (see Sec. 2.1.1.1). One obtains the following linear solutions[23] for the domain wall profiles of 180° domain walls

$$\eta_{1,2} = \eta_{\mathrm{s}} \tanh\left(\frac{x}{t_{\mathrm{th}}}\right) \tag{2.14}$$

and 90° domain walls

$$\eta_1 = \frac{\eta_{\mathrm{s}}}{2}\left[1 + \tanh\left(x/t_{\mathrm{th}}\right)\right] \tag{2.15}$$

$$\eta_2 = \frac{\eta_{\mathrm{s}}}{2}\left[1 - \tanh\left(x/t_{\mathrm{th}}\right)\right]. \tag{2.16}$$

Obviously from both domain-wall profiles, the stable wall width $t_{\mathrm{w}} = 2t_{\mathrm{th}}$ is determined by the Landau coefficients of the primary order parameter (see Eq. 2.4), which is thus independent of the polarization. Moreover, the depolarizing field emerging at a charged domain wall in improper systems does not induce a drop in the critical temperature T_{c}[22] and is usually weaker than in proper systems as it arises as a secondary effect (Sec. 2.1.1.2). Consequently, the domain structure and the stable domain-wall configurations of improper ferroelectrics are not bound to the electrostatic compatibility condition.

For example, a plethora of charged domain walls is observed in the as-grown state of the following geometrically driven improper systems $R\mathrm{MnO}_3$[11,12,53] and $(\mathrm{Ca,Sr})_3\mathrm{Ti}_2\mathrm{O}_7$[18] due to the reasons discussed above. In addition, these two examples highlight that the resulting domain wall architecture depends strongly on the primary order parameter. In the uniaxial ferroelectric $R\mathrm{MnO}_3$, domain walls meander continuously through the crystal allowing all kinds of domain wall angles. In contrast, domain walls in the multiaxial ferroelectric $(\mathrm{Ca},\mathrm{Sr})_3\mathrm{Ti}_2\mathrm{O}_7$ orient preferentially along certain crystallographic planes (compare Fig. 2.5 and 2.7).

---

[i] Translation domain wall are often called antiphase boundaries due to a phase shift in the order parameter by 180°.

Domain-wall conductance The microscopic origin responsible for enhanced conductance at domain walls can be different for charged and neutral domain walls. **Charged domain walls** reflect a divergence in polarization, which requires screening by intrinsic charge carriers in order to be stabilized (see above). Screening can be facilitated by electrons, holes, and charged defects, e. g., oxygen vacancies. The total charge density at the wall can be split into the individual components[22]. This yields

$$\rho = \rho_\mathrm{b} + \rho_\mathrm{free} + \rho_\mathrm{mobile\ defects} + \rho_\mathrm{immobile\ defects} + \ldots, \tag{2.17}$$

where ρ_free corresponds to the density of free charger carriers, i. e., electrons and holes. The density and mobility of the screening charges determine the local electronic transport properties of a charged domain wall.

The screening length over which the charge carriers screen the polarization divergence at the wall is influenced by the strength of the polarization and the dopant concentration. Both factors can, e. g., determine whether a classical or a degenerate electron gas forms at the domain wall (an overview is found in Ref. 80). For small polarization values and dopant concentrations a classical gas is found and the screening length corresponds to the Debye length, i. e.,

$$\lambda_\mathrm{D} \propto \frac{1}{\sqrt{n_\mathrm{i}}}, \tag{2.18}$$

being inversely proportional to the equilibrium concentration n_i of the intrinsic, free charge carriers in the neutral region of the semiconducting ferroelectric[80,81]. The Debye screening length refers to the electrostatic domain-wall potential and can be considered as the nominal wall width[82].

Several theoretical studies have addressed formation, screening, and static conductivity properties of charged domain walls[80,83–85]. An important framework has been published by Eliseev et al.[84], who used Landau-Ginzburg-Devonshire theory in order to describe static domain-wall conductivity in a donor-doped (n-type), semiconducting, uniaxial ferroelectric. The results can be transferred on p-type materials by simply changing the sign of domain wall, dopant, and charge carrier. It was found that the increase of the static conductivity at head-to-head (→←) walls is attributed to the accumulation of electrons, which form a space-charge layer of about 40 – 100 correlation lengths r_c (see Fig. 2.4a). The fully charged domain-wall configuration shows an increase in conductivity by three orders of magnitude. The width of the conductive region changes slightly, if the charge carrier concentration is changed by

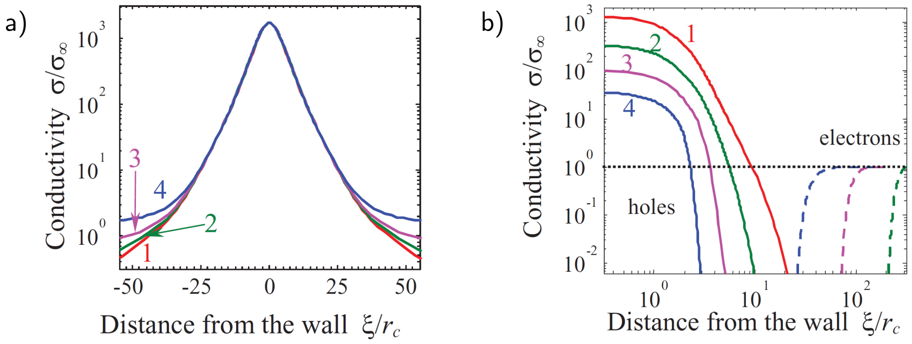

Figure 2.4.: Calculated static domain-wall conductivity of an n-type semiconductor. a), b) Relative conductivity as function of electron (n-type) doping at majority and minority carrier screened domain walls, respectively. In an n-type system the wall in (a) corresponds to a head-to-head configuration, whereas the wall in (b) is of tail-to-tail type. Curves 1 to 4 represent bulk dopant concentrations of $N_{\mathrm{d}0} = 10^{-17}, 10^{-18}, 10^{-19}, 10^{-20}\mathrm{cm}^{-3}$. Reprinted graphs (a) and (b) with permission from Ref. 84, copyright (2011) by the American Physical Society.

doping[j] (see Fig. 2.4a). Note that this is in agreement to the Debye screening length in (2.18).

On the contrary, tail-to-tail (←→) walls are screened by accumulation of holes and ionized, positively charged donors, while electrons are depleted in their vicinity. The hole accumulation width is in the order of 5 – 10 r_{c}, whereas the width of accumulated ionized donors and depleted electrons is the same and corresponds to 100 – 200 r_{c}. Due to this combination of a narrow region of accumulated mobile holes and a wider region of depleted electrons, the static conductivity at the tail-to-tail wall should be increased right at the center of the wall and reduced further outside. The increase in conductivity at the head-to-head wall is expected to be an order of magnitude lower due to the low mobility of the heavy holes, which represent the minority carriers of the investigated n-type system. Due to the combination of donor and minority carrier screening, the head-to-head wall shows a strong width dependence on dopant concentration. Remarkably, wall width and conductivity increase with decreasing doping concentration.

The correlation length r_{c} depends on the parameters of the Landau-Ginzburg-Devonshire model. Here, LiNbO$_3$ was used as a model system, which yields $r_{\mathrm{c}} = 0.4\,\mathrm{nm}$. Consequently, we obtain the following width-values: for majority carrier accumulation 16 – 40 nm, for majority carrier depletion/ ionized donor accumulation 40 – 80 nm, and for minority carrier accumulation 2 – 4 nm. Experimentally, the first two values have been confirmed in two individual studies that compared the width of conducting tail-to-tail and insulating head-to-head walls in p-type RMnO$_3$[11,12] (see Sec. 2.2.2). Yet, increased conduction contributions due to a narrow sheet of minority charges has so far not been observed.

---

[j] Note that this becomes apparent if all conductivity profiles in Fig. 2.4a are normalized to the background value of the bulk σ_∞.

At **neutral domain walls**, we can exclude charge carrier accumulation due to a divergence in the polarization since it is nominally zero, i. e., $\operatorname{div} P \approx 0$. Other mechanisms have been discussed to dictate the electronic transport properties of neutral domain walls. Here, defect agglomeration[8,86,87], band-gap lowering[7,88], local strain[89,90], and parent phases[53] can, in principle, alter the domain-wall conductance (see Sec. 2.1.2). The reason for the accumulation of defects at the domain wall, for example, is the associated lowering of the domain-wall energy described by (2.8).

2.1.1.4. Electronic conduction mechanisms in ferroelectrics

As the electronic transport at ferroelectric domain walls can have different origins, several electronic transport mechanisms are possible. Ferroelectrics represent semiconductors with a band gap E_g and an electron affinity χ[81,91]. As transport at domain walls is usually probed via metallic coated probes or electrodes, a barrier can form at the metal-ferroelectric interface. For example, the ideal barrier between a metal and a p-type semiconductor can be described by

$$\phi_\mathrm{b} = E_\mathrm{g} + \chi - \phi_\mathrm{m}, \tag{2.19}$$

where ϕ_m presents the work function of the metal[91]. For $(E_\mathrm{g} + \chi) > \phi_\mathrm{m}$, a finite barrier develops and electronic transport becomes interface dominated. Vice versa, an ohmic contact develops and the transport is governed by the bulk[k].

Based on these two scenarios, we explain possible transport mechanisms, considering the following configuration of a two-point measurement: A p-type semiconducting sample is sandwiched between two metal contacts, where one contact is always ohmic and the other one can form a barrier as described above. This description fits well to our experimental configuration, in which one contact dominates the transport scenario, i. e., a small probe in contact with a thick sample.

Interface-limited transport One typical interface-limited mechanism that has been discussed with respect to domain-wall transport is thermionic emission[9,86,92]. Here, electrons are thermally emitted over the barrier and the current density $J = I/A$ can be described by

$$J(V) = J_0 \left[\exp\left(\frac{eV}{\eta k_\mathrm{B} T} \right) - 1 \right], \tag{2.20}$$

where the saturation current density

$$J_0 \propto T^2 \exp\left[-\frac{\phi_\mathrm{b} - e\sqrt{eE/4\pi\varepsilon_0\varepsilon}}{k_\mathrm{B} T} \right] \tag{2.21}$$

---

[k] Strictly, Eq. (2.19) only holds, if no interface states or layers are present. The latter often lead to a barrier that is independent of the metal work function ϕ_m[91].

is dependent on temperature T, electric field E, and the dielectric constant ε. Elementary charge, Boltzmann constant, vacuum permittivity, ideality constant, and applied voltage are represented by e, k_{B}, ε_0, η, and V, respectively. For forward bias (negative voltage at the barrier-forming contact)[1] one obtains

$$J(V) = J_0 \exp\left(\frac{eV}{\eta k_{\mathrm{B}} T}\right), \tag{2.22}$$

if $V > 3\eta k_{\mathrm{B}} T/e$[91]. Plotting $\ln(J)$ vs. V results in a linear function that allows to determine the ideality constant η from its slope. The ideality constant is close to unity when thermionic emission currents dominate, i. e., at high temperatures and for low dopings. At low temperatures and high dopings, tunneling and recombination currents become dominant and η can substantially differ from unity[91]. Other reasons for high ideality constants can be edge/shunt currents or a high density of defects[93,94].

Under reverse-bias (positive voltage at the barrier-forming contact) the current gets blocked and (2.20) turns into the Richardson-Schottky equation

$$J(V) \approx J_0 \propto T^2 \exp\left[-\frac{\phi_{\mathrm{b}} - e\sqrt{eE/4\pi\varepsilon_0\varepsilon}}{k_{\mathrm{B}} T}\right], \tag{2.23}$$

for $V > 3\eta kT/e$[91]. The current density is now dominated by image-force lowering of the barrier described by the exponential-square-root field-dependence. Linearization is obtained by plotting $\ln(J)$ versus $E^{1/2}$. If the mean free path of the charge carriers gets smaller then the thickness of the semiconductor, Simmons' modification of (2.23) holds[95] and the current density reads as follows

$$J \approx J_0 \propto T^{3/2} E \exp\left[-\frac{\phi_{\mathrm{b}} - e\sqrt{eE/4\pi\varepsilon_0\varepsilon}}{k_{\mathrm{B}} T}\right]. \tag{2.24}$$

Plotting $\ln(J/E)$ over $E^{1/2}$ gives a linear relationship. The linear plots of (2.23) and (2.24) provide access to the dielectric constant ε of the semiconductor. Whether the dielectric constant corresponds to the static ε_{s} or optical permittivity ε_∞ depends on the transit time of the charge carrier to cross the barrier[91]. Experiments have shown that transport in silicon and insulating oxides is determined by permittivities close to the static[91] and optical values[96], respectively.

Bulk-limited transport If no barrier forms at the contact, the standard bulk-limited transport mechanism would be ohmic conduction, but this is rarely observed in oxide materials[37]. Other bulk-limited mechanisms can be space-charge-limited conduction (SCLC), hopping conduction, and Poole-Frenkel emission[97].

---

[1] We note that this only holds for a p-type semiconductor; the sign of the voltage for forward bias will change if the semiconductor is n-type.

In SCLC the injected charges drive the field and thus control the current density[91] that has the following non-linear relationship[98,99]

$$J \propto V^m, \tag{2.25}$$

with the exponent $m = T^*/T + 1$ depending on inter-band-gap states (traps). For a conductor with no or shallow traps $m = 2$, which leads to the typical Child's law with quadratic voltage dependence. For $m > 2$, the traps are distributed in energy with the following energy dependence $\propto \exp(-E/k_\mathrm{B}T^*)$ from the valence-band maximum (VBM) / the conduction-band minimum (CBM). Plotting $I(V)$ data in a double logarithmic plot allows to determine the exponent and to obtain information about the trap states in the material.

Hopping conduction corresponds to tunneling of charge carriers between different trap states[97]. The expression for the current density is

$$J \propto \exp\left(-\frac{E_\mathrm{a}}{k_\mathrm{B}T}\right)\exp\left(\frac{eaE}{k_\mathrm{B}T}\right), \tag{2.26}$$

with the mean hopping distance a and the energy difference between the trap level and the bottom of the conduction band, i. e., the activation energy E_a. Determining the slope of a $\ln(J)$ over E plot, allows to obtain the trap spacing a[97].

In contrast to hopping, Poole-Frenkel emission describes thermionic emission of charge carriers between trap states[97]. The current density is then described by

$$J \propto E\exp\left[-\frac{E_\mathrm{t} - e\sqrt{eE/\pi\varepsilon_0\varepsilon}}{k_\mathrm{B}T}\right], \tag{2.27}$$

where E_t is the trap energy. Poole-Frenkel emission transport yields a linear plot of $\ln(J/E)$ versus $E^{1/2}$ and leads to the dielectric constant ε. In this case linearization is equal to thermionic emission by Simmons (2.24), but the dielectric constants are different, i. e., $\varepsilon_\mathrm{PF} = 4\varepsilon_\mathrm{Simmons}$.

Whether the dominating transport mechanism is bulk- or interface-limited can be determined from temperature- and thickness-dependent measurements[96,97]. Yet, this can be a cumbersome task, because often several transport mechanisms are present and their interplay can be influenced by complicated field distributions and device geometry. In scanning probe microscopy, an additional complication arises due to the unknown field underneath the tip (see Sec. 3.1.2) and thus only crude estimations about the dominating transport mechanism can be made.

2.1.2. A short review on electronic domain-wall transport

Electronic transport at ferroic domain walls was first discussed in 1973. Fully charged walls in ferroelectrics were predicted to exhibit metallic conductivity within a layer thickness of roughly 1 nm, due to screening of the bound charges by intrinsic mobile charge carriers[100]. Three years later experimental evidence was found at interfaces with encountering polarization in SnSI single crystals showing enhanced conductivity[17]. Since then scientific interest in domain-wall conductance remained rather low. It was only in 2009 that the seminal discovery of conducting domain walls in multiferroic $BiFeO_3$ triggered broad attention in domain-wall functionality, because of its possible application in nanoelectronic devices[16,101,102]. The following section provides a brief overview of domain-wall conduction sorted by the investigated thin film and bulk compounds, before we end with a general summary.

Thin films Seidel et al. detected enhanced conductance at 109° and 180° domain walls in $BiFeO_3$ thin films by mapping the current response around shortly before switched domains (Figure 2.5a). Based on results obtained from transmission electron microscopy (TEM) measurements and density functional theory (DFT) calculations, the authors named two mechanisms responsible for the increase in conductance: (i) increased carrier concentration screening a detected potential step at the domain wall and (ii) local band gap lowering of 0.1 - 0.2 eV within the wall. The latter was confirmed later by scanning tunneling microscopy (STM) investigations[88] pointing towards electron-dominated (n-type) conductance.

Since then many studies were published showing that additional factors are responsible to facilitate transport at the domain walls in $BiFeO_3$ thin films. Increasing the amount of oxygen vacancies by adjusting the growth conditions causes larger domain wall currents[86] and triggers conduction even at the 71° walls[9], at which initially no potential step or band-gap lowering was observed[7]. Field-controlled, reversible distortions of the wall were used to induce higher domain-wall currents[103], which is possibly attributed to reversible movement of wedge-domains near the surface[104]. Besides, it was possible to create head-to-head and tail-to-tail wall configurations (Sec. 2.1.1.3) by switching ring-shaped domains[105] or using trailing-fields[106]. In both studies, domain-wall conductance was only observed for head-to-head configurations. This observation and the fact that domain-wall conductance can be optimized with increasing oxygen vacancy concentrations (Details in Sec. 2.2.3) corroborates electron-dominated (n-type) conductance in $BiFeO_3$ thin films. Studies on mixed-phase $BiFeO_3$ thin films observed localized strain-gradients and changes in the Fe L-edge spectra at phase boundaries[89,90], which could also play a role in domain-wall transport.

Significant domain-wall currents in $BiFeO_3$ were only measured under negative tip bias and conduction mechanisms were identified as interface-limited Schottky-emission[9,86] and Fowler-Nordheim tunneling[86,103,105]. Yet, domain wall conduction in $BiFeO_3$ thin films does not seem to be solely an interface effect as demonstrated by bipolar domain-wall studies on bulk $BiFeO_3$[107], the observation of bulk-determined SCLC[9], and the detection of increased microwave AC conductivity at the walls[108]. Besides, intrinsic behavior was tested by temperature-dependent cAFM measurements. These could determine semi-conducting behavior at naturally-grown 71°[9,106]/109°[86] walls and metallic-type conduction at artificially-produced

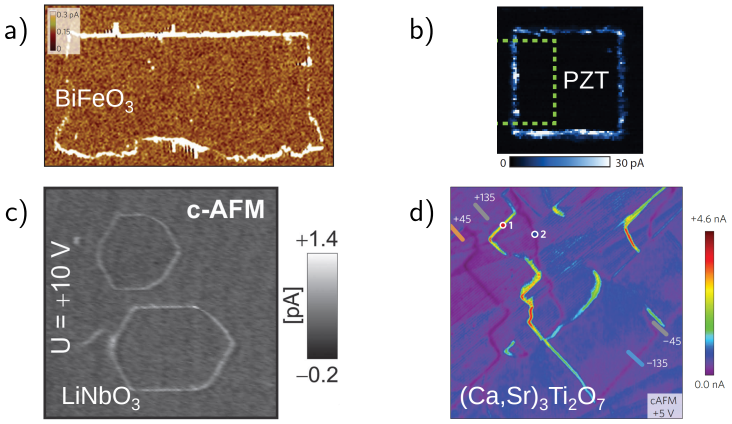

Figure 2.5.: Conduction at domain walls in different ferroic compounds. a) Multiferroic thin film, b) Ferroelectric thin film, c) Ferroelectric single crystal, and d) Improper ferroelectric single crystal. Graph (a) reprinted by permission from Macmillan Publishers Ltd: Nature, Ref. 7, copyright (2009). Graph (b) republished with permission of John Wiley & Sons Inc, from Ref. 8, copyright (2011). Graph (c) republished with permission of John Wiley & Sons Inc, from Ref. 13, copyright (2012). Graph (d) reprinted by permission from Macmillan Publishers Ltd: Nature, Ref. 18, copyright (2015).

head-to-head walls[106]. The latter walls are stabilized by electron injection from the tip and give the highest currents in the order of some nA (naturally-grown walls: fA – pA).

Aside from thin film BiFeO$_3$, domain-wall transport has been extensively studied in Pb[Ti$_{1-x}$Zr$_x$]O$_3$ thin films. In 2012, increased currents were observed at straight 180° boundaries that had been electrically switched into a single domain film (Fig. 2.5b). Local traps and polarization rotation were identified to increase conductance with $I(V)$ characteristics most-likely described by an interface- and bulk-limited mechanism (see Sec. 2.1.1.4)[8]. Later that year, tunnel-assisted metallic conductance was discovered at domain walls of field-induced nano domains. This behavior was attributed to charged and bent parts of the domain wall and supported by theoretical calculations including flexoelectric contributions[10]. Toggling domain-wall conductance on and off by consecutive ultra-high-vacuum (UHV) annealing and exposure to ambiance, respectively, further substantiated the role of oxygen vacancies in domain-wall transport[109]. Furthermore, Stolichnov et al. studied transport of 90° walls in mixed a/c-domain films. By mechanically writing new, instantaneously conducting domain walls at low temperatures, the authors verified intrinsic (non-defect) conductance, which was attributed to domain-wall bending towards the substrate interface and local valence changes[110].

Bulk ferroelectrics Enhanced conductance at domain walls is not restricted to thin film systems as has been demonstrated on several bulk systems[11–14,18]. Defect-stabilized, inclined domain walls reaching from top to bottom over 0.5 mm-thick LiNbO$_3$ single crystals show increased conductance from the surrounding bulk under UV illumination (Fig. 2.5c). Optimization of domain wall currents could be demonstrated by increasing the inclination angles and by adjusting the UV wavelength[13]. The authors attributed the enhanced current to charged segments of the domain walls, which were visualized by second harmonic generation (SHG) experiments[111] and observed in TEM[112]. Contrary to $LiNbO_3$, no UV-illumination was required to induce domain-wall conduction in $BaTiO_3$ by creating an array of head-to-head and tail-to-tail domain walls. The charged configurations caused band bending at the wall, i. e., shifting the conduction band below and the valence band above the Fermi energy for head-to-head and tail-to-tail walls, respectively. This resulted in metallic-type conduction at the head-to-head walls due to the formation of a quasi-2D electron gas. The lack of increase in conduction at the tail-to-tail walls was explained by a screening-scenario involving oxygen vacancies instead of holes. Directly accessing the two-dimensional electron gas for further studies seems yet to be a tricky task due to electron-depletion and the formation of wedge domains near the electrodes[14].

Next to proper ferroelectrics, domain-wall conductance was observed in the following improper bulk systems, too: $R\mathrm{MnO}_3$[11,12] and $(\mathrm{Ca,Sr})_3\mathrm{Ti}_2\mathrm{O}_7$[18]. For the former we will describe the details in Section 2.2.2. In the latter, plenty of charged ferroelastic 90° and ferroelectric 180° walls form in the as-grown state with both head-to-head and tail-to-tail configurations. Conducting head-to-head and insulating tail-to-tail walls showing angular conductance dependence were observed in a reduced compound $\mathrm{Ca}_{2.44}\mathrm{Sr}_{0.56}\mathrm{Ti}_2\mathrm{O}_{7-\delta}$ (see Figure 2.5d). The increased amount of oxygen vacancies in the reduced compound provides n-type carriers (see Sec. 2.2.3), which accumulate and deplete at the conducting head-to-head and insulating tail-to-tail walls, respectively[18].

Other ferroics So far, all of our discussed systems showing enhanced domain-wall conductance were ferroelectric. Yet, ferroelastics and magnetic insulators can exhibit this phenomenon, too. Enhanced conductance was observed for reduced $\mathrm{WO}_{3-\delta}$[113]. In this compound the domain walls even become superconducting at low temperatures[114]. The all-in-all-out magnetic insulator $\mathrm{Nd}_2\mathrm{Ir}_2\mathrm{O}_7$ showed enhanced conductance at the wall, which was detected by scanning-probe impedance microscopy[115]. Agglomeration of oxygen vacancies or the presence of a high-temperature parent phase were discussed to be responsible for the modified domain-wall conductance in the ferroelastic and ferromagnetic materials, respectively.

Summary From the above-discussed observations on electronic-transport properties of domain walls in ferroic materials, we can make the following statements:

(i) Enhanced conductance at ferroic domain walls is a general phenomenon that has been observed for as-grown or artificially-induced walls over a broad temperature range ($4\,\mathrm{K} \lesssim T \lesssim 430\,\mathrm{K}$) in different environmental conditions (UHV, ambient).

(ii) The microscopic origins for enhanced conductance strongly depend on the system and its growth conditions. They include polarization discontinuities screened by mobile charge carriers, oxygen vacancy agglomeration, local band or barrier lowering, strain, and conductive parent phases.

(iii) The variety of underlying microscopic origins lead to the observation of all sorts of possible conduction mechanisms (interface- and/or bulk-limited) which are typical for oxide materials (see Ref. 97 for a review).

(iv) Temperature-dependent studies allowed distinguishing between semiconducting and metallic-like domain walls.

We see that many different factors influence domain-wall conductance, which is probably owed to the different systems investigated. Nevertheless, even on individual systems, no coherent picture exists, yet. In order to develop coherent understanding, we scrutinize the domain-wall properties of a single system in this thesis.

2.2. Multiferroic hexagonal RMnO$_3$

2.2.1. General properties

The hexagonal manganites RMnO$_3$ (R = Sc, Y, In, Dy-Lu) define a family of materials that accommodate a multitude of interesting physical phenomena, reaching from exotic domain structures[53,54] with conductive domain walls[11,12] to coupling of magnetic, ferroelectric, and structural antiphase boundaries[116]. Their properties can be generalized, because they all show room-temperature improper ferroelectricity following the same underlying geometrically driven mechanism[60] and order antiferromagnetically at temperatures $T < 130\,\mathrm{K}$[117]. Since ferroelectric and antiferromagnetic order arise individually at different temperatures, the hexagonal manganites belong to the class of type-I multiferroics (see Sec. 2.1). As we will see later, the different rare-earth ions modify the critical temperatures of the electric and magnetic order[117,118], the type of antiferromagnetic order[117], and the rate of oxygen uptake[119,120].

Ferroelectric order We start with the structural transition that provides the origin of ferroelectricity in the hexagonal manganites[60,121], as it is crucial for the formation of their characteristic domain structure. Figure 2.6a shows the views along z- and x-direction of the high-temperature paraelectric phase with $P6_3/mmc$ symmetry. Layers of corner-shared trigonal Mn-O$_5$ bipyramids (polyhedra) are separated by layers of rare-earth R^{3+} ions. From the side and top view we see that the axes of the polyhedra are aligned perfectly along z and that the R^{3+} layers are flat in the xy-plane. This configuration is only stable at high temperatures, as the lattice mismatch between the rare-earth ions favors a more densely-packed structure[39,118]. Thus, upon reaching a critical temperature T_c the Mn-O$_5$ polyhedra start to buckle, which results in the more-densely packed[60] and non-centrosymmetric structure with $P6_3cm$ symmetry presented in Figure 2.6b. In terms of lattice vibrations (phonons), this process can be described by an instability of the K_3 mode[121]. The instability becomes stronger with decreasing size of the rare-earth ion R^{3+} leading to higher transitions temperatures, which range from $\approx$ 1206 K to 1708 K for $DyMnO_3$[122] and $LuMnO_3$[118], respectively.

Buckling causes certain of the apical oxygen ions O_{ap} to tilt towards the rare-earth ions while others move away. The R^{3+} ions shift up or down accordingly as demonstrated in the top view of Figure 2.6b. Obviously, the tilting of the oxygen ions towards the rare-earth ion leads to an upward shift of the latter (see white arrows). To fully describe this complex deformation, a structural order parameter composed of a buckling amplitude Q and a rotation angle Φ can be used[50]. If we look along the x-direction of the structure, we can distinguish that this complex deformation leads to a *up-down-down* pattern of the rare-earth ions. Note that the arrangement changes into *down-up-up* if the tilting is inverted. Yet, both configurations do not give rise to a spontaneous polarization, due to the net compensation of all dipole moments[60,121]. The instability of the antiferrodistortive K_3 mode though, creates a nonzero equilibrium position for the Γ_2 mode directly coupling to the spontaneous polarization[121]. We can understand this nonzero equilibrium position as an additional shift of the R^{3+} ions with respect to the equatorial oxygen O_{eq} adding up to a non-vanishing dipole moment. A *up-down-down* configuration will then exhibit a spontaneous polarization $P_s \equiv P = (0, 0, P_z)$ pointing down (Fig. 2.6b)[m]. From this consideration, it becomes apparent that due to this geometrically driven ferroelectricity the polarization state is predetermined directly by the direction of the distortion.

Although the emergence of ferroelectricity in the hexagonal manganites had been described by the coupling of two phonon modes[60,121], it still remained unclear, if buckling of the polyhedra and onset of polarization happen at one and the same temperature (see Ref. 123 for an overview). Just recently, the puzzle has been solved. Second harmonic generation (SHG) and piezoresponse force microscopy (PFM) in combination with Monte-Carlo simulations could prove that the polarization arises together with the onset of the geometrical distortion at T_c[124].

Domain structure Now we want to discuss how this improper transition affects the ferroelectric domain structures in the hexagonal manganites. The buckling mode causes the unit cell to triple in volume (trimerization) as being illustrated by the top views of both structures in Figure 2.6. Depending on the lattice site acting as the origin of trimerization, three antiphase domains, named α, β, γ, can form as indicated in Figure 2.6a. As we know, with respect to the tilting direction of the Mn-O_5 polyhedra the polarization state can be either pointing up (+) or down (−), rendering a total of six domain states ($\alpha^{\pm}, \beta^{\pm}, \gamma^{\pm}$) possible (see white arrows and

---

[m] In the following, we will refer to the spontaneous polarization P_s of the hexagonal manganites plainly as P.

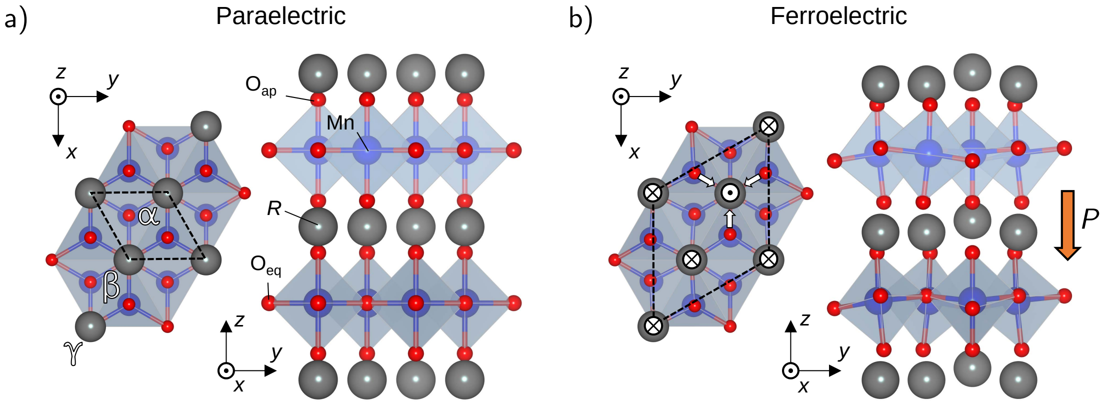

Figure 2.6.: Crystal structure of the hexagonal RMnO$_3$. a), b) Crystal structure in the paraelectric and ferroelectric phase, respectively. Below T_c the manganese polyhedra start to buckle away from their initial alignment parallel to the z-direction (a). This causes a net displacement of the rare-earth ions R^{3+} giving rise to a spontaneous polarization along z (b). Atomic structures illustrated by using the VESTA software[45] and the crystallographic data from Ref. 123. Further details in the text.

Greek letters in Fig. 2.6). The presence of these six domain states should, in principle, allow antiphase-only, ferroelectric-only, and antiphase-ferroelectric (APB-FE) domain walls. But only the latter have been observed in experiments analyzing the domain-structure in detail[52–54].

One of the first studies discussing the microscopic domain topology in RMnO$_3$[53] pointed out that only at the APB-FE boundary the R^{3+}-distortions are compensated fully, which should favor these boundaries energetically over the others. Thereafter, a density functional theory (DFT)-study addressing structure and energy-costs of neutral domain walls in RMnO$_3$ revealed that antiphase- or ferroelectric-only walls always consist of a energetically-favored superposition of two or three APB-FE domain walls, respectively[125] (see Fig. 2.7a). Likewise, it was nicely illustrated by a simple cartoon that meeting of an α^+ and a β^+ domain always results in a γ^- domain, no matter if the domain walls are parallel or perpendicular to the z-axis of the crystal[51]. This was further corroborated by Landau theory analysis demonstrating that changing the order parameter step-wise by 60°, which corresponds to the energetically-lowest change[n], leads to the following domain sequence [α^+, β^-, γ^+, α^-, β^+, γ^-], each domain separated by an APB-FE boundary[50].

Continuous variation of the order parameter around one point results in the structures depicted in Figure 2.7b. The structure on top describes a vortex of winding number $n = +1$ since the order parameter describes a phase change of $+2\pi$ for traversing around the vortex once[24]. The corresponding anti-vortex with $n = -1$ is depicted below. Like domain walls, vortices represent topological defects (Sec. 2.1). On the contrary, vortices cannot be moved or erased by an electric field and are hence topologically protected[53,54,122,126]. Note that each vortex is always connected

---

[n] Note that, antiphase- and ferroelectric-only domain walls correspond to an energetically less-favorable phase change of 120° and 180°.

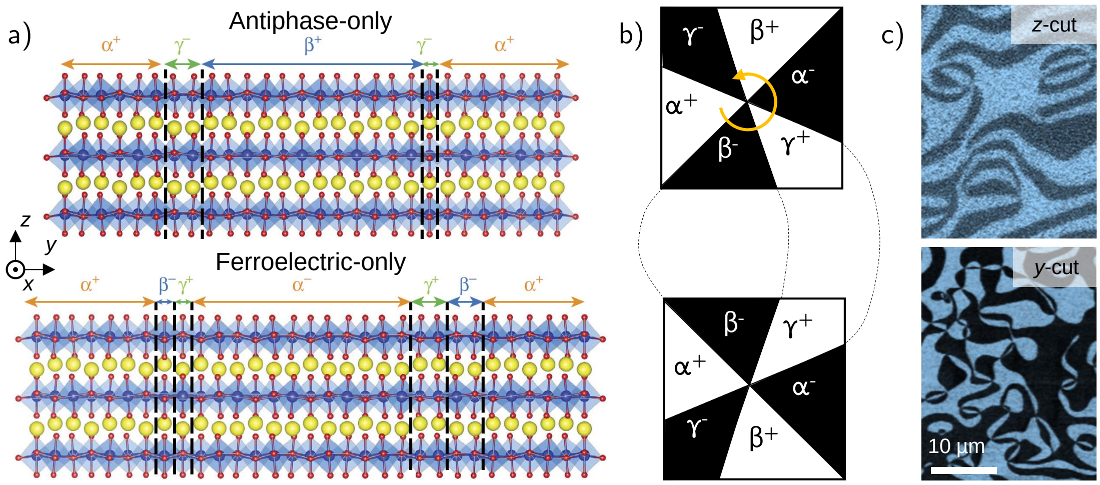

Figure 2.7.: Antiphase / FE boundaries and topological protected vortices. a) Atomic structure of antiphase- and ferroelectric-only domain boundaries, which decompose into two and three energetically more stable APB-FE boundaries, respectively. b) Schematic of a vortex and an anti-vortex with different winding order: [α^+, β^-, γ^+, α^-, β^+, γ^-] and [α^+, γ^-, β^+, α^-, γ^+, β^-]. c) Typical domain structure of $R\mathrm{MnO}_3$ with the characteristic six-fold meeting points. Lower and upper panel show PFM scans performed on a z- and y-cut of an ErMnO_3 crystal, respectively. Graph in (a) reprinted by permission from Macmillan Publishers Ltd: Nature Commun., Ref. 125, copyright (2013).

to an anti-vortex (dashed lines Figure 2.7b). Due to the fact, that only APB-FE boundaries are stable, solely domain walls and the six-fold meeting points (vortices) represent the allowed topological defects in $R\mathrm{MnO}_3$. It has been proven, that always six domain states with a specific order meet at a vortex and that each domain is connected to an even number of vortices[51,127].

The density of vortices in a crystal can be controlled by adjusting the cooling rate while crossing the transition temperature[118,122,128]. Starting at low cooling rates the vortex density increases continuously for faster cooling rates until a point is reached, at which the vortex density starts to drop if the cooling rate is further increased. The full description of the complete scenario is still under debate, but it has been shown that the dependence at low cooling rates follows a Kibble-Zurek scaling law[118,128,129]. Despite the hexagonal anisotropy, vortices are found on all three faces (x, y, z) of the crystal, which can be seen in the PFM scans performed on a z-cut and a y-cut of ErMnO_3 in Figure 2.7c. Experiments have confirmed that the vortex density is homogeneous in all three dimensions of the crystal[54,122]. In two dimensions vortices represent points of zero-dimension, in bulk crystals they meander as one-dimensional vortex lines[129,130]. Consequently, as-grown crystals exhibit neutral and charged domain walls, where the polarization is parallel or meets in head-to-head / tail-to-tail configuration, respectively (see Sec. 2.1.1.3). Deviations from the topologically protected vortex-domain structure have been observed in highly defective crystals, in which defects (e. g. dislocations) locally break the translation symmetry[131]. In addition, samples that are grown and subsequently annealed below T_c develop stripe and bubble domains, respectively[118].

Domain-wall structure Modern transmission electron microscopy (TEM) provides access to the atomic structure of the domain walls in RMnO$_3$ with picometer precision[130–135]. Most of the studies analyzed the position of the rare-earth ions, which directly relate to the polarization orientation and thus provide a local measure for the reorientation of P across the domain walls. Four different types of neutral domain walls with normal vector parallel to the y-direction could be determined; including sharp (change of polarization from one unit cell to the other) as well as wide configurations. Neutral walls with normal vectors in other directions are difficult to access in TEM, but is has been demonstrated that these can be decomposed into two sharp or two wide configurations[125]. Apart from neutral walls, charged walls have been characterized. Fully charged walls have been detected to be nearly atomically sharp for both head-to-head and tail-to-tail configuration[130,134]. Since the real ferroelectric state depends on the order parameter amplitude and rotation (see above), the shift of the rare-earth ions only partially captures the complex structure at the domain walls. Theoretical studies have shown, that the order parameter changes orientation over two to four unit cells ($\sim 1.2 - 2.4\,\mathrm{nm}$)[50].

Magnetic properties Finally, we want to discuss briefly the magnetic properties of the hexagonal manganites. Ordering of the manganese spins within the xy-plane starts to develop at temperatures of about 100 K. On the triangular lattice, three distinguishable spin configurations are possible: type-X (spins parallel to x-axis), type-Y (spins parallel to y-axis), or a mixture of both. Magnetic ordering of the rare-earth ions happens at temperatures of about $5 - 10\,\mathrm{K}$[117]. The transition temperatures and type of antiferromagnetic order are determined by the rare-earth ion[117,136]. SHG has proven to be a versatile tool helping to unravel the underlying magnetic order[136] and to show the coexistence and partial coincidence of ferroelectric and antiferromagnetic domain walls[116].

2.2.2. Electronic transport at the domain walls

Hexagonal manganites represent p-type semiconducting ferroelectrics[137], in which the p-type carriers result from oxygen interstitials[138]. Therefore, the majority charge carriers are holes and transport happens predominantly via the valence band. This is different from most examples showing pronounced n-type domain-wall conduction (see Sec. 2.1.2). The band-gap of RMnO$_3$ lies between $1.5 - 1.6\,\mathrm{eV}$$RMnO_3$[92,139] and the bulk conductivity σ at room temperature ranges over several orders of magnitude ($10^{-7}\,\mathrm{S\,cm^{-1}} < \sigma < 10^{-3}\,\mathrm{S\,cm^{-1}}$)[140]. Regarding domain-wall transport in the hexagonal manganites, we have to distinguish between neutral and charged domain walls, which are accessible on out-of-plane oriented crystals, where P is perpendicular to the surface (z-cut), or in-plane samples, where

P lies parallel to the surface plane (x-, y-cut), respectively. The difference between these two orientations is that on out-of-plane samples all domain walls are neutral, whereas on in-plane samples domain walls range from neutral to fully positively / negatively charged. We begin our discussion with the former.

Neutral walls In 2010, Choi and coworkers studied the domains and their conductance properties on a z-cut of $YMnO_3$ using conductive atomic force microscopy (cAFM)[53]. They found a polarization-modulation in the current response of the cAFM signal perfectly revealing the typical topology of the domain structure. Figure 2.8a represents the scan showing highly conducting $-P$ domains and more insulating $+P$ domains[o]. The difference in current response was related to a modulation of the Schottky barrier due to the polarization charge which is presented in Figure 2.8c. The bound positive or negative charge at the surface of the p-type $YMnO_3$ causes the valence bands to bent down or upwards, respectively. Due to a lowered Schottky barrier ϕ_b, the $-P$ domains show higher current responses. By analyzing the $I(V)$ curves of the two domain states the authors could estimate a difference in Schottky barrier of $\Delta\phi_\mathrm{b} = 44\,\mathrm{meV}$. At higher bias voltage, Schottky contrast disappears and the domain walls become more insulating than the surrounding bulk. This effect has been attributed to a change from Schottky-dominated to space-charge-limited conduction (SCLC) conduction and to the paraelectric properties persisting at the domain walls, respectively. Temperature-dependent measurements showed that the paraelectric phase is more insulating than the ferroelectric counterpart, which the authors related to a contraction along the z-axis happening when cooling through the ferroelectric phase transition (see Sec. 2.2.1).

Further studies have been performed on z-oriented samples of $HoMnO_3$[92] and $ErMnO_3$[11], basically confirming the results though with some minor differences. The experiments on $HoMnO_3$ revealed the same domain modulation with higher currents for $-P$ domains but with a larger $\Delta\phi_\mathrm{b} = 270\,\mathrm{meV}$. At higher tip voltage a change to SCLC was observed, but no insulating domain-wall peculiarities. The change to SCLC even lead to the inversion of the current response of both domains (higher current for $+P$). In contrast, the results on $ErMnO_3$ showed insulating walls with bias-dependent width and a non-vanishing Schottky domain contrast. The authors of this study explain their results by the depletion and accumulation of holes within a thin surface layer provoked by the up and down polarization of the domains. Non-trivial current spreading at the wall was declared responsible for the observed bias-dependent current decrease at the wall.

Charged domain walls A completely different scenario of domain-wall transport exists on in-plane oriented $R\mathrm{MnO}_3$. In 2012, Meier and coworkers could demonstrate on $ErMnO_3$ that tail-to-tail and head-to-head domain walls show increased and decreased conductance, respectively[11]. The phenomenon was attributed to the

---

[o] In this case + and − define domains with their polarization pointing up $+P = (0, 0, +P_\mathrm{z})$ or down $-P = (0, 0, -P_\mathrm{z})$, respectively.

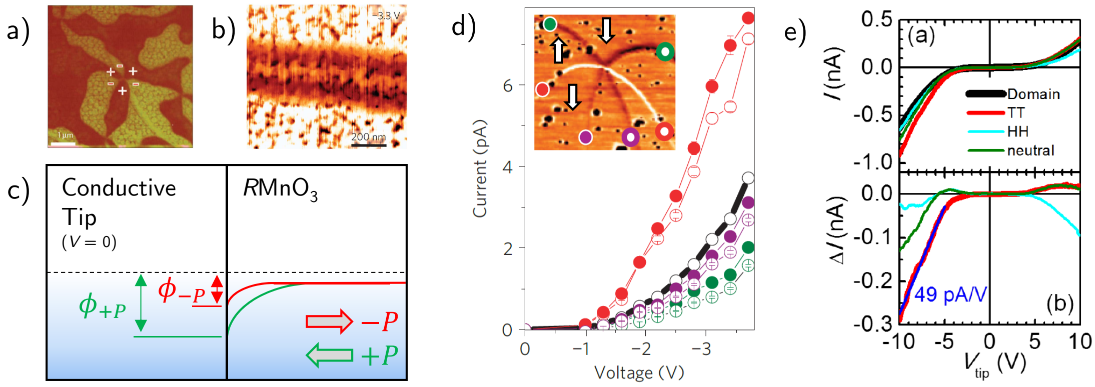

Figure 2.8.: Domain and domain-wall transport in the hexagonal manganites. a) cAFM scan on out-of-plane oriented YMnO$_3$ (z-cut) showing a Schottky-barrier modulated contrast with increased current for $-P$ domains. b) Suppressed conduction at the neutral domain walls on z-cut ErMnO$_3$. c) Illustration of the the polarization-modulated barrier height. Bound positive and negative polarization charges bend the bands up and downward, respectively, resulting in a reduced barrier for $-P$ domains. d) Enhanced and suppressed domain-wall conductance at the respective charged tail-to-tail and head-to-head walls measured on in-plane oriented ErMnO$_3$. $I(V)$ curves were derived from several scans at the positions indicated on the inset. e) $I(V)$ curves of charged tail-to-tail, head-to-head, and neutral domain walls measured on in-plane oriented HoMnO$_3$. The lower part shows the difference of the wall currents with respect to the bulk. Graphs (a) and (b, d) reprinted by permission from Macmillan Publishers Ltd: Nature Materials, Refs. 53 and 11, copyright (2010) and (2012), respectively. Graph (c) is partially adapted from Ref. 92. Graph (e) is reprinted with permission from the Ref. 12, copyright (2012) by the American Physical Society.

redistribution of mobile charge carriers (p-type) screening the static charges at the walls. Accumulation of mobile holes at tail-to-tail and depletion at head-to-head walls are responsible for the increase and decrease in conductance, respectively. Besides, DFT revealed a shift of the Fermi level below the broad O($2p$)-Mn($3d$) valence band the tail-to-tail wall. Due to the high density of states present at the valence-band maximum, one can expect a high mobility of the holes. On the contrary, at head-to-head walls the Fermi level raises above the narrow d_{z^2} conduction band with small density of states and limited electron mobility. Electronic conduction at this wall had been ruled out since electrons are expected to be scarce in p-type ErMnO$_3$[11,137,138].

Figure 2.8d presents $I(V)$ curves that are extracted from several scans at different domain-wall locations, all following a Schottky-like trend (see Sec. 2.1.1.4). Note that tail-to-tail walls always show higher current, while head-to-head walls are always lower in current with respect to the bulk. Further analysis could determine that both domain-wall conductance and width are a continuous function of domain-wall orientation. The variation of the domain-wall conductance (DWc) is in agreement with the change of static polarization charge as a function of domain wall (DW) angle: $2P_{\mathrm{z}} \cdot \cos(\alpha)$ (see Sec. 2.1.1.3). The change of DW width stems from the difference in screening length for hole accumulation / depletion and from the spreading of the current from the point-shaped tip. The width changes continuously from 30 nm at the tail-to-tail wall to 150 nm at the head-to-head wall.

In the same year, experiments on $\mathrm{HoMnO_3}$ confirmed the results obtained on $\mathrm{ErMnO_3}$, which substantiates that this is a more general phenomenon of the hexagonal manganites. $I(V)$ spectroscopy (see Sec. 3.1.2) revealed increased and decreased conductance at the tail-to-tail and head-to-head walls, respectively, in the low-voltage regime of the forward bias (0 to $-6\,\mathrm{V}$, Fig. 2.8e). At higher forward bias ($V_{\mathrm{tip}} < -6\,\mathrm{V}$) the neutral and the insulating head-to-head walls become more conductive than the bulk, which is clearly shown in the lower panel of Figure 2.8e. The authors only vaguely discuss this observation and relate it to a slight band gap reduction similar to that in $\mathrm{BiFeO_3}$ thin films (see Sec. 2.1.2). The variation of the DW width was larger than in $\mathrm{ErMnO_3}$ ranging from 80 nm to 250 nm for conducting and insulating walls, respectively. The larger width of the head-to-head walls had been explained by hole repulsion creating a space charged region. The different widths measured on $\mathrm{HoMnO_3}$ with respect to $\mathrm{ErMnO_3}$ could be attributed to different AFM-tip widths or bulk charge-carrier concentrations[84].

2.2.3. Chemically doped compounds

Theory and experiment demonstrated that domain-wall conductance strongly depends on the electronic properties of the surrounding bulk[9,84,86,109]. Hence, one idea of my thesis is to manipulate the bulk conductance by means of chemical doping in order to open a new pathway to control and tune the transport properties of domain walls. This section provides the background of chemical doping of $R\mathrm{MnO_3}$. The results related to domain-wall engineering via chemical doping are presented in the Sections 4.3, 4.4, and 5.2.

General description Like in semiconductors, electronic bulk properties of oxides can be drastically changed by the deliberate introduction of donors or acceptors, which provide electron or hole carriers via charge-transfer, respectively[141]. In $R\mathrm{MnO_3}$, doping can be achieved by substituting the rare-earth and manganese ions with impurity cations of a different valence (aliovalent) or by changing the oxygen content. In the following, we will only consider R substitution, when discussing impurity doping. The exact chemical composition of the doped compound is $R_{1-x}\mathrm{A}_x\mathrm{MnO}_{3+\delta}$, where x denotes the concentration of the impurity A and δ describes deviations from oxygen stoichiometry.

In the ideal configuration, both R and Mn are trivalent (3+). While R is presumed to remain in its stable 3+ configuration, Mn can adapt other oxidation states in $R\mathrm{MnO_3}$, as e. g., reduced $\mathrm{Mn^{2+}}$ ($\mathrm{Mn}'_{\mathrm{Mn}}$) or oxidized $\mathrm{Mn^{4+}}$ ($\mathrm{Mn}^{\bullet}_{\mathrm{Mn}}$). Due to the multivalency of manganese and the medium band gap ($E_{\mathrm{g}} = 1.5 - 1.6\,\mathrm{eV}$ in $R\mathrm{MnO_3}$[92,139]), introduced charge carriers are believed to reside at the manganese

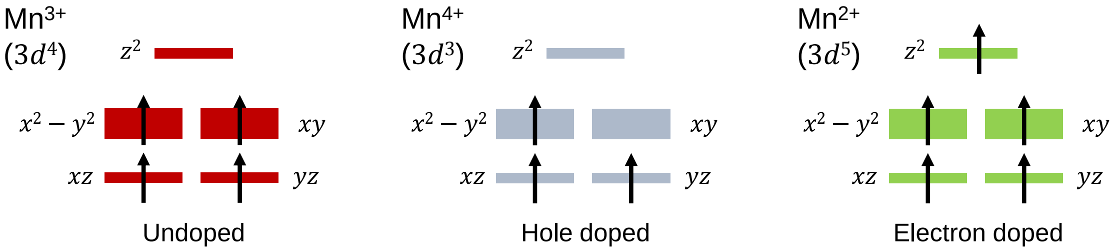

Figure 2.9.: Simplified illustration of the Mn d bands in doped RMnO$_3$. Hole doping creates Mn^{4+} states with holes in the dispersive d_{xy} or $d_{x^2-y^2}$ bands increasing the conductivity. Electron doping leads to Mn^{2+} states with electrons in the localized d_{z^2} bands. In this case no increase in electrical conductivity could be observed[142]. Graphs were derived following the discussion from Aken et al. in Ref. 142.

site at room temperature[142–144]. The following scenarios for p- and n-type doping result:

$$\mathrm{Mn}_{\mathrm{Mn}}^{\mathrm{x}} + \mathrm{h}^{\bullet} \xrightarrow{\mathrm{h-}R\mathrm{MnO_3}} \mathrm{Mn}_{\mathrm{Mn}}^{\bullet} \tag{2.28}$$

$$\mathrm{Mn}_{\mathrm{Mn}}^{\mathrm{x}} + \mathrm{e}' \xrightarrow{\mathrm{h-}R\mathrm{MnO_3}} \mathrm{Mn}_{\mathrm{Mn}}'. \tag{2.29}$$

Here, we use the established Kröger-Vink defect-notation[145]: subscripts refer to the lattice site of the original ion, superscripts describe the charge difference with respect to the original ion (positive $^{\bullet}$, negative $'$, neutral ^{x}), whereas v and i denote vacancies and interstitials, respectively.

The introduction of holes leads to a $d^4 \leftrightarrow d^3$ (Mn^{3+} / Mn^{4+}) transition of the valence-electron configuration of the Mn ion, whereas electron doping leads to a $d^4 \leftrightarrow d^5$ (Mn^{2+} / Mn^{3+}) mixed valence state (see Fig. 2.9). Looking at the d-band configuration that results from the trigonal bi-pyramidal coordination of Mn in RMnO$_3$, p-type doping creates holes in the dispersive d_{xy} / $d_{x^2-y^2}$ bands[142]. N-type doping on the other hand introduces electrons into the more localized d_{z^2} band. As a consequence, we would expect an asymmetry in electron and hole doping with respect to the conductance properties of RMnO$_3$. This has been experimentally confirmed in Ca^{2+}-doped (p-type) YMnO$_3$ with strongly increased conductance[146] and in Zr^{4+}-doped (n-type) YMnO$_3$, where neither an increase nor decrease in conductance could be observed[142].

Impurity doping Impurity doping demands oxygen stoichiometry ($\delta = 0$), which is achieved for divalent acceptors A^{2+} and quadrivalent donors D^{4+} by oxygen uptake and release, respectively[p]:

$$2\,\mathrm{AO} + \frac{1}{2}\,\mathrm{O}_2 \xrightarrow{\mathrm{h-}R\mathrm{MnO}_3} 2\,\mathrm{A}'_R + 3\,\mathrm{O}^{\mathrm{x}}_{\mathrm{O}} + 2\,\mathrm{h}^{\bullet} \tag{2.30}$$

$$2\,\mathrm{DO}_2 \xrightarrow{\mathrm{h-}R\mathrm{MnO}_3} 2\,\mathrm{D}^{\bullet}_R + 3\,\mathrm{O}^{\mathrm{x}}_{\mathrm{O}} + 2\,\mathrm{e}' + \frac{1}{2}\,\mathrm{O}_2\uparrow . \tag{2.31}$$

If oxygen stoichiometry is violated, more complicated scenarios can arise, which involve cation / oxygen interstitials or vacancies[141]. Most important is that these alternative scenarios can cause compensation of charge carriers and by this decreased doping efficiency.

The amount of impurity doping can be precisely controlled during synthesis and measured afterwards by chemical analysis. Yet, once the materials has been grown, the doping concentration can be hardly changed due to low cation diffusion rates[143]. The stability of the hexagonal phase limits the maximum concentration of added impurities (e. g. $x \approx 22\,\%$ for Ca^{2+}[146], $x \approx 30\,\%$ for Zr^{4+}[142]).

Oxygen doping Doping via changing the oxygen content is described by the following equations:

$$\frac{1}{2}\,\mathrm{O}_2 \xrightarrow{\mathrm{h-}R\mathrm{MnO}_3} \mathrm{O}''_{\mathrm{i}} + 2\,\mathrm{h}^{\bullet} \tag{2.32}$$

$$\mathrm{O}^{\mathrm{x}}_{\mathrm{O}} \xrightarrow{\mathrm{h-}R\mathrm{MnO}_3} \mathrm{V}^{\bullet\bullet}_{\mathrm{O}} + 2\,\mathrm{e}' + \frac{1}{2}\,\mathrm{O}_2\uparrow . \tag{2.33}$$

We see, that oxygen interstitials favor p-type conductance, whereas vacancies contribute to n-type conductance. The former has been identified to be the source for the natural p-type conductance of $R\mathrm{MnO}_3$[138].

Depending on the material system, charge carriers introduced by oxygen defects can be trapped at their respective defect site[141]. Oxygen-deficient samples have shown a higher activation energy in conductance measurements, which was attributed to a higher ionization energy of oxygen vacancies[138,144]. Hence, charge trapping at defect sites might be relevant for oxygen vacancies rather than for interstitials. A complete description of defect states and stabilities is yet missing for $R\mathrm{MnO}_3$. The precise control of the amount of oxygen doping, especially during growth, is less than for impurity doping. Yet, it provides the possibility to change the electronic properties of the material after synthesis. Strikingly, it allows to change from p- to n-type conduction according to (2.32) and (2.33).

Studies focusing on the uptake of interstitial oxygen under oxygen atmosphere showed that for temperatures above ~ 350 °C interstitial oxygen gets unstable and $\delta \approx 0$[119,120,138,143]. Below this temperature, oxygen of up to $\delta = 0.38$ can be incorporated under high-pressure oxygen atmosphere. This is accompanied with the formation of additional hexagonal phases of different symmetry ($\neq P6_3cm$). Whether these phases show the same distinct ferroelectricity is not known and could thus limit the maximum oxygen uptake, e. g., $\delta < 0.28$ in HoMnO$_3$[120]. Among the hexagonal compounds that have been investigated with respect to oxygen incorporation, HoMnO$_3$ shows the fastest rate of oxygen uptake[120].

---

[p] Note that in order to keep oxygen stoichiometry the 2:3 ratio between cation and oxygen needs to be maintained, as it is the case for the educts of $R\mathrm{MnO}_3$, i. e., $\mathrm{R}_2\mathrm{O}_3$ and $\mathrm{Mn}_2\mathrm{O}_3$.

Oxygen-deficient samples can be prepared by growing or annealing in nitrogen or reducing hydrogen atmospheres at elevated temperatures[144,147,148]. For YMnO$_3$ the maximum oxygen deficiency was found to be $-\delta < 0.2$ before the ferroelectric phase becomes unstable[148]. Samples of YMnO$_3$ with higher oxygen vacancy concentrations have been already examined with respect to domain-wall transport and mobility[149,150]. The authors of this study could measure enhanced domain-wall conductivity and mobility of neutral domain walls in as-grown and poled crystals that had been reduced under an Ar atmosphere during synthesis. Unfortunately, their studies lack a direct comparison between cAFM and PFM measurements, which leaves it open whether real domain-wall currents and movements have been detected. Still, this strategy of domain-wall engineering is interesting for post-growth modifications and we are going to address this topic in Section 5.2.

3. Experimental methods

The following chapter provides the overview and background of the experimental techniques that have been applied during this thesis. The chapter begins with an introduction to atomic force microscopy (Sec. 3.1), the technique that has been extensively used for the investigations in Chapter 4 and 5. Thereafter, the basics of cathode-lens microscopy are explained (Sec. 3.2), which helps to comprehend the results presented in Chapter 6. Finally, we explain how our samples are prepared by floating-zone growth, Laue back-scattering, and surface treatments (Sec. 3.3).

3.1. Atomic force microscopy

Atomic force microscopy (AFM) belongs to the branch of scanning probe microscopy (SPM), in which surface properties are characterized by measuring interactions of a physical probe that scans the sample. AFM originated as a spin-off from scanning tunneling microscopy (STM) in 1986[151,152], and since then it developed quickly into a versatile tool for materials characterization on the nanoscale. AFM offers a multitude of different measurement modes and is not restricted to conducting materials or vacuum conditions, as it is in many cases for its ancestor SPM[153].

In the 1990s, scientists started using AFM to study ferroelectrics, in order overcome the limitations of the existing techniques by that time[154]. The developments during those years helped to establish AFM as one of the standard techniques for characterizing ferroelectric (FE) materials. At first, electrostatic force microscopy (EFM) and friction force microscopy were used to image domain structures by sensing electrostatic stray-fields and tribological differences arising at domains and domain walls[155–157] (see Sec. 3.1.4). Later, the invention of piezoresponse force microscopy (PFM)[158,159] improved resolution and sensitivity of FE domain imaging significantly by locally-measuring the deformations caused by the inverse-piezoelectric effect present in these materials (Sec. 3.1.3). Operating in contact mode (see Sec. 3.1.1), PFM furthermore allowed to manipulate the ferroelectric domains in-situ, i. e., during imaging[158–161]. The observation of conducting domain walls[7] – which were discovered by a combination of PFM and conductive atomic force microscopy (cAFM) – highlights the importance of AFM techniques for investigating emergent properties of ferroelectric materials.

The following chapter will give a brief overview of the AFM setup and an introduction to the various measurement modes that have been used during the course of this thesis.

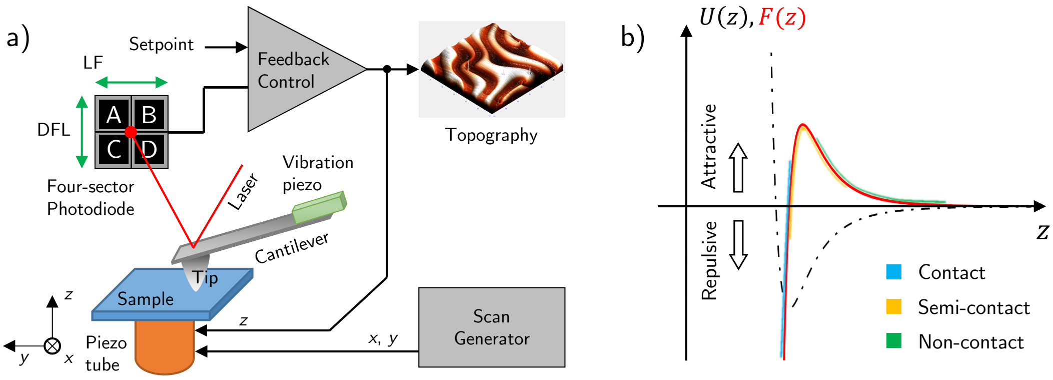

Figure 3.1.: Basic principle of atomic force microscopy. a) Schematic of an AFM working with the beam-deflection method. The movement of a cantilever caused by tip-sample interactions is tracked by reflecting a laser-beam from the backside of the cantilever onto a four-sector photodiode. During scan operation a feedback loop controls the voltage applied to the z-piezo in order to keep the laser deflection (DFL) signal at a given setpoint. The signal from the deformation of to the z-piezo allows to reconstruct the topography. b) Lennard-Jones potential $U(z)$ and its derivative corresponding to the force $F(z)$ between the sample and the tip. The different modes of operation (contact, non-contact, semi-contact) correspond to different regimes on the curve as indicated by the color code.

3.1.1. Basic principle and experimental setup

AFM principle The basic principle of AFM is to sense forces acting on the tip of a cantilever and to map their spatial distribution[153]. Nowadays, most AFM systems detect small motions of the cantilever by the beam-deflection method[162], due to its good stability and high signal-to-noise ratio limited only by the thermal noise of the cantilever[153]. Figure 3.1a shows a schematic of a general AFM-setup that bases on this principal. A laser beam is reflected from the backside of the cantilever onto a four-sector photodiode, which monitors vertical and lateral displacements of the cantilever by the respective signals DFL = (A+B) − (C+D) and LF = (A+B) − (C+D).

In order to achieve stable scanning conditions, a piezotube connected to a scan generator and feedback controller precisely moves the sample in all three dimensions of space (x, y, z). Usually the sample is moved towards the cantilever until a defined setpoint of the laser signal is established. The value of the setpoint depends on the mode of operation (see below). During scanning operation, forces developing between the tip and the sample will change the bending of the cantilever and thus the laser signal. A constant tip-sample interaction is provided by the feedback controller that maintains the laser signal at the setpoint value, by adjusting the height of the z-piezo accordingly. The exact displacement of the z-piezo, which is read-out from by a calibrated capacitive sensor, can be used to reconstruct the topography of the surface.

Tip-sample interaction The relevant forces for AFM can be divided into short- and long-range forces. This classification is important for AFM, because different parts of tip and cantilever contribute differently to the overall detected force[153]. Short-range forces extent over distances comparable to electronic wave functions ($< 1\,\mathrm{nm}$) including attractive forces due to the formation of chemical bonds and repulsive forces caused by the Pauli exclusion principle, which forbids the occupation of the same quantum state by two electrons. Long-range forces can be dispersion (van-der-Waals), electrostatic, and magnetic forces. Other forces like capillary forces become important when measuring under ambient and humid conditions.

In the simplest case, repulsive Pauli and attractive van-der-Waals forces dominate and the situation can be described by the Lennard-Jones (LJ) potential

$$U(r) = 4\varepsilon \left[\left(\frac{\sigma}{z} \right)^{12} - \left(\frac{\sigma}{z} \right)^{6} \right], \tag{3.1}$$

where σ, ε are material parameters and z is the inter-atomic distance between two neutral atoms. For describing tip-sample interactions properly, one needs to calculate the interactions as a superposition of many individual atoms, which results in a more shallow LJ potential and a modification of (3.1)[163]. In order to obtain the force acting on the cantilever, we derive $U(z)$ with respect to z yielding

$$F(z) = -24 \frac{\varepsilon}{\sigma} \left[2 \left(\frac{\sigma}{z} \right)^{13} - \left(\frac{\sigma}{z} \right)^{7} \right]. \tag{3.2}$$

This force is presented by the red curve in Figure 3.1a (dashed line corresponds to LJ-potential), and we refer to it as tip-sample force F_{ts}.

If a cantilever approaches the sample, it first gets pulled towards the surface by the attractive, long-range van-der-Waals force described by the second therm of (3.2). The cantilever deflects by δ_{c} until the force created by its elastic deformation is in equilibrium with the tip-sample force ($F_{\mathrm{el}} = F_{\mathrm{ts}}$)[164]. The former is proportional to the elastic spring constant k of the cantilever ($F_{\mathrm{el}} = -k\delta_{\mathrm{c}}$). Upon further approaching, the gradient in tip-sample force F_{ts} can get larger than the gradient in elastic force F_{el} causing the cantilever to snap to the sample, which is commonly defined as 'jump-to-contact'[153,164].

Now that the cantilever is in contact with the sample, atomic orbitals of tip and sample start to overlap creating a repulsive force due to the Pauli force described by the first term in (3.2). This force will become dominant, if the tip-sample distance is decreased below z_{c} at which $F(z_{\mathrm{c}}) = 0$. Upon retracting, the cantilever remains in contact due to the attractive forces, before is snaps off at the 'jump-off-contact' position[153,164].

Modes of operation The modes of operation in atomic force microscopy are contact, semi-contact, and non-contact mode. The three modes differ from each other, in principle, mostly by the tip-sample spacing and are hence sensitive to different forces.

Contact mode is a static mode, in which the cantilever is brought in contact with the sample, i. e., into the regime where Pauli forces start contributing to the interaction, which is highlighted blue in Figure 3.1a. Contact mode operation allows, e. g. to detect cantilever distortions resulting from piezoresponse or friction. The setpoint for the feedback in contact-mode is a fixed value of the DFL-signal, which corresponds to a constant force if the investigated material is elastically-homogeneous. The actual force can be derived by determining the cantilever spring constant and measuring force-distance curves[164].

Non-contact and semi-contact mode exploit the fact, that the tip-cantilever system can be described as a harmonic oscillator[165]. In both modes the cantilever is excited mechanically at its resonance frequency f by a vibrating actuator (see Fig. 3.1a), which enhances its sensitivity with respect to weaker long-range forces. Consequently, these two modes are chosen for measuring long-range interactions, as e. g., electrostatic and magnetic forces.

Non-contact mode is mostly performed under ultra-high-vacuum (UHV) conditions and the cantilever is oscillated with small amplitudes to prevent it from crashing into the sample (jump-to-contact)[153]. In UHV the resonance peak of the cantilever gets extremely narrow, due to a strong increase of the cantilever quality factor Q[153]. Slight changes in the tip-sample interaction shift the resonance peak immediately leading to off-resonant conditions. This is why a phase-locked loop is required to keep the cantilever at resonance and hence to maintain stable scanning conditions[153].

Semi-contact or tapping-mode operation is established if the oscillation amplitude A is increased and the tip-sample distance reduced (orange region, Fig. 3.1a). Semi-contact is the preferred oscillating mode under ambient conditions. In semi-contact operation the cantilever is oscillated at a fixed frequency and distance-control is established by damping the free oscillation amplitude of the cantilever A_0 to a certain value, e. g. $A_{\text{set}} = 0.5A_0$.

Experimental setup All AFM measurements of this thesis were performed on an NT-MDT Ntegra Prima system. This modular system consists of two different measurement heads (SMENA and SF005) and a bottom scanner. The SMENA scan head is a tip-scanning system, i. e., the tip is moved in all three directions (x, y, z) by a piezo-tube, which allows operation with or without the bottom scanner. In combination with the bottom scanner the system reaches scan sizes of up to $250\times250\,\mu\text{m}^2$. In contrast, the SF005 system can only be used in combination with the bottom scanner (Scan size $120\times120\,\mu\text{m}^2$). Here, the sample is moved while the tip remains fixed. In comparison to the SMENA head, the fixed-tip system SF005 can show less noise in topography imaging due to a better mechanical stability. Both heads can be operated in contact- and semi-contact-mode.

The SF005 system is somewhat special, as it can be equipped with three different tip insets, i. e., the SKM, the high-voltage SKM, and the AU050, each of which bearing its own advantages and exclusive measurement modes. The first two insets are identical except that the latter is equipped with a BNC cable connection to the tip, which allows applications of up to 0.5 kV. The SKM heads can operate in contact and non-contact mode, however, they are not able to perform cAFM. The AU050 head has the advantage to perform cAFM measurements with high-current resolution (see Section 3.1.2), but is limited to contact-mode. Further details on the system are given in the sections below and in Reference 122.

Tip overview The geometry of the probe (cantilever + tip) crucially determines the performance of the measurement. For example, detection of small forces requires soft cantilevers with small spring constants, as hard cantilevers would be barely sensitive to them. Table 3.1 provides an overview of the tips that have been used in our experiments. Explanations why these probes are suitable for a certain measurement mode are given in the respective sections below.

Table 3.1.: Cantilever and tip parameters including cantilever length l / thickness d, spring constant k, resonance frequency f, and tip radius r_{tip}.

Probe name: Manufacturer:	**ANSCM-Pt** AppNano	**ANSCM-PA** AppNano	**DCP-20** NT-MDT
l (µm)	225	125	90
d (µm)	3	4.5	2
k ($\mathrm{N\,m^{-1}}$)	1 to 5	25 to 75	28 to 110
f (kHz)	43 to 81	200 to 400	260 to 630
r_{tip} (nm)	30	60	100 †
Coating	Pt/Ir	Pt/It	n-doped diamond
Hallmark	LPFM, resolution	VPFM, EFM, wear	VPFM, EFM, wear

† Over the course of the PhD thesis, NT-MDT changed the specifications of the DCP-20 tip to 50 - 70 nm.

3.1.2. Conductive atomic force microscopy

Figure 3.2 shows the configuration of our system that is used to measure cAFM with the bias voltage $V_{\text{BV}} = V_{\text{DC}} + V_{\text{AC}} \sin(\omega t)$ applied to the back electrode of the sample, where the angular frequency is $\omega = 2\pi\nu$. The back electrode is usually a metallic holder onto which the samples are glued with conductive silver paint. cAFM is operated in contact mode and can be performed with both our SMENA and SF005+AU020 heads. The difference between the two heads lies in the accessible current range (SMENA: 1 pA ↔ 50 nA, SF005+AU020: 10 fA ↔ 100 pA). Our system allows to perform temperature-dependent studies (SMENA head in combination with a home-built heating stage) and operation under a dry nitrogen atmosphere.

cAFM In conventional conductive atomic force microscopy two different methods are commonly used to determine local conductance properties, i. e., current mapping and (grid) spectroscopy[166]. Mapping refers to usual topography imaging while applying a constant voltage V_{DC} ($V_{\text{AC}} = 0$) to the sample and monitoring the current

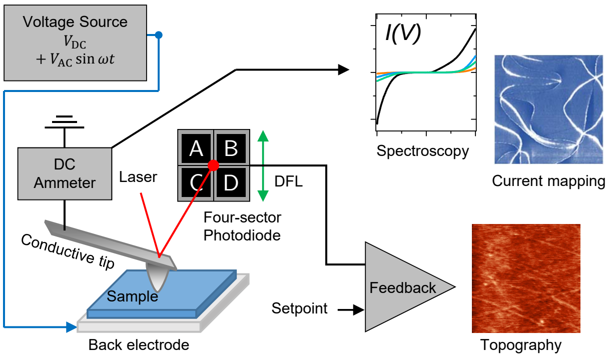

Figure 3.2.: Setup for DC- and AC-cAFM measurements. A voltage source provides direct V_{DC} or alternating voltages V_{AC} of frequency $\omega = 2\pi\nu$ to the back of the sample. The resulting current response is measured by the built-in ammeter and reconstructed into two-dimensional current images or $I(V)$ curves. Small DFL setpoints are maintained during scanning to prevent fast tip degradation.

flowing through the tip. As a result, one obtains a two-dimensional map of the local conductance properties. The process can be automated by a script so that a series of conductance maps can be recorded as function of V_{DC} at a position of interest. From a series of current maps local current-voltage $I(V)$ characteristics can be extracted.

The spectroscopy mode provides the possibility to record local $I(V)$ curves with a defined ramp ($\partial V/\partial t$ = const). The AFM operating software allows to define single or multiple points (arbitrary, line-, or grid-arrangement), at which the curves are recorded. The $I(V)$ curves obtained from grid spectroscopy can be derived into a series of images with constant V_{DC} making this technique complementary to current mapping. The signal-to-noise ratio of both techniques can be reduced significantly if internal low-pass filter is adjusted to fit to the actual sampling time $\tau = 1 - 10\,\mathrm{ms\,pnt}^{-1}$.

Both current mapping and spectroscopy bear their own advantages and limitations. Current mapping benefits from better resolution and lower charge-injections due to a constantly moving tip. But the effects arising from the transient (non-equilibrium) currents can be higher in mapping mode as local points on the sample experience a fast on/off scenario when the tip passes by. Any current features detected by current mapping should consequently be measured locally as a function of time or by spectroscopy to rule out transient origins. In spectroscopy mode, contributions from transient currents can be reduced if slow ramps are chosen. Furthermore, drift issues and tip-wear are reduced because the cantilever is moved slowly compared to scanning. Yet, charge injection – as it is often occurring in case of insulating materials – can be detrimental for spectroscopy.

Although cAFM is a powerful and straightforward technique it has one main limitation, i. e., the uncertainty about the tip-sample contact. The geometry of the tip is described by the tip radius r_{tip}, which defines the contact area and electric-field distribution. The contact area can be determined from a given contact model (Hertz, JKR, etc.)[164], if one knows r_{tip} and the force applied to the cantilever. The former can be taken from the tip specifications provided that no tip degradation happens during landing or measuring. In terms of accuracy, scanning electron microscopy (SEM) measurements give more precise information. The force can be calculated from a deflection-vs-distance curve using the spring constant of the cantilever, which is usually determined by a thermal noise spectrum[153]. A simpler alternative would be to estimate the contact area by measuring a known width of a domain wall by PFM (see Sec. 3.1.3) and determine the contact diameter by the full width at half maximum (FWHM) of the DW profile[167].

The electric-field distribution underneath a tip has been investigated analytically by Molotskii[168]. The actual field distribution can be rather complex, but a rough maximum electric field at the tip-sample interface for a given tip with radius r_{tip} can be approximated by $E \approx V_{\text{DC}}/r_{\text{tip}}$[110,168]. Any changes to the tip geometry, e. g., caused by tip wear, chemical reactions, residues, etc. impede proper quantitative analysis of cAFM data. One can prevent significant tip-wear by using hard coatings (e. g. n-doped diamond), low-contact forces (low DFL-setpoints), slow scanning speeds, inert atmospheres (e. g. N_2, Ar), or by reducing the current way below the damage threshold of the tip.

Besides tip geometry, contact resistances (e. g. Schottky barriers, surface layer) and inhomogeneous field distributions within electrically-heterogeneous materials need to be considered for reliable quantitative statements[166,169,170]. Strategies to address these challenges include calibrating the tip with defined reference samples (doped semiconductors)[166] and finite-element studies to simulate the spreading field and current[11,169,170]. The latter is especially important for oxide materials, where in most cases the manufacturing of defined reference samples is not as advanced as for industrial semiconductors.

AC-cAFM Alternating-current conductive atomic force microscopy (AC-cAFM) is a modification of our standard cAFM method (see Fig. 3.2). Instead of applying a constant bias voltage, we apply solely an alternating voltage to the back of the sample $V = V_{\text{AC}} \sin(\omega t)$[a] ($V_{\text{DC}} = 0$) and measure the DC component of the alternating current I_{DC} by the built-in ammeter. During our experiments the ammeter sampling rate τ^{-1} ($\sim 1\,\text{kHz}$) is kept significantly smaller than the current oscillations ($\nu > 20\,\text{kHz}$) and I_{DC} can be estimated by integrating over the local $I(V)$ curve

$$I_{\text{DC}} = \langle I(t) \rangle \propto \int_{-V_{\text{AC}}}^{+V_{\text{AC}}} I(V)\,\mathrm{d}V. \tag{3.3}$$

Eq. (3.3) states that the DC contribution of the current deviates from zero, if the $I(V)$ curve is asymmetric (see Sec. 5.3, Fig. 5.6 for an illustration). The data obtained with this method hence provide locally resolved information on rectification properties as function of AC frequency ν. In order to rule out internal capacities or cut-offs, we tested our NT-MDT instrument with an external oscilloscope over the whole frequency range (see Sec. A.1). The following parameter space is, in principle, accessible: $0.1\,\text{kHz} < \nu \lesssim 4\,\text{MHz}$, $10\,\text{mV} < V_{\text{AC}} < 10\,\text{V}$.

---

[a] Here, $\omega = 2\pi\nu$.

During all our conductive atomic force microscopy measurements we applied small DFL setpoints, i. e., low forces, to avoid fast tip-wear and stress-induced conductance changes[166,171]. Basically all tips of Table 3.1 were used. The ANSCM-Pt tips can provide high-resolution images due to their 30 nm tip-radius. Yet, compared to the other listed models, their coating wears quite fast.

3.1.3. Piezoresponse force microscopy

Piezoresponse force microscopy PFM is a powerful tool to image and manipulate ferroelectric domain structures on the nanoscale[161,167,172]. It bases on the converse piezoelectric effect, which is present in all ferroelectrics due to their non-centrosymmetric crystal symmetry (see Sec. 2.1). The effect describes the elastic deformation ϵ_{ij} of a sample that is exposed to an electric field E_k according to

$$\epsilon_{ij} = d_{ijk} E_k, \tag{3.4}$$

with $\{i, j, k\} \in \{1, 2, 3\}$[b] and the (inverse) piezoelectric tensor d_{ijk}[26]. Since the elastic tensor is symmetric ($\epsilon_{ij} = \epsilon_{ji}$), d_{ijk} can hold up to 18 independent components. The allowed (non-vanishing) components are determined by the crystal symmetry (Neumann principle; see Refs. 173 and 26 for details). Typical tensor coefficients range from $\sim 1\,\text{pm}\,\text{V}^{-1}$ in quartz to $\sim 1000\,\text{pm}\,\text{V}^{-1}$ in $\text{Pb}[\text{Ti}_{1\text{-x}}\text{Zr}_x]\text{O}_3$ (PZT)[26].

The goal of PFM is to spatially resolve changes in the piezoelectric coefficient related to different domain orientations. For this purpose, a conductive-coated tip is brought in contact with the ferroelectric specimen. The voltage applied between the back electrode and the tip causes piezoelectric deformations and hence cantilever motions, which are monitored by the laser signal on the photodiode (see Fig. 3.3a).

The cantilever displacement Δl_i due to longitudinal piezoelectric deformations does not depend on the thickness of the sample, but rather on the applied bias voltage[174]:

$$\Delta l_i \propto d_{iii} V_{\text{BV},i}. \tag{3.5}$$

The piezoelectric deformation causes a displacement of the cantilever in proportionality to the applied voltage. The resulting driving force acts on the apex of the tip and can be separated into three components F_{Defl}, F_{Buck}, and F_{Tors}, which correspond to the displacements that leads to deflection, buckling, and torsion movements of the cantilever[167] (Figure 3.3b). Deflection and buckling modes are detected by the vertical (DFL) signal, whereas torsion of the cantilever causes a modulation of the lateral (LF) signal of the photodiode (see Figure 3.3a).

Depending on the piezoelectric constant the cantilever displacements can be quite small (∼ pm). In order to separate these from other tip-sample movements, e. g.

---

[b] The numbers 1, 2, 3 refer to certain directions in the crystal, e. g., x, y, z in hexagonal systems[173].

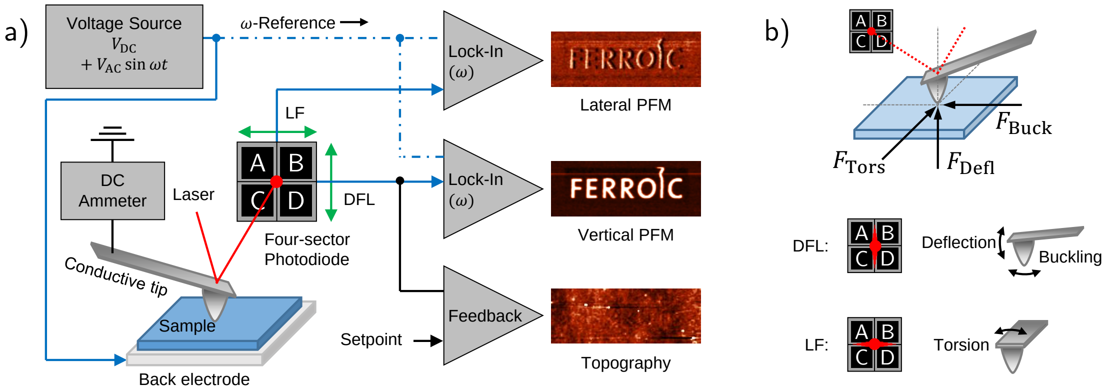

Figure 3.3.: Setup for piezoresponse force microscopy. a) Application of an oscillating voltage $V_{AC}\sin(\omega t)$ to the back electrode leads to a ω-modulation of the laser signal due to deformations of the ferroelectric sample caused by the inverse piezoelectric effect. Analyzing the deflection (DFL) and lateral (LF) laser signal by lock-in amplifiers referenced at ω provides vertical and lateral PFM images, respectively. b) Illustration of forces acting on the tip and their detection by the photodiode. F_{Defl} causes deflection, F_{Buck} causes buckling, and F_{Tors} causes torsion of the cantilever. Deflection and buckling modes are registered by the DFL signal, while only torsional modes result in modulations of the LF signal of the photodiode. Graph (b) partially adapted from Ref. 167, copyright IOP Publishing (2011). Reproduced with permission.

caused by topography, an alternating voltage V_{AC} of frequency ω is applied to the sample and the ω-modulated DFL and LF signals of the photodiode are analyzed by two individual lock-in amplifiers. We refer to this two signals as vertical (VPFM) and lateral piezoresponce (LPFM) (Figure 3.3a).

Changes in both VPFM and LPFM signals will occur, if the cantilever crosses domains with different orientation. For a uniaxial ferroelectric with its polarization oriented parallel to the surface normal (out-of-plane), the piezoelectric deformation will predominantly cause deflection movement of the cantilever. Crossing two oppositely-oriented domains will cause a phase shift of 180° in the VPFM signal, provided that the signal is background free (see below)[167]. Uniaxial FE samples with in-plane polarization can be oriented with their polarization direction perpendicular to the cantilever. Now, the torsional mode is excited and modulations caused by differently oriented domains are sensed by the LPFM signal. In a case of a multiaxial ferroelectric, all three cantilever modes are excited, which makes the analysis of the domain structure quite complex[175].

Any system-inherent background – basically present in every atomic force microscope – causes additional phases and offsets in the signals of the lock-in amplifiers, which impedes proper interpretation of the PFM signal (see Ref.[167] for a discussion). In order to remove background signals and photo-diode crosstalk, we calibrate our system with periodically-poled $\mathrm{LiNbO_3}$ (see Ref. 122 for details). Instead of recording amplitude- and phase-signal of each lock-in amplifier, we follow the procedure form Soergel[167] and use the Cartesian x- and y-channels for domain imaging. Now, the x-channels contain the complete, background corrected PFM-information, i. e., domain orientation and piezoelectric strength, while the y-channels show only error signals provoked by shifts in the background. Besides the reduction of the background signal, the calibrated signal allows us to determine the direction of the orientation of the domains.

3.1.4. Electrostatic force microscopy

Electrostatic force microscopy (EFM) offers the unique opportunity to detect changes in surface potentials, and furthermore to distinguish between fixed and mobile charges / dipoles[163,176,177]. The EFM configuration used in this thesis is shown in Figure 3.4a. Here, the AFM is operated in non-contact mode, i. e., the tip is driven by a piezo at is mechanical resonance frequency f and moved over the sample in close distance. In addition to van-der-Waals interactions, which are exploited to map the topography of the surface, electrostatic forces can act on the probe. The sensitivity to this interaction is usually rather weak, but can be increased by applying an alternating voltage with ω_{AC} to the tip and analyzing the response by lock-in amplifiers.

The electrostatic force acting on a conductive-coated probe consists of a capacitive force F_{Cap} that is quadratically proportional to the sum of the tip-sample contact-potential μ and the applied tip voltage V_{BV} (first term of Eq. 3.6). If the sample exhibits free charges q_{s} at its surface, an additional Coulomb force term F_{Coulomb} arises due to the interaction between q_{s} and the total charge on the tip Q_{tot}. The resulting force is described by

$$F = F_{\text{Cap}} + F_{\text{Coulomb}} = \frac{1}{2}\frac{\partial C}{\partial z}(\mu + V_{\text{BV}})^2 + \frac{q_{\text{s}} Q_{\text{tot}}}{4\pi\varepsilon_0 z^2}, \tag{3.6}$$

where $\partial C/\partial z$ denotes the capacitive coupling with respect to sample distance z, μ the contact potential between tip and sample, $V_{\text{BV}} = V_{\text{DC}} + V_{\text{AC}}\sin(\omega t)$ the applied bias voltage, and ε_0 the vacuum permittivity.

The total amount of charge on the tip is the sum of induced mirror charges q_{i} and charges arising from the applied bias voltage $Q_{\text{BV}} = C[V_{\text{DC}} + V_{\text{AC}}\sin(\omega t)]$. Hence $Q_{\text{tot}} = q_{\text{i}} + Q_{\text{DC}} + Q_{\text{AC}}$ and the expansion of (3.6) can be separated into a static, an ω-, and a 2ω-dependent part:

$$F_{\text{stat}} = \frac{q_{\text{s}} q_{\text{i}}}{4\pi\varepsilon_0 z^2} + \frac{q_{\text{s}} C}{4\pi\varepsilon_0 z^2} V_{\text{DC}} + \frac{1}{2}\frac{\partial C}{\partial z}\left[(\mu + V_{\text{DC}})^2 + \frac{1}{2}V_{\text{AC}}^2\right] \tag{3.7}$$

$$F_{\omega} = \left[\frac{q_{\text{s}} C}{4\pi\varepsilon_0 z^2} + \frac{\partial C}{\partial z}(\mu + V_{\text{DC}})\right] V_{\text{AC}}\sin(\omega t) \tag{3.8}$$

$$F_{2\omega} = -\frac{1}{4}\frac{\partial C}{\partial z} V_{\text{AC}}^2 \cos(2\omega t) \tag{3.9}$$

The first contribution leads to a static displacement of the cantilever, but is often difficult to detect[176]. The second contribution (3.8) is sensitive to fixed surface charges q_{s}, to the capacitive coupling, and to the contact-potential between tip and

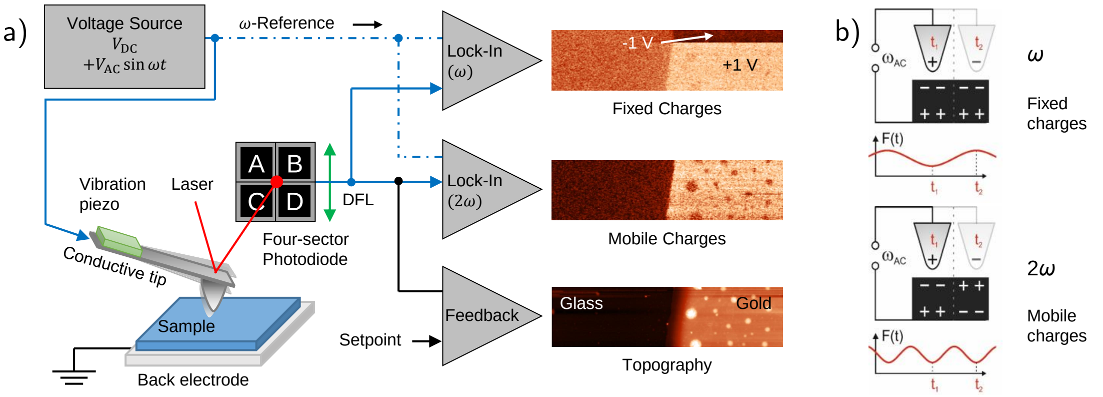
a)
Voltage Source
V_{DC}
$+V_{\mathrm{AC}} \sin \omega t$
ω-Reference
Lock-In (ω)
Lock-In (2ω)
Feedback
Setpoint
A
B
C
D
DFL
Four-sector Photodiode
Vibration piezo
Laser
Conductive tip
Sample
Back electrode
-1 V
+1 V
Fixed Charges
Mobile Charges
Glass
Gold
Topography
b)
ω_{AC}
t_1
t_2
F(t)
ω
Fixed charges
2ω
Mobile charges

Figure 3.4.: Principles of electrostatic force microscopy. a) Electrostatic force signals are enhanced by applying an alternating voltage V_{AC} of frequency ω to the tip that is driven at its resonance frequency f. While scanning in semi-contact mode, the deflection signal of the photodiode is analyzed by two lock-ins operating at ω and 2ω, which correspond to signals arising from static and mobile charges, respectively. Scan images show the response of our gold-glass calibration sample. b) Illustration of the EFM-signals taken from Ref. 82: Fixed charges result in an attractive or repulsive force that modulates with the applied voltage. Mobile carriers move to screen the alternating charge of the tip (positive at time t_1, negative at t_2). This leads to a modulated attractive force $F(t)$, alternating at doubled frequency compared to the applied voltage at ω.

sample μ. The second term in (3.8) can be zeroed by a feedback loop controlling V_{DC}, which is the basic principle of Kelvin-probe force microscopy (KPFM)[177]. The capacitive coupling includes contributions from apex, cone, and cantilever capacitances, but if the tip sample distance is reduced ($\lesssim 1\,\mathrm{nm}$) contributions from the apex of the tip dominate[176]. Using the description for the tip-sample capacity C by Hudlet[178,179], one can show, that for a flat sample with no strong variations in μ and $\partial C/\partial z$, signals arising from surface charges q_{s} dominate in the AFM scan, if the cantilever is in close proximity z to the sample (see first term $\propto z^{-2}$ in Eq. 3.8). Depending on V_{BV} bound charges will exert an attractive or a repulsive force onto the tip (see Fig. 3.4b). This interaction will happen with frequency ω and a sign change of the fixed charge will lead to phase shift of 180° in the signal[163].

The third contribution (3.9) is only sensitive to changes in the capacitive coupling $\partial C/\partial z$, which are directly proportional to changes in the dielectric constant ε of the samples. Since ε is influenced by mobile charges and dipoles, the 2ω-signal in EFM allows to detect their variations, which can be understood as follows. Mobile charges and dipoles will always create a mirror charge contrary to the tip charge, which will lead to an attractive force between the sample and the tip. The modulation of this attractive force happens at frequency 2ω, as illustrated in Figure 3.4b.

In order to make qualitative statements on the ω and 2ω signal in EFM, a calibration prior to the measurement with a known sample is mandatory. For this purpose, we scan over a glass slide that is partially covered with gold. Compared to the glass, the gold layer defines a region with a high density of mobile charges (good polarizability). Once a bias is applied to this metallic layer, negative and positive charges can be simulated with respect to the neural glass (see Fig. 3.4a). After calibration, the ω-signal of the lock-in amplifiers can be attributed to more positive (bright) / less positive (dark) charges, whereas more / less mobile charges (polarizability) correspond by bright and dark contrasts in the 2ω signal, respectively.

During our experiments we applied $V_{\mathrm{AC}} = 14\,\mathrm{V}$ at frequency $\omega = 37.4\,\mathrm{kHz}$, which is significantly below the mechanical resonance frequency f of the used cantilevers. We chose ANSCM-PA5 and DCP20 cantilevers due to their high force constants (see Table 3.1) allowing us to obtain stable imaging conditions while scanning in very close proximity to the sample. The rather large tip radius of both probes might limit their resolution, but then again ensures high contributions from the apex of the tip and minor contributions from cone and cantilever to the EFM signal[176]. The chosen setpoints for semi-contact operation ranged down to 1 % damping of the initial amplitude ($A_{\mathrm{set}} = 0.01A_0$).

3.2. Principles of cathode-lens microscopy

One of the first cathode-lens microscopes was the electron microscope used by Brüche in the 1930s to investigate photoelectrons emitted from metal surfaces. Similar to optical microscopy, Brüche optimized the imaging capabilities of his microscope with the help of an electronic ‘immersion’ field, which he created by applying high voltages of up to 30 kV between the sample (cathode) and the objective lens (extractor)[180,181]. This particular design, where the sample itself acts as a part of the lens[182,183], constitutes the principle of cathode-lens microscopy (CLM).

Nowadays microscopes still base on this concept, although their resolution has been drastically enhanced, due to the steady development in electrostatic and magnetic lenses as well as ultra-high vacuum (UHV) technology. A UHV environment, for example, facilitates designs with reduced sample-to-objective distance, which in turn leads to higher acceptance angles and aberration reduction due to electrons being closer to the optical axis. Compared to other electron-imaging techniques, e. g., scanning electron microscopy (SEM) and transmission electron microscopy (TEM), CLM is a complete non-scanning technique that captures full-field images in real time[184].

The strong electric potential $V_0 \approx 5 - 20\,\mathrm{kV}$ between the sample and the extractor serves two purposes in CLM (see Fig. 3.5). First, it allows to extract low-energetic electrons, which have small inelastic mean free paths (IMFPs) ranging from 0.5 – 20 nm[185,186], which makes CLM extremely surface sensitive. Second, the relative energy spread $\Delta E/E$ of the electrons gets significantly reduced, as the electrons are accelerated to a defined kinetic energy of $E_{\mathrm{kin}} = eV_{\mathrm{a}}$. The decreased energy and angular spread reduces chromatic and spherical aberration, respectively, which finally leads to higher lateral resolutions[187]. Modern cathode-lens systems contain additional electrostatic and/or magnetic lenses that allow to project the image from the objective onto a photon-generating detector[c], which is read out by a CCD camera for fast data acquisition. In combination with different types of energy filters[188–190], CLM allows to image surface sensitive electrons spatially and energetically resolved, making it a powerful tool in surface science.

The cathode-lens microscope that has been used during this thesis is a FE-LEEM P90, which bases on a design by Tromp[191–193] and is now distributed commercially by SPECS[194]. The microscope serves as endstation of the soft x-ray beamline UE56/1-SGM at Bessy II Berlin operated by the PGI-6 group of Forschungszentrum Jülich. The aberration-corrected microscope is designed to perform photoemission electron microscopy (PEEM)[195] (Sec. 3.2.1) and low-energy electron microscopy (LEEM)[196,197] (Sec. 3.2.2) experiments with high spatial resolution. Aberration correction is achieved by a tetrode mirror[192,198,199] providing resolutions down to 20 nm in PEEM mode and 2 nm in LEEM mode[193,194]. The energy resolution in LEEM is $\Delta E = 0.05\,\mathrm{eV}$. In PEEM, a resolution of $\Delta E = 0.15\,\mathrm{eV}$ can be achieved with the smallest energy slit. The microscope operates at pressures of about 6×10^{-10} mbar. Heating and cooling stages provide sample temperatures ranging from about 160 to 1200 K. The CCD camera can record automatized imaging sequences with exposure times down to 100 ms. Further information on the microscope including optical components, alignment, and corrections can be found in the following references: 183, 190, 200, 192, and 193.

3.2.1. Photoemission electron microscopy

Photoemission electron microscopy (PEEM) bases on photon-electron interaction. In this particular case, it is the photoelectric effect that describes emission of electrons by photons with energy $E = h\nu$[201]. Aside from the photon energy, the kinetic energy of the emitted electrons depends on the work function ϕ of the material and the binding energy E_bind of the excited electronic state:

$$E_\mathrm{kin} = h\nu - \phi - E_\mathrm{bind}. \tag{3.10}$$

In the experiment, photons from a suitable light source (e. g. discharge lamp, x-ray tube, synchrotron) are focused on the sample causing electron emission. The emitted electrons are accelerated by the electric 'immersion' potential $V_\mathrm{a} = -V_0 + V_\mathrm{st}$ towards the optics of the microscope, where they pass the objective lens, the energy filter, and further optics before reaching the detector (see Fig. 3.5). The settings of the optics and magnetic sector field (prism) of the microscope are optimized for electrons passing with an kinetic energy of $E_\mathrm{kin} = eV_0$. Due to the bending properties of the sector field, the kinetic energy distribution of the emitted electrons can be measured by taking a series of images as function of start voltage V_st.

---

[c] Such a detector can be, e. g., a phosphorous screen placed behind a signal-enhancing multichannel plate.

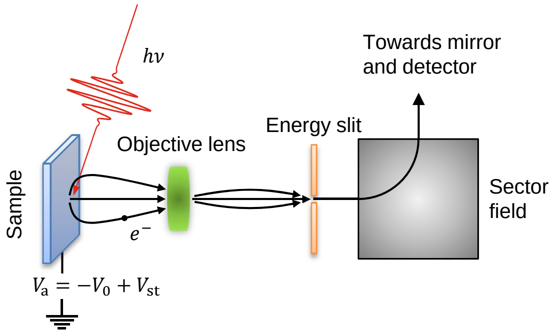

Figure 3.5.: Principle of photoemission electron microscopy (PEEM). Photons excite electrons that are accelerated towards the electron optics of the microscope with an electronic drift energy corresponding to the applied voltage $E_{\mathrm{kin}} = eV_a$. An energy slit after the objective cuts out an 0.2 eV slice, reducing the total energy spread of the electrons. Behind the energy slit the electron beam is deflected by an energy-selective magnetic sector field (prism) towards further optics as, for example, an aberration-compensating mirror and a detector connected to a CCD camera.

Threshold PEEM The minimum photon energy required to emit weakly-bound electrons corresponds to the work function ϕ (see Eq. 3.10). Typical work functions range over 2 – 6 eV and depend on material, crystal orientation, and surface conditions[91,202]. In threshold PEEM, a broad-band mercury discharge lamp with a characteristic energy peak at 4.9 eV is used to emit valence electrons with small binding energies, i. e., close to the Fermi energy E_F[189,195]. The low-energy emission leads to an electronic energy-spread with a typical width of around 1 eV (Fig. 3.6a). The low energy width in threshold PEEM reduces chromatic aberration and allows to image work-function differences and topography features. The reason for work function sensitivity is given by (3.10), whereas topography contrasts arise from surface protrusions distorting the electric field lines. The distortions of the field affect the electron trajectories, which gives rise to additional contrast features and changes in the apparent size of the imaged objects[195].

X-PEEM In x-ray photoemission electron microscopy (X-PEEM), electrons are evoked by x-rays produced from laboratory sources or electron storage rings (synchrotrons). The advantage of synchrotron light is that it provides x-rays of high brilliance tunable in both energy and polarization (linear horizontal/vertical; circular left/right)[203]. Since electronic transitions obey well-defined selections rules[204], wavelength and polarization of the x-rays can be tuned to excite specific transitions. For example, resonant excitation of the manganese L_3 edge, which is described by a transition from a 2p core shell to an empty 3d valence state, requires a photon energy of 638.7 eV[205].

Exposure to x-rays with $E = h\nu$ ionizes the material by emission of photoelectrons that leave holes in the core shells behind. This soft-x-ray excited state relaxes predominantly via Auger electron processes[183,195]. A part of the photo and Auger electrons scatter within the illuminated material and cause a cascade of secondary electrons (SEs), which escape the sample in addition to unscattered photo- and

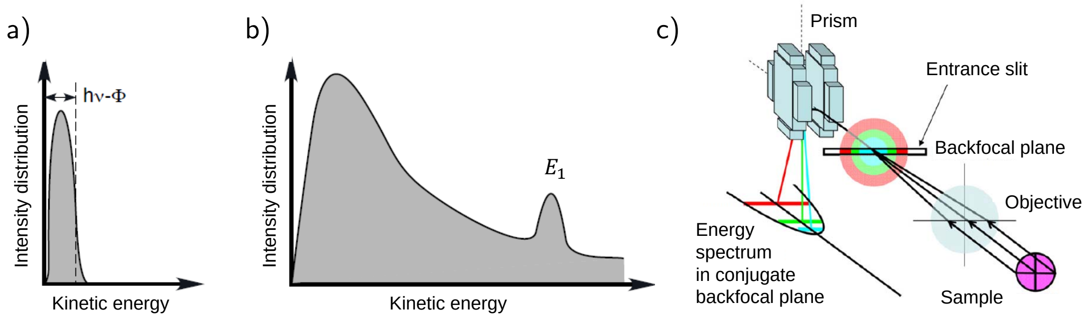

Figure 3.6.: Secondary electron emission and energy filtering in PEEM. a), b) Kinetic-energy spectra of emitted electrons in threshold PEEM and X-PEEM, respectively. The energy E_1 corresponds to a characteristic transition, e. g., from a shallow electron level, allowing to calibrate the energy filter. Graphs in (a) and (b) reproduced from Ref. 206, copyright Forschungszentrum Jülich (2016). c) Energy filter of the FE-LEEM P90 with details given in the text. Graph (c) reproduced from Ref. 191, copyright IOP Publishing (2009). Reproduced with permission.

auger electrons[195]. Figure 3.6b shows a typical energy spectrum of the emitted electrons in an X-PEEM experiment with the high-intense SE peak shown on the left. The low-energetic electrons created in soft x-ray photoemission processes have small IMFPs limiting the probing depth of X-PEEM to about 10 nm. The small peak at energy E_1 in Fig. 3.6b corresponds to an electronic transition, e. g., from a shallow core level, which can be used for offset calibration of the energy filter (see below).

X-PEEM imaging can, in principle, also be performed with the direct photoelectrons[195,206]. In the framework of this thesis though, we focus on imaging with the high-intense secondary electrons. As given by the core hole decay process, the intensity of the secondary electron peak is proportional to the amount of core holes produced by direct photoemission. Thus, it contains all information that can be related to electronic transitions, i. e., chemical, magnetic, and structural properties. Work function contrasts are dominant at low photon energy (threshold PEEM) and might be restrained in X-PEEM, because of the excitation with high-energetic photons[206]. In addition, local surface charging of insulating regions in the material can create shifts in the energetic spectrum[195]. In our study we fit the SE peak by a Gaussian function and use the fit-determined maximum of the peak E_{peak} to determine relative differences in the kinetic energy of the electrons.

In order to achieve high-quality spectra, energy filtering in X-PEEM is mandatory. The relatively broad distribution in energy (see Fig. 3.6b) causes chromatic and spherical aberration and thus reduces both spatial and energy resolution. The angular distribution of electrons provoked by their energy spread can be decreased by placing an energy slit into a cross-over of the beam path[187,191]. The spatial position of the slit significantly influences the offset in the energy scale. Thus, calibration of the filter (see above) is mandatory if absolute energy values are required.

The energy filter in the FE-LEEM P90 bases on such a principle and is shown in Figure 3.5. The angular distribution (k_x, k_y) of electrons emitted from a homogeneous surface is a function of electron energy and can be represented by a paraboloid of revolution in the $(k_x, k_y, E_{\mathrm{kin}})$ space[191]. The energy slit allows to extract a slice of this paraboloid, which is then projected to the (k_y, E_{kin}) plane by the prism behind the objective and the slit. Figure 3.6c shows how three energy levels, represented by colored circles in the backfocal plane, can be reduced to lines in the electron spectrum of the conjugated backfocal plane (k_y, E_{kin}) by placing the energy slit at $k_x = 0$[191]. The parabolic shape is due to the dispersion relation of free electrons. In combination with the energy filter, which reduces the error in energy down to 0.15 eV, the aberration-corrected FE-LEEM P90 is capable of 20 nm resolution in PEEM under optimal settings.

3.2.2. Low-energy electron microscopy

Low-energy electron microscopy images reflected or back-scattered electrons of low energy[189,207]. Electrons are created via field-emission inside an electron gun with a defined current I_{gun} and kinetic energy $E_{\mathrm{kin}} = eV_0$ (V_0 usually 5 - 20 kV). The electrons travel to the surface of the sample, where they get decelerated by the sample potential $V_{\mathrm{a}} = -V_0 + V_{\mathrm{st}}$ (Fig. 3.7a). Depending on the start voltage V_{st} the electrons get reflected or interact with the sample. The strong field between sample and objective accelerates the reflected and back-scattered electrons back into the microscope, which projects them onto a detector. A magnetic sector field separates the incident beam created by the electron gun from the reflected electron beam. Similar to PEEM, optics and sector-fields of the microscope are set to fit to the initial energy of the electrons $E_{\mathrm{kin}} = eV_0$ and spatially-resolved distributions in the kinetic energy of the electrons can be obtained by taking an image series as function of V_{st}.

A typical electron reflectivity curve for regions with two different surface potentials ϕ is shown in Figure 3.7b. At low V_{st}, the kinetic energy of the electrons is not sufficient to reach the sample and the electrons get reflected above the surface, which corresponds to the mirror-electron microscopy (MEM) mode. Increasing the potential further allows some of the electrons to penetrate into the surface. Consequently, not all electrons get back-reflected, which manifests in a drop in intensity (electron yield) and refers to the LEEM mode (Fig 3.7b). The inflection point in the curve is defined as mirror-electron to low-energy electron microscopy (MEM-LEEM) transition[189,208–211] and is a relative measure for the surface potential. We note that regions with higher surface potential ϕ_1 attract electrons already at low kinetic energy, thus leading to an earlier MEM-LEEM transition. The difference in potential between regions can be obtained from the difference in energy of their MEM-LEEM transitions. The final increase in intensity at higher energies is primarily caused by beam-induced secondary electrons.

The resolution in MEM or LEEM mode can, in principle, be optimized down to 2 nm in the FE-LEEM P90 microscope[193,194]. Yet, local changes in the electric field provoked by topography and static charges strongly influence the electron trajectories, which can limit the interpretation of LEEM images. The resulting intensity

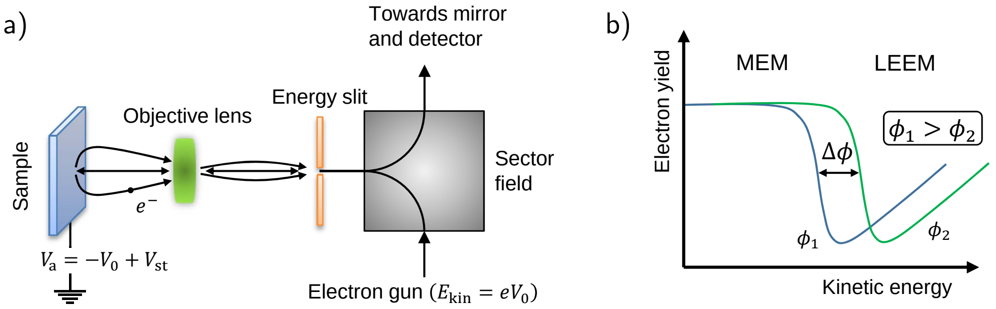

Figure 3.7.: Principle of low-energy electron microscopy (LEEM). a) Electrons with an energy of $E_{\mathrm{kin}} = eV_0$ are transferred by a sector field onto the sample. The cathode-lens field decelerates the electrons according to $V_a = -V_0 + V_{st}$, which leads to direct reflection or electron-surface interaction. The low-energetic electrons above the surface of the sample get re-accelerated into the microscope and projected onto a detector. b) Schematic of electron reflectivity curves for a material with regions of two different surface potentials ϕ. At low kinetic energy, electrons get reflected above the surface (MEM). In LEEM mode, higher kinetic energies lead to electron-surface interactions, which happen at lower energies for larger surface potentials ϕ. The potential difference $\Delta\phi$ is obtained from the inflection points of the two curves.

variations on the detector caused by potential variations have been mathematically described by Nepijko and coworkers[212–214]. Their framework can help to better understand contrasts observed in high-resolution MEM or LEEM experiments.

During this thesis we focus on mainly on MEM-LEEM transitions to determine variations in local surface potentials. From a recorded series of energy-dependent images we extract the MEM-LEEM transition curves pixel-by-pixel and fit them with complementary error functions[210,211]. Relative surface potential maps are then created by plotting the inflection points obtained from each fit.

3.3. Sample preparation

3.3.1. Single-crystal growth

Hexagonal manganite single crystals can be grown by the floating-zone- or by the flux-growth method. Our $\mathrm{ErMnO_3}$ samples were synthesized in collaboration with Zewu Yan and Edith Bourret–Courchesne at LBNL Berkeley. All samples presented in this thesis are grown by Zewu Yan using the pressurized floating-zone method[215] and a detailed description is given in Ref. 216. In comparison to the flux-growth method, floating-zone growth has the advantage to produce high-quality stoichiometric and doped single-crystals of $\mathrm{ErMnO_3}$ with large dimensions: up to 5 mm in diameter and up to 60 mm in length (see Fig. 3.8a). Large sample dimensions are mandatory for the cathode-lens experiments presented in Chapter 6. During growth a high-pressure we apply an atmosphere of 0.8 MPa containing a mixture of Ar gas balanced with 5 % $\mathrm{O_2}$ in order to prevent manganese evaporation and to maintain oxygen stoichiometry. The latter is especially important for electron- or hole-doped crystals (see Sec. 2.2.3).

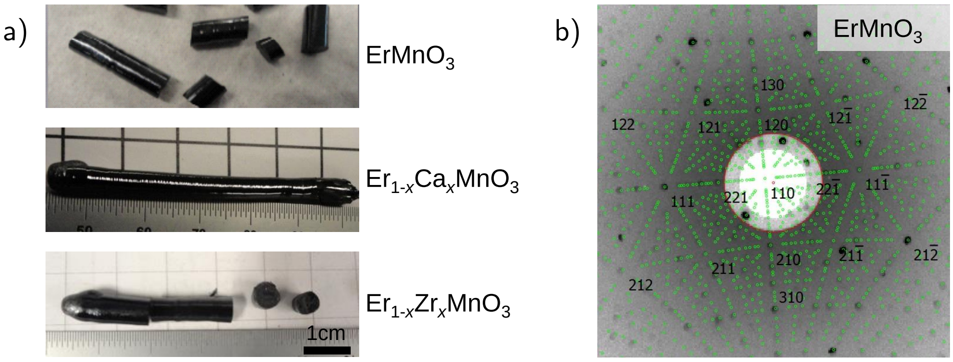

Figure 3.8.: Growth and orientation of ErMnO$_3$ single crystals. a) Top to bottom: Single-crystal rods of un-, hole-, and electron-doped ErMnO$_3$, respectively. b) Back-scattered Laue pattern of undoped ErMnO$_3$ obtained by exposing the crystal for 3 min to the white x-rays of a Mo-tube working at 50 kV, 35 mA. Crystal orientation along (110) as indexed by using the Cologne Laue Indexation Program (CLIP)[217].

Although flux and floating-zone crystals exhibit the same hexagonal structure, they can show quite different defect densities, which impact on their electronic properties. Flux-grown crystals are expected to have a lower defect concentration than floating-zone-grown crystals, but might contain a higher percentage of impurity ions originating from the flux[215]. Both defects and impurity ions can influence charge-carrier concentration, pinning, and scattering.

3.3.2. Crystal orientation by back-reflection Laue method

Crystals of defined orientation need to be prepared for our envisaged scanning probe (Chapters 4, 5) and cathode-lens experiments (Chapter 6). For this we constructed a goniometer compatible with both the in-house Laue camera and diamond-wire saw. Backscattered Laue images are recorded with white x-rays from a Molybdenum tube. The tube works at 50 kV, 35 mA and an optimized image contrast for ErMnO$_3$ was obtained for exposure times of about three minutes. Figure 3.8b shows a typical Laue pattern for a crystal that is oriented parallel to the (110) direction of the lattice (corresponds to y-cut, see Fig. 2.6). For indexation of the diffraction spots we use the Cologne Laue Indexation Program (CLIP)[217] with the following parameters[218]: space group $P6_3cm$ (185), lattice constants $a = 6.1121$ Å, and $c = 11.42$ Å. After Laue diffraction, the goniometer is mounted to the diamond-wire saw and the sample is cut perpendicular to the normal vector of the desired lattice plane that has been previously aligned by x-ray reflection.

3.3.3. Surface treatments

After growth and orientation, all samples are lapped with a 9 µm-grained Al$_2$O$_3$-water suspension until the desired thickness d is reached (usually $d \approx 1$ mm). In order to achieve high-quality surfaces, we polish the samples for 45 min using the silica slurry '2EX' from Eminess. By applying this treatment, we achieve roughness values down to 0.2 nm (RMS). Prior to the measurements, samples are cleaned with high-purity acetone and isopropanol to remove any residuals, as e. g., dust from the surface.

4. Electronic transport phenomena at charged domain walls

Charged domain walls in ferroelectrics are intensively studied due to their intriguing functional properties[6,10,14,59,106]. In contrast to neutral domain walls, charged domain walls exhibit bound charges, which leads to diverging electrostatic potentials making them energetically costly. The electrostatic potentials require charge compensation leading to charge carrier redistribution and band bending. As a consequence, these walls exhibit diverse transport characteristics ranging from highly conductive to strongly insulating[11,12,18].

Charged domain walls are, however, rarely found in the as-grown state of proper ferroelectrics and their stabilization often requires sophisticated switching procedures[10,14,72,79,106]. This complicates the engineering of their electronic properties. In contrast, charged domain walls are stabilized naturally in improper ferroelectrics, where ferroelectricity arises as a secondary effect[11,12,18]. Thus, improper systems present an ideal template for imposing the desired behavior.

In this chapter, we follow the idea of chemical impurity doping that is well established in semiconductor physics, in order to alter the electric transport at charged domain walls. In addition, we investigate the possibility to use electric fields to control the domain wall behavior. For this, we use hexagonal $\mathrm{ErMnO_3}$, which is a ferroelectric p-type semiconductor that readily develops charged domain walls in the as-grown state. We begin with a comprehensive characterization of undoped $\mathrm{ErMnO_3}$ (Sec. 4.1). Second we demonstrate how chemical doping (Sec. 4.2) can be used to tune domain-wall currents (Sec. 4.3, 4.4). In the final part we will go beyond transport phenomena associated with majority carriers and focus on additional functionality that arises due to minority carriers (Sec. 4.5).

4.1. Charged domain walls in $\mathrm{ErMnO_3}$

Previous studies characterized the basic conductance properties of charged domain walls in hexagonal manganite ($R\mathrm{MnO_3}$) crystals[11,12] and explained their unusual transport behavior by the redistribution of the intrinsic mobile hole carriers (see also Sec. 2.2.2). Up to now, however, different fundamental questions remain to be clarified. It remains to be shown how domain-wall currents evolve over time and whether domain-wall currents directly reflect the intrinsic properties of the domain wall. Furthermore, possible conduction mechanisms at the walls and in the bulk have not been discussed in detail. In this section, we address these fundamental

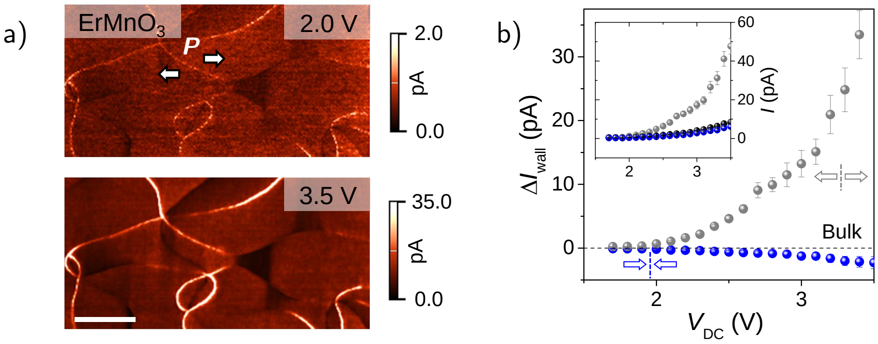

Figure 4.1.: Fundamental transport properties of ErMnO$_3$. a) cAFM scans performed at the same position while applying different biases to the sample. Conductive and insulating domain walls can be clearly distinguished. The shadow-like insulating regions might be attributed to the propagation of insulating domain walls into the depth. Scale bar is 2 µm. b) $I(V)$ characteristics derived by plotting the current of the bulk and the domain walls. Error bars represent the statistical variation over five domain-wall positions.

questions by performing a series of conductive atomic force microscopy (cAFM) measurements. The results provide the basis for our following studies on charged domain walls in the subsequent sections.

4.1.1. Fundamental transport properties

We begin with the basic conductance properties of floating-zone-grown ErMnO$_3$. Analogous to the first study on flux-grown ErMnO$_3$ crystals in Ref. 11, we perform a series of cAFM scans as function of bias voltage V_{DC}. Figure 4.1a shows two representative scans at bias voltages of 2.0 and 3.5 V. Our floating-zone crystals exhibit domain walls being less (dark) and more conductive (bright) than the surrounding bulk. PFM analysis identifies these walls as head-to-head ($\rightarrow\leftarrow$) and tail-to-tail ($\leftarrow\rightarrow$) type, respectively. Increasing the bias-voltage leads to more pronounced domain-wall currents and over the whole voltage range the conductive tail-to-tail, insulating head-to-head wall behavior remains. On a closer inspection, one observes insulating regions between the walls (see center of the scans in Fig. 4.1a), which we attribute to the propagation of the insulating head-to-head walls into the depth of the material. These walls act as a barrier to the spreading tip-injected current, consistent with macroscopic dielectric spectroscopy measurements[219].

From the series of scans we derive $I(V)$ curves for the bulk, the head-to-head, and the tail-to-tail walls. The corresponding raw data are shown in the inset of Figure 4.1b; all of them following a Schottky-like trend ($\propto \exp\left(eV/\eta kT\right)$, see Sec. 4.1.3). Relative domain-wall currents $\Delta I_{\text{wall}} = I_{\text{wall}} - I_{\text{bulk}}$ are shown in Figure 4.1b. Aside from a slight asymmetry in the relative current, the results are consistent with earlier studies performed on flux-grown systems[11]. This implies that both flux-grown and floating-zone-grown crystals exhibit qualitatively the same transport properties. Quantitative differences are likely to arise because of different defect densities associated with the synthesis (see Sec. 3.3.1).

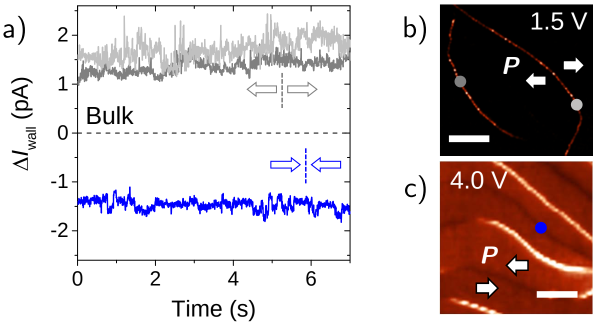

Figure 4.2.: Time-dependent domain-wall currents in ErMnO$_3$. a) Time dependence of currents measured for two conductive tail-to-tail (←→) walls and one insulating head-to-head (→←) wall, which were recorded at $V_{DC} = 1.5\,V$ and 4.0 V, respectively. Domain-wall currents remain stable over seven seconds. The relative currents ΔI_{wall} were derived by subtracting average domain currents, i. e., 0.07 pA and 10.33 pA for 1.5 V and 4.0 V, respectively. Average ΔI_{wall} for dark-gray, light-gray, and blue curve are 1.43 ± 0.19 pA, 1.67 ± 0.21 pA, and -1.47 ± 0.11 pA respectively. b), c) Positions of the time-dependent measurements as indicated by the colored dots. cAFM scans taken with the same bias voltage as the time-dependent measurements. Scale bars in (b) and (c) are 1 µm.

4.1.2. Time-dependent domain-wall currents

After characterizing the basic transport properties, we investigate the stability of the domain-wall currents over time. Time-dependent measurements are a powerful tool in order to distinguish real domain-wall conductance from transient or switching currents. The latter can be caused, e. g., by the trailing-field from the scanning tip[106]. Furthermore, we will learn about the time-stability of the currents, which is crucial for application purposes.

The evolution of the relative current ΔI_{wall} over time under a constant voltage of $V_{DC} = 1.5\,V$ is shown for two tail-to-tail walls in Figure 4.2a (gray curves). We observe that the current remains roughly constant over a time of seven seconds with slight oscillations probably stemming from mechanical instabilities in tip-sample contact (see caption for average current values and noise). The current values of the tail-to-tail walls are in agreement with the reported orientation-dependence of domain-wall currents in RMnO$_3$[11] (see tip positions in Fig. 4.2b). In addition, Figure 4.2a shows the time-dependent current ΔI_{wall} measured at a head-to-head wall, which was recorded at $V_{DC} = 4.0\,V$ (blue curve, position shown in Fig. 4.2c). The current is stable for the time of the experiment and the average current value (see caption) follows the trend in Figure 4.1b.

Based on the data we conclude that both domain-wall currents are not attributed to transient or switching currents. The currents measured in scanning-based experiments correspond to a real change in conductance at the domain walls and are stable over several seconds.

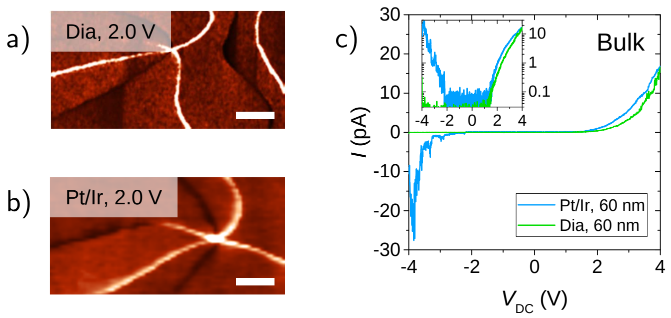

Figure 4.3.: Tip-coating dependence on electronic transport in $\mathrm{ErMnO_3}$. a), b) cAFM scans for both tips at a bias voltage of 2.0 V. Scale bars in (a) and (b) are 1 µm. c) Bulk $I(V)$ curves obtained on in-plane oriented domains measured with a Pt/Ir- and a diamond-coated tip, both having the same tip radius r_{tip}. Further details on the tips are found in Table 3.1. The two $I(V)$ curves describe a similar trend under forward bias $V_{\mathrm{DC}} > 0$ (see inset).

4.1.3. Possible electronic conduction mechanisms

The $I(V)$ curves presented in Fig. 4.1b suggest a Schottky-like trend for positive tip biases. In order to better understand the local variations in conductance, we next perform measurements with different tip coatings and investigate potential conduction mechanisms.

Figure 4.3a and b show cAFM scans obtained on an in-plane oriented $\mathrm{ErMnO_3}$ sample with a Pt/Ir- and a diamond-coated tip, respectively, both with a nominal tip radius of $r_{\mathrm{tip}} = 60\,\mathrm{nm}$. The two scans reflect similar domain-wall behavior. We next measured bipolar $I(V)$ curves of the domains, which are presented in Figure 4.3c. The data show almost equal currents and the same trend under forward bias ($V_{\mathrm{DC}} > 0\,\mathrm{V}$), although the work functions of Pt/Ir ($\phi_{\mathrm{tip}}^{\mathrm{Pt/Ir}} = 5.12 - 5.93\,\mathrm{eV}$[91,202]) and diamond ($\phi_{\mathrm{tip}}^{\mathrm{Dia}} = 3.1 - 5\,\mathrm{eV}$[91,220]) are different. In case of an ideal barrier (Eq. (2.19)), the lowest difference in work function $\Delta\phi_{\mathrm{b}} = \phi_{\mathrm{tip}}^{\mathrm{Pt/Ir}} - \phi_{\mathrm{tip}}^{\mathrm{Dia}} = 0.12\,\mathrm{eV}$ would lead to at least two orders of magnitude higher currents for a Pt/Ir-coated tip than for a diamond-coated tip in an interface-dominated scenario[a] (see Eq. (2.20)).

We thus exclude that contact resistance due to a difference in work function dominates the obtained transport behavior. Analogous to other semiconductors, however, it is reasonable to assume that a barrier caused by interface layers and states is present[91], explaining the asymmetry of the asymmetry of the $I(V)$ curves in Figure 4.3c.

In order to better understand the influence of the barrier on the current signals, we compare our data to different conduction mechanisms (see Sec. 2.1.1.4). For this we perform a careful current spectroscopy analysis (see Sec. 3.1.2) and derive $I(V)$ characteristics for bulk, head-to-head (→←), and tail-to-tail (←→) domain walls. Figure 4.4a to c show the linearized curves according to different conduction mechanisms: (a) Thermionic emission forward (Schottky) / Hopping conduction

---

[a] For $\mathrm{ErMnO_3}$ we took the following band energy $E_{\mathrm{g}} = 1.6\,\mathrm{eV}$[139] and electron affinity of $\chi = 3.83\,\mathrm{V}$[221] to calculate $\phi_{\mathrm{b}} = E_{\mathrm{g}} + \chi - \phi_{\mathrm{tip}}$.

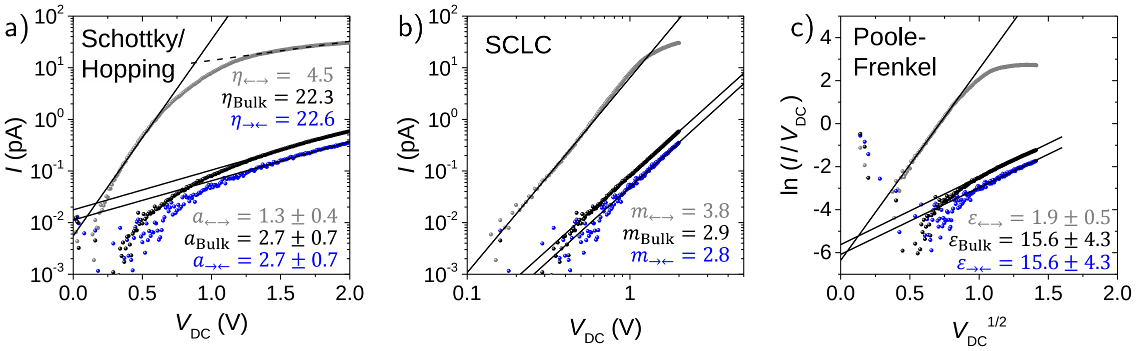

Figure 4.4.: Possible conduction mechanisms in $ErMnO_3$. a) to c) Linearization according to thermionic emission forward (Schottky) / hopping conduction, space-charge-limited conduction, and Poole-Frenkel emission, respectively. The derived fit constants are shown in the graphs.

($\ln(I) \propto V_{\mathrm{DC}}$), (b) space-charge-limited conduction (SCLC; $\ln(I) \propto \ln(V_{\mathrm{DC}})$), and (c) Poole-Frenkel emission ($\ln(I/V_{\mathrm{DC}}) \propto V_{\mathrm{DC}}^{1/2}$).

For thermionic emission according to (2.20), we find an ideality constant $\eta = 4.5$ at the tail-to-tail wall, while η is about 22 for the bulk and the head-to-head wall. The former is in agreement with typical ideality constants found in other oxide systems[222,223] and hence (2.20) also holds for lower voltages at the tail-to-tail wall[b]. The ideality constant of the bulk and the head-to-head wall is significantly higher, pointing towards a different injection mechanism (see Sec. 2.1.1.4). The exact microscopic reason for the differing ideality constants is not clear at this point, but the different values of η show that the transport scenario at the interface is connected to the electronic properties of the material underneath.

Aside from a barrier-determined scenario, we analyze the data with respect to different bulk-determined mechanisms (see Sec. 2.1.1.4). Hopping conduction might be a possible scenario for bulk and head-to-head wall with reasonable hopping lengths $a = 2.7 \pm 0.7\,\mathrm{nm}$, which is in agreement to observation of hopping conduction in macroscopic measurements[219]. At the tail-to-tail walls hopping might be present at voltages larger $V_{\mathrm{DC}} > 1.25\,\mathrm{V}$, yielding tunneling distances of $a = 1.3 \pm 0.7\,\mathrm{nm}$ (dashed line in Fig. 4.4a).

Considering space-charge-limited conduction results in good fits over the whole voltage range with exponents m greater than two (Fig. 4.4b). The exponent $m = 3.8$ for the tail-to-tail wall is rather high, but similar values have been observed in ZnO[224]. For bulk and head-to-head wall the exponent m is between 2.5 and 3.0, which is close to values observed in $BiFeO_3$ and HfO_2 thin films[9,225]. The high values of the exponents can be related to deep trap states[226], partially filled trap states[227], and broad trap distributions[224].

Figure 4.4c presents the fits according to Poole-Frenkel emission. The obtained dielectric constants for head-to-head wall and bulk are in agreement with the literature value of the static dielectric constant[228] ($\varepsilon_{\mathrm{s}} \approx 20$). At the tail-to-tail wall, the dielectric constant is lower, which would be in agreement with the higher conductance at this wall.

---

[b] At $V_{\mathrm{DC}} > 1.25\,\mathrm{V}$ a linear relation might be found (dashed line in Fig. 4.4a), too, and $\eta = 46.7$, but then the condition $V > 3\eta kT/e$ is violated.

In conclusion, all investigated models are likely conduction mechanisms over certain voltage ranges in our floating-zone $ErMnO_3$ system, but further insight can be gained from thickness- and temperature-dependent studies. Most important for our subsequent studies is that unrelated to the dominating conduction mechanism, all models point towards intrinsic differences between the bulk and the domain walls. Thus, our cAFM measurements are able to reveal changes of the local electronic properties.

4.2. Macroscopic properties of doped $ErMnO_3$

After demonstrating the sensitivity of our experiments to intrinsic changes at the wall, we now turn to chemically doped RMnO$_3$ systems. One goal of this thesis is to apply impurity doping of the bulk in order to control the conductance performance at domain walls in RMnO$_3$. As a first step, we will present macroscopic transport data, demonstrating that the synthesized sample series displays the desired electronic properties. The microscopic ferroelectric domain structure and the macroscopic electronic conduction properties of both n- and p-doped $ErMnO_3$ will be discussed.

4.2.1. Robustness of the ferroelectric domain structure

For our doping-dependent study we prepared p-doped $Er_{1-x}Ca_xMnO_3$ and n-doped $Er_{1-x}Zr_xMnO_3$ both with dopant concentrations of $x = 0.002$ and $x = 0.01$ by the floating-zone method (see Sec. 3.3.1). Figure 4.5 presents the respective piezoresponse force microscopy (PFM) scans gained on samples with in-plane orientation. We observe that the domain structure – showing the characteristic six-fold meeting points (vortices) – is preserved in the investigated doping range ($x \leq 0.01$). We find that the as-grown domains are usually in the order of a few microns. Only $Er_{1-x}Zr_xMnO_3$ exhibits slightly smaller domains, possibly attributed to a different cooling rate during synthesis[122,128]. Since the domain wall charge state is supposed to be independent of the domain size and in order to avoid any compositional changes by annealing[119,120,138,143], we keep the as-grown state of our samples for our further investigations.

4.2.2. Electronic conductance properties of the bulk

In order to confirm that our impurity-doped samples efficiently changed their electronic properties, macroscopic two-point transport measurements were performed to detect relative changes in conductance[229]. First, we measure the transport parallel and perpendicular to the polarization. In Figure 4.6a the corresponding current densities $J = I/A$ are plotted as function of electric field E. The obtained Schottky-like $J(E)$ curves are almost symmetric to the origin and show higher conductance for

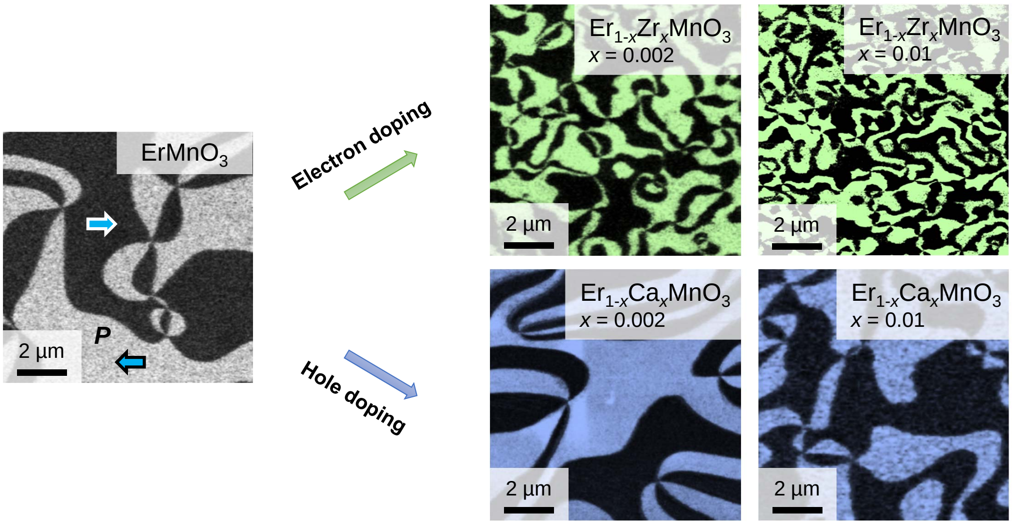

Figure 4.5.: Ferroelectric domain structures in doped $ErMnO_3$. The left scan reveals the as-grown domain structure of undoped $ErMnO_3$. On the right, lower and upper rows present the as-grown domain structures of the respective hole- and electron-doped compounds. All scans are of same size and dark and bright domains point to the right and left, respectively.

transport perpendicular to the polarization ($J_{xy} \perp P$). The conductance anisotropy is attributed to the layered Mn-O arrangement and the two-dimensional nature of the electronic structure in $R\mathrm{MnO}_3$[140,142] (see Secs. 2.2.1, 2.2.3).

Figure 4.6b compares the $ErMnO_3$ data ($J_{xy} \perp P$) with $J(E)$ characteristics of hole-doped $\mathrm{Er}_{1-x}\mathrm{Ca}_x\mathrm{MnO}_3$ ($x = 0.002$, $x = 0.01$) and electron-doped $\mathrm{Er}_{1-x}\mathrm{Zr}_x\mathrm{MnO}_3$ ($x = 0.002$). The current density J_{xy} shows a pronounced doping-dependence. J_{xy} continuously increases with increasing hole concentration. At a field of $E = 0.075\,\mathrm{kV\,cm^{-1}}$, J_{xy} increases by almost two orders of magnitude for a Ca doping level of $x = 0.01$. In contrast, the Zr-doped sample exhibits suppressed conductance. The result is in agreement with the p-type nature of the $R\mathrm{MnO}_3$ family and can be explained by the electronic structure of the manganese valence bands[142] (see Sec. 2.2.3). Holes are introduced into the dispersive xy and $x^2 - y^2$ d-bands which causes the conductivity to increase. In contrast, small amounts of introduced electrons decrease the conductivity as they either compensate pre-existing holes or occupy localized $3z^2 - r^2$ bands with weak orbital overlap. The results in Fig. 4.6 thus demonstrate that the applied doping allows for enhancing / suppressing the p-type conductance of the bulk.

In order to introduce a qualitative change in the conduction properties and go from p-type to n-type characteristics, we further synthesized $\mathrm{Er}_{1-x}\mathrm{Zr}_x\mathrm{MnO}_3$ with a higher doping level ($x = 0.01$). Corresponding results are shown in Figure 4.7. Here, we present average $I(V)$ characteristics measured by cAFM grid spectroscopy over several domains.

By recording the data with the same tip we avoided unwanted tip-dependent contributions (e. g. resistivity, contact-force, tip-area, etc); the $\mathrm{Er}_{1-x}\mathrm{Zr}_x\mathrm{MnO}_3$ samples were characterized in the following sequence: $x = 0,\ 0.002,\ 0.01,\ 0$. The data in

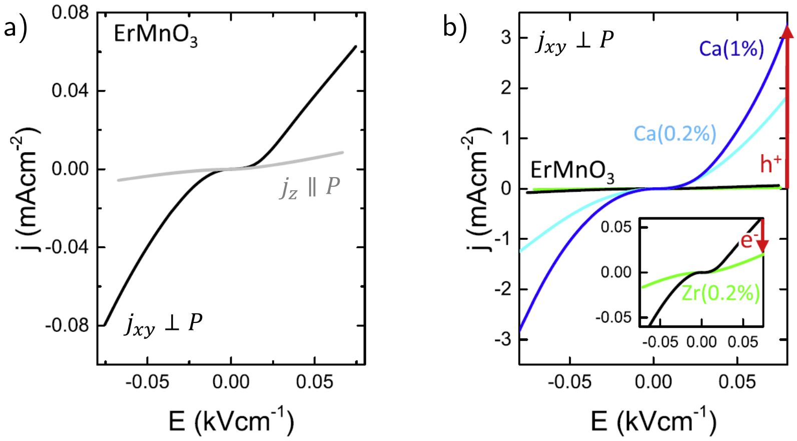

Figure 4.6.: Bulk $J(E)$ characteristics of differently doped $\mathrm{ErMnO_3}$ compounds. a) Room temperature $J(E)$ curves as function of orientation obtained on in-plane and out-of-plane oriented $\mathrm{ErMnO_3}$ with $J_{xy} \perp P$ and $J_z \parallel P$, respectively. b) Comparison of the $J(E)$ characteristics of undoped $\mathrm{ErMnO_3}$ with hole-doped $\mathrm{Er_{1-x}Ca_xMnO_3}$ ($x = 0.002, 0.01$) and electron-doped $\mathrm{Er_{1-x}Zr_xMnO_3}$ ($x = 0.002$, see inset). The red arrows indicate how hole doping continuously increases the conductance, while slight electron doping suppresses the conduction. Figure taken from Ref. 229.

Fig. 4.7 shows that with increasing Zr-content the conductance first drops and then starts to increase again. $I(V)$ data obtained on the sample with $x = 0$ before and after measuring $x = 0.002$ and $x = 0.01$ are equivalent (not shown), excluding that tip-degradation obscured the experiment.

The observed crossover in conductance suggests that a concentration of $x = 0.01$ Zr, which compares to an electron concentration $n \lesssim 1.6 \times 10^{20}\,\mathrm{cm^{-3}}$ and consistent with $p_0 = 2 \times 10^{19}\,\mathrm{cm^{-3}}$ for undoped bulk[11], evokes contribution of n-type carriers to the transport properties of our floating-zone-grown samples. A more quantitative statement on the n-type influenced state of our $\mathrm{Er_{1-x}Zr_xMnO_3}$ sample with $x = 0.01$ requires, e. g., four point or Hall measurements. For a first test on domain-wall behavior, however, the observed change represents a convenient starting point.

In summary, we could demonstrate that the applied doping allowed for adjusting the macroscopic electronic properties as intended. In the next two sections we will discuss to which extent impurity doping enables to control the transport properties of charged domain walls (p- and n-type doping in Sec. 4.3 and 4.4, respectively).

4.3. Tuning transport of the p-type screened walls

In the next step we scrutinize the effect of hole doping (Sec. 2.2.3) on the local domain-wall properties. For this purpose we consider the conductive tail-to-tail (←→) wall of $\mathrm{Er_{1-x}Ca_xMnO_3}$ ($0 \leq x \leq 0.01$). The goal is to push domain-wall conductance towards technologically working ranges. The results presented in this section have been published in Ref. 82.

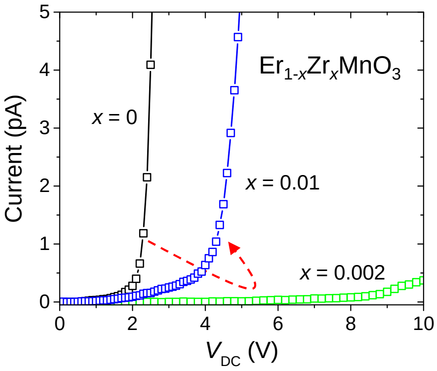

Figure 4.7.: Bulk conductance of Zr-doped samples. $I(V)$ curves obtained by cAFM. Red arrow indicates how Zr doping first decreases and then increases the bulk conductance. The data were measured with one single AFM tip to gain comparative data without any contributions from tip variation.

4.3.1. Electrostatic responses at the domain walls

We begin by demonstrating experimentally the previous assumption that the electronic domain-wall properties in $Er_{1-x}Ca_xMnO_3$ are determined by mobile carriers that accumulate or deplete at the ferroelectric domain walls. For probing these carriers we employ electrostatic force microscopy (EFM). This AFM mode is explicitly sensitive to variations in the density of mobile and fixed charges without unwanted contributions from contact resistance that may obscure the data (see Sec. 3.1.4).

In Figure 4.8 we present EFM images taken on $Er_{1-x}Ca_xMnO_3$ crystals with the ferroelectric polarization lying in the image plane as indicated by the white arrows. The maps of mobile and fixed charges were obtained simultaneously by recording the EFM signals at 2ω and ω, respectively, while scanning in semi-contact mode with an AC voltage applied to the tip. Figure 4.8a shows the relation between EFM and piezoresponse force microscopy (PFM, in-plane) measurements that were performed in order to unambiguously determine the polarization direction.

In Figure 4.8b and c we present EFM(2ω)- and EFM(ω)-images for our parent compound $ErMnO_3$, i. e., $x = 0$. The detected 2ω-signal (Figure 4.8b) reveals dark and bright contrasts at head-to-head and tail-to-tail domain walls, respectively. The pronounced contrasts indicate that the density of mobile carriers, ρ, at these charged domain walls is significantly reduced (dark) / enhanced (bright) compared to the bulk. The simultaneously recorded ω-image in Figure 4.8c displays inverted contrast levels at the two types of domain walls with bright head-to-head and dark tail-to-tail walls. Since the signal is not related to any work function difference (see Sec. 6.2.1), this result can be translated into the following hierarchy in the local electrostatic potential ϕ: $\phi_{\leftarrow\rightarrow} < \phi_{\text{bulk}} < \phi_{\rightarrow\leftarrow}$.

The EFM scans thus provide evidence for two key aspects that were previously reasoned based on transport measurements. The EFM(2ω)-image unambiguously reveals local variations in the hole density at domain walls, corroborating that emer-

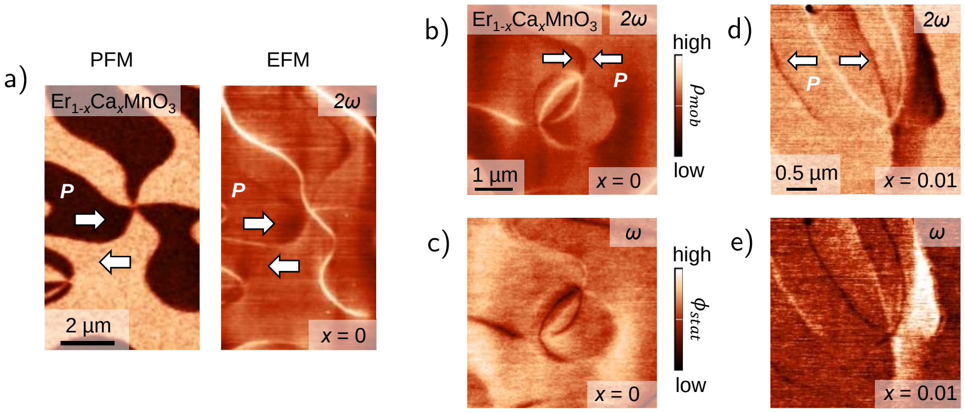

Figure 4.8.: EFM response of the domain walls in Er$_{1-x}$Ca$_x$MnO$_3$. a) Relation between in-plane PFM and EFM contrasts obtained on ErMnO$_3$. White arrows indicate the respective polarization orientation. b), c) EFM(2ω)- and EFM(ω)-images gained on ErMnO$_3$, revealing relative changes in the density of mobile charges (ρ) and the electrostatic potential (ϕ). d), e) Same as in (b, c) for Er$_{1-x}$Ca$_x$MnO$_3$ with a Ca doping of $x = 0.01$.

gent differences in electronic conductance are intrinsic and do not originate from contact resistance[11,12] (see discussion in Sec. 4.1.3).

In addition, the EFM(ω)-image provides experimental confirmation of the previous assumption that negative and positive bound charges do exist at tail-to-tail and head-to-head walls in hexagonal manganites. In Figure 4.8d and e we present analogous EFM data taken on Er$_{1-x}$Ca$_x$MnO$_3$ with $x = 0.01$, i. e., the highest doping level we investigated. In qualitative agreement with Figure 4.8b and c we find that holes accumulate at tail-to-tail walls and deplete from head-to-head walls to screen the bound negative and positive charges, respectively. Occasionally, a gradual decrease of contrast is observed on one side of the insulating walls, which we attribute to their propagation within the bulk. The same effect is also seen in cAFM transport data (Ref. 12 and Fig 4.1) and becomes more pronounced for higher bulk conductance.

The obtained behavior reveals that the Ca doping preserves the basic electronic p-type features of the parent compound with mobile holes as the majority charge carriers. Thus, via the corresponding increase in the hole density (see Sec. 4.2.2), Ca doping provides a handle for tuning the electronic domain-wall properties, which we will investigate in more detail in the following.

4.3.2. Current-voltage characteristics

In order to quantify the relative variations between domain walls and bulk probed by EFM, and to analyze the effects due to Ca doping, we used conductive atomic force microscopy (cAFM). Spatially resolved cAFM data for the lowest and highest doping levels we investigated are presented in Figure 4.9a and b. In both cases we find enhanced conductance at the tail-to-tail walls and suppressed conductance at the head-to-head walls for negative tip bias-voltages (see caption of Figure 4.9 for details).

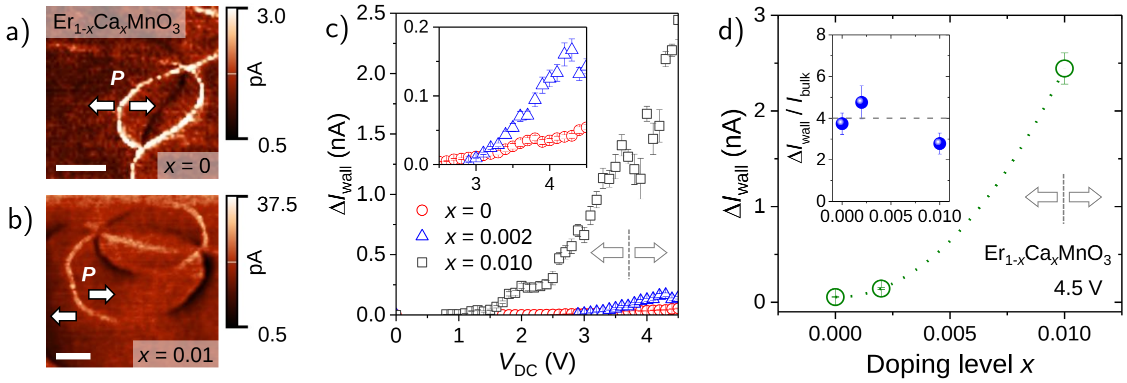

Figure 4.9.: cAFM and $I(V)$ characteristics of $\mathrm{Er}_{1-x}\mathrm{Ca}_x\mathrm{MnO}_3$. a), b) Spatially resolved cAFM images gained on $\mathrm{Er}_{1-x}\mathrm{Ca}_x\mathrm{MnO}_3$ with in-plane polarization as indicated by the white arrows. For (a) and (b), $V_{\mathrm{DC}} = 2.3\,\mathrm{V}$ and $0.9\,\mathrm{V}$, while scale bars are 500 nm and 250 nm, respectively. c) Relative $I(V)$ characteristic measured at tail-to-tail ($\longleftarrow\!\!\longrightarrow$) domain walls in $\mathrm{Er}_{1-x}\mathrm{Ca}_x\mathrm{MnO}_3$ at three different doping levels x. Error bars correspond to the standard deviation of cAFM measurements taken at different tail-to-tail domain walls. In the inset to (c) a zoom-in is presented, showing the difference between $I(V)$ data taken on $\mathrm{Er}_{1-x}\mathrm{Ca}_x\mathrm{MnO}_3$ with $x = 0$ and $x = 0.002$. d) Domain-wall current ΔI_{wall} as function of the doping level x. The data points were derived by fitting a Gaussian profile to cross-sections perpendicular to the domain walls. Error bars represent the error of the fit parameter for the maximum value. The dotted line ($\propto x^2$) is a guide to the eye. The ratio between domain wall and bulk currents is almost constant within the investigated doping range as shown in the inset to (d).

A qualitative analysis of the cAFM scans gained on our $\mathrm{Er}_{1-x}\mathrm{Ca}_x\mathrm{MnO}_3$ doping series at different voltages is shown in Figure 4.9c. Here, we present the relative domain-wall current $\Delta I_{\mathrm{wall}} = I_{\leftarrow\rightarrow} - I_{\mathrm{bulk}}$ as function of the applied voltage for three doping levels. The data reveal that the domain-wall current ΔI_{wall} strongly depends on the doping level x. This pronounced doping dependence is further highlighted by Figure 4.9d, where we present the evolution of ΔI_{wall} as function of x at a constant bias voltage $V_{\mathrm{DC}} = 4.5\,\mathrm{V}$. The $\Delta I_{\mathrm{wall}}(x)$ data in Figure 4.9d show that a Ca doping level of 1 % increases the domain-wall conductance by a factor of ≈ 50 compared to the undoped system. Most important, the relative difference in conductance between domains and domain walls is preserved ($\Delta I_{\mathrm{wall}}/I_{\mathrm{bulk}} \approx 4$) and robust against the applied carrier-density modifications as shown in the inset to Figure 4.9d.

The data presented in Figure 4.9d thus demonstrate that domain-wall currents in $\mathrm{Er}_{1-x}\mathrm{Ca}_x\mathrm{MnO}_3$ can readily be enhanced and fine-tuned by the aliovalent substitution of Er^{3+} by Ca^{2+}. A natural upper limit for the gainable domain-wall current is given by the maximum substitution level maintaining the hexagonal phase, which can be as high as 15 % in solid-solutions of $\mathrm{Er}_{1-x}\mathrm{Ca}_x\mathrm{MnO}_3$[142,146]. The x^2-trend observed for $x \leq 0.01$ (see dotted line in Fig. 4.9c) remains to be verified for higher doping levels so that its extrapolation has to be taken with caution. The extrapolation, however, allows for a rough estimate for the upper threshold for domain-wall currents ($\Delta I_{\mathrm{wall}} \leq 500\,\mathrm{nA}$ for $x = 0.15$), holding out the prospect of a further significant enhancement by aliovalent chemical substitution.

With respect to domain-wall engineering, it is very important to note that the impact of the enhanced density of majority carriers goes beyond the discussed enhancement in conductance. In fact, we observed that the Ca doping also has a significant influence on the conduction path as we will discuss in the following.

4.3.3. Electronic domain-wall width

A closer inspection of the conducting tail-to-tail walls in Figure 4.9a and b shows that the detected electronic wall width, $w_{\leftarrow\rightarrow}$, is different for $x = 0$ and $x = 0.01$ (note the different lengths of the 500 nm scale bars in Figure 4.9a and b). A systematic analysis of the relation between electronic wall width and doping level x at comparable domain-wall currents is presented in Figure 4.10a. Comparable domain-wall currents $I_{\leftarrow\rightarrow} \approx 100\,\mathrm{pA}$ were achieved by adjusting the applied bias voltage according to Figure 4.9c. The viewgraph in Figure 4.10a indicates that the wall width monotonously decreases for increasing x, being reduced by about 50% from $\approx 100\,\mathrm{nm}$ at $x = 0$ to $\approx 50\,\mathrm{nm}$ at $x = 0.01$.

The reduction in width can be interpreted in terms of the corresponding increase in the hole density introduced by the Ca doping. Assuming the extra amount of mobile carriers is proportional to the Ca content (i. e.$\approx x/x_0$) the doping translates into a more effective screening of the static domain-wall charge in the sense that the corresponding accumulation of mobile carriers takes place over a smaller region (we note that, in any case, the static charge is always screened far enough from the wall). The effect can be quantified via the corresponding Debye length $\lambda_\mathrm{D}(x) \approx \lambda_\mathrm{D}(0) \cdot (1 + x/x_0)^{-1/2}$ (see Sec. 2.1.1.3 and Eq. 2.18).

Regarding transport properties, however, it is reasonable to rather define the nominal width by the hole-accumulation region $\lambda_\mathrm{acc}(x)$[84]. The latter is the region in which the density of holes, and hence the conductivity, is enhanced exponentially compared to the bulk. In collaboration with Andres Cano at the University of Bordeaux, we calculated the profiles for $\lambda_\mathrm{D}(x)$ and $\lambda_\mathrm{acc}(x)$ as function of doping content. Both quantities decrease with increasing Ca content as shown by the dashed and the solid line in Figure 4.10a for $\lambda_\mathrm{D}(x)$ and $\lambda_\mathrm{acc}(x)$, respectively. The qualitative agreement between the data and the theoretically derived scaling behavior confirms that the obtained doping dependence of $w_{\leftarrow\rightarrow}$ is caused by an increase in screening efficiency and the corresponding reduction in $\lambda_\mathrm{acc}(x)$, resp. $\lambda_\mathrm{D}(x)$. Here, we restrict ourselves to pinpointing the origin of the doping-induced trends. For a more quantitative statement, one would have to perform, e. g., supplementary Hall measurements to specify x_0.

Next, we analyze the factor relating the experimentally obtained domain-wall width $w_{\leftarrow\rightarrow}$ to its nominal value (see y-axes in Figure 4.10a). Since the measured width is a convolution of the finite tip-surface contact area and the actual wall properties, it is typically larger than the nominal wall width[164]. In addition to this extrinsic contribution, pronounced intrinsic leakage effects occur that lead to a further broadening of $w_{\leftarrow\rightarrow}$ as we elaborate in Figure 4.10b and c.

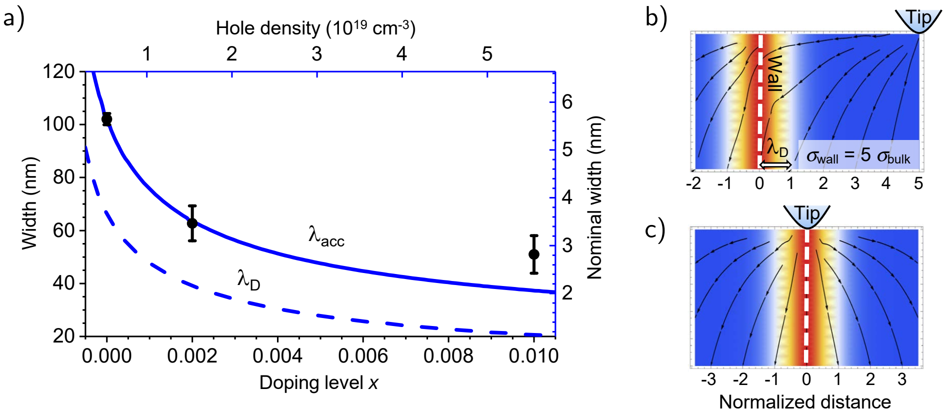

Figure 4.10.: Electronic domain-wall width in Er$_{1-x}$Ca$_x$MnO$_3$. a) Doping dependence of $w_{\leftarrow\rightarrow}$. Data points were obtained for comparable domain-wall peak currents ($I_{\leftarrow\rightarrow} \approx 100\,\mathrm{pA}$) by fitting a Gaussian profile to cross-sections perpendicular to the tail-to-tail (←→) domain walls. Error bars represent the error of the fit parameter for the FWHM. Lines represent the calculated wall width ($P = 5\,\mu\mathrm{C\,cm^{-1}}$ and $\epsilon = 50\epsilon_0$[11]) defined by the hole-accumulation region $\lambda_{\mathrm{acc}}(x)$ (solid line) and the Debye length $\lambda_{\mathrm{D}}(x)$ (dashed line). b) Calculated distribution of the injected current with the tip situated away from the wall. Due to the enhanced conductance at the wall (blue $\leftrightarrow$ σ_{bulk}, red $\leftrightarrow$ σ_{max}), the mobile carriers are deflected and flow preferentially through the wall as illustrated by the black arrows. c) Same as in (b) for the tip being placed on top of a tail-to-tail wall.

Figure 4.10b and c present the distribution of tip-injected currents, which was obtained from the equation of continuity $\nabla \cdot j = 0$ under the boundary conditions imposed by a point-like source[11]. The displayed current distributions summarize two key findings: i) When the tip is placed at a distance larger than the nominal domain-wall width, injected currents still experience a substantial deflection that enhances the probed wall width (Figure 4.10b). ii) Currents injected at a conducting domain wall spread into the adjacent bulk (Figure 4.10c). The intrinsic effects i) and ii) become crucial when designing, domain-wall based devices, because they always occur, even when a point-like injection source is used, and will ultimately limit the minimum spacing between functionalized domain walls. Overall, for our study, the measured wall width has to be regarded as a superposition of extrinsic and intrinsic effects which explains the larger absolute values of $w_{\leftarrow\rightarrow}$ compared to the nominal width in Figure 4.10a.

In summary, we have studied the impact of chemical doping on the electric conductance at charged domain walls in a ferroelectric semiconductor. A doping level of 1% is found to enhance the local electronic conductance by a factor of ≈ 50. In addition, leakage effects at the domain walls are suppressed, reducing the effective width of these conducting nanochannels by about 50%. This together enhances the current density at conducting domain walls in ErMnO$_3$ by more than two orders of magnitude. Our findings suggest that even higher current densities may be achieved at domain walls in highly doped solid solutions ($\lesssim 15\%$) and RMnO$_3$ thin films, where substantial chemical substitutions can be applied without suppressing the hexagonal phase due to the clamping to the substrate.

4.4. Impact of n-type doping on domain-wall transport

In the previous section, we demonstrated that hole doping can be efficiently applied to enhance the local conductance of tail-to-tail (←→) walls. We now analyze how electron doping of the bulk alters the domain-wall conductance in $\mathrm{Er}_{1-x}\mathrm{Zr}_x\mathrm{MnO}_3$ as function of donor (Zr) concentration. The goal is to gain full control of the semiconducting domain wall behavior – complementary to Ca doping – and impose p- and n-type characteristics on demand.

4.4.1. Persisting p-type transport

The macroscopic transport measurements in Section 4.2 show that bulk conductance is first suppressed before it increases again, if the Zr-content is continuously raised. We first focus on the compound with suppressed conductance ($\mathrm{Er}_{1-x}\mathrm{Zr}_x\mathrm{MnO}_3$, $x = 0.002$). In Figure 4.11a, we characterize the corresponding domain-wall properties by conductive atomic force microscopy (cAFM) and piezoresponse force microscopy (PFM). On the upper left of Fig. 4.11a, the cAFM scan at $V_{\mathrm{DC}} = 5.5\,\mathrm{V}$ reveals conductive domain walls with a width of $\sim 110\,\mathrm{nm}$ embedded in an insulating bulk. At this voltage, insulating walls are barely detectable, but their contrast becomes more pronounced for higher voltages. By comparing the cAFM scan with a PFM scan performed at the same position we identified the conductive and insulating domain walls as tail-to-tail (←→) and head-to-head (→←) walls, respectively (PFM scan on the lower left, direction of P indicated by blue arrows). Thus, the domain walls display the same behavior as in the undoped case, implying that domain-wall conductance is still dominated by p-type carriers.

After revealing the basic wall behavior, we studied their transport as function of voltage by analyzing a series of cAFM maps. The corresponding $I(V)$ characteristics are presented on the right of Figure 4.11a. Bulk, tail-to-tail, and head-to-head currents steadily increase in a non-linear manner (see inset for raw data). Maximum current values of about $3\,\mathrm{pA}$ are reached at $V_{\mathrm{DC}} = 25\,\mathrm{V}$, which is in good agreement with the suppressed conductance observed in the macroscopic transport measurement (see Fig. 4.6). Over the whole voltage range we observe no change in the conductive and insulating nature of the respective tail-to-tail and head-to-head walls, which is highlighted by the bulk-subtracted currents $\Delta I_{\mathrm{wall}} = I_{\mathrm{wall}} - I_{\mathrm{bulk}}$ shown in Figure 4.11a on the eight. Moreover, we find that ΔI_{wall} evolves quite symmetrically for both types of wall, reaching values up to $500\,\mathrm{fA}$.

The analysis above demonstrates that doping ErMnO_3 with $x = 0.002$ Zr significantly reduces the overall currents but preserves conductive tail-to-tail and insulating

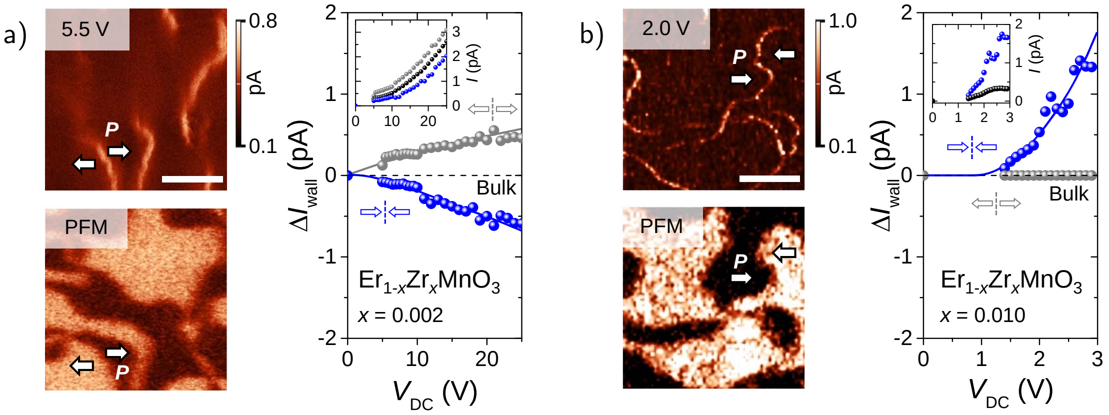

Figure 4.11.: Nanoscopic conductance properties of $Er_{1-x}Zr_xMnO_3$. a) A dopant concentration of $x = 0.002$ retains conductive tail-to-tail (←→) and insulating head-to-head (→←) walls over the whole probed voltage range, as demonstrated by the $I(V)$ characteristics in the graph on the right. b) A concentration of $x = 0.01$ Zr is sufficient to change from insulating to conductive head-to-head walls (comp. cAFM and PFM scans on the left). While head-to-head walls remain conductive over the investigated voltage range, tail-to-tail walls show no detectable insulating behavior (see $I(V)$ data on the right). In both (a) and (b), graphs show bulk-subtracted currents $\Delta I_{\mathrm{wall}} = I_{\mathrm{wall}} - I_{\mathrm{bulk}}$ with the raw data on the inset (Solid lines represent guides-to-the-eye). Walls have been identified by comparing a cAFM scan (upper-left) with a PFM scan at the same spot (lower-left, polarization-directions as indicated by the arrows). Scale bars in (a) and (b) are 1 µm and 500 nm, respectively.

head-to-head walls. Both results point toward partial but not full hole compensation, and hence the domain walls still behave as expected from a p-type ferroelectric semiconductor.

4.4.2. N-type dominated domain-wall transport

In the next step, we investigate the nanoscale transport properties of the electron-doped sample $Er_{1-x}Zr_xMnO_3$ with $x = 0.01$. Figure 4.11b presents the resulting scanning probe microscopy (SPM) data including $I(V)$ curves derived from a series of cAFM scans. One species of narrow conductive walls ($w \approx 35$ nm) can be seen on the cAFM scan shown on the upper left. PFM data obtained at the same position unambiguously identifies the walls as head-to-head domain walls. The walls remain more conductive than the surrounding bulk over the complete examined voltage range, which is demonstrated by the relative current, ΔI_{wall}, plotted as function of voltage (right graph in Fig. 4.11b). We note that the tail-to-tail walls do not show any detectable signature of reduced or increased conduction with respect to the bulk (gray dots in graph).

In order to demonstrate the intrinsic nature of the increased conductance at the head-to-head walls and exclude contributions from transient or switching currents, we perform additional spectroscopy and time-dependent measurements at the head-to-head wall in comparison to the bulk. Figure 4.12a shows three spectroscopy-derived $I(V)$ curves confirming the trend observed by mapping: the two $I(V)$ curves

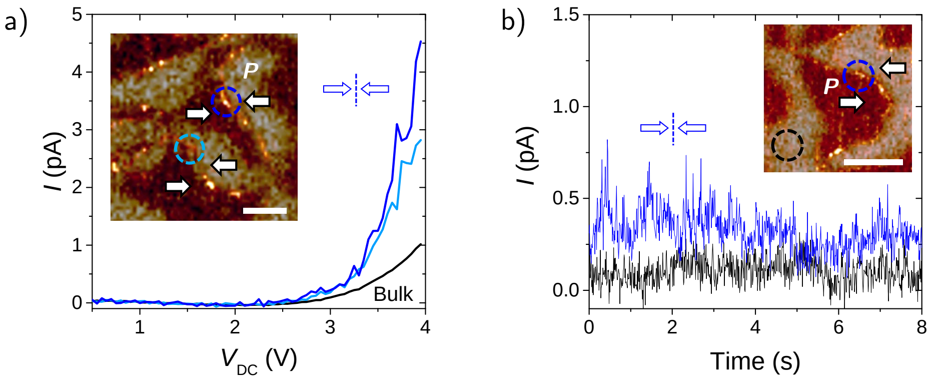

Figure 4.12.: Head-to-head wall transport in $Er_{0.99}Zr_{0.01}MnO_3$. a) $I(V)$ spectroscopy shows increased conductance at head-to-head (→←) walls confirming the results from mapping (Fig. 4.11b). Positions of the head-to-head $I(V)$ curves are marked on the inset showing a cAFM-PFM overlay. The bulk curve is derived by averaging the current of several domains. b) Evolution of head-to-head and bulk currents as function of time during application of a constant voltage $V_{DC} = 5\,V$. Average current values are $0.23 \pm 0.12\,pA$ and $0.09 \pm 0.07\,pA$ for head-to-head and bulk, respectively. $I(t)$ curves are extracted at the positions highlighted on the inset showing a cAFM-PFM overlay. Scale bars in (a) and (b) are 500 nm.

of the head-to-head wall exhibit higher currents than the surrounding bulk. The increased head-to-head currents are further substantiated by the time-dependent measurements shown in Figure 4.12b: At the head-to-head wall, the current remains higher than the bulk current over several seconds (average current values are given in the caption). Similar to Fig. 4.2, minor instabilities in the current signal arise, which may be attributed to mechanical instabilities or interactions with ambient gases.

Based on the above results we conclude that the increased donor concentration in $ErMnO_3$ induces a transition from insulating to conductive head-to-head walls. This result is consistent with the observed increase in bulk conductance under Zr doping due to contributions from n-type charge carriers as discussed in Sec. 4.2.2. Our cAFM measurements indicate that n-type carriers contribute to screen the charged head-to-head walls and govern their transport characteristics. The change in the screening scenario is further substantiated by the observed electronic domain wall widths. We find $\sim 110\,nm$ for $x = 0.002$ and $\sim 35\,nm$ for $x = 0.01$ Zr doping, which is in tune with the Debye screening length $\lambda_D \propto n^{-1/2}$, depending on the amount of free charge carriers n (see Sect. 2.1.1.3). An interesting follow-up experiment would be to determine density and mobility of the mobile carriers at the different walls, e. g., with advanced atomic force microscopy techniques[230].

In summary, our results demonstrate that impurity doping provides full control over conductance and carrier-type at charged domain walls. By moderate hole doping we achieve two orders of magnitude higher current densities at the conducting tail-to-tail walls. Electron doping, on the contrary, allows to change from insulating to conducting head-to-head walls due to n-type contributions to the domain-wall screening. Moreover, minimization of current spread can be achieved by increasing the amount of present mobile charge carriers, optimizing the screening efficiency. Analogous to doping of classical semiconductors, chemical substitution can be used to alter the properties of ferroelectric semiconductors and hence their domain walls. This opens up a promising pathway for domain-wall engineering, with its full potential yet to be explored.

4.5. Functional electronic inversion layers

In the previous sections, we explored the electronic response of chemically altered hexagonal manganite ($R\mathrm{MnO}_3$). In the next step, we study reversible control of domain-wall transport via applied electric fields. For this purpose, we will focus on the insulating head-to-head walls, investigating their nanoscale properties by a combination of scanning probe (SPM) and transmission electron microscopy (TEM). We analyze our results with two theoretical models based on density functional theory (DFT). The results presented in this section have been accepted for publication in Ref. 231.

4.5.1. Voltage-driven insulating to conducting transition

We begin our analysis with an $I(V)$ characterization of the domain-wall properties at head-to-head (→←) walls in ErMnO_3 over an extended voltage range. In Figure 4.13a to c we present conductive atomic force microscopy (cAFM) data obtained with a conductive diamond-coated tip (DCP20 in Table 3.1) under sample bias voltages of up to 6 V. Test measurements with different tip-coatings and the analysis of various conduction mechanisms reveal bulk-influenced transport behavior, ensuring that intrinsic domain wall properties are probed (see also Sec. 4.1.3).

At low bias voltage ($V_{\mathrm{DC}} = 2.5\,\mathrm{V}$), we observe the established transport behavior with conducting tail-to-tail (bright) and insulating head-to-head (dark) domain walls[11,12] (Fig. 4.13a, see also Sec. 4.1.1). A qualitatively different transport phenomenon, however, arises at higher voltage as shown by the scan in Figure 4.13b, taken at $V_{\mathrm{DC}} = 6\,\mathrm{V}$. The spatially resolved data highlights that both tail-to-tail (←→) and head-to-head (→←) walls can exhibit a higher electronic conductance than the surrounding domains. A more detailed study is shown in Figure 4.13c, which is conducted in an area with well-separated walls to exclude crosstalk effects[231].

Figure 4.13c shows the relative domain-wall conductance, ΔI_{wall}, after subtracting the bulk current, which for reference, is shown in the inset to Figure 4.13c ($\Delta I_{\mathrm{wall}} = I_{\mathrm{wall}} - I_{\mathrm{bulk}}$). The comparison with respect to the bulk (black dotted line in Fig. 4.13c) reveals that the head-to-head domain walls become more conducting than the bulk above $V_{\mathrm{c}} > 4.8V$, approaching the conductance measured at the tail-to-tail walls for $V > V_{\mathrm{c}}$.

The transition from resistive ($I_{\mathrm{wall}} < I_{\mathrm{bulk}}$) to conductive ($I_{\mathrm{wall}} > I_{\mathrm{bulk}}$) behavior occurs gradually, which is demonstrated by Figure 4.14a comparing $I(V)$ data from

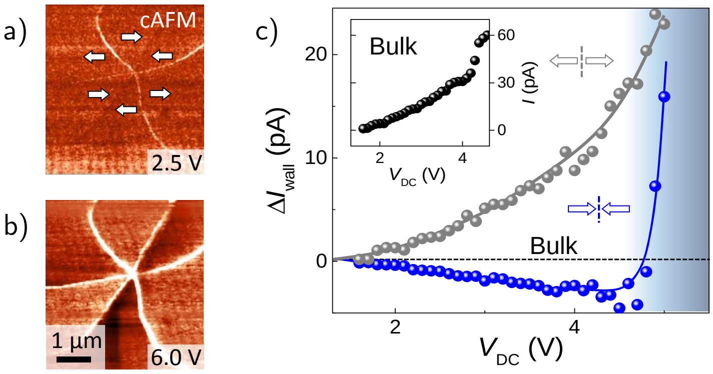

Figure 4.13.: Electronic transport at tail-to-tail and head-to-head walls. a) cAFM scan obtained at a bias voltage of 2.5 V on $ErMnO_3$ with in-plane polarization as indicated by the white arrows (the orientation corresponds to a y-cut with the (110)-direction normal to the sample surface). The image reveals a sixfold meeting point of conducting tail-to-tail (bright) and insulating head-to-head (dark) domain walls. b) cAFM image obtained with a bias voltage of 6 V at the same position as shown in (a) with both tail-to-tail and head-to-head walls exhibiting enhanced conductance compared to the bulk. c) Relative current-voltage characteristics measured at tail-to-tail (←→) and head-to-head (→←) walls after subtraction of the bulk current (for reference, the bulk conductance is shown in the inset).

the bulk (black) and a head-to-head wall (blue, see inset). Similar to Fig. 4.13c, obtained for forward bias only, a crossover is observed at about $V_c \approx \pm 4$ V in Fig. 4.14a. We find that currents are less stable for negative than for positive bias voltages, which obscures imaging by cAFM. Despite the higher noise level, however, spatially resolved measurements show the same crossover behavior as observed for negative voltages (see Fig. 4.14b). We note that the $I(V)$ curve exhibits a slight asymmetry (see rectification ratio R in Fig. 4.14a for a quantitative measure), which is often observed for $R\mathrm{MnO}_3$[12]. The bipolar $I(V)$ data in Fig. 4.14a is consistent with the results from the analysis in Sec. 4.1.3, that is, bulk-influenced transport, with a small asymmetry arising from, e. g., electronic interface states.

It is further worth mentioning, that the field strength in our measurements is about one order of magnitude lower than electric fields, which are applied to induce domain wall currents in $BiFeO_3$ or $Pb[Ti_{1\text{-x}}Zr_x]O_3$ (PZT) thin films[7,10,167]. The low electric field energy suggests a qualitative change in the electronic transport at head-to-head walls rather than, e. g., an electric breakdown of the insulating domain wall state. Interestingly, this qualitative change, however, cannot be explained based on the depletion of majority carriers (holes) alone.

To better understand this particular transport phenomenon, a DFT-based semi-classical model was built in collaboration with Massimiliano Stengel from the Institució Catalana de Recerca i Estudis Avançats (ICREA) in Barcelona. The model analyzes the redistribution of mobile charge carriers. We assume that $ErMnO_3$ acts as a simple band insulator and solve the Poisson equation self-consistently whilst treating the carriers semi-classically. The obtained band diagram is shown in Fig. 4.15a. Far from the domain walls, we obtain a flat potential, with the Fermi level, E_{Fermi},

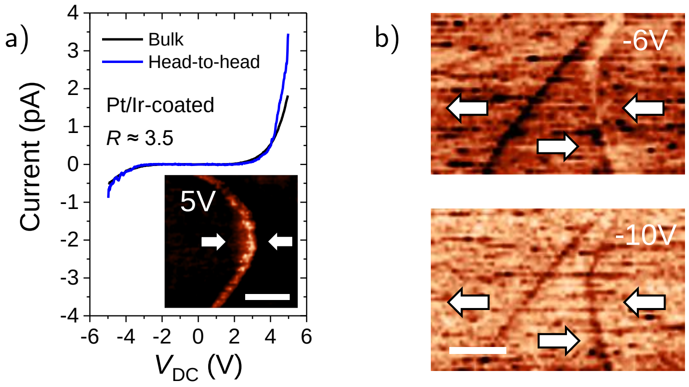

Figure 4.14.: Bipolar $I(V)$ curves at head-to-head walls. a) $I(V)$ measured with a Pt/Ir-coated tip on (blue) and away (black) from the head-to-head wall (→←) shown in the inset. Scale bar is 500 nm. The wall becomes more conducting than the bulk at about ±4 V. R denotes the rectification ratio, defined as the ratio of the forward bias current at +5 V divided by the reverse bias current at −5 V. b) Spatially resolved cAFM scans obtained with negative bias voltages. At −6 V the head-to-head wall is insulating and conducting at −10 V, indicating a slightly higher value V_c than in (a). Scale bar is 1 µm.

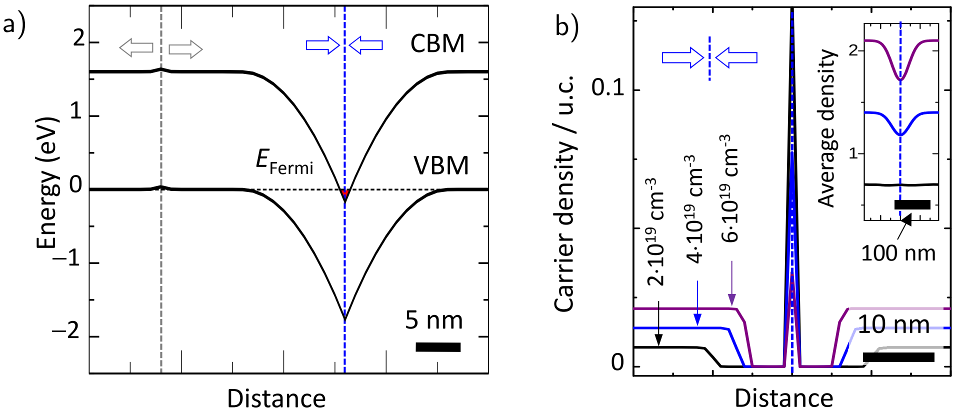

Figure 4.15.: Band structure at tail-to-tail and head-to-head walls. a) Polarization-dependent band bending calculated for the head-to-head (→←) and tail-to-tail (←→) walls (vertical dashed lines) with arrows showing the orientation of the spontaneous polarization of neighboring domains. For $p_0 = 2 \times 10^{-19}\,\mathrm{cm}^{-3}$, conduction-band minimum (CBM) and valence-band maximum (VBM) correspond to the black solid lines, while the Fermi level E_{Fermi} is indicated by the horizontal dashed line. b) Calculated density of all mobile charge carriers (holes and electrons) at head-to-head domain walls. An increasing hole density favors screening by hole depletion, which decreases the local electron density. The inset shows moving averages of the carrier density calculated with a Gaussian convolution function ($\propto \exp(-x^2/s^2)$, $s = 30\,\mathrm{nm}$), which mimics a realistic spatial resolution when current is mapped by cAFM.

lying right below the valence-band maximum (VBM). The obtained carrier density is realistic, i. e., $p_0 = 2 \times 10^{-19}\,\mathrm{cm}^{-3}$, and corresponds to 0.007 hole carriers per unit cell. Right at the tail-to-tail wall, we observe a slight upward shift of the VBM, which generates additional holes screening the bound negative domain-wall charge $-2P$ (see Sec. 2.1.1.3); this is in agreement with the enhanced conductance properties of the tail-to-tail walls[11,12] (see Fig.4.13a).

We observe a different scenario at the head-to-head walls. Here, strong band bending causes the conduction-band minimum (CBM) to drop below E_{Fermi}. Consequently, the bound charge of the head-to-head walls is screened by depletion of holes, occurring over a range of approximately 22 nm, and an electron accumulation directly at the wall where the CDM dips below E_{Fermi} (see Fig. 4.15a). Hence, this simple model shows that the density of minority carriers, i. e., the electrons, is significantly increased at the head-to-head walls. The result is consistent with previous analytical calculations[84] (see Sec. 2.1.1.3, Fig. 2.4b), emphasizing that our alternative DFT-based approach is sound.

In order to describe the experimentally observed insulating behavior of the head-to-head walls (for $V < V_{\mathrm{c}}$ (Fig. 4.13a)), however, hole depletion must exceed electron accumulation in both models. For our model, this is illustrated in Fig. 4.15b, where the total density of mobile charge carriers (electrons and holes) is shown as a function of position around the head-to-head wall. The spatially averaged carrier density, which is directly proportional to the local conductance, is presented in the inset. Above V_{c}, probably the electrons determine the domain-wall conductance since they represent the only available charge carriers for transport at the head-to-head domain walls.

4.5.2. Manganese valence change at the domain wall

To gain additional insight into the microscopic domain-wall structure, electron energy loss spectroscopy (EELS) spectroscopy data was recorded in close collaboration with David Muller's group at Cornell University. Figure 4.16a shows an atomically-resolved image of a head-to-head wall obtained by high-angle annular dark field scanning transmission electron microscopy (HAADF-STEM). The domain wall is imaged parallel to the [100] zone axis. In this configuration one distinguishes clear shifts of the erbium ions with respect to the Mn-O polyhedra with either down-up-up ($+P$ domain) or up-down-down ($-P$ domain) arrangement[132]. The displacements allow to locally determine the spontaneous polarization and its reorientation across the domain wall. The change of the polarization orientation across the domain wall is rather abrupt, being consistent with previous work[132].

Next, we investigate the electrochemical domain-wall structure by measuring the local manganese valence change with spatially resolved EELS. Figure 4.16b shows the corresponding Mn $L_{2,3}$-edge EELS spectra over the head-to-head wall. A magnification of the Mn L_3-edge is shown in Figure 4.16c. For comparison, the experimental data points are shown together with a manganese Mn^{3+} reference spectrum that has been recorded away from the domain wall on the same $\mathrm{ErMnO_3}$ sample. The spectra

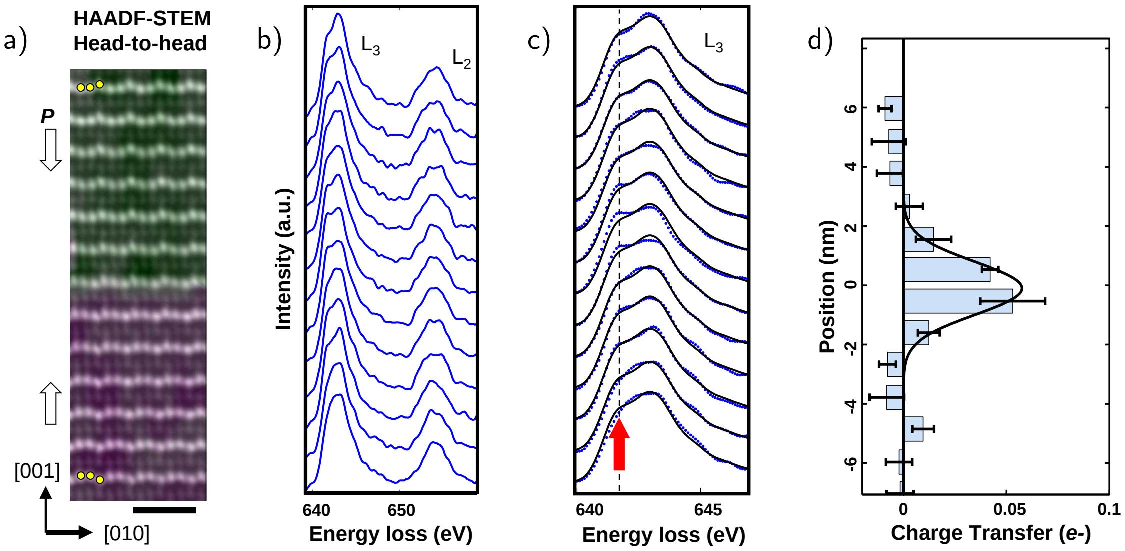

Figure 4.16.: Change of Mn valence at head-to-head domain walls. a) Head-to-head domain wall imaged by HAADF-STEM. False colors in the image represent the magnitude and direction of the erbium-ion displacement. The transition between the $+P$ and $-P$ domains is sharp ($+P$ domain: down-up-up; $-P$ domain: up-down-down as indicated by yellow circles)[132]. The scale bar is 1 nm. b) Layer-by-layer EELS measurement revealing the evolution of the Mn $L_{2,3}$ spectra over the head-to-head domain wall. c) Magnification of the L_3-edge in (b). A comparison of the EELS data (dots) with Mn^{3+} reference spectra shows a distinct feature at approximately 641 eV (highlighted by red arrow and dashed line), occurring in the proximity of the head-to-head wall. d) Electron transfer per Mn ion across the domain wall derived from the local Mn valence detected by EELS. Error bars correspond to the standard error of the mean.

of the domain areas show minor differences corresponding to inhomogeneities of the electrical background. In the spectra close to the head-to-head wall, we can distinguish a clear feature at 641 eV (red arrow), which cannot be described well enough by the Mn^{3+} reference spectrum[231].

For quantification of the observed change in the Mn $L_{2,3}$ spectra at the head-to-head wall, we fit the full Mn $L_{2,3}$-edge with two spectra that correspond to $Mn^{2.8+}$ and Mn^{3+} valence states. The $Mn^{2.8+}$ spectrum is obtained from a linear combination of Mn^{3+} and Mn^{2+} spectra as descried in Ref. 231 (we emphasize that the spectrum of six-fold coordinated Mn^{2+} is taken as reference, because this is the first study examining the Mn^{2+} electronic state in trigonal bipyramidal coordination by spectroscopy). The statistics of the fit show a significant change in the percentage of the lower valence state over an area of $2-3$ unit cells around the head-to-head wall. Using the obtained valence states, we derive the excess charge of the Mn ions at the domain wall in comparison to the bulk valence state of Mn^{3+}[232]. The charge transfer is plotted as a function of position in Fig. 4.16d.

Averaging over several such head-to-head walls at individual positions in the material, we obtain a valence change that corresponds to a negative charge accumulation of 0.09 ± 0.04 electrons per Mn ion at the position of the head-to-head wall. As for $ErMnO_3$ the bulk polarization is about $6\,\mathrm{C\,cm^{-2}}$[233], the approximate number of negative charge density required to fully screen the bound polarization charge at the head-to-head wall is $12\,\mathrm{C\,cm^{-2}}$ (see Eq. 2.7). In terms of carrier density, this value equals to ~ 0.1 and ~ 0.3 electrons per Mn ion or unit cell, respectively, which is in good agreement with our experimental results.

Additional EELS spectra recorded over the oxygen K-edge exhibit no statistically relevant deviations[231], ruling out that the formation of oxygen vacancies is causing the local change of the Mn valence. Moreover, EELS studies at tail-to-tail domain walls and x-ray photoemission electron microscopy (X-PEEM) further substantiate that the reduced valence state is a unique feature of the 2 – 3 unit cell wide area in the vicinity of the head-to-head walls (see Ref. 231). In accord with the semi-classical calculations, the EELS study confirms that accumulation of electrons, in addition to depletion of holes, governs the charge compensation of the bound polarization charge at the head-to-head walls of $\mathrm{ErMnO_3}$.

4.5.3. Theoretical explanation

In order to derive the orbital nature of the electrons and to understand the relationship between electron accumulation and local changes in the manganese valence, we worked closely together with Nicola A. Spaldin and Yu Kumagai, who took $\mathrm{YMnO_3}$ as a model hexagonal manganite to conduct density functional theory (DFT) calulations from first principles employing the local density approximation (LDA)+U method (compared to $\mathrm{ErMnO_3}$, $\mathrm{YMnO_3}$ is structurally and electronically similar, yet absent f electrons simplify the DFT calculations).

The obtained orbital-resolved density of states is shown in Fig 4.17a for the valence and conduction bands. In agreement with literature results[60,234], the density of states of the conduction band is small as it results from localized d_{z^2}-orbitals, which hybridize only marginally with adjacent apical oxygen p_z-orbitals. Broad valence bands form due to a strong hybridization and delocalization of manganese d- and oxygen $2p$-states. At the head-to-head wall, we can thus expect localized electrons if the CBM drops below the Fermi level, whereas delocalized holes are found at the VBM. The expectation is in agreement with our EELS data, showing a change in Mn valence attributed to local electron accumulation.

Although our theoretical study provides a good qualitative description of our experiment, we find a quantitative deviation between the density of electrons at the head-to-head wall derived by the semi-classical model and that obtained by the EELS measurements. As evident from the low-voltage cAFM measurements (see Fig. 4.13), hole depletion needs to surmount electron accumulation, whereas EELS indicates dominant electron-like compensation. This poses the question: 'Is there an additional mechanism present in the hexagonal manganites?' Both models, i. e., the semi-classical and DFT band picture, represent a crude simplification of the present problem, particularly in a material as $\mathrm{ErMnO_3}$, in which many-body interactions and correlations likely play a major role. Against this background, it is crucial to realize that electrons in the spatially confined manganese d_{z^2}-orbitals will feel a considerable

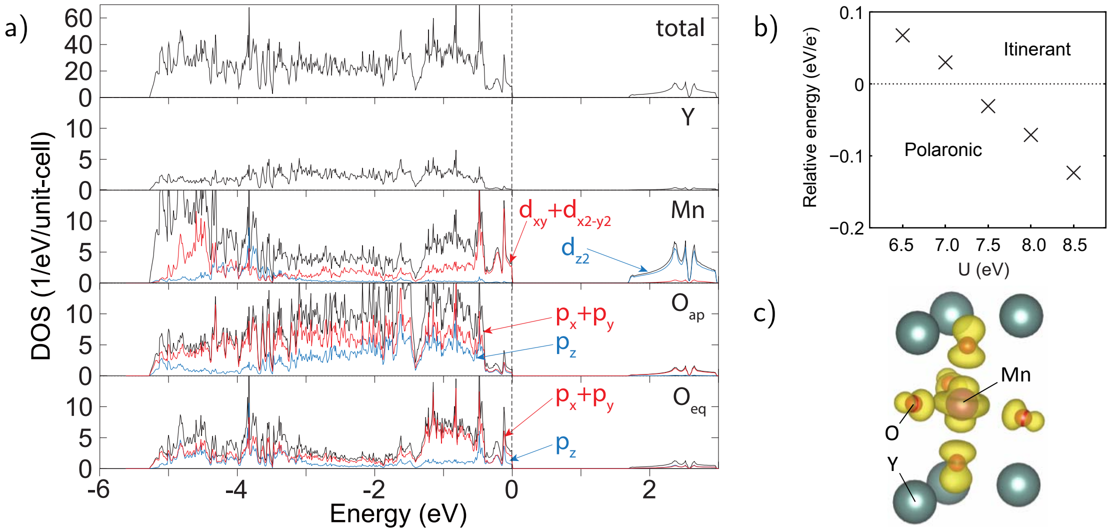

Figure 4.17.: Orbital character of electrons at head-to-head walls. a) Orbital-resolved density of states (DOS), with black lines indicating the sum of the corresponding DOS, while colored lines represent contributions from individual orbitals. The Fermi level at 0 eV is indicated by the black dashed line. Apical and equatorial oxygen sites of the trigonal MnO bipyramids (see Fig. 2.6) are indicated by O_{ap} and O_{eq}. b) Computed relative energy between localized polaronic and itinerant Bloch states of the electron. Above the dashed line, data points (black crosses) correspond to a stable Bloch state, whilst below the dashed line, data points indicate a stable polaron state for respective U values. c) Animation of the derived electronic polaron state.

local Coulombic repulsion, which usually prefers the formation of electronic states with localized polaronic character rather than itinerant Bloch electrons[235].

To analyze if such a scenario might be present in our case, the energy costs of fictitious polaronic states for both holes and electrons were calculated by incorporating a single hole or electron into a supercell of 120 atoms and reducing the local symmetry in proximity to a manganese site. For an isolated electron polaron, we find lower energies than for an itinerant Bloch electron, if the Hubbard U parameter exceeds 7.5 eV[c] (see Fig. 4.17b).

At the position of the head-to-head wall, we can assume that polarons order in a two-dimension array, which reduces their energy of formation significantly in comparison to isolated defects. Through a combination of the latter effect with our band-bending model[231] and the data shown in Fig. 4.17b, we obtain that polarons most likely form directly at the position of the wall, for reasonable values of both doping level of the bulk and Hubbard parameter U ($U = 6 - 6.5\,\mathrm{eV}$)[231]. The presence of polarons is expected to add an additional barrier to the electronic transport at lower voltages, which is consistent with the observed behavior shown in Fig. 4.13. This also lifts the condition of the semi-classical band model, stating that hole depletion overrides electron accumulation at head-to-head domain walls (Fig. 4.15a).

---

[c] On the contrary, hole polarons are always unstable compared to the itinerant Bloch state for U values up to 8.5 eV.

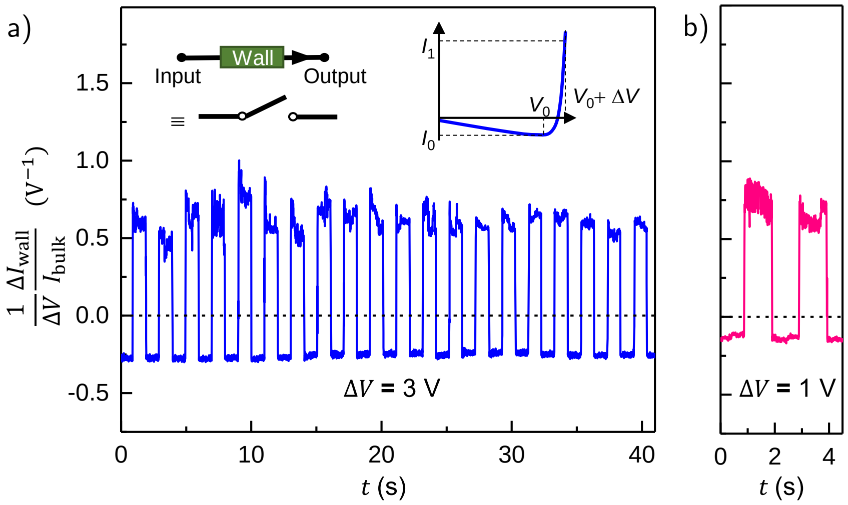

Figure 4.18.: Electric-field control of electronic transport at head-to-head walls. a) Normalized domain-wall current measured as a function of time over 20 switching cycles between resistive ($I_0 < I_{\mathrm{bulk}}$) and conducting ($I_1 > I_{\mathrm{bulk}}$) behavior. For voltages $V_0 = 2\,\mathrm{V}$ and $\Delta V = 3\,\mathrm{V}$ (see inset to (a) for a schematic illustration), reversible control can be reliably realized for 20 switching cycles, which is the largest number of cycles we investigated. b) Enhanced gain can be achieved, e. g., by increasing I_0, yielding $\Delta I_{\mathrm{wall}}/\Delta V \approx 15\,\mathrm{pA\,V}^{-1}$ for $V_0 = 4\,\mathrm{V}$ and $\Delta V = 1\,\mathrm{V}$. The increase in gain, however, requires larger currents, which cause degradation as described in the main text.

Altogether, both theory and experiment support electron accumulation at the head-to-head domain walls, which leads to the emergence of an inversion layer. At low voltage, electrons remain in a localized polaronic state and are thus negligible for charge transport. Yet, these electrons will dominate the transport if the bias voltage exceeds the critical threshold voltage ($V > V_{\mathrm{c}}$), as only they function as available mobile charge carriers. Within the polaronic description, the critical voltage V_{c} correlates with the transition from localized polarons to itinerant electrons and corresponds to the state, where domain-wall transport is governed through the activation of an inversion layer[231].

4.5.4. Novel functional properties

In Figure 4.18a and b we show how this behavior can be used in order to realize, e. g., a domain-wall-based binary switch. The cAFM data in Fig. 4.18a is collected at a head-to-head wall as a function of time with the bias voltage V_{DC} varying repeatedly between $V_0 = 2\,\mathrm{V}$ and $V_0 + \Delta V = 5\,\mathrm{V}$ (the data has been recorded at the marked points in Fig. 4.2b). Due to the unusual $I(V)$ characteristic at the head-to-head wall, the change in electric field allows reversible switching between resistive ($I_0 < I_{\mathrm{bulk}}$) and conductive ($I_1 > I_{\mathrm{bulk}}$) behavior as reflected by the normalized domain-wall current $1/\Delta V(\Delta I_{\mathrm{wall}}/I_{\mathrm{bulk}})$ in Fig. 4.18a.

Figure 4.18b shows that the related electric-field induced gain, $\Delta I_{\mathrm{wall}}/\Delta V$, can be enhanced by increasing the base voltage V_0. The enhancement in gain, however,

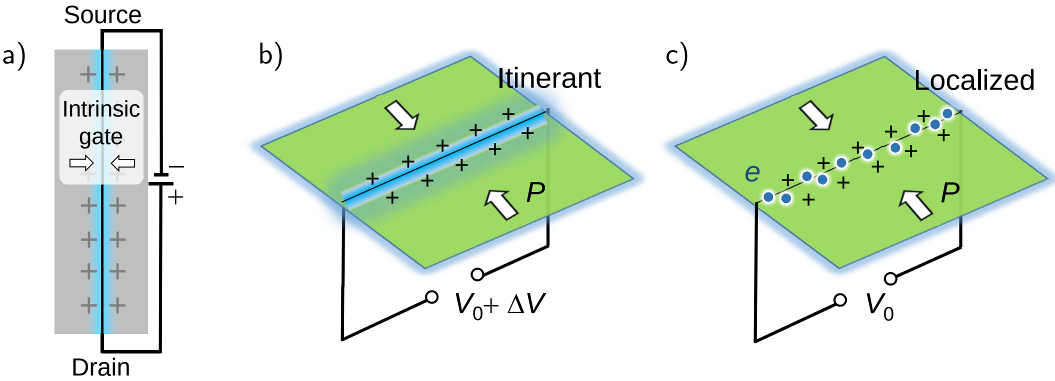

Figure 4.19.: Conceptual domain-wall functionality. a) Sketch of a domain-wall-based field-effect transistor with polarization charges playing the role of the gate. The amount of domain-wall charge – which determines band bending and thus inversion layer – can be altered, e. g., by the domain-wall angle, temperature, and pressure. b) Sketch showing the conductive domain-wall state for $V = V_0 + \Delta V$ with itinerant electrons illustrated in blue. c) Resistive domain-wall state with localized electrons for V_0.

is accompanied by the flow of a larger current I_0, which causes irreversible changes in the electronic surface structure and fast degradation of the domain-wall-based binary switch after only two to three cycles (not shown).

Going beyond binary switches, the domain-wall behavior may be exploited to mimic the functionality of other electronic compounds such as transistors or gates. For instance, the field effect associated with the polarization charges can, in principle[11,106], be used to modulate conductivity at the wall and, hence, serve as a natural, intrinsic gate. This concept, however, is not specific to the head-to-head wall discussed above and can be expanded to any charged-type domain wall. If a charged domain wall exhibits increased conductance due to an accumulation of charge carriers, the amount of charge carriers and hence its conductance can be adjusted by manipulating the polarization charge at the wall, e. g., by domain-wall angle, temperature, and pressure[11,90,110]. This would allow to adjust the conductance by external fields analog to transistors.

A unique feature of the head-to-head walls that is not available at the tail-to-tail wall is the formation of an inversion layer, which can be activated by the electric field. This allows to change between hole- and electron-dominated transport by changing the external voltage, which accesses so far unknown possibilities (see Fig. 4.19b and c).

To summarize, the head-to-head domain walls studied in this work thus represent a natural type of semiconducting oxide interface at which the nature of the electronic transport can be manipulated at will and in a fully reversible fashion. This new degree of freedom becomes possible as the local transport behavior is determined by the interplay between holes and electrons.

4.6. Summary

We showed how intrinsic electronic transport at charged domain walls in $ErMnO_3$ can be manipulated by internal chemical impurities and external electric fields. At the tail-to-tail walls of moderately p-doped $Er_{1-x}Ca_xMnO_3$ ($x = 0.01$), we observe an increase in the intrinsic conductance by a factor of 50, while current spreading gets limited down to $\approx 50\,\mathrm{nm}$. Continuously increasing the amount of n-type carriers in $Er_{1-x}Ca_xMnO_3$ leads from an insulating p-type state to a conductive state with n-type carriers contributing to the transport. On top, electron doping allows to change the screening scenario at the domain walls transforming the properties of the head-to-head wall from insulting to conducting.

In undoped $ErMnO_3$, we switch the electronic transport at the head-to-head domain-wall reversibly between an insulating and a conductive state by changing the applied bias voltage. We find that the transition is attributed to the formation of an inversion layer, at which electrons with polaronic properties accumulate. Based on the results, we present potential concepts for domain-wall based electronic components that incorporate these functional layers.

5. Manipulating electronic transport at neutral domain walls

Similar to charged domain walls, neutral domain walls can display varying conduction properties[8,53,92,109], giving rise to additional functionality. In contrast to the intensively studied charged walls, however, little is known about the conductance at neutral walls, which arises due to a complex interplay of accumulation of defects, band lowering, strain, and secondary phases.

The goal of this study is to understand and control the diverse conduction phenomena at neutral walls. In hexagonal manganite ($R\text{MnO}_3$), the neutral domain walls in $R\text{MnO}_3$ show a wide variety of conductance properties including insulating, bulk-like, and conducting behavior[11,12,53,92,149,150]. In order to develop a coherent picture and separate intrinsic domain-wall effects from extrinsic contributions (e. g. contact resistances), we perform an SPM-based variant of dielectric spectroscopy.

Our study begins with a in-depth characterization of the direct-current transport properties at the neutral walls of as-grown hexagonal ErMnO_3 (Sec. 5.1). We then fine-tune the electronic conductance state of both bulk and neutral domain walls by oxygen annealing (Sec. 5.2). In the final part of this section, we demonstrate emergent functionality at neutral walls, i.e., half-wave rectification under AC voltage. Our results provide new insight into the intrinsic domain-wall properties of neutral walls and expand domain wall related applications to the realm of AC technology (Sec. 5.3).

5.1. Direct-current transport properties

Transport properties at neutral domain walls in bulk hexagonal manganites range from insulating[11,53] and conducting domain walls[149,150] to walls that behave like the bulk[92]. To demonstrate the domain-wall properties of our floating-zone ErMnO_3 samples, we start with basic conductive atomic force microscopy (cAFM) measurements. Figure 5.1a presents a cAFM scan performed on an out-of-plane oriented sample at a bias voltage $V_{\text{DC}} = 2.0\,\text{V}$. Interestingly, all neutral domain walls show higher current responses than the surrounding bulk, while no difference in domain currents is observed. This observation is different from previous studies that reported reduced domain-wall currents[11,53] and bulk-like behavior[53,92] (see Sec. 2.2.2). In

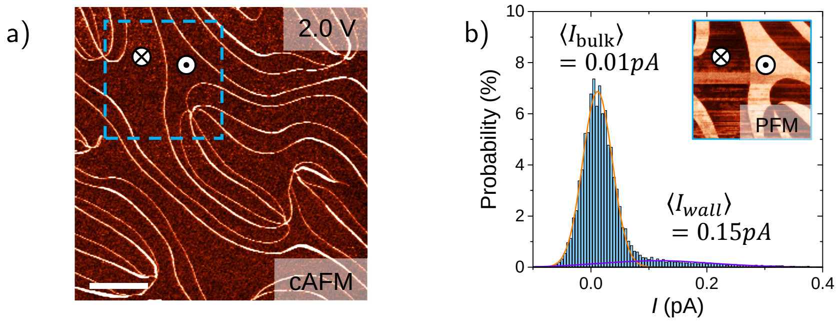

Figure 5.1.: Conduction at neutral domain walls of $\mathrm{ErMnO_3}$. a) cAFM scan at $V_{\mathrm{BV}} = 2.0\,\mathrm{V}$ revealing increased currents (bright) at the neutral domain walls of an $\mathrm{ErMnO_3}$ sample with polarization pointing out-of-plane. The scan shows no polarization-modulated Schottky-contrasts stemming from the domains. Scale bar is 2 µm. b) Histogram analysis showing the probability of domain-wall and bulk currents from the scan in (a). Average bulk and domain-wall currents are derived by fitting the probability distribution with two Gauss functions as indicated.

the inset to Figure 5.1b a PFM scan taken at the same position is presented, corroborating that the current signal originates from the domain walls.

The distinct contribution from the domain walls is also visible in Figure 5.1b, showing the histogram of the cAFM scan in Figure 5.1a. We can determine two peaks that correspond to bulk and domain-wall currents, respectively (Figure 5.1b). Best fits are obtained with two Gaussian functions yielding average currents $\langle I \rangle = 10\,\mathrm{fA}$ for the bulk and $\langle I \rangle = 150\,\mathrm{fA}$ for the walls. Thus, the domain walls exhibit one magnitude larger currents at $V_{\mathrm{BV}} = 2.0\,\mathrm{V}$.

In order to rule-out that the measured currents are dominantly consisting from transient or switching-related currents, we perform additional grid spectroscopy and time-dependent measurements (see Sec. 3.1.2). The derived $I(V)$ characteristics shown in Figure 5.2a describe a Schottky-like trend between 0 and 6 V for the neutral domain walls and the $-P$ domains. In contrast, $+P$ domains show no significant increase in current for voltages up to 6 V. The difference in the $I(V)$ characteristics of the domains can be explained by the modulation of the Schottky barrier through the polarization, which is in agreement with previous studies[11,53,92]. We observe that Schottky-determined domain currents dominate at voltages greater 3.5 V. At lower voltage, domain walls provide higher currents than the domains. Occasionally, some domain walls remains more conductive over the whole voltage range (see black $I(V)$ curve). Possibly, these walls are not perfectly perpendicular to the surface and thus not completely neutral, i. e., partially of tail-to-tail type.

After scrutinizing the local $I(V)$ curves, we continue with time-dependent measurements using a new probe tip. We move the tip over the domain / domain wall and apply a bias voltage of $V_{\mathrm{BV}} = 2.5\,\mathrm{V}$. Figure 5.2b shows the recorded current signals after they have stabilized from AFM-related switch-on capacitances. The local currents remain stable over at least 10 s and show distinctly different values for the $-P$ domain and the neutral domain wall (see caption for average current). In comparison to the spectroscopy data, the current values of the time-dependent measurement

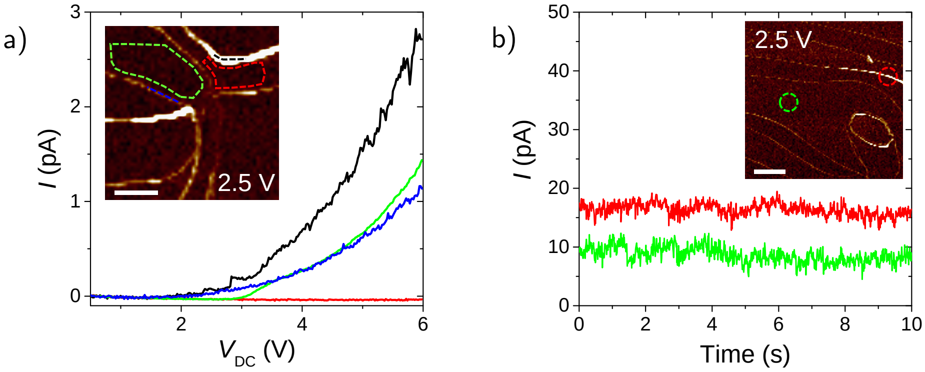

Figure 5.2.: Current spectroscopy and time dependence at neutral domain walls. a) $I(V)$ curves of neutral domain walls (black, blue), $-P$ (green), and $+P$ domains (red) extracted from cAFM grid-spectroscopy data as indicated on the inset. Between $\sim 2\,\mathrm{V}$ and $\sim 3\,\mathrm{V}$ both domain walls (black, blue) are more conductive than the bulk. Currents of $-P$ (green) become more dominant above 4 V, while currents of $+P$ show no significant increase. Scale bar is 1 µm. b) Time-dependence of $-P$ domain (green) and domain-wall currents (red) recorded at $V_{\mathrm{BV}} = 2.5\,\mathrm{V}$ with average currents of $8.65 \pm 1.34\,\mathrm{pA}$ and $16.38 \pm 1.06\,\mathrm{pA}$, respectively. Currents remain stable over a period of 10 s. Curves are plotted after the stabilization from capacitive currents resulting from switching on the voltage. Scale bar is 2 µm.

show about ten times higher values. The difference between the two techniques can be caused either by the different tips or by a slower equilibration to a steady-state current compared to the sampling rate in grid spectroscopy ($t_{\mathrm{eq}} > \tau = 2\,\mathrm{ms\,pnt}^{-1}$).

Most importantly, based on the SPM data we can conclude that increased domain-wall conductance at the neutral walls in our hexagonal manganite $R\mathrm{MnO}_3$ sample is related to an intrinsic effect. The temporal stability of the currents is in the order of several seconds, similar to currents in, e. g., BiFeO_3 thin films[7]. Furthermore, one order of magnitude higher domain-wall currents can be achieved with respect to the bulk.

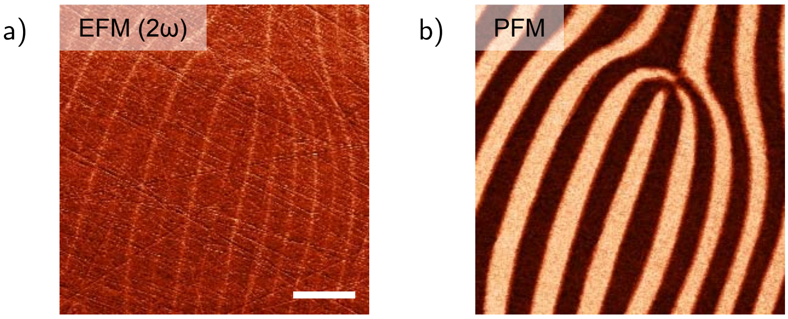

Figure 5.3.: Evidence of intrinsic conductance properties at neutral domain walls. a) EFM-2ω signal showing increased response at the domain walls, which can be attributed to higher concentrations of mobile charge carriers. Scale bar is 2 µm. b) Corresponding vertical PFM signal showing that the enhanced EFM signal coincides with the domain walls. Bright and dark domains correspond to an out-ot-plane polarization pointing up and down, respectively.

In the next step, we investigate possible contributions from interface effects that may obscure the data. For this purpose, we perform EFM, as it is a powerful tool that allows to distinguish bound and mobile charges / polarizability (see Sec. 3.1.4). A representative EFM scan is shown in Figure 5.3a. Clearly, we see a higher signal at the domain wall in the 2ω channel, which probes mobile charges / polarizability. The corresponding PFM scan is shown in Figure 5.3a. EFM thus corroborates a higher intrinsic domain-wall conductance (note that EFM is a contact-free technique). An alternative scenario for the enhanced domain-wall signal would be an increased polarizability due to a local increase in dielectric constant. The dielectric constant, however, should be smaller compared to the domains, as the domain wall partially resembles the parent phase[23,53]. Higher polarizability can thus be excluded.

In summary, our investigations in terms of cAFM and EFM reveal: (i) Neutral domain walls in the $R\mathrm{MnO}_3$ can show increased currents, (ii) domain-wall current response is not provoked by transient effects or by domain-wall movement, and (iii) the current response reflects an enhanced intrinsic DW conductance.

5.2. Tuning transport properties by oxygen annealing

In the next step, we discuss the correlation between the domain-wall behavior and the electronic properties of the material. Since the amount of hole carriers in hexagonal manganite ($R\mathrm{MnO}_3$) is related to the concentration of oxygen interstitials[138], adjusting the oxygen content is a versatile approach for manipulating the bulk electronic properties (see Sec. 2.2.3). This can be realized by annealing under different atmospheres[119,120,143] and first investigations already suggested a close relation between the oxygen content and the domain-wall properties[149,150].

For our study, we generated a series of samples with varying oxygen content starting from specimens that were cut from the same single crystal we investigated in Section 5.1. The samples were annealed at 1470 K for several hours and afterwards cooled with different rates. Depending on the cooling rate, the annealing time and thus the internal oxygen concentration changes[119].

Figure 5.4 presents the respective current maps, all taken at a bias voltage of 1.3 V, except for the one in Fig. 5.4e, where $V_{\mathrm{DC}} = 2.5\,\mathrm{V}$ to obtain detectable currents. Aside from the previously discussed change in vortex density[118,122,128] (note that all scans are of the same size), we observe a reduction in the overall conductance with increasing cooling rate (Fig. 5.4f). Interestingly, only the sample with the lowest conductance shows features of enhanced domain-wall conductance. All other samples show domain contrast created by the typical polarization-modulation in the Schottky-barrier[11,53,92]. Figure 5.4f shows the conductance of the individual samples (orange) together with their vortex density (black) as function of cooling rate. The data reveal that the conductance of the samples, which was determined with a single AFM tip, primarily correlates with the annealing time, but not with

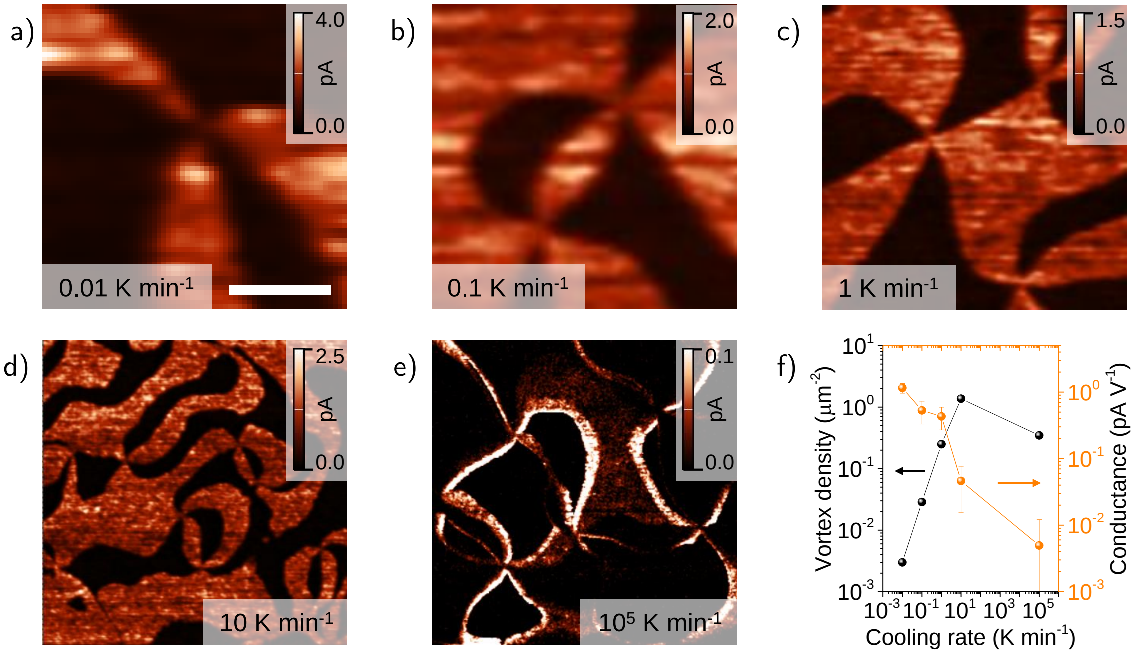

Figure 5.4.: cAFM characteristics of annealed $ErMnO_3$ samples. a) to e) Current maps of oxygen treated samples that have been cooled with certain cooling rates over the ferroelectric phase transition. Aside from the cooling-rate dependence of the vortex-density[122,128], the samples show increasing resistivity the higher the cooling rate (see current scale). Strikingly, the most insulating sample (e) shows enhanced domain-wall currents. Scale bar in (a) is the same for all scans and corresponds to 1 µm. f) AFM-determined conductance and vortex density as function of cooling rate. Vortex-density data taken from Ref. 122.

the vortex density. The latter is evident from the slopes of the two curves. While the vortex density goes through a maximum at $10\,\mathrm{K\,min^{-1}}$, the conductance decreases monotonously with increasing cooling rate.

The reason for reduction in conductance with increasing cooling rate can be understood as follows. Because oxygen interstitials are unstable for temperatures above 620 K[119,120,143], upon heating the samples will lose their intrinsic interstitial oxygen O_i, which acts a hole donor[138]. The high temperature during dwelling at 1470 K creates entropy-stabilized defects, e. g., vacancies, Frenkel-, and Schottky-defects[236]. The faster the cooling rate, the smaller the chance for the system to reduce the amount of entropy-induced defects. Higher concentrations of quenched-in defects will increase the probability of charge carriers to scatter during electronic transport, hence leading to a higher resistance. This scenario is consistent with the observed decrease in conductivity with increasing cooling rate[a].

Although the microscopic details remain to be demonstrated, Fig. 5.4f shows that the electrical resistance can be manipulated via the annealing time. Crucial for our following domain-wall studies is that the annealing procedure allows us to generate a series of out-of-plane oriented $ErMnO_3$ samples with continuously varying bulk

---

[a] The actual conductivity values of the samples in Fig. 5.4a–d are given in Fig. 5.9c and Fig. 5.11.

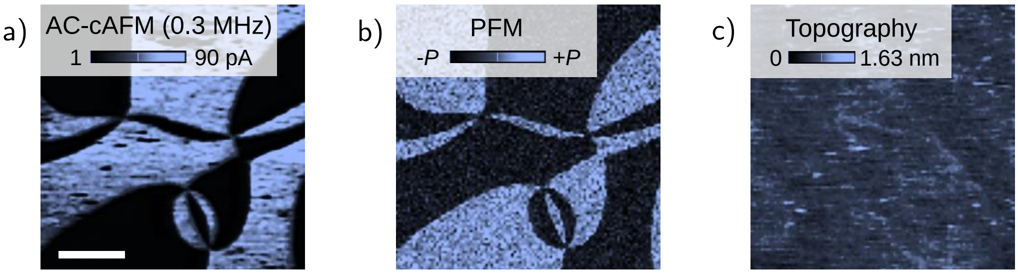

Figure 5.5.: Comparison of AC-cAFM and PFM signals. a) AC-cAFM response I_{DC} recorded at $\nu = 0.3\,\mathrm{MHz}$ revealing the characteristic domain pattern of the hexagonal manganites with six-fold meeting points. Higher currents are obtained for the $-P$ domains. b) Simultaneously recorded PFM signal shows the same domain pattern with dark and bright domains pointing down ($-P$) and up ($+P$), respectively. c) Topography signal at the same position shows no strong variations, e. g., due to selective domain etching[127]. Sample corresponds to Fig. 5.4b. Scale bar in (a) is 2 µm.

conductance. This facilitates a systematic analysis of the domain-wall transport properties, which we present in the next chapter. Most important though, our data provide a first hint that the domain-wall conductance, or more precisely, their emergence in cAFM, is in direct correlation with the bulk conductance / defect density (see Fig. 5.4).

5.3. Frequency-dependent rectification at domain walls

In the next step, we study the evolution of the electronic response at the neutral walls of our sample series under applied alternating voltages. For this purpose we devised a microscopy-based experiment combining the capacity of dielectric spectroscopy with the local resolution provided by scanning probe microscopy (SPM). We refer to this method as alternating-current conductive atomic force microscopy (AC-cAFM); all technical details plus a description of the setup are given in Sec. 3.1.2. In our AC-cAFM study, we measure the current responses I_{DC} as function of frequency over the $\mathrm{ErMnO_3}$ series of test samples (Sec. 5.2) with continuously changing conductance (see Figure 5.4, samples a to d).

AC-cAFM measures the direct current response I_{DC} when an oscillating voltage of angular frequency $\omega = 2\pi\nu$ is applied (see Sec. 3.1.2). Figure 5.5a shows a representative AC-cAFM scan recorded at a frequency of $\nu = 0.3\,\mathrm{MHz}$ with an amplitude $V_{\mathrm{AC}} = 3\,\mathrm{V}$[b]. At this settings the AC-cAFM signal corresponds to the structure of the domains, which have been imaged simultaneously by recording the PFM signal (Fig. 5.5b). In the AC-cAFM response domains with polarization pointing downward ($-P$) exhibit a higher signal in current than domains with polarization pointing upward ($+P$), whereas no signature corresponding to the neutral domain walls

---

[b] For all the following measurements we apply the same AC voltage: $V_{\mathrm{AC}} = 3\,\mathrm{V}$

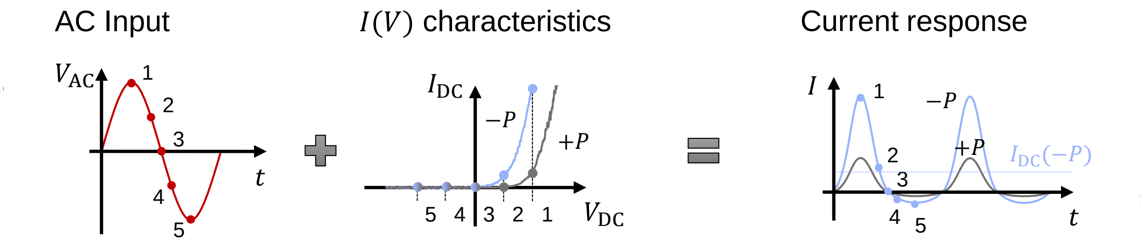

Figure 5.6.: How AC voltages lead to DC-current responses. Illustration showing that the asymmetric $I(V)$ characteristics of (001)-oriented $ErMnO_3$ lead to a non-vanishing current response I_{DC} under alternating bias.

can be distinguished. The AC-induced DC current measurement is in accordance with previous results where alternating domain contrasts have been attributed to a modulation of the Schottky barrier caused by the spontaneous polarization[92] (see Fig. 5.4a to d). This barrier is higher at the surface of $+P$ domains compared to $-P$ domains (comp. Fig. 2.8c), giving rise to a pronounced conductance contrast in DC measurements. A modulation of the current signal caused by topography imprint can be excluded, as the sample is flat with a roughness of about 0.2 nm (RMS; see Fig. 5.5c).

The contrast in AC-cAFM is visible because of the asymmetric $I(V)$ characteristics associated with the Schottky barrier[92] at the tip-sample interface as described in Fig. 5.6; the current that flows for forward bias ($V > 0$) is higher than for reverse bias ($V < 0$) and, as a consequence, a nonzero DC signal arises; the latter is defined as I_{DC} (see Eq. 3.3). AC-cAFM can thus be used to visualize asymmetries in the local $I(V)$ characteristics and hence provides information about spatial variations in the electronic structure. Most importantly, the frequency of the AC voltage can be tuned, which allows to separate different contributions to the local conductance, analogous to classical dielectric spectroscopy measurements at the macroscopic scale[237].

A frequency-dependent AC-cAFM image series is shown in Fig. 5.7a to c ($V_{\mathrm{AC}} = 3\,\mathrm{V}$). The data reveals that the domain-related conductance contrast of $ErMnO_3$ decreases with increasing frequency ν. In parallel, a new signal arises at the domain walls (Fig. 5.7b), which is observed up to much higher frequencies than the domain-related signal (Fig. 5.7c). A more detailed analysis is presented in Fig. 5.7d, showing the evolution of the AC-cAFM signal as function of ν, evaluated for the cross-section marked in Fig. 5.7a. Starting from low frequencies, the current for both $+P$ and $-P$ domains first increases, reaching its maximum at $\nu_{\mathrm{max}} \approx 0.273\,\mathrm{MHz}$. This is the frequency at which the most pronounced domain contrast is observed.

Towards higher frequencies the signal quickly decreases and the difference in domain current $\Delta I_{\mathrm{domains}} = I_{\mathrm{DC}}(-P) - I_{\mathrm{DC}}(+P)$ goes beneath 0.5 pA[c] at 0.84 MHz. The domain-wall-related signal arises for $\nu \approx \nu_{\mathrm{max}}$; it exhibits a weak frequency-dependence and persists up to 3.1 MHz, i. e., the highest frequency we measured.

---

[c] This threshold value of $\Delta I_{\mathrm{domains}} = 0.5\,\mathrm{pA}$ is used to determine the boundary for domains contributions in the contrast diagram (blue dots in Fig. 5.11).

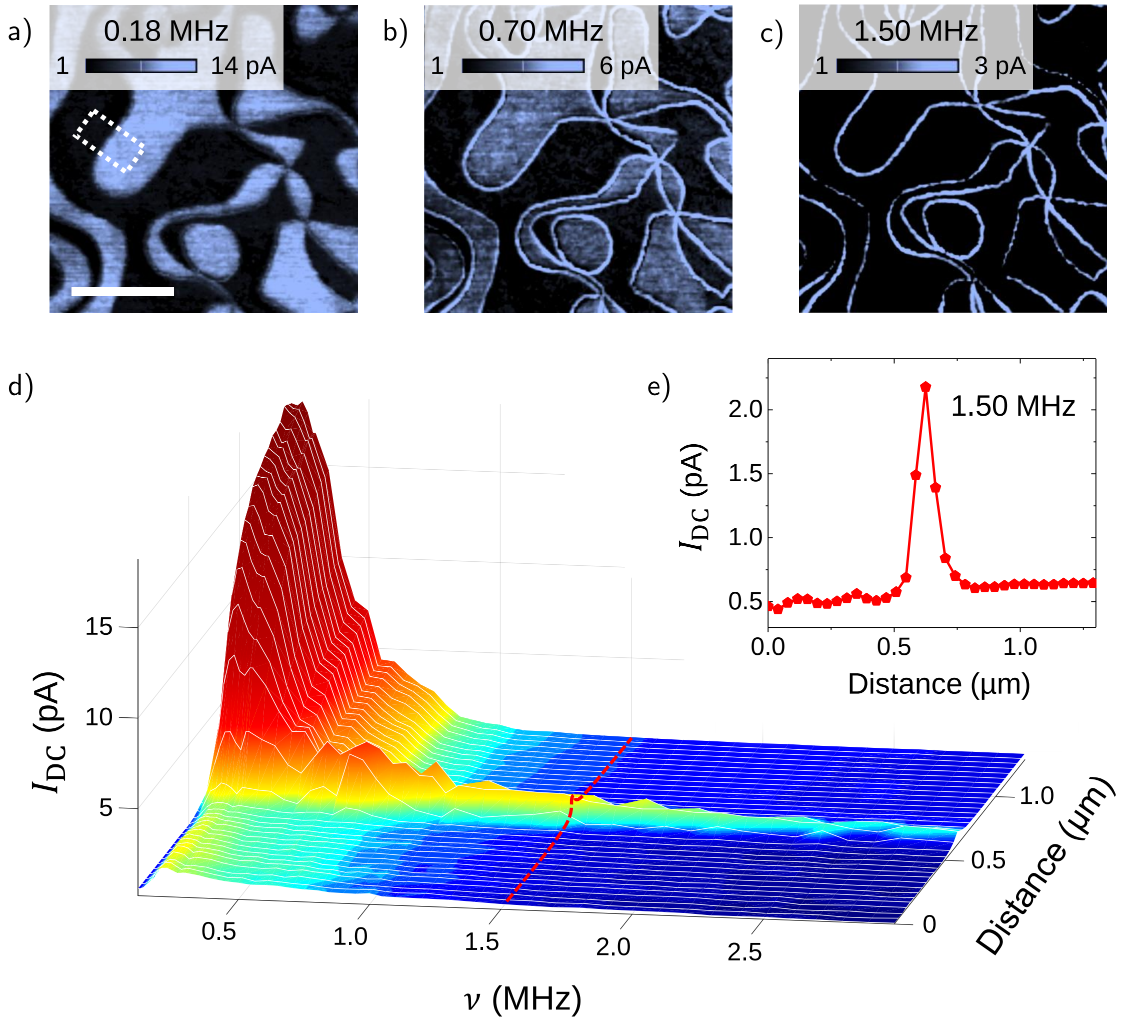

Figure 5.7.: Current response I_{DC} as function of frequency ν. a) AC-cAFM image of sample with intermediate conductivity ($2.0 \times 10^{-6}\,\mathrm{S\,cm^{-1}}$, Fig. 5.4c) at $\nu = 0.18\,\mathrm{MHz}$, $V_{\mathrm{AC}} = 3\,\mathrm{V}$. Clear domain structures are visible with $I_{\mathrm{DC}}(-P) > I_{\mathrm{DC}}(+P)$. b) Current signal resulting at higher frequency of the input voltage (0.70 MHz) at the same position. Now, additional signals arise at the domain walls while domain currents have decreased. c) At even higher frequencies (1.50 MHz), domain-wall currents predominate the signal. d) Evolution of the current response averaged over the domain wall section highlighted in (a) as function of frequency. Domain currents steadily rise with increasing frequency and peak at 0.273 MHz. Contributions from domain walls start to appear 0.268 MHz while domain currents decline. At high frequencies, the current signal has shifted from domains to domain walls. e) Domain-wall cross-section extracted from the graph in (d) at 1.50 MHz. 350 % enhancement of the domain-wall current signal with respect to the bulk. Scale bar in (a) is 2 µm.

This persistence implies that rectification at the walls occurs over a much wider frequency range than for the domains. As an example, we show the AC-cAFM signal for $\nu = 1.5\,\mathrm{MHz}$ in Fig. 5.7e. At this frequency, the domains have almost lost their rectifying properties, whereas the domain walls still exhibit a pronounced AC-cAFM signal. Based on the data, we estimate an effective wall width of $w \approx 90\,\mathrm{nm}$, which is comparable to the electronic width of the charged walls observed in standard cAFM scans[82] (see Sec. 4.3.3). In contrast to the charged walls, however, the neutral walls carry no bound charges that could explain their anomalous electronic transport and rectifying properties.

In order to understand the AC-cAFM spectrum and the surprising domain-wall behavior, we perform additional measurements on the $ErMnO_3$ sample series introduced in the previous Sec. 5.2. AC-cAFM spectra for two samples with suppressed and enhanced conductivity, compared to Fig. 5.7, are presented in Fig. 5.8a and b, respectively. Interestingly, all recorded spectra show qualitatively equivalent features: First, a low-frequency regime where only domain contrast is observed and, second, a high-frequency regime in which only the domain walls lead to a detectable AC-cAFM signal. In the transition region, both domain and domain-wall signals coexist. The frequency associated with the transition, ν_c, however, strongly depends on the bulk conductivity, shifting to higher values as the conductivity increases.

The behavior is consistent with the formation of a Schottky-like barrier at the tip-sample interface. This insulating barrier acts as a capacitor and can be bypassed at sufficiently high frequency. The effect is commonly described by a simple equivalent circuit model, assuming two RC-circuits connected in series[237]. The two circuits represent the surface barrier layer and the bulk properties, respectively, with $R_\mathrm{surf} >> R_\mathrm{bulk}$ and $C_\mathrm{surf} >> C_\mathrm{bulk}$. The associated loss peak position[d] is $\nu_\mathrm{c} = 1/(2\pi\tau) = 1/(2\pi R_\mathrm{bulk} C_\mathrm{surf})$, which in agreement with the AC-cAFM results, shifts to higher frequencies for increasing bulk conductivity[237]. This leads to the conclusion that the rectifying properties observed for $\nu > \nu_\mathrm{c}$ are an intrinsic feature of the neutral domain walls.

In collaboration with Stephan Krohns at the University of Augsburg, we performed macroscopic dielectric spectroscopy on all investigated samples to determine possible relaxations and the conductivity of the bulk material. Figure 5.9a to c show the frequency dependence at 300 K of the dielectric constant ε', the 'loss tangent' δ, and the conductivity σ, respectively. For all samples, the dielectric constant remains roughly constant in the low frequency regime before showing a step-like decrease to a lower $\varepsilon \approx 30$. This is a typical signature of a relaxation process, which in the presence of a Schottky-like barrier is most likely a Maxwell-Wagner relaxation[237]. The observation is in agreement with the observations made for hexagonal $YMnO_3$[228]. Clearly, the drop in dielectric constant happens at different frequencies for our samples, shifting to higher ω values for increasing conductivity. The observed insulating surface layers also dominate the DC conductivity at low frequencies. From the frequency dependent dielectric measurements we determine intrinsic bulk conductivity values σ_DC (plateaus in Fig. 5.9c) in the range of 0.7 to $19 \times 10^{-6}\,\mathrm{S\,cm^{-1}}$, being in good agreement with previously reported values[140] (see Fig. 5.9).

The dielectric data were fitted with an equivalent circuit model as described above[237,238] to estimate the frequency of the lower tails of the relaxations. The frequencies are marked in the plot of the dielectric loss tangent δ (Figure 5.8d).

---

[d] In this case, the relaxation time $\tau = R_\mathrm{bulk} C_\mathrm{surf}$[237].

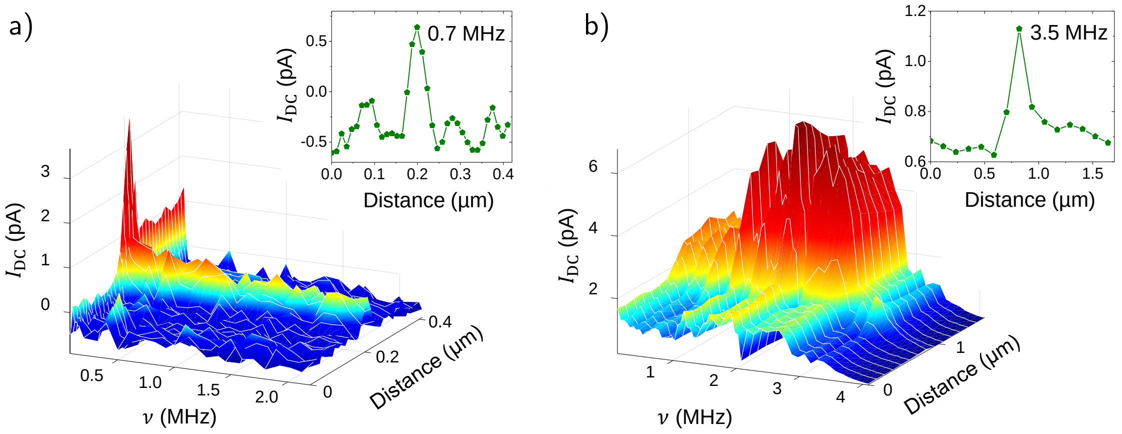

Figure 5.8.: Current response of the samples with lowest and highest conductivity. a) Frequency plot of current signal extracted from a domain-wall cross-section of the sample with the lowest conductivity ($0.7 \times 10^{-6}\,\mathrm{S\,cm^{-1}}$, Fig. 5.4d). Starting at low frequencies domain currents fade out and are only visible at frequencies $< 0.1\,\mathrm{MHz}$. Over the whole measured frequency range domain-wall currents contribute to the signal. b) Frequency-dependence of domain-wall cross-section currents from the sample with highest conductivity ($19.0 \times 10^{-6}\,\mathrm{S\,cm^{-1}}$, Fig. 5.4a). Currents from domains rise with increasing frequency and go through a maximum at $\sim 2.2\,\mathrm{MHz}$. At 3.37 MHz domain currents become negligible with respect to contributions from domain walls.

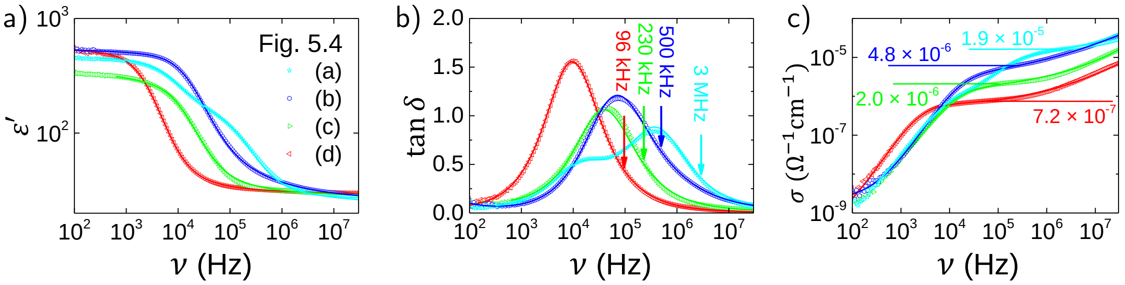

Figure 5.9.: Dielectric spectroscopy measurements at room temperature. a) to c) Spectral dependence of dielectric constant ε', loss tangent δ, and conductivity σ the four samples (Fig. 5.4a to d) at 300 K, respectively. The dielectric constants shows a plateau at lower frequencies before they drop due to a Maxwell-Wagner relaxation. With increasing conductivity of the samples, relaxations are shifted towards higher frequencies. The dielectric loss peaks are located at frequencies that are alike to the peaks of the current signal in the frequency-dependent AC-cAFM measurements. The intrinsic bulk conductivity σ_{DC} corresponds to the plateau values as indicated in the frequency-dependent conductivity plots in (c).

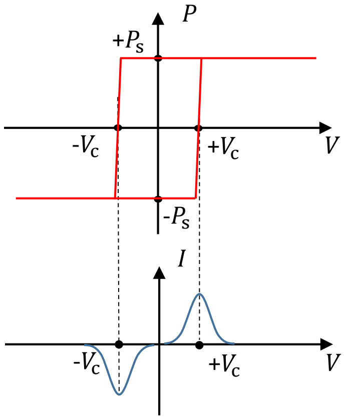

Figure 5.10.: Schematic ferroelectric hysteresis and switching currents. In an ideal case, the switching currents for switching forth and back are of same magnitude. Hence, moving a domain wall back and forth with an AC electric field should lead to an averaged-out current response I_{DC} in AC-cAFM. Schematic adapted from Ref. 239.

Compared to the current versus frequency plots in Figure 5.7d, 5.8a, and b, it is obvious that the frequency values of the dielectric relaxations are in good agreement with the frequencies where domain contrast vanishes and domain-wall currents become dominant. This leads to the conclusion that the I_{DC} currents measured in AC-cAFM are related to the same dielectric relaxations in the material as probed by the macroscopic spectroscopy. Thus, by tuning the frequency in AC-cAFM experiments contributions from, e. g., contact resistance can be bypassed providing access to the conductive properties of the domain walls.

We note that the obtained domain-wall currents have a fundamentally different origin than the displacement currents, previously discussed in connection with neural domain walls[8,109]. As an AC voltage is applied, domain-wall movement would lead to a symmetric current response as illustrated by the switching currents in Figure 5.10. Such contributions would thus average to zero in AC-cAFM. Moreover, time-dependent measurements show stable domain-wall currents over several seconds (see Fig. 5.2b), so that we exclude current contributions related to domain-wall movement.

A possible microscopic origin for the intrinsically enhanced current response I_{DC} at neutral walls are defects. For example, the concentration of oxygen interstitials $\mathrm{O_i}$ – responsible for the p-type behavior in the $R\mathrm{MnO_3}$ family[138] – could be increased in the vicinity of the domain walls due to the different local symmetry[53]. The driving force for increasing the amount of $\mathrm{O_i}$ at the domain-wall originates from an effective lowering of the total free wall energy through defect agglomeration (see Sec 2.1.1.3). The latter may promote a locally increased hole concentration and hence lead to pronounce domain-wall currents[e]. Defect accumulation at domain

---

[e] We note that we exclude oxygen interstitial movement due to the following reasons: (i) Higher activation energy than hole transport, (ii) Ionic movement, i. e., material transport, would lead to changes in the topography at the wall, which we do not observe.

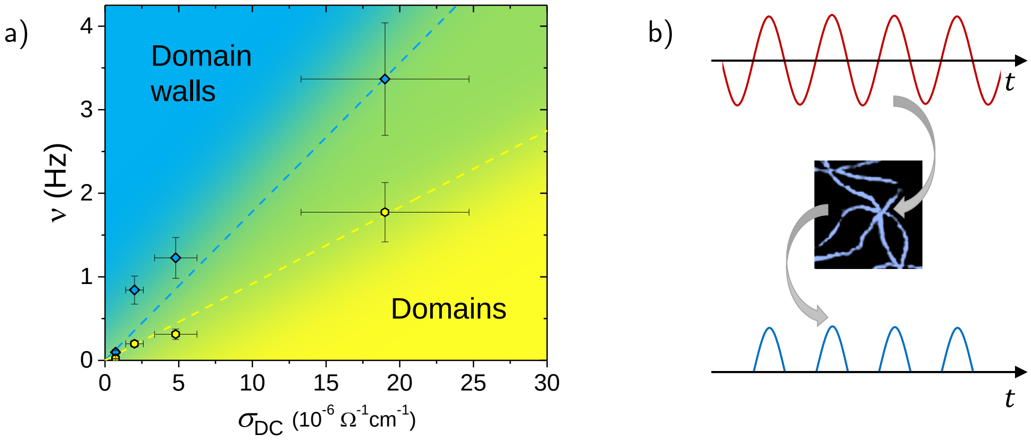

Figure 5.11.: Frequency-dependent current response I_{DC}. a) Contrast diagram of the current response I_{DC} as function of sample conductivity and AC voltage frequency ν. Blue and yellow points respectively define the frequencies where domain currents cease ($\Delta I_{\mathrm{domains}} < 0.5\,\mathrm{pA}$) and domain-wall currents start to contribute to the signal (i. e., visible in the scan). Domain currents are always favored at low frequencies and stable towards higher frequencies for larger sample conductivity. At high frequency, domain wall currents dictate the current signal. Lower sample conductivity results in lower frequencies for the onset of domain wall currents. For a given sample conductivity, the diagram predicts how to manipulate the current response by adjusting the frequency of the input voltage. b) Schematic of half-wave rectification exploiting domain walls. The AC input signal is modulated by the domain wall, leading to an asymmetric current response.

walls has been already discussed in relation to domain-wall conductance in other systems[8,9,86]. In the case of $R\mathrm{MnO}_3$, additional experiments (e. g. investigation of defect-related current footprints after domain switching[240]) and density functional theory (DFT) could provide further insight regarding this question. In the following, however, we will focus on related functional properties, i. e., half-wave rectification at neutral walls and its dependence on the material's electronic properties.

5.4. Contrast diagram of local current responses

The systematic AC-cAFM study can be summarized in a 'contrast diagram' as presented in Figure 5.11a. This diagram shows the correlation between bulk conductivity σ_{DC} and local current responses I_{DC} in correlation with the frequency ν of the applied bias voltage (Fig. 5.11a). The boundaries for the onset of domain-wall currents (yellow) and the ceasing of domain currents (blue) are extracted from the I_{DC}-vs-frequency plots of the four investigated samples (Fig. 5.7d, 5.8a, 5.8b, and A.1).

The diagram highlights two major trends: a) The onset of current response I_{DC} at the domain walls shift towards higher frequencies with increasing bulk conductivity, and b) the region of mixed contrasts covers a wider frequency range for samples with increased conductivity. The data can explain the discrepancies between previous studies, which observed bulk-like and conducting domain walls on (001)-oriented $R\mathrm{MnO}_3$ samples[92,149,150]. Most important, the 'contrast diagram' shows that rectifying properties of domain walls can be adjusted with respect to the practical frequency regime. In this case, the domain wall represents a tunable half-wave rectifier as illustrated in Figure 5.11b.

5.5. Summary

We have shown that neutral domain walls in the hexagonal manganites ($R\mathrm{MnO}_3$) exhibit interesting functional properties. Their electronic transport behavior and its microscopic origin are substantially different from the charged domain walls (see Chapter 4). The electronic transport properties of the neutral walls are related to the conductivity of the bulk, i. e., increased domain-wall conductance is observed in insulating samples, whereas the transport scenario in samples with higher conductivity is 'hidden' by a Schottky barrier. One way to enable enhanced domain-wall currents is to adjust the bulk conductivity by thermal annealing.

Alternatively, the application of an AC voltage in the kHz/MHz-regime shortcuts the barrier and allows to access covered domain-wall properties. Plotting the characteristic frequencies versus sample conductivity reveals the existence of different transport regimes. The diagram provides the necessary information on how to enable domain-wall functionality by changing AC frequency or bulk conductivity, thus expanding the possibilities of domain-wall application into the realm of AC technology (e. g. half-wave rectification). From an experimental point of view the results are interesting for studying emergent domain-wall properties, bridging the frequency gap between conventional DC measurements and scanning microwave impedance microscopy[108,177,241].

6. Cathode-lens microscopy for domain-wall characterization

6.1. Motivation and state of the art

State-of-the-art scanning probe microscopy (SPM) is a powerful tool for the investigation of transport properties and correlation phenomena of ferroelectric domain walls as well as the characterization of functional nano-materials in general. It was due to SPM that the nanoscale physics of domain walls became accessible, which created a boost in the field[7]. The resolution of SPM, however, is ultimately limited by the probe size. For experiments where conductive coated tips have to be used, the best resolution up to now is about 20 nm[167,242]. Other challenges include the often unknown, inhomogeneous, and complicated probing field and the presence of surface potentials. Furthermore, acquisition times are in the range of minutes and longer, since SPM is a scanning technique. Thus, complementary imaging and characterization techniques are highly desirable to improve the understanding of emergent properties arising at domain walls.

A promising method is cathode-lens microscopy (CLM). CLM is a powerful technique in surface science and well established to characterize metals, semiconductors, and inorganic compounds. The basic principle of CLM is to measure reflected or emitted electrons spatially and energetically resolved, which provides access to surface potentials, band-structure, chemical information, magnetism, and other properties (see Ref. 207 for on overview). Further benefits of this contact-free technique are its high lateral resolution of up to 2 nm, its high surface sensitivity due to a probing depth smaller than 10 nm, and fast acquisition times down to $\sim$ 100 ms. Occasionally, CLM is also referred to as spectromicroscopy, as it yields spectroscopic and microscopic information simultaneously[189].

Two CLM techniques that have already been used to characterize ferroelectrics at the level of domains are photoemission electron microscopy (PEEM) and low-energy electron microscopy (LEEM). PEEM images photoelectrons, and LEEM images reflected or elastically backscattered electrons[189]. In the recent years, PEEM has, for instance, been applied to gain access to work-function differences at domains and polarization-induced changes in valence and core levels in ferroelectrics[243]. A combination of LEEM and PEEM was used to determine the thickness-dependent increase in polarization of ultra-thin multiferroic $BiFeO_3$ films[210]. Domain imaging with resolutions better than 15 nm were achieved by LEEM[244]. Moreover, LEEM allowed to examine the influence of adsorbates on the surface potential of domains[245] and to deterministically switch in-plane ferroelectric domains by an electron beam[246]. Yet, CLM studies that directly address electronic properties at the wall are scarce and first results have been published only recently[211,247].

In this study, we apply cathode-lens microscopy to investigate functional ferroelectric domain walls and demonstrate the potential of CLM beyond and complementary to SPM. As our model system we use hexagonal $\mathrm{ErMnO_3}$, because it exhibits neutral and charged domain walls in the as-grown state. Building up on our SPM studies presented in Chapters 4 and 5, opportunities and limits will be discussed.

The following part is divided into two sections. We successively present our results on domain-wall imaging and characterization with PEEM and LEEM, respectively. Experimental background and details on the two techniques are found in Section 3.2.

6.2. X-PEEM studies on hexagonal $\mathrm{ErMnO_3}$

Photoemission electron microscopy (PEEM) was performed on $\mathrm{ErMnO_3}$ with in-plane polarization (Sec. 6.2.1, 6.2.2), exhibiting neutral and charged domain walls (see also Chapters 4). PEEM on in-plane samples measures the local conductance contact-free with data acquisition times down to two seconds. The results presented in Sec. 6.2.1 have been published in Ref. 247.

6.2.1. Characterization of charged domain walls

For our X-PEEM studies on charged domain walls we use $\mathrm{ErMnO_3}$, oriented by Laue diffraction and cut into platelets with the spontaneous ferroelectric polarization ($P \parallel z$) lying in the surface plane (see Sec. 3.3.2). The prepared samples have lateral dimensions of about 4 mm and a thickness of 1 mm. The surface was chemo-mechanically polished to achieve a roughness of about 0.2 nm (RMS), analogous to the sample preparation for SPM (Sec. 3.3.3).

In Fig. 6.1a, we present the ferroelectric domain structure of our $\mathrm{ErMnO_3}$ sample, which was imaged measuring the lateral piezoresponse (LPFM) response under ambient conditions (Sec. 3.1.3). The PFM image reveals the typical $R\mathrm{MnO_3}$ domain pattern with its characteristic six-fold meeting points composed of alternating $+P$ and $-P$ domains[53,54]. To develop a coordinate system that allows for reproducibly finding certain surface positions, Pt-markers with a size of $10 \times 10\,\mu\mathrm{m}$ were designed using electron-beam lithography. The markers are visible in the upper and lower left corner of the PFM scan, as well as in the inset to Fig. 6.1a, which shows an enlarged PEEM image gained by illuminating the sample with an Hg-lamp (threshold PEEM).

Figure 6.1b shows a zoom-in to the ferroelectric domain structure in Fig. 6.1a (LPFM). The corresponding cAFM data is presented in Fig. 6.1c. This data set evidences that the $\mathrm{ErMnO_3}$ crystal exhibits the same electronic domain-wall properties as discussed in Section 4.1, i.e., insulating head-to-head and conducting tail-to-tail domain walls at $V_{\mathrm{DC}} = 4\,\mathrm{V}$. An X-PEEM image taken at the same sample position

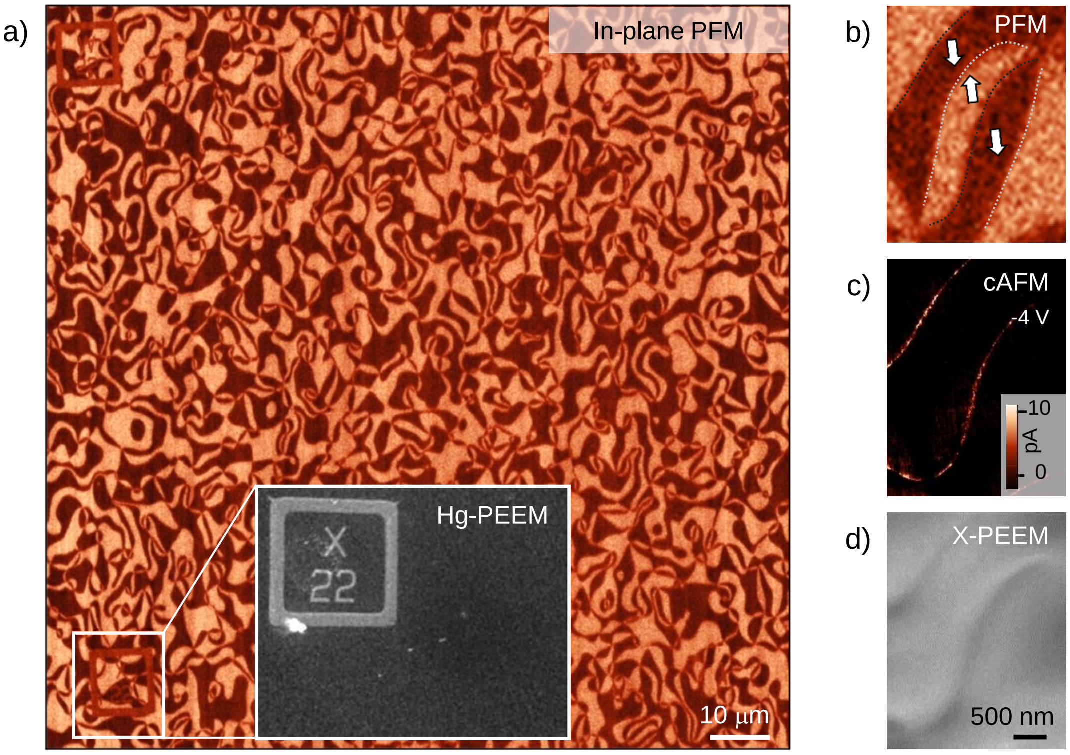

Figure 6.1.: Comparison of PFM, cAFM, and X-PEEM data on $ErMnO_3$. a) PFM image of the ferroelectric domain structure in $ErMnO_3$ with the spontaneous polarization lying in the plane. Pt-markers on the surface, as shown by the threshold PEEM (Hg lamp, $E = 4.9\,\mathrm{eV}$) image in the inset to (a), allowed for investigating the same sample position by different microscopy methods. b), c), and d) compare PFM, c-AFM, and X-PEEM data imaging the same area.

and photon energy of 641.5 eV (Mn L_3 edge) is shown in Fig. 6.1d. Here, two dark lines clearly distinguish from an otherwise homogeneously gray background. A comparison with the PFM and cAFM scans in Figs. 6.1b and c identifies these dark lines as electrically conducting tail-to-tail domain walls. In the X-PEEM data, however, only the tail-to-tail walls are visible, while insulating head-to-head domain walls are indistinguishable from domain areas.

To better understand the mechanism responsible for the obtained X-PEEM contrast, we perform additional measurements as summarized in Fig. 6.2. Figure 6.2a shows an X-PEEM image of a tail-to-tail wall (641.5 eV) taken with optimized contrast. Here, maximum brightness of domain areas was achieved by fine-tuning the sample voltage $V_a = -V_0 + V_{st}$, which accelerates emitted electrons so that primarily those from bulk regions can pass the microscopes energy filter ($V_0 = 15\,\mathrm{kV}$, $-10\,\mathrm{V} \leq V_{st} \leq 10\,\mathrm{V}$; see Sec. 3.2.1). We further find that the contrast was inverted when reducing the acceleration voltage as a comparison of Figs. 6.2a and b reveals. This behavior indicates that photo-excited electrons from domain-wall regions have a markedly higher kinetic energy, E_{kin}, than those from the bulk. In consequence, they are able to pass the energy filter even at reduced acceleration voltage, whereas pho-

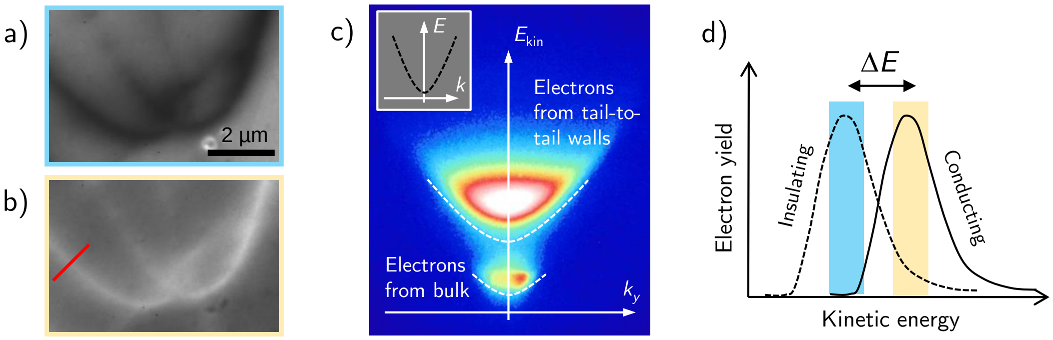

Figure 6.2.: Energy-dispersion from bulk and domain-wall electrons. a), b) X-PEEM images of tail-to-tail domain walls taken on $\mathrm{ErMnO_3}$ at a photon energy of 641.5 eV (Mn L_3 edge). Contrasts are inverted for the two images due to different analyzer settings of the microscope as sketched in (d). The red line in (b) corresponds to the evaluated cross section shown in Fig. 6.3a. c) Kinetic energy distribution of emitted photoelectrons when illuminating the sample with x-rays at 641.5 eV as seen in the dispersive plane of the microscope. High and low intensity levels are color-coded white and blue, respectively, and white dotted lines highlight the presence of two distinct parabolas in the (k_y, E_{kin}) plane. d) Schematic illustration of the energy distribution of photoelectrons emitted from insulating and conducting sample areas. Color-coded boxes indicate energy filter settings that yield contrasts as observed in (a) and (b).

toelectrons from the bulk are largely blocked leading to the bright walls in Fig. 6.2b. The difference in E_{kin} can directly be seen in the dispersive plane of the microscope as shown in Fig. 6.2c[191].

Figure 6.2c provides insight to the photoelectron distribution in k-space when illuminating the sample with x-rays at an energy of 641.5 eV. The two-dimensional plot displays a projection of the photoelectron distribution onto the dispersive (k_y, E_{kin}) plane, $\mathrm{I}(k_y, E_{\mathrm{kin}})$, for a single k_x with the latter being selected by the energy filter settings[191] as explained in Sec. 3.2.1. A typical distribution is limited by a parabola due to the $E_{\mathrm{kin}}^{1/2}$-dependence of the size of the Ewald sphere as sketched in the inset to Fig. 6.2c. In the present case, however, two parabolas are clearly distinguishable with the low-energy parabola being associated to electrons emitted from the bulk. The corresponding electron energy distribution is sketched in Fig. 6.2d, where we illustrate the electron yield as function of energy[248]. Depending on the energy-filter settings (indicated by the two colored bars) either bulk or domain-wall photoelectrons can pass which explains the energy contrasts in Figs. 6.2a and b, respectively.

In order to quantify the observed difference in kinetic energy ΔE_{kin} (Fig. 6.2d), we measured the electron yield as function of the so-called start energy V_{st} and analyzed local intensity variations. The result gained for the domain-wall cross-section marked in Fig. 6.2b is presented in Fig. 6.3a, where we plot the secondary electron yield against position and V_{st}. The three-dimensional plot reveals that the electron-energy distribution at the domain wall is shifted towards higher energies with $\Delta E_{\mathrm{kin}} \approx 1\,\mathrm{eV}$. This shift is also evident in the associated projection onto the xy-plane showing lines of equal intensity.

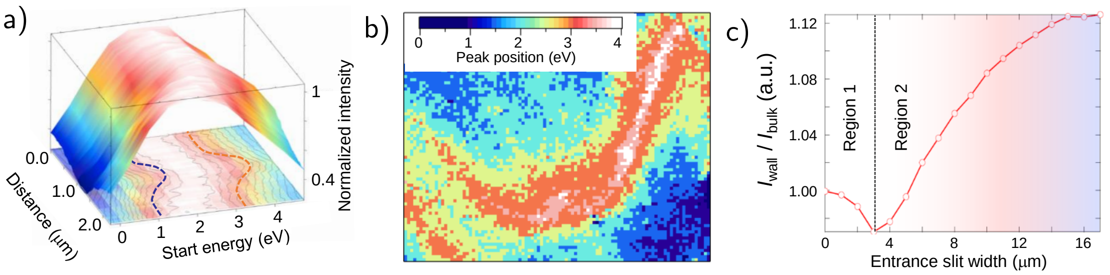

Figure 6.3.: X-PEEM conductance map of ErMnO$_3$. a) Evolution of the photoelectron energy distribution along the domain-wall cross-section marked red in Fig. 6.2b. At the position of the domain wall the energy distribution is shifted towards higher energies by about 1 eV. b) Conductance map derived from the X-PEEM data shown in Fig. 6.2a. The color code reflects the peak position of the photoelectron distribution in eV as shown in the inset to (b). c) Dependence between domain-wall contrasts and x-ray intensity.

A complete photoelectron-energy map for the domain walls in Figs. 6.2a and b is depicted in Fig. 6.3b. The map presents the peak position E_{peak} of the energy distribution (averaged over 2×2 pixels) with higher energy values corresponding to faster electrons (see Sec. 3.2.1). In addition to the above discussed difference between domain-wall and bulk regions, the spatially resolved data uncovers a correlation between ΔE and the domain-wall orientation. The latter is reminiscent of the orientation-dependent electronic conductance observed by cAFM (Sec. 4.1) and suggests a connection between the domain-wall transport properties and the emergent energy contrasts in X-PEEM, which we will discuss in the following.

The illumination with intense x-rays leads to photoexcitation of charge carriers (electrons). In case of an insulating or poorly conducting ferroelectric, like the ErMnO$_3$ test system, the bulk material cannot compensate for the emitted photoelectrons and hence gets positively charged. Due to the positive charging photoelectrons get slowed down and the associated energy distribution shifts to lower energies. At the tail-to-tail walls, however, charging effects are largely suppressed because of the locally enhanced conduction properties that allow compensating for the photoinduced charging. This difference in electronic transport can explain the presence of two maxima in the energy distribution and resulting contrasts, as well as the angular dependence evident in Fig. 6.3b. Thus, we conclude that photo-induced charging is responsible for the X-PEEM contrast at the conducting tail-to-tail domain walls.

We note that domain-wall contrasts only occur at the Mn L$_3$ edge, where the absorption coefficient is high and a large number of photoelectrons are emitted. No difference between bulk and tail-to-tail domain walls is observed at lower x-ray energies, i. e., below the Mn L$_3$ edge. Work function differences as possible explanation can be excluded, as no domain-wall contrasts are observed in threshold PEEM using the radiation of a mercury lamp (see Sec. 3.2.1 and inset to Fig. 6.1a). The missing differences in work functions between tail-to-tail wall and bulk supports our statements on the SPM measurements, that is, cAFM on ErMnO$_3$ reveals bulk-influenced (intrinsic) changes in the conductance of domain walls, which are unrelated to local variations in the barrier (see Secs. 4.1.3, 4.3.1).

To further support the conclusion that the observed X-PEEM contrasts emerge due to photo-induced charging effects, we performed imaging experiments with variable synchrotron beam intensity. For this experiment, the beam intensity and profile width were controlled by changing the width of the entrance slit that x-rays pass before reaching the experiment. The result is presented in Fig. 6.3c and shows a striking dependence of the domain-wall contrast, $\frac{I_{\text{wall}}}{I_{\text{bulk}}}$, on the synchrotron intensity which is in tune with the above interpretation of the X-PEEM contrasts: At low intensity (region 1), the electron yield in bulk areas is higher compared to the tail-to-tail walls because mobile holes accumulate at this type of domain wall and hence electrons that may be emitted are rare. At higher intensity (region 2), however, the sample drastically charges positively so that local differences in conductance dominate the X-PEEM contrast leading to a crossover from $\frac{I_{\text{wall}}}{I_{\text{bulk}}} < 1$ to $\frac{I_{\text{wall}}}{I_{\text{bulk}}} > 1$. The intensity-dependent measurement highlights that domain-wall contrasts can be improved using a higher x-ray intensity. Vice versa, unwanted charging effects can be largely suppressed by limiting the beam intensity for, e.g., recording reliable domain-wall spectra after detecting its position (see Ref. 231).

6.2.2. Temperature-dependent conductance mapping

In the previous section, we demonstrated that photon-induced charging effects can be exploited to image domain walls by X-PEEM. Next, we will use this effect to gain additional insight to the local conductance properties by performing X-PEEM experiments as function of temperature.

For our temperature-dependent X-PEEM study, we focus on the hole-doped compound $\mathrm{Er}_{1-x}\mathrm{Ca}_x\mathrm{MnO}_3$ ($x = 0.01$) oriented in a way that the polarization lies parallel to the surface. Prior to measurement, the sample was chemo-mechanical polished to achieve a roughness of 2 nm (RMS), minimizing defocussing effects provoked by topography (details in Sec. 3.3.3). To enable direct comparison of our X-PEEM data with ex-situ SPM measurements, we patterned the surface of the sample with Pt-markers by e-beam lithography. We begin our experiments by performing X-PEEM at room temperature. After measuring an x-ray absorption spectrum, the photon energy was adjusted to the Mn L_3 edge at 643.2 eV to achieve beam-induced surface charging[247] (see previous section for details). In contrast to undoped ErMnO_3, $\mathrm{Er}_{1-x}\mathrm{Ca}_x\mathrm{MnO}_3$ with $x = 0.01$ was found to exhibit no domain-wall contrasts at room temperature, even for the highest beam intensity (fully opened entrance slit). The absence of domain-wall contrasts is expected due to the higher conductance (see also Sec. 4.2.2), which suppresses x-ray induced surface charging.

Next, we cooled the sample down to the minimum accessible temperature of about 160 K. After stabilization of the temperature, we optimized the energy of the x-rays to 643.1 eV to compensate for shifts in the Mn L_3 edge. The recorded X-PEEM image presented in Figure 6.4a reveals clear dark and bright contrasts, which were not observed at room temperature under the same imaging conditions. Due

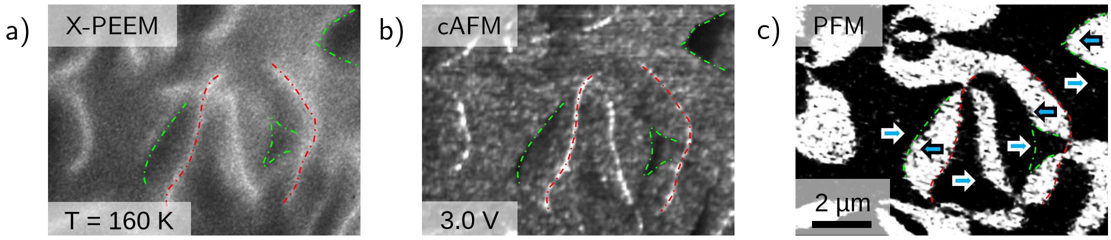

Figure 6.4.: X-PEEM contrasts at 160 K compared with cAFM and PFM. a) X-PEEM image taken with dark and bright contrasts arising at head-to-head (→←) and tail-to-tail (←→) domain walls, respectively. b) cAFM scan at $V_{\mathrm{BV}} = 3.0\,\mathrm{V}$ of the same position reveals how insulating and conductive regions coincide with the dark and bright contrasts observed in (a). c) PFM scan showing domains pointing to the right (dark) and to the left (bright). Green and red-dashed lines highlight head-to-head and tail-to-tail domain-wall positions determined from PFM, respectively.

to the semiconducting properties of the hexagonal manganite (RMnO$_3$)[137], the lower temperature reduces the conductivity of our sample and thus provokes beam-induced charging. Comparison with conductive atomic force microscopy (cAFM) and piezoresponse force microscopy (PFM) measurements taken at the same position reveals that dark and bright contrasts in X-PEEM arise in the vicinity of insulating head-to-head (→←) and conducting tail-to-tail (←→) domain walls, respectively (Figs. 6.4b and c; wall positions indicated by colored lines). Note that only one type of domain wall was detected on ErMnO$_3$ at room temperature (Sec. 6.2.1), possibly due to differently pronounced surface charging.

After optimizing the desired imaging conditions, we analyze the shifts in kinetic energy of the electrons emitted from bulk, head-to-head, and tail-to-tail domain walls by measuring the electron yield as function of start energy V_{st} along the cross-section indicated in Figure 6.5a. The energy-dependent electron yield is normalized and shown as function of position as a contour-plot in Fig. 6.5b. Maxima of the electron distributions (light blue contrast) show distinct shifts in energy when a domain wall is crossed. With respect to the average bulk value, the electron distributions of head-to-head and tail-to-tail walls shift towards lower and higher energy values, respectively (highlighted in (b) by the green and red dashed lines). The hierarchy in shifts corroborates the emergence of charging induced domain-wall contrasts: At insulating regions, the x-ray induced positive surface charging is increased, which leads to deceleration and hence lower kinetic energies of the electrons. In Figure 6.5c we show the energy-dependent electron yield for both the head-to-head and tail-to-tail domain walls indicated by the respective green and red dots on the dashed line in Fig. 6.5a. Along this profile we determine an energy shift of $2.3 \pm 0.2\,\mathrm{eV}$ between the two domain walls.

In order to quantify the evolution of our charging contrasts as function of temperature, we measure the spatial energy-distributions of photoelectrons at a single location for four different temperatures. Fitting of the secondary electron distributions results in the kinetic-energy maps that are presented in Fig. 6.6 (procedure given in Sec. 3.2.1). At 160 K strong energy-shifts can be distinguished, which cor-

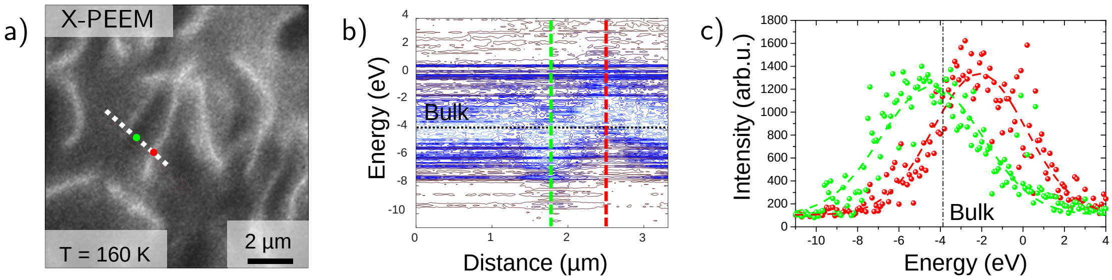

Figure 6.5.: Shift of E_{kin} at head-to-head and tail-to-tail domain walls. a) X-PEEM image revealing dark and bright contrasts caused by head-to-head and tail-to-tail domain walls. b) Start-energy dependence of the normalized electron intensity as function of position along the white-dashed line marked in (a). Gray and light-blue values correspond to low and high intensity, respectively. The maxima of the distributions show a clear shift depending on position reaching lowest and highest values for head-to-head (green-dashed line, in (a)) and tail-to-tail domain walls (red-dashed line). Respective spatial domain-wall positions are marked in (a) by a green and a red dot. The black-dashed line indicates average kinetic energy of the bulk. c) Electron yield as function of start energy V_{st} plotted for head-to-head (→←) and tail-to-tail (←→) wall showing a shift of $\Delta E = 2.3 \pm 0.2\,\mathrm{eV}$. Energy shift is determined from the maxima E_{peak} of the fitted Gaussian functions. Average kinetic energy of electrons emitted from the bulk as indicated by the black dashed line.

relate with position and conductance properties of the charged domain walls, i. e. reduced and increased kinetic energies in the vicinity of insulating head-to-head and conductive tail-to-tail walls, respectively (comp. the fitted energy distributions in Figure 6.5c). Upon increasing temperature the beam-induced energy contrasts weaken until at 181 K only head-to-head walls (blue) provide detectable contrasts.

This decrease in contrast can be explained as follows. Over the whole series of images the x-ray intensity was maintained constant causing a finite probability to emit electrons. The resulting electric field at the surface of the sample depends on the equilibrium between x-ray emitted electrons and the conductivity of the sample. As the latter changes with temperature, the energy-maps in Fig. 6.6 correlate with the local transport properties and can hence be considered as two-dimensional conductance maps. Due to the unknown exact photo-induced current, however, these maps only give relative differences in conductance. The temperature dependence furthermore corroborates the proposed contrast mechanism, i. e., spatial variations in photo-induced surface charging due to variations in the nanoscopic conductance. In order to exclude beam-induced surface damage as cause for the vanishing domain-wall contrasts, we perform subsequent measurements at 160 K. The results reveal the same contrast as before, thus excluding beam-induced damage.

For a more detailed insight into the relative energy shifts between domain walls and bulk, we analyze the determined E_{peak} in the electron distribution along a domain-wall cross-section more closely. The data shown in Figure 6.7a reflect the reduced and increased domain wall energies with respect to the bulk as indicated by the green and red bar for respective head-to-head and tail-to-tail walls (The small peak to the left of the insulating wall at $T = 160\,\mathrm{K}$ is probably attributed to charge-

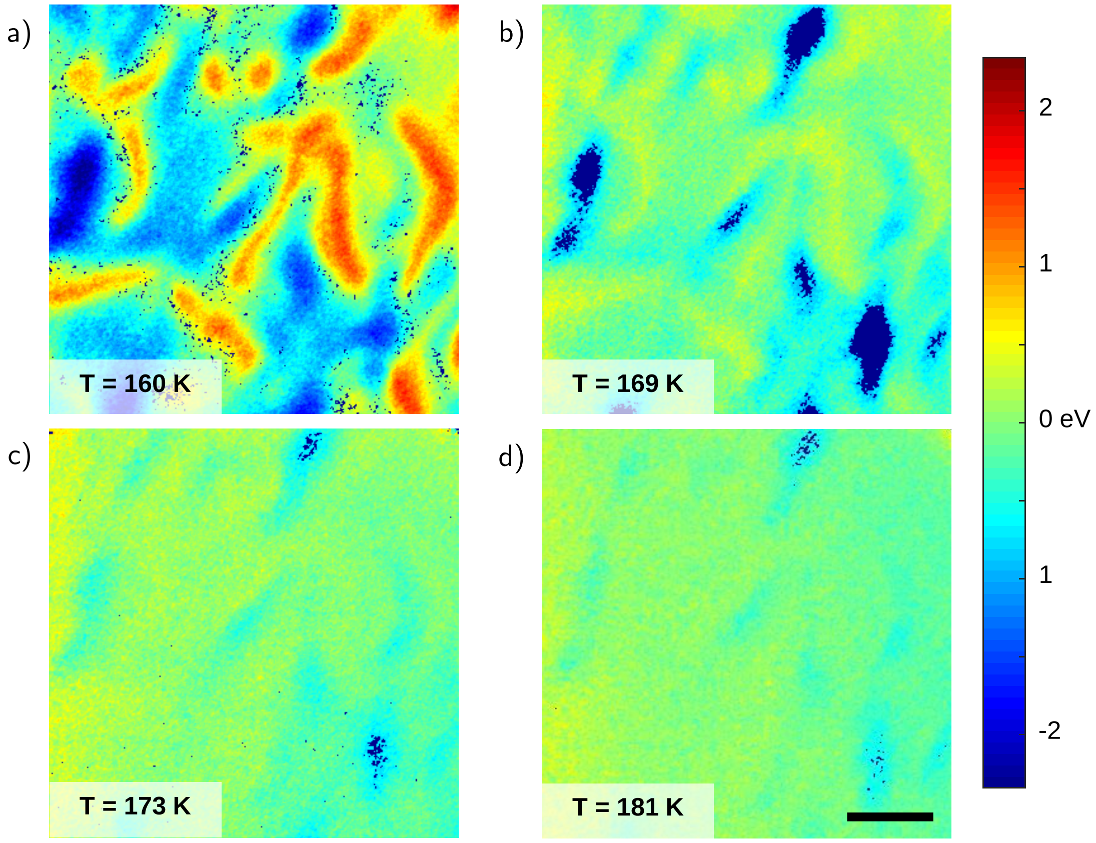

Figure 6.6.: Contact-free conductance mapping as function of temperature. a) to d) Spatial distribution of the photoelectron energy at different temperatures. At 160 K (a) contrasts attributed to the differences in conductance of both head-to-head and tail-to-tail domain walls can be seen. Increasing the temperature reduces features and energy-spread of the charging-induced contrast; contrasts from insulating head-to-head walls (blue) remain visible up to 181 K (d). Maps are derived by extracting the energy-distribution at each pixel from a series of energy-dependent images and fitting by Gaussian functions. The plotted values correspond to the maxima value E_{peak} taken from the fit. Color scheme on the right is the same for all graphs for comparative reason. Since the energy filter was not calibrated by reference measurements (see Sec. 3.2.1), we take the positions of the Gaussian fits to the histograms of each map as zero level of the energy scale. The scale bar is 2 µm and applies to all images.

induced defocusing effects). From these curves we derive the average bulk energy (black dashed line) and peak domain-wall energies, which we show in Figure 6.7 as function of temperature. The graph illustrates how changing the temperature allows to manipulate the resulting X-PEEM contrasts. Predominantly head-to-head walls are imaged in the range from $165\,\mathrm{K} \lesssim T \lesssim 180\,\mathrm{K}$. For lower temperatures contrast from the head-to-head wall dominate.

On a closer inspection, one can see that the temperature evolution of tail-to-tail and head-to-head contrasts are not symmetric and follow different trends (Figure 6.7b). The earlier observation of head-to-head walls upon cooling can be attributed to the reduced capacity of this insulating structure to compensate for

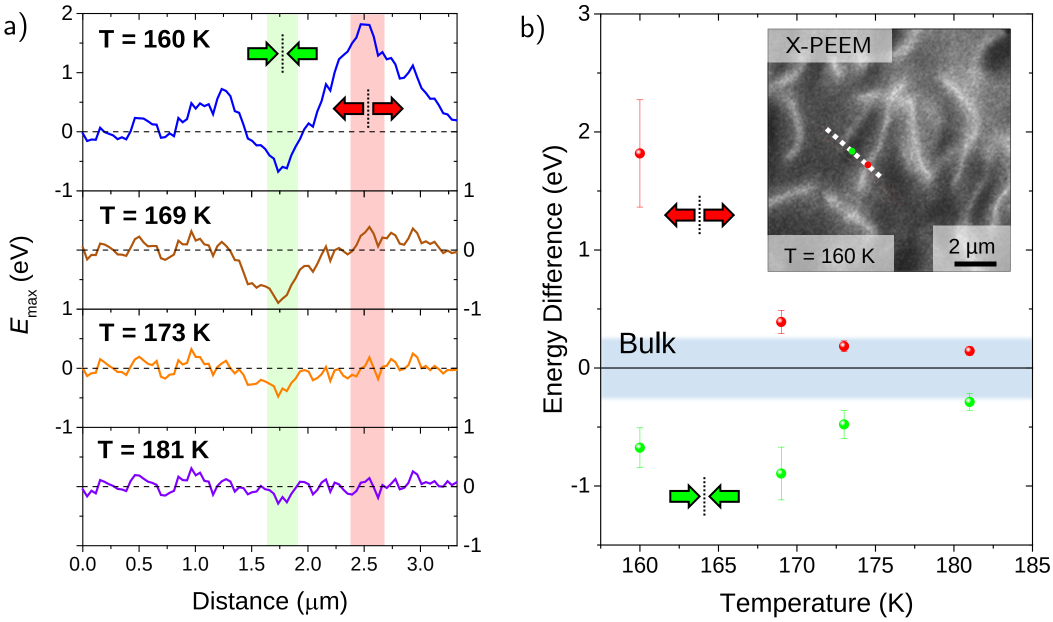

Figure 6.7.: Controlling X-PEEM contrasts via temperature. a) Energy profile of photoelectrons along the white-dashed line marked on the inset to (b). Features attributed to tail-to-tail (←→) domain walls vanish before those of the head-to-head (→←) wall with increasing temperature. The domain-wall widths are in the range of several 100 nm. The green and red bars indicate positions of head-to-head wall and tail-to-tail wall, respectively. Equal energy scaling in all graphs for comparative reason. b) Adjusting imaging conditions by temperature enables to detect head-to-head walls only ($T = 173\,\mathrm{K}; 181\,\mathrm{K}$), both walls ($T = 169\,\mathrm{K}$), and predominantly tail-to-tail walls ($T = 160\,\mathrm{K}$). Values of the domain walls are derived from the maxima / minima of the line-plots in (a) and subtracted from the average bulk energy. The latter is the average energy between position 0 and 1.0 µm on the distance axis. The gray bar indicates noise in the bulk energy.

beam-emitted electrons. With decreasing temperature the head-to-head wall contrast increases before it seems to weaken again at 160 K. This could be a hint that upon further cooling photo-induced charging gets equal for bulk- and head-to-head wall, leading to similar kinetic energies of the emitted electrons. Finally, only the conductive tail-to-tail would be observable, as it is the case in the X-PEEM studies performed on undoped ErMnO$_3$ at room temperature (Sec. 6.2.1). The tail-to-tail wall gets only distinct from the bulk at temperatures $\leq 169\,\mathrm{K}$ (gray bar represents noise in bulk energy). Upon cooling the contrast difference to the bulk increases more strongly than for the head-to-head wall, which can be attributed to the better transport properties of the former.

In summary, we showed that conducting domain walls in a ferroelectric bulk material can be visualized using high-resolution X-PEEM. By performing intensity- and temperature-dependent measurements, we demonstrated that the emergent contrasts base on photo-induced charging effects caused by intense x-ray illumination. The charging contrast, in its turn, is determined by the local conductivity at the domain wall. Controlling the conductivity of the samples by temperature allows to adjust the X-PEEM imaging conditions to be sensitive to either insulating or conductive walls. The X-PEEM method offers data acquisition times for imaging in the order of 0.1–10 s, which is significantly faster compared to conventional SPM scans. Moreover, domain-wall related anomalies and subtle variations in electronic conductance can be detected contact-free and hence without contributions from contact resistance by analyzing the energy distribution of photo-excited electrons. The demonstrated ability of X-PEEM to directly probe domain walls opens the door for element-specific investigations that can provide access to ferroelectric domain-wall properties such as chemical structure, local valence states, and symmetry violations.

6.3. LEEM studies on domain walls

Low-energy electron microscopy is a CLM method that bases on reflected and backscattered electrons[189] as explained in Section 3.2.2. LEEM is sensitive to local variations in the surface potential, band structure, conductivity, or density of states[207,249] with spatial resolutions down to 2 nm. Thus, LEEM presents a promising tool for investigating local electronic domain-wall phenomena, beyond the resolution limit of PEEM and SPM. Here, we apply LEEM to scrutinize neutral (Sec. 6.3.1) and charged domain walls (Sec. 6.3.2) in $ErMnO_3$, the same model system we investigated by SPM (Chapters 4 and 5) and PEEM (Sec. 6.2), and discuss new opportunities and limitations of this technique.

6.3.1. Imaging of neutral domain walls

We begin our analysis with the neutral domain walls on an out-of-plane oriented $ErMnO_3$ crystal, at which we observed increased domain-wall conductance (see Sec. 5.1). First, we perform energy-dependent reflectivity measurements to reveal the associated surface potentials. At low kinetic electron energies, i. e., small V_{st}, all electrons are reflected before reaching the sample surface (MEM mode) and a homogeneous intensity distribution is obtained in the detected images (not shown). At higher energy (LEEM mode), the incident electrons overcome the sample vacuum potential leading to a transition from reflection to backscattering that causes a drop in electron reflectivity (see Sec. 3.2.2).

At electron energies around the MEM-to-LEEM transition, the $+P$ and $-P$ domains have markedly different reflectivity, so the measured reflected electron count yields directly domain images with a resolution of $\sim$ 5 nm. Figure 6.8a shows the corresponding spatially resolved LEEM image. The characteristic ferroelectric $+P$ and $-P$ domains merging in a six-fold meeting point[53,54] are clearly visible resulting from the different electrostatic surface potentials of opposite domain states[189]. In addition to this spatial imaging mode, the energy at which the MEM-LEEM transition occurs above the surface of the $+P$ and $-P$ domains yield quantitative information about the difference in surface potentials. We obtain a difference in surface potentials between the two domains of $\Delta E = 0.3 \pm 0.1$ eV, which is of the

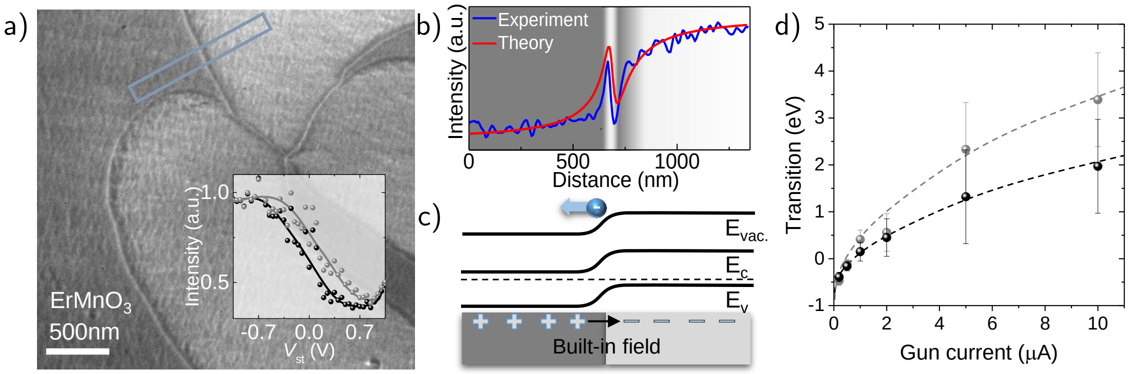

Figure 6.8.: Imaging ferroelectric domains with LEEM. a) LEEM image taken on z-cut $ErMnO_3$ with V_{st} set to the mean energy value of the MEM-to-LEEM transition (0 eV) as indicated on the inset. The ferroelectric domains merge in characteristic six-fold meeting points, but the contrast change between bright and dark domains with different polarization is nontrivial. Inset: The black and gray data reflect different MEM-LEEM transition energies at the surfaces of domains showing dark and bright contrast, respectively. Solid lines are guides to the eye. b) Line plot showing the averaged intensity (blue line) measured along the cross section marked in blue in (a). The red solid line is the result of the phenomenological model explained in the text. c) Schematic of the surface band bending across a domain wall. Due to the different surface potentials of the domains backscattered electrons feel an in-plane electric field that leads to lateral deflection and bends their trajectories (see text). d) MEM-LEEM transitions of the bright (gray) and dark domains (black) as function of electron-gun current. Energy of the transitions rise with in increasing gun current together with the potential difference between the two domains. Dashed lines are guides to the eye.

same order of magnitude as earlier estimations for the potential difference between $+P/-P$ made on the basis of local conductance data[92]. We omit here to assign the bright and dark domains to the $-P$ and $+P$ state, since we do not have a comparative PFM scan at the same position. Adsorbates and surface charging due to limited sample conductivity can alter the usually observed behavior, i. e., $+P$ domains showing MEM-LEEM transitions at lower energies[189].

On a close inspection, the spatially resolved reflectivity shows an alternating contrast at the neutral domain walls between the oppositely polarized domains (Fig. 6.8a and b). In collaboration with Andres Cano at the University of Bordeaux, we calculate the lateral distribution of backscattered electrons, and find, however, that this feature is consistent with the measured step in the surface potential. The surface-potential step causes a local in-plane electric field at the domain wall (schematic in Fig. 6.8c) that bends the trajectories of backscattered electrons. Following Nepijko et al.[213], the LEEM distribution of current at the LEEM detector screen can be written as

$$j(x + S(x)) = \frac{j_0(x)}{1 + S'(x)}, \tag{6.1}$$

where $j_0(x)$ is the zero-order distribution, in which local fields are ignored, $S(x)$ is the shift of the LEEM object point x due to the local field, and $S'(x)$ its derivative. Since the width of the neutral domain walls is almost zero (see Refs. 125, 132, and

Fig. 2.7a), the local in-plane field takes the simple form $\mathcal{E}_{\mathrm{loc}}(x) = -\phi_0\delta(x - x_0)$, giving

$$S(x) = -\frac{\phi_0}{\pi\mathcal{E}} \ln\left(1 + \frac{l^2}{(x - x_0)^2}\right). \tag{6.2}$$

Here $\mathcal{E}$ and l are the effective LEEM accelerating field and the effective distance between the LEEM anode and the sample surface, whereas ϕ_0 determines the strength of the local potentials.

We show the intensity change across neutral domain walls obtained from this analytical expression for the LEEM current j as the red curve in Fig. 6.8b. We see that it corresponds closely to the experimental data (blue curve), in particular reproducing the unusual bright-dark feature observed at the domain wall. We conclude, therefore, that the potential landscape probed by LEEM in the vicinity of a neutral domain wall is determined by the difference in surface potential from the adjacent domains, with no anomalous electrostatics or conductance features at the domain wall contributing to the response. This is in agreement with studies characterizing surface potentials of $\mathrm{LiNbO_3}$ revealing in-plane fields at neutral domain walls[211].

Thus, LEEM can provide information about the position of the neutral domain walls. Their intrinsic electronic properties, however, are not accessible, with potential differences between $\pm P$ domains governing the LEEM data. To understand this potential difference and its relation to the properties of the underlying bulk, we perform LEEM as function of the electron-gun current I_{gun} (dose-dependent). As we showed in Ref. 249, dose-dependent LEEM allows to identify conductivity-related signals, revealing the presence of multiple / coexisting LEEM contributions.

Figure 6.8d shows the determined MEM-LEEM transitions of domains, which are negatively (gray) and positively charged (black) at the surface. The data show that the transition energies of both domains rise non-linearly for increasing gun currents and that the difference in contact potential between the domains increases, too. Taking into account that dose-dependent LEEM is co-determined by inverse $I(V)$ characteristics[249], Fig. 6.8d suggests a non-linear conduction mechanism. At present, however, the interaction of low-energy electrons with oxide surfaces is not fully understood and coherent models are yet to be derived. It is important to note, though, that LEEM does not simply couple to surface potentials, as assumed earlier, but represents a convolution of at least two contributions for the case of out-of-plane $\mathrm{ErMnO_3}$, including variations of local transport properties and surface potentials. The latter impedes the access to neutral domain walls on polar surfaces, adding a new degree of complexity to the analysis of LEEM.

In summary, we could demonstrate that LEEM can be used to image domains and analyze domain-wall signatures of a semiconducting ferroelectric. The domain-wall signatures, however, are attributed to in-plane fields caused by the adjacent domains, and not to local changes in electronic conductance. The surface potential between the domains and thus the in-plane field strongly depend on the gun emission, which obscures quantitative analysis of the unperturbed surface potential between the domains. The dose-dependence furthermore points towards a fully compensated out-of-plane surface, as barely any contrast is observed at a dose of 0.1 µA. This leaves the question to which extent LEEM is capable to determine the real surface potentials of semiconducting ferroelectrics, since it is strongly depending on the screening scenario and the surface-induced charging provoked by the electron-gun current.

6.3.2. Highly-resolved charged domain walls

We now turn to the charged domain walls that are observable on samples with in-plane polarization. In this case, no potential differences exist between the $\pm P$ domains. Representative PFM and cAFM images for this configuration reveal insulating head-to-head (→←) and conductive tail-to-tail (←→) domain walls (Figure 6.9a and b) as discussed in Sec. 4.1.1.

We begin by performing LEEM-reflectivity measurements as function of energy with standard microscope settings ($I_{\text{gun}} = 2.0\,\mu\text{A}$ and a focus slightly above the surface, 'overfocused'). Figure 6.9c presents the reflectivity values of the bulk and domain walls as function of energy, revealing a step-like decrease that corresponds to the mirror-electron to low-energy electron microscopy (MEM-LEEM) transition. We observe the following sequence in MEM-LEEM transition energies: $E_{\rightarrow\leftarrow} < E_{\text{bulk}} < E_{\leftarrow\rightarrow}$. Figure 6.9d shows corresponding LEEM images at different start energies V_{st}. At low start energy both domain walls appear as faint bright contrasts (MEM mode). At higher energy ($-2.75\,\text{eV}$), we observe two distinct domain-wall contrasts (bright and dark), which get more pronounced with increasing start energy ($-2.4\,\text{eV}$). The dark and bright domain walls correspond to the head-to-head and tail-to-tail configurations, respectively.

The data reveal that LEEM is clearly sensitive to differences in local electronic structure and properties. Similar to out-of-plane ErMnO_3, however, the microscopic origin / interaction that leads to the observed MEM-LEEM transitions is unclear. In this case, a combination of intrinsic (conductance, potential) and extrinsic (focus) effects determine the imaging.

To evaluate the role of conductivity-related contributions, we measure the MEM-LEEM transitions as function of electron dose. Figure 6.10a presents the results, where blue and gray data points indicate the MEM-LEEM transitions energies of head-to-head and tail-to-tail walls, respectively, whereas the black data points correspond to the transitions of the bulk. The dose-dependent data show that the transition energies shift towards higher values with increasing gun current, and that over the whole voltage range the sequence in transitions ($E_{\rightarrow\leftarrow} < E_{\text{bulk}} < E_{\leftarrow\rightarrow}$) remains the same as observed in Fig. 6.9c. Apparently, the signal obtained at the walls follow the same trend as the signal obtained in the bulk, with increasing energy differences ΔE for increasing gun current I_{gun}. This is consistent with the results obtained on out-of-plane ErMnO_3 (Sec. 6.3.1) and SrMnO_3[249]. The effect on the MEM-LEEM transition by the gun current is shown by the two reflectivity maps in Figure 6.10b and c, revealing stronger contrasts (potential differences) and wider domain-wall features with increasing dose I_{gun}.

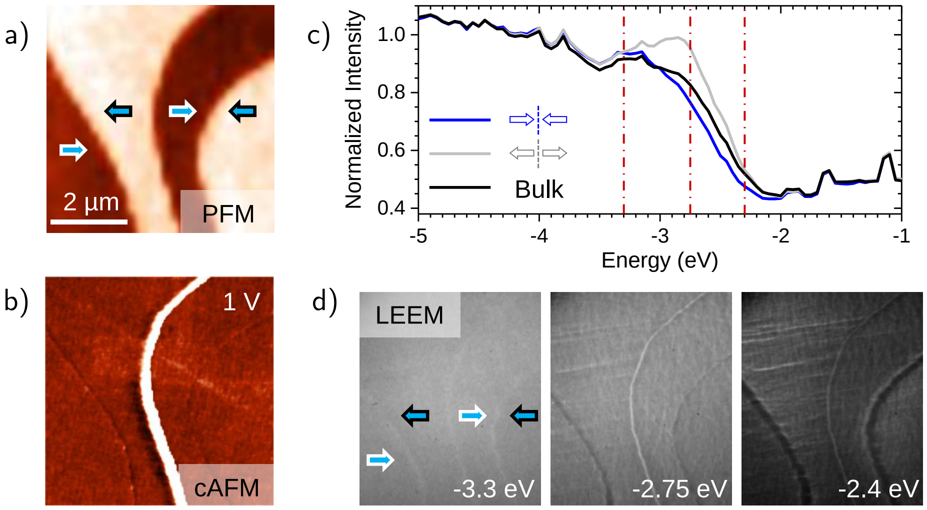

Figure 6.9.: LEEM reflectivity at charged domain walls. a), b) PFM and cAFM scans of an in-plane oriented ErMnO$_3$ sample identifying conductive tail-to-tail (←→) and head-to-head (→←) walls. c) Reflectivity measurement as function of energy at the same position. MEM-LEEM transitions of head-to-head and tail-to-tail domain walls happen at lower and higher energy compared to the bulk. d) LEEM images as function of start energy showing how domain-wall contrasts develop over the MEM-LEEM transition as indicated by the red-dashed lines in (c).

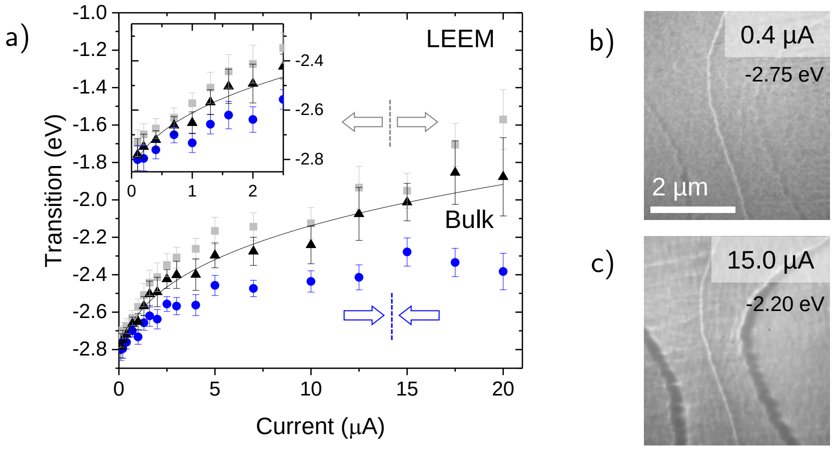

Figure 6.10.: MEM-LEEM transitions of domain walls as function of I_{gun}. a) Dose-dependence of MEM-LEEM transitions of bulk (black), head-to-head (→←, blue) and tail-to-tail domain walls (←→, gray). The transitions shift to higher values and apart from each other with increasing gun current. Sequence in transition energy remains the same over the investigated current range ($E_{\rightarrow\leftarrow} < E_{\text{bulk}} < E_{\leftarrow\rightarrow}$). Inset shows transitions values at low I_{gun}. b), c) show reflectivity maps at low and high gun-current, respectively.

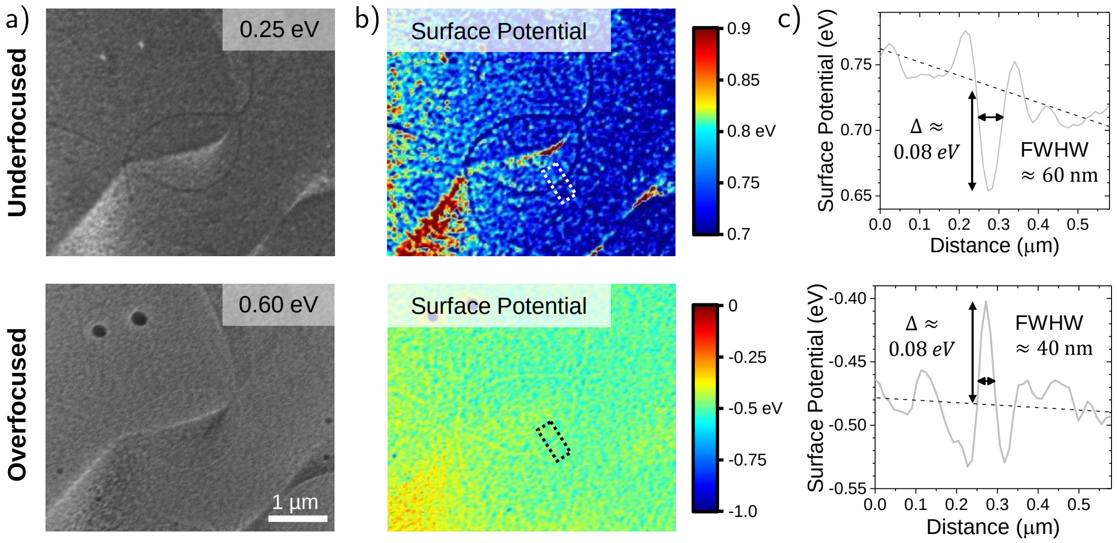

Figure 6.11.: Focus-dependence of MEM-LEEM transitions at charged walls. Underfocusing and overfocusing conditions correspond to upper and lower row, respectively. a) LEEM images of $Er_{1-x}Ca_xMnO_3$ ($x = 0.002$) showing how focus settings invert the contrast. b) Surface-potential maps from the locations in (a) revealing inversion of the wall-potentials with respect to bulk. c) Surface-potential profile of the tail-to-tail wall as indicated in (b).

Aside from the gun current, focus effects are found to play an important role as also discussed in Ref. 211. Such focus effects co-determine the measured values in energy difference ΔE adding yet another degree of complexity that requires adequate control. In order to study focus-related effects at charged walls and reduce imaging artifacts stemming from strong surface charging, we switch to $Er_{1-x}Ca_xMnO_3$ with $x = 0.002$, which shows increased bulk conductance (see Sec. 4.2.2). Fig. 6.11a presents clear LEEM images with pronounced domain-wall contrasts. Again, we observe two domain-wall contrasts: one sharp that corresponds to a conductive tail-to-tail wall and one rather blurred line corresponding to an insulating head-to-head wall. We note that the blurred domain-wall signal can be attributed to the domain-wall propagation into the depth of the sample, which is similar to the observations made in SPM (see Figs. 4.1a and b).

The derived surface potential maps in Fig. 6.11b demonstrate that the domain-wall potentials get inverted by changing the focus value. This is in agreement with the observations made on neutral domain walls[211]. Furthermore, it explains the sequence of MEM-LEEM transition energies observed in Figure 6.10a. To explore this further we look at profiles crossing a tail-to-tail wall as indicated in Fig. 6.11b. The derived profiles in Figure 6.11c show that the differences between the bulk and the wall potential are the same $\Delta E \approx 0.08\,\mathrm{eV}$, but their signs differ. The domain-wall widths, estimated by the full width at half maximum (FWHM), are slightly different and lie between 40 and 60 nm. These values are in reasonable agreement with the widths determined by cAFM in Fig. 4.10a.

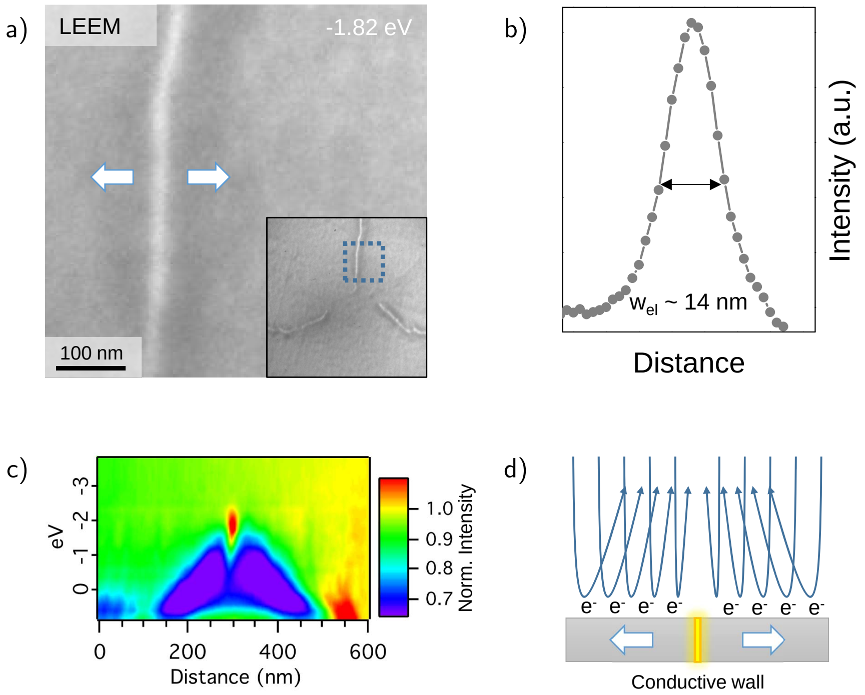

Figure 6.12.: Resolution limit for domain-wall imaging with LEEM. a) High-resolution LEEM-image of a conductive tail-to-tail (←→) wall at a start energy of −1.82 eV. Energy corresponds to setting, where only tail-to-tail walls contribute to image as shown by the inset revealing a vortex. b) Cross-section of the domain wall presented in (a) showing a domain-wall width w of 14 nm, that is the best resolution we achieved. c) Start-energy dependence of the domain-wall contrast. High intensity and sharp domain-profiles are achieved around −2 eV. Color code represents normalized intensity. d) Schematic explanation how electron-beam-induced surface charging leads to bending of electron trajectories around conductive tail-to-tail domain walls.

In LEEM, however, the focus can be optimized further, which is not possible in tip-limited SPM studies. Figure 6.12a shows a highly-resolved tail-to-tail domain wall taken on an $\mathrm{ErMnO_3}$ sample with in-plane polarization, analogous to Fig 6.9. Here, the focus-value was optimized to have the MEM-LEEM transition of tail-to-tail walls at lower energies (see vortex structure and zoom location on inset; no head-to-head walls are visible). The domain wall shows a sharp bright contrast with some slightly dark corona reminiscent of the domain-wall profiles in Fig. 6.11c. The cross-section in Fig. 6.12b reveals the actual domain-wall profile with a width of $w = 14\,\mathrm{nm}$, i. e., about two times thinner than the best resolution we achieved in cAFM (Sec. 4.4, $w \sim 35\,\mathrm{nm}$ for $\mathrm{Er}_{1-x}\mathrm{Zr}_x\mathrm{MnO}_3$, $x = 0.01$).

The observed domain-wall width in LEEM coincides well with the Debye screening length λ_D of undoped $\mathrm{ErMnO_3}$ (see Fig.4.10 and Sec. 2.1.1.3), possibly explaining the emerging contrast. Fig. 6.12c presents the domain-wall profile as function of start energy. Optimized imaging conditions are obtained at $-1.82\,\mathrm{V}$. At higher start energies, the domain wall gets distorted due to increased charging of the surrounding bulk. Figure 6.12d shows a schematic on how the variation in surface potential leads to electron focusing at a tail-to-tail wall.

In summary, we showed how LEEM provides access to functional properties of domain walls. At neutral walls, in-plane fields from the adjacent out-of-plane domains impede characterization of the functional domain-wall properties. But this issue could possibly be bypassed in future LEEM studies by analyzing the domain walls at very low gun currents in order to minimize surface charging and thus the arising in-plane fields. At charged domain walls, where these in-plane fields do not exist, LEEM is sensitive to the functional domain wall properties and allows to probe them contact free. Moreover, LEEM can be used to capture images of the functional domain walls with acquisition times in the order of milliseconds. The presented data thus show the potential of LEEM to go beyond the lateral resolution limit in cAFM. At present, however, it remains to be demonstrated to what extend focus effects obscure the high-resolution data. According to Nepijko[212], the apparent size can differ from the actual size determined in LEEM. The latter may be resolved in the future by better modeling capabilities and additional domain-wall experiments in LEEM; a method rather new to domain-wall characterization.

6.4. Summary

We applied cathode-lens microscopy (CLM) for domain-wall imaging both contact-free and with resolutions beyond scanning probe microscopy (SPM). In x-ray photoemission electron microscopy (X-PEEM), spatial variations in x-ray induced surface charging lead to different kinetic energies of the emitted electrons with an average kinetic energy proportional to the amount of surface charging. Peak values in the kinetic energy are fitted and translated into relative conductance maps with spatial resolutions of about 50 – 100 nm. Temperature-dependent measurements substantiate the charging-provoked contrast mechanism, which is at play when imaging domain walls by X-PEEM.

Low-energy electron microscopy (LEEM) allows to couple to charged domain walls with lateral resolutions higher than in SPM, which is demonstrated by the obtained domain-wall width of 14 nm. Although some challenges in LEEM need to be solved, e. g., surface charging, focusing effects, etc., this CLM method is very promising for the field of domain-wall research.

In conclusion, we introduced PEEM and LEEM for characterizing emerging domain-wall properties. The difference between the two methods lies in the accessible parameters and the spatial resolution (see above and Sec. 3.2). The advantage of X-PEEM is to provide information on chemical changes, which might be obtained in future experiments probing domain walls with x-rays of suitable polarization and energy generated by a synchrotron facility. LEEM bears the potential to study conductance properties of domain walls with variable electron doses, which might give access to high-resolution $I(V)$/conductance maps even lab-based.

7. Conclusion and outlook

Understanding and controlling electronic domain-wall properties is of academic and technological interest and may enable the development of future domain-wall-based devices. This thesis investigated different approaches to characterize and manipulate the electronic transport at functional domain walls in improper-ferroelectric hexagonal manganites (RMnO$_3$). The key findings of our studies are summarized in the following.

In semiconducting ErMnO$_3$, where domain-wall transport is attributed to p-type carriers, we modified domain-wall conductance by replacing trivalent Er^{3+} for divalent Ca^{2+}. In the hole-doped compounds Er$_{1-x}$Ca$_x$MnO$_3$ ($0 \leq x \leq 0.01$), a moderate doping concentration of $x = 0.01$ leads to fifty times higher domain-wall conductance and narrows the electronic wall width down to $\sim 50\,\mathrm{nm}$. The higher conductance together with the reduced electronic domain-wall width lead to a significant enhancement of the current density carried by the walls. Complementary to hole doping, we substituted Er^{3+} by tetravalent Zr^{4+} in Er$_{1-x}$Zr$_x$MnO$_3$ and induced a state where n-type carriers contribute to the screening and transport characteristics of the charged head-to-head walls, which we achieved at a Zr concentration of $x = 0.01$. As a consequence, previously insulating walls become conductive and vice versa.

By an in-depth study of insulating walls in ErMnO$_3$, we demonstrated that their electronic domain-wall states can be manipulated by external fields. A voltage-driven transition allows reversible switching between insulating and conductive domain-wall properties. The behavior can be explained by the formation – and eventual activation – of an inversion layer that arises due to strong band bending at this type of charged wall. Another important discovery was the distinct behavior of neutral walls under alternating electric fields. Their properties can be manipulated by the oxygen content, facilitating controllable half-wave rectification at the domain wall in the kHz/MHz regime.

Aside from scanning probe microscopy (SPM), we established cathode-lens microscopy (CLM) as powerful tool for advanced high-resolution studies at domain walls. Using photoemission electron microscopy (PEEM), we image domain walls by exploiting charging contrasts and track the evolution of the local transport properties as function of temperature. By closely analyzing the spatial distribution of the kinetic electron energy, PEEM provides access to record domain-wall conductance maps in contact-free manner with a resolution limit of 20 nm. Low-energy electron microscopy (LEEM) presents a complementary alternative to image domain walls contact-free with millisecond exposure times. Once the focus effects at domain walls are controlled adequately, LEEM will allow to push the resolution to a few nanometers ($\sim 2\,\mathrm{nm}$).

Overall, our results provide new impulses for future domain-wall research and engineering. Chemical doping holds as a promising pathway for controlling the electronic behavior at charged domain walls and eventually tuning their properties towards a technologically feasible working range. The findings of our study highlight an important crosslink between classical semiconductor physics and modern domain-wall engineering, which can be generalized to manipulate stable charged domain walls in other systems[18].

Fully reversible control of functional domain-wall states spawns novel ideas for device concepts, and we presented conceptual schematics on how these entities could be used in domain-wall transistors. In general, an involvement of both minority and majority carriers is appealing as it allows device paradigms to be extended into the realm of minority-carrier devices, including bistable switches and bipolar transistors. Minority-carrier devices are typically slower, but offer better on-state performance and larger breakdown voltages[250].

Aside from static transport, the understanding of AC domain-wall transport is still at its infancy. Since half-wave rectification might be also present in other systems with conductive domain walls, this could be a start to apply our presented advanced SPM technique: AC-cAFM. In addition, AC-cAFM, which probes electronic properties locally resolved in the kHz/MHz regime, closes the gap between conventional DC-cAFM and scanning impedance microscopy operating in the GHz regime[108].

With this, our results foreshadow conceptually new domain-wall applications that go beyond conducting 2D channels that can be written, moved, and erased on demand. The next consequent step is to go from an SPM-based proof-of-principle to the actual construction of a domain-wall based device. Nano strip lines of $R\mathrm{MnO}_3$ that can be contacted by electrodes, may be produced from thin lamellae cut by focused-ion beam microscopy[251] or thin films with back electrodes grown by pulsed laser deposition. The latter has been recently achieved in our labs and together with our results brings us one step closer to the realization of reconfigurable all-domain-wall circuits.

Non-scanning CLM offers fast and contact-free characterization possibilities for domain-wall devices and oxide electronics in general. One example would be conductance mapping by X-PEEM[247] and LEEM[249], but in addition CLM offers the unique possibility for fast and time-resolved in-operando experiments[252,253]. Moreover, quality control in industrial manufacturing might be realized by implementing CLM and using its millisecond acquisition times.

A. Appendix

A.1. AC-cAFM addendum

Current response of sample with intermediate conductivity

Figure A.1 shows the evolution of current response I_{DC} as function of frequency ν of the sample with intermediate conductivity (see Fig. 5.4b), which is not shown in Sec. 5.3. The diagram shows similar characteristics compared to the ones in Figures 5.7d, 5.8a, and 5.8b: at lower frequencies the current response from the domains dominates the signal, whereas at higher frequencies the signal is determined by domain-wall currents.

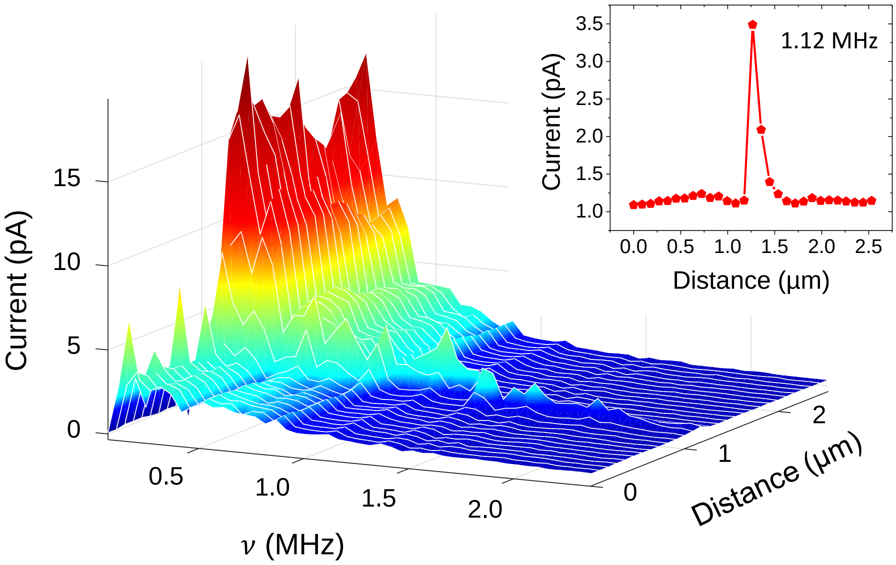

Figure A.1.: Current response I_{DC} of the sample with intermediate conductivity, i. e., $4.8 \times 10^{-6}\,\mathrm{S\,cm^{-1}}$ (see Fig. 5.4b). Frequency plot of current signal measured across a domain wall. Current response originating from domains go through a maximum at $\sim 0.17\,\mathrm{MHz}$ before they cease and domain-wall currents prevail, being emphasized by the domain-wall profile at 1.12 MHz shown on the inset.

Characterization of the AFM output in AC-cAFM mode

Prior to our AC-cAFM studies presented in Sec. 5.3 and 5.4 we characterized voltage output, voltage offset, and noise of our scanning probe microscope. By this we can assure that the measured current responses of domains and domain walls do not originate from cut-offs or capacities of the internal electronics. Figure A.2 shows the characteristics of our NT-MDT NTEGRA system.

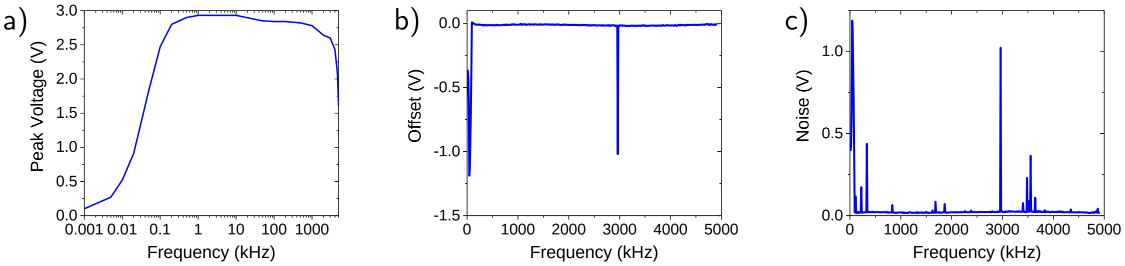

Figure A.2.: Output, offset, and noise of the NT-MDT NTEGRA system. a) Output voltage plotted as function of frequency. The curve was determined by measuring the amplitude of the output voltage directly after the signal access module with an external oscilloscope. b) Internal offsets in the current response measured as function of the applied AC frequency. c) Noise of the system derived from the root mean square of the current response.

If the internal frequency generator is set to a nominal output voltage of 3 V, we measure a voltage amplitude (peak value) as presented in Fig. A.2a. The voltage output matches the set value between 0.1 kHz and $\sim$ 4000 kHz, which covers the range of our measurements in Sec. 5.3.

Offset and noise are determined by performing several scans at different frequencies while the tip remains retracted from the surface. The average current response value of each scan is taken as the offset in the signal, whereas the root mean square (RMS) of the response is defined as noise. The signal is offset free to the greatest extent, yet at some frequencies, the noise increases drastically due to resonances of the internal electronics. Scans with high noise level are excluded from the evaluations.

A.2. List of measurements

Table A.1.: Raw data of the measurements presented in chapters 2 to 4

Figure	Label	Sample	File
2.7	c	EMO#15254-502	2014.07.11 EMO (op) - EFM, PFM, cAFM_2.mdt
	c	EMO#15254-001	2013.08.28 ErMnO3 (in-plane), LEEM sample.mdt
4.1	a, b	EMO#15254-001	2013.08.28 ErMnO3 (in-plane), LEEM sample.mdt
4.2	a, b	EMO#15254-002	2016.05.23 EMOx(V) after LEEM 2.mdt
	a, c	EMO#15254-003	2016.02.29 EMOX hh wall on off_2.mdt
4.3	a	EMO#15254-001	2013.08.28 ErMnO3 (in-plane), LEEM sample.mdt
	b	EMO#15254-003	2016.03.30 EMOX hh wall on off_9.mdt
	c	EMO#15254-001	2014.11.12 EMOx polished LEEM sample, cAFM tip-comp.mdt
4.4		EMO#15254-002	2016.05.23 EMOx(V) after LEEM.mdt
4.5		EMO#15254-001	2013.08.28 ErMnO3 (in-plane), LEEM sample.mdt
		ECo2MO#15286-001	2013.10.04 Ca(0.2%)-ErMnO3 cAFM local.mdt
		EC1MO#15343-001	2013.09.02 Ca(1.0%)-ErMnO3#15343.mdt
		EZo2MO#15311.1-001	2013.04.11 Zr-ErMnO3#15311.1.mdt
		EZ1MO#15400-002	2014.11.08 EZ1MOx 1&2 comp anneling stuff.mdt
4.7		EMO#15254-002	2015.08.05 EMOx with Pt-Tip Spectroscopy_2.mdt
		EZo2MO#15311.1-001	2015.08.05 EZ0o2MOx Pt-Tip Spectroscopy_2.mdt
		EZ1MO#15400-001	2015.08.05 EZ1MO with Pt-Tip Spectroscopy_2.mdt
4.8	a	EMO#15254-001	2014.03.29 ErMnO3 (LEEM sample) – EFM vs. PFM.mdt
	b, c	EMO#15254-001	2013.09.13 ErMnO3, LEEM Sample – EFM.mdt
	d, e	EC1MO#15343-001	2014.01.27 Ca(1.0%)-ErMnO3 – EFM.mdt
4.9	a, c, d	EMO#15254-001	2013.08.28 ErMnO3 (in-plane), LEEM sample.mdt
	c, d	ECo2MO#15286-001	2013.11.17 Ca(0.2%)-ErMnO3#15286, LEEM sample - cAFM_round 3.mdt
	b	EC1MO#15343-001	2013.09.06 Ca(1.0%)-ErMnO3#15343_2.mdt
	c, d	EC1MO#15343-001	2014.01.13 Ca(1.0%)-ErMnO3#15343 - cAFM series.mdt
4.10	a	EMO#15254-001	2014.05.15 dmn_wall comparisson_2.mdt
	a	ECo2MO#15286-001	
	a	EC1MO#15343-001	
4.11	a	EZo2MO#15311.1-001	2013.10.14 Zr(0.2%)-ErMnO3#15311.1 - cAFM.mdt
	b	EZ1MO#15400-001	2015.07.24 EZ1MOx with TiIr-tip.mdt
4.12	a	check notes	2016.12.08 EZ1MOx.mdt
	b	001 or 003 I think	2016.12.08 EZ1MOx_2.mdt
4.13	a, b	EMO#15254-001	2013.08.20 ErMnO3 (in-plane), LEEM sample.mdt
	c	EMO#15254-001	2013.08.22 ErMnO3 (in-plane), LEEM sample.mdt
4.14	a	EMO#15254-003	2016.10.21 EMOx-003 Pt spec_3.mdt
	b	EMO#15254-003	2016.10.29 EMOx-003 Pt spec13-3negbias.mdt
4.18	a	EMO#15254-003	2016.03.24 EMOX hh wall on off_8.mdt
	b	EMO#15254-003	2016.03.30 EMOX hh wall on off_9.mdt

Table A.2.: Raw data of the measurements presented in chapters 5 to A.1

Figure	Label	Sample	File
5.1	a, b	EMO#15254-502	2016.04.07 Switching EMOz, not succesful.mdt
5.2	a	EMO#15254-502	2016.12.05_EMOz#15254-502 before switch.mdt
	b	EMO#15254-502	2016.12.08 EMOz I(t).mdt
5.3	a, b	EMO#15254-502	2014.07.11 EMO (op) - EFM, PFM, cAFM.mdt
5.4	a, b	1290-3B, -1A	2015.05.12_BulkConductance_3B&1A&1B&1C -tip#30-IprCorr.mdt
	c, d	1290-1B, -1C	2015.05.12_BulkConductance_3B&1A&1B&1C -tip#30-IprCorr.mdt
	e	1290 - 3A	2015.03.04 Sample 3A -cAFM, PFM.mdt
	f		2015.05.12_BulkConductance_3B&1A&1B&1C -tip#30-IprCorr.mdt 2015.03.04 Sample 3A -cAFM, PFM.mdt
5.5		1290 - 1A	2015.07.21 Sample 1A - cAFM, resPFM, PFM.mdt
5.6	$I(V)$	1290 - 1A	2015.06.02_Sample1A&E1_cAFM_tip#36_spot1.mdt
5.7		1290 - 1B	2015.04.14_Sample1B-resPFM-tip#18-script.mdt 2015.04.15_Sample1B-resPFM-tip#19-script.mdt
5.8	a	1290 - 1C	2015.05.08_Sample1C-resPFM-tip#29-script.mdt
	b	1290 - 3B	2015.04.23_Sample3B-resPFM-tip#22-script.mdt
6.1	a	EMO#15254-001	2013.06.25 ErMnO3 (in-plane), LEEM sample.mdt
	b, c	EMO#15254-001	2013.09.19 ErMnO3s cAFM @ the LEEM spot.mdt
	a, d	EMO#15254-001	\\042 Cathode Lens Microscopy\2013-06 June\00_data\
6.2		EMO#15254-001	\\042 Cathode Lens Microscopy\2013-06 June\00_data\
6.3		EMO#15254-001	\\042 Cathode Lens Microscopy\2013-06 June\00_data\
6.4	a	EC1MO#15343-002	\\042 Cathode Lens Microscopy\2016-04 April\12_EC1MOx\
	b	EC1MO#15343-002	2016.05.04 EC1MOx(V) after PEEM.mdt
	c	EC1MO#15343-002	2016.07.05 EC1MOx(V) after PEEM_cAFM.mdt
6.5		EC1MO#15343-002	\\042 Cathode Lens Microscopy\2016-04 April\12_EC1MOx\
6.6		EC1MO#15343-002	\\042 Cathode Lens Microscopy\2016-04 April\12_EC1MOx\
6.7		EC1MO#15343-002	\\042 Cathode Lens Microscopy\2016-04 April\12_EC1MOx\
6.8	a, b	EMO#15254-501	beamtime prior to my doctorate, raw data @ Dennis Meier
	d	EMO#15254-502	\\042 Cathode Lens Microscopy\2013-12 December\EMOz_set2\
6.9		EMO#15254-002	\\042 Cathode Lens Microscopy\2016-04 April\16_EMOx\
6.10		EMO#15254-002	\\042 Cathode Lens Microscopy\2016-04 April\16_EMOx\
6.11		ECo2MO#15286-001	\\042 Cathode Lens Microscopy\2013-06 June\00_data\
6.12		EMO#15254-001	beamtime prior to my doctorate, raw data @ Dennis Meier
A.1		1290 - 1A	2016.01.04 reproducing sample 1A 2nd.mdt
A.2			2015.09.21 noise and offset.mdt

A.3. List of figures

2.1. Primary types of ferroic orders and their coupling in multiferroics . . 5
2.2. Hysteresis, microscopic mechanism, and free energy of ferroelectrics . 6
2.3. Species of charged and neutral domain walls in ferroelectrics 10
2.4. Calculated static DW conductivity of an n-type semiconductor 14
2.5. Conduction at domain walls in different ferroic compounds 19
2.6. Crystal structure of the hexagonal $R\mathrm{MnO}_3$ 23
2.7. Antiphase / FE boundaries and topological protected vortices 24
2.8. Domain and domain-wall transport in the hexagonal manganites . . . 27
2.9. Simplified illustration of the Mn d bands in doped $R\mathrm{MnO}_3$ 29

3.1. Basic principle of atomic force microscopy 34
3.2. Setup for AC and DC cAFM measurements 38
3.3. Setup for piezoresponse force microscopy 41
3.4. Setup and principle of electrostatic force microscopy 43
3.5. Principle of photoemission electron microscopy (PEEM) 46
3.6. Secondary electron emission and energy filtering in PEEM. 47
3.7. Principle of low-energy electron microscopy (LEEM) 49
3.8. Growth and orientation of ErMnO_3 single crystals 50

4.1. Fundamental transport properties of ErMnO_3 54
4.2. Time-dependent domain-wall currents in ErMnO_3 55
4.3. Tip-coating dependence on electronic transport in ErMnO_3 56
4.4. Possible conduction mechanisms in ErMnO_3 57
4.5. Ferroelectric domain structures in doped ErMnO_3 59
4.6. Bulk $J(E)$ characteristics of differently doped ErMnO_3 compounds . 60
4.7. Bulk conductance of Zr-doped samples 61
4.8. EFM response of the domain walls in $\mathrm{Er}_{1-x}\mathrm{Ca}_x\mathrm{MnO}_3$ 62
4.9. cAFM and $I(V)$ characteristics of $\mathrm{Er}_{1-x}\mathrm{Ca}_x\mathrm{MnO}_3$ 63
4.10. Electronic domain-wall width in $\mathrm{Er}_{1-x}\mathrm{Ca}_x\mathrm{MnO}_3$ 65
4.11. Nanoscopic conductance properties of $\mathrm{Er}_{1-x}\mathrm{Zr}_x\mathrm{MnO}_3$ 67
4.12. Head-to-head wall transport in $\mathrm{Er}_{0.99}\mathrm{Zr}_{0.01}\mathrm{MnO}_3$ 68
4.13. Electronic transport at tail-to-tail and head-to-head walls 70
4.14. Bipolar $I(V)$ curves at head-to-head walls 71
4.15. Band structure at tail-to-tail and head-to-head walls 71
4.16. Change of Mn valence at head-to-head domain walls 73
4.17. Orbital character of electrons at head-to-head walls 75
4.18. Electric-field control of electronic transport at head-to-head walls . . 76
4.19. Conceptual domain-wall functionality 77

5.1. Conduction at neutral domain walls of ErMnO_3 80
5.2. Current spectroscopy and time dependence at neutral DWs 81
5.3. Evidence of intrinsic conductance properties at neutral DWs 81

5.4. cAFM characteristics of annealed $\mathrm{ErMnO_3}$ samples 83
5.5. Comparison of AC-cAFM and PFM signals 84
5.6. How AC voltages lead to DC-current responses 85
5.7. Current response I_{DC} as function of frequency ν 86
5.8. Current response of the samples with lowest and highest conductivity 88
5.9. Dielectric spectroscopy measurements at room temperature 88
5.10. Schematic ferroelectric hysteresis and switching currents 89
5.11. Frequency-dependent current response I_{DC} 90

6.1. Comparison of PFM, cAFM, and X-PEEM data on $\mathrm{ErMnO_3}$ 95
6.2. Energy-dispersion from bulk and domain-wall electrons 96
6.3. X-PEEM conductance map of $\mathrm{ErMnO_3}$ 97
6.4. X-PEEM contrasts at 160 K compared with cAFM and PFM 99
6.5. Shift of E_{kin} at head-to-head and tail-to-tail domain walls 100
6.6. Contact-free conductance mapping as function of temperature 101
6.7. Controlling X-PEEM contrasts via temperature 102
6.8. Imaging ferroelectric domains with LEEM 104
6.9. LEEM reflectivity at charged domain walls 107
6.10. MEM-LEEM transitions of domain walls as function of I_{gun} 107
6.11. Focus-dependence of MEM-LEEM transitions at charged walls 108
6.12. Resolution limit for domain-wall imaging with LEEM 109

A.1. Current response I_{DC} of the sample with intermediate conductivity. . 113
A.2. Output, offset, and noise of the NT-MDT NTEGRA system. 114

A.4. List of abbreviations

AC-cAFM	Alternating-current conductive atomic force microscopy
AFM	Atomic force microscopy
APB-FE	Antiphase-ferroelectric
CBM	Conduction-band minimum
cAFM	Conductive atomic force microscopy
CLM	Cathode-lens microscopy
DFT	Density functional theory
DW	Domain wall
DWc	Domain-wall conductance
EFM	Electrostatic force microscopy
FE	Ferroelectric
FWHM	Full width at half maximum
→←	Head-to-head
IMFP	Inelastic mean free path
LEEM	Low-energy electron microscopy
MEM	Mirror-electron microscopy
MEM-LEEM	Mirror-electron to low-energy electron microscopy
PEEM	Photoemission electron microscopy
PFM	Piezoresponse force microscopy
PZT	$\mathrm{Pb[Ti_{1\text{-}x}Zr_{\mathit{x}}]O_3}$
$R\mathrm{MnO_3}$	Hexagonal manganite
SCLC	Space-charge-limited conduction
SE	Secondary electron
SEM	Scanning electron microscopy
SHG	Second harmonic generation
SPM	Scanning probe microscopy
STM	Scanning tunneling microscopy
T_c	Critical temperature
TEM	Transmission electron microscopy
←→	Tail-to-tail
UHV	Ultra-high vacuum
VBM	Valence-band maximum
X-PEEM	X-ray photoemission electron microscopy

Bibliography

[1] M. Lorenz *et al.*: The 2016 oxide electronic materials and oxide interfaces roadmap, *Journal of Physics D: Applied Physics* **49**, 433001 (2016)

[2] A. Ohtomo & H. Y. Hwang: A high-mobility electron gas at the $LaAlO_3/SrTiO_3$ heterointerface, *Nature* **427**, 423–426 (2004)

[3] B. Förg, C. Richter & J. Mannhart: Field-effect devices utilizing $LaAlO_3$-$SrTiO_3$ interfaces, *Applied Physics Letters* **100**, 053506 (2012)

[4] V. Wadhawan: *Introduction to Ferroic Materials*, Taylor & Francis (2000)

[5] S. Y. Yang *et al.*: Above-bandgap voltages from ferroelectric photovoltaic devices, *Nature Nanotechnology* **5**, 143–147 (2010)

[6] T. Sluka, A. K. Tagantsev, D. Damjanovic, M. Gureev & N. Setter: Enhanced electromechanical response of ferroelectrics due to charged domain walls, *Nature Communications* **3**, 748 (2012)

[7] J. Seidel *et al.*: Conduction at domain walls in oxide multiferroics, *Nature Materials* **8**, 229–234 (2009)

[8] J. Guyonnet, I. Gaponenko, S. Gariglio & P. Paruch: Conduction at domain walls in insulating $Pb(Zr_{0.2}Ti_{0.8})O_3$ thin films, *Advanced Materials* **23**, 5377–5382 (2011)

[9] S. Farokhipoor & B. Noheda: Conduction through 71° domain walls in $BiFeO_3$ thin films, *Physical Review Letters* **107**, 127601 (2011)

[10] P. Maksymovych *et al.*: Tunable metallic conductance in ferroelectric nanodomains, *Nano Letters* **12**, 209–213 (2012)

[11] D. Meier *et al.*: Anisotropic conductance at improper ferroelectric domain walls, *Nature Materials* **11**, 284–288 (2012)

[12] W. Wu, Y. Horibe, N. Lee, S.-W. Cheong & J. R. Guest: Conduction of topologically protected charged ferroelectric domain walls, *Physical Review Letters* **108**, 077203 (2012)

[13] M. Schröder *et al.*: Conducting domain walls in lithium niobate single crystals, *Advanced Functional Materials* **22**, 3936–3944 (2012)

[14] T. Sluka, A. K. Tagantsev, P. Bednyakov & N. Setter: Free-electron gas at charged domain walls in insulating $BaTiO_3$, *Nature Communications* **4**, 1808 (2013)

[15] Q. He *et al.*: Magnetotransport at domain walls in $BiFeO_3$, *Physical Review Letters* **108**, 067203 (2012)

[16] G. Catalan, J. Seidel, R. Ramesh & J. F. Scott: Domain wall nanoelectronics, *Reviews of Modern Physics* **84**, 119–156 (2012)

[17] A. A. Grekov, A. A. Adonin & N. P. Protsenko: Encountering domains in SbSl, *Ferroelectrics* **13**, 483–485 (1976)

[18] Y. S. Oh, X. Luo, F.-T. Huang, Y. Wang & S.-W. Cheong: Experimental demonstration of hybrid improper ferroelectricity and the presence of abundant charged walls in $(Ca,Sr)_3Ti_2O_7$ crystals, *Nature Materials* **14**, 407–413 (2015)

[19] K. Aizu: Possible species of “ferroelastic” crystals and of simultaneously ferroelectric and ferroelastic crystals, *Journal of the Physical Society of Japan* **27**, 387–396 (1969)

[20] D. B. Litvin: Ferroic classifications extended to ferrotoroidic crystals, *Acta Crystallographica Section A* **64**, 316–320 (2008)

[21] B. D. Cullity & C. D. Graham: *Introduction to Magnetic Materials*, Wiley-IEEE Press, 2nd edition (2008)

[22] J. Seidel (ed.): *Topological Structures in Ferroic Materials: Domain Walls, Vortices and Skyrmions*, Springer Series in Materials Science, Springer International Publishing (2016)

[23] A. Tagantsev, L. Cross & J. Fousek: *Domains in Ferroic Crystals and Thin Films*, Springer New York (2010)

[24] N. D. Mermin: The topological theory of defects in ordered media, *Reviews of Modern Physics* **51**, 591–648 (1979)

[25] F. Neumann: *Vorlesungen über die Theorie der Elastizität der festen Körper und des Lichtäthers*, B. G. Teubner-Verlag (1885)

[26] R. Newnham: *Properties of Materials: Anisotropy, Symmetry, Structure*, Properties of Materials: Anisotropy, Symmetry, Structure, OUP Oxford (2004)

[27] C. Kittel: Physical theory of ferromagnetic domains, *Reviews of Modern Physics* **21**, 541–583 (1949)

[28] J. Valasek: Piezo-electric and allied phenomena in rochelle salt, *Physical Review* **17**, 475–481 (1921)

[29] K. Rabe, C. Ahn & J. Triscone (eds.): *Physics of Ferroelectrics: A Modern Perspective*, Topics in Applied Physics, Springer Berlin Heidelberg (2007)

[30] E. K. Salje: Ferroelastic materials, *Annual Review of Materials Research* **42**, 265–283 (2012)

[31] B. B. Van Aken, J.-P. Rivera, H. Schmid & M. Fiebig: Observation of ferrotoroidic domains, *Nature* **449**, 702–705 (2007)

[32] A. A. Gorbatsevich & Y. V. Kopaev: Toroidal order in crystals, *Ferroelectrics* **161**, 321–334 (1994)

[33] N. A. Spaldin, M. Fiebig & M. Mostovoy: The toroidal moment in condensed-matter physics and its relation to the magnetoelectric effect, *Journal of Physics: Condensed Matter* **20**, 434203 (2008)

[34] A. S. Zimmermann, D. Meier & M. Fiebig: Ferroic nature of magnetic toroidal order, *Nature Communications* **5**, 4796 (2014)

[35] N. A. Spaldin & M. Fiebig: The renaissance of magnetoelectric multiferroics, *Science* **309**, 391–392 (2005)

[36] H. Schmid: Multi-ferroic magnetoelectrics, *Ferroelectrics* **162**, 317–338 (1994)

[37] J. F. Scott: Room-temperature multiferroic magnetoelectrics, *NPG Asia Mater* **5**, e72 (2013)

[38] M. Fiebig, T. Lottermoser, D. Meier & M. Trassin: The evolution of multiferroics, *Nature Reviews Materials* **1**, 16046 (2016)

[39] D. I. Khomskii: Classifying multiferroics: Mechanisms and effects, *Physics* **2**, 20 (2009)

[40] S.-W. Cheong & M. Mostovoy: Multiferroics: a magnetic twist for ferroelectricity, *Nature Materials* **6**, 13–20 (2007)

[41] A. P. Levanyuk & D. G. Sannikov: Improper ferroelectrics, *Soviet Physics Uspekhi* **17**, 199 (1974)

[42] B. Strukov & A. Levanyuk: *Ferroelectric Phenomena in Crystals: Physical Foundations*, Springer (1998)

[43] V. Janovec: A symmetry approach to domain structures, *Ferroelectrics* **12**, 43–53 (1976)

[44] Y. Kuroiwa *et al.*: Evidence for Pb-O covalency in tetragonal $PbTiO_3$, *Physical Review Letters* **87**, 217601 (2001)

[45] K. Momma & F. Izumi: VESTA3 for three-dimensional visualization of crystal, volumetric and morphology data, *Journal of Applied Crystallography* **44**, 1272–1276 (2011)

[46] L. D. Landau: Theory of phase transformations I, *Journal of Experimental and Theoretical Physics* **7**, 19 (1937)

[47] L. D. Landau: Theory of phase transformations II, *Journal of Experimental and Theoretical Physics* **627**, 19 (1937)

[48] A. Devonshire: Theory of ferroelectrics, *Advances in Physics* **3**, 85–130 (1954)

[49] L. E. Cross, A. Fouskova & S. E. Cummins: Gadolinium molybdate, a new type of ferroelectric crystal, *Physical Review Letters* **21**, 812–814 (1968)

[50] S. Artyukhin, K. T. Delaney, N. A. Spaldin & M. Mostovoy: Landau theory of topological defects in multiferroic hexagonal manganites, *Nature Materials* **13**, 42–49 (2014)

[51] D. Meier *et al.*: Translation domains in multiferroics, *Phase Trans* **86**, 33–52 (2013)

[52] M. Šafránková, J. Fousek & S. A. Kižaev: Domains in ferroelectric $YMnO_3$, *Czechoslovak Journal of Physics B* **17**, 559–560 (1967)

[53] T. Choi *et al.*: Insulating interlocked ferroelectric and structural antiphase domain walls in multiferroic $YMnO_3$, *Nature Materials* **9**, 253–258 (2010)

[54] T. Jungk, A. Hoffmann, M. Fiebig & E. Soergel: Electrostatic topology of ferroelectric domains in $YMnO_3$, *Applied Physics Letters* **97**, 012904 (2010)

[55] R. E. Cohen & H. Krakauer: Electronic structure studies of the differences in ferroelectric behavior of $BaTiO_3$ and $PbTiO_3$, *Ferroelectrics* **136**, 65–83 (1992)

[56] H. H. Wieder: Electrical behavior of barium titanate single crystals at low temperatures, *Physical Review* **99**, 1161–1165 (1955)

[57] J. Wang *et al.*: Epitaxial $BiFeO_3$ multiferroic thin film heterostructures, *Science* **299**, 1719–1722 (2003)

[58] D. Khomskii: *Transition Metal Compounds*, Cambridge University Press (2014)

[59] D. Meier: Functional domain walls in multiferroics, *Journal of Physics: Condensed Matter* **27**, 463003 (2015)

[60] B. B. Van Aken, T. T. M. Palstra, A. Filippetti & N. A. Spaldin: The origin of ferroelectricity in magnetoelectric $YMnO_3$, *Nature Materials* **3**, 164–170 (2004)

[61] N. A. Benedek & C. J. Fennie: Hybrid improper ferroelectricity: A mechanism for controllable polarization-magnetization coupling, *Physical Review Letters* **106**, 107204 (2011)

[62] J. van den Brink & D. I. Khomskii: Multiferroicity due to charge ordering, *Journal of Physics: Condensed Matter* **20**, 434217 (2008)

[63] J. de Groot *et al.*: Charge order in $LuFe_2O_4$: An unlikely route to ferroelectricity, *Physical Review Letters* **108**, 187601 (2012)

[64] N. Ikeda *et al.*: Ferroelectricity from iron valence ordering in the charge-frustrated system $LuFe_2O_4$, *Nature* **436**, 1136–1138 (2005)

[65] I. K. Yang, J. Kim, S. H. Lee, S.-W. Cheong & Y. H. Jeong: Charge ordering, ferroelectric, and magnetic domains in $LuFe_2O_4$ observed by scanning probe microscopy, *Applied Physics Letters* **106**, 152902 (2015)

[66] M. Mostovoy: Ferroelectricity in spiral magnets, *Physical Review Letters* **96**, 067601 (2006)

[67] M. Fiebig: Revival of the magnetoelectric effect, *Journal of Physics D: Applied Physics* **38**, R123 (2005)

[68] I. Dzyaloshinskii: Theory of helicoidal structures in antiferromagnets. I. Nonmetals, *Journal of Experimental and Theoretical Physics* **19**, 960 (1964)

[69] T. Moriya: Anisotropic superexchange interaction and weak ferromagnetism, *Physical Review* **120**, 91–98 (1960)

[70] H. Katsura, N. Nagaosa & A. V. Balatsky: Spin current and magnetoelectric effect in noncollinear magnets, *Physical Review Letters* **95**, 057205 (2005)

[71] I. A. Sergienko & E. Dagotto: Role of the Dzyaloshinskii-Moriya interaction in multiferroic perovskites, *Physical Review B* **73**, 094434 (2006)

[72] P. S. Bednyakov, T. Sluka, A. K. Tagantsev, D. Damjanovic & N. Setter: Formation of charged ferroelectric domain walls with controlled periodicity, *Scientific Reports* **5**, 15819 (2015)

[73] P. Zubko, G. Catalan & A. K. Tagantsev: Flexoelectric effect in solids, *Annual Review of Materials Research* **43**, 387–421 (2013)

[74] V. K. Wadhawan: Ferroelasticity and related properties of crystals, *Phase Transitions* **3**, 3–103 (1982)

[75] J. C. Tolédano: Phenomenological model for the structural transition in benzil, *Physical Review B* **20**, 1147–1156 (1979)

[76] G. De Luca *et al.*: Domain wall architecture in tetragonal ferroelectric thin films, *Advanced Materials* **29**, 1605145 (2016)

[77] A. Saxena & A. Planes: *Mesoscopic Phenomena in Multifunctional Materials: Synthesis, Characterization, Modeling and Applications*, Springer Series in Materials Science, Springer Berlin Heidelberg (2014)

[78] C.-L. Jia *et al.*: Atomic-scale study of electric dipoles near charged and uncharged domain walls in ferroelectric films, *Nature Materials* **7**, 57–61 (2008)

[79] P. Bednyakov, T. Sluka, A. Tagantsev, D. Damjanovic & N. Setter: Free-carrier-compensated charged domain walls produced with super-bandgap illumination in insulating ferroelectrics, *Advanced Materials* **28**, 9498–9503 (2016)

[80] M. Y. Gureev, A. K. Tagantsev & N. Setter: Head-to-head and tail-to-tail 180° domain walls in an isolated ferroelectric, *Physical Review B* **83**, 184104 (2011)

[81] V. Fridkin: *Ferroelectric semiconductors*, Consultants Bureau, New York and London (1980)

[82] J. Schaab *et al.*: Optimization of electronic domain-wall properties by aliovalent cation substitution, *Advanced Electronic Materials* **2**, 1500195 (2016)

[83] B. Meyer & D. Vanderbilt: Ab initio study of ferroelectric domain walls in $PbTiO_3$, *Physical Review B* **65**, 104111 (2002)

[84] E. A. Eliseev, A. N. Morozovska, G. S. Svechnikov, V. Gopalan & V. Y. Shur: Static conductivity of charged domain walls in uniaxial ferroelectric semiconductors, *Physical Review B* **83**, 235313 (2011)

[85] E. A. Eliseev, A. N. Morozovska, G. S. Svechnikov, P. Maksymovych & S. V. Kalinin: Domain wall conduction in multiaxial ferroelectrics, *Physical Review B* **85**, 045312 (2012)

[86] J. Seidel *et al.*: Domain wall conductivity in La-doped $BiFeO_3$, *Physical Review Letters* **105**, 197603 (2010)

[87] T. Rojac *et al.*: Domain-wall conduction in ferroelectric $BiFeO_3$ controlled by accumulation of charged defects, *Nature Materials* **16**, 322–327 (2016)

[88] Y.-P. Chiu *et al.*: Atomic-scale evolution of local electronic structure across multiferroic domain walls, *Advanced Materials* **23**, 1530–1534 (2011)

[89] J. Seidel *et al.*: Electronic properties of isosymmetric phase boundaries in highly strained Ca-doped $BiFeO_3$, *Advanced Materials* **26**, 4376–4380 (2014)

[90] Y. Heo *et al.*: Enhanced conductivity at orthorhombic-rhombohedral phase boundaries in $BiFeO_3$ thin films, *NPG Asia Mater* **8**, e297 (2016)

[91] S. M. Sze & K. K. Ng: *Physics of Semiconductor Devices*, John Wiley & Sons, Ltd., Hoboken, New Jersey (2007)

[92] W. Wu *et al.*: Polarization-modulated rectification at ferroelectric surfaces, *Physical Review Letters* **104**, 217601 (2010)

[93] O. Breitenstein, P. Altermatt, K. Ramspeck & A. Schenk: The origin of ideality factors $n > 2$ of shunts and surfaces in the dark I-V curves of SI solar cells, in *21st European Photovoltaic Solar Energy Conference, Dresden, Germany* (2006)

[94] J. F. Scott: Magnetoelectric memories – a disruptive techology?, *ChemPhysChem* **10**, 1761–1762 (2009)

[95] J. G. Simmons: Richardson-schottky effect in solids, *Physical Review Letters* **15**, 967–968 (1965)

[96] J. F. Scott: There's no place like Ohm: Conduction in oxide thin films, *Journal of Physics: Condensed Matter* **26**, 142202 (2014)

[97] F.-C. Chiu: A review on conduction mechanisms in dielectric films, *Advances in Materials Science and Engineering* **2014**, 578168 (2014)

[98] A. Rose: Space-charge-limited currents in solids, *Physical Review* **97**, 1538–1544 (1955)

[99] M. A. Lampert & P. Mark: *Current Injection in Solids*, Academic Press, Inc., New York and London (1970)

[100] B. M. Vul, G. M. Guro & I. I. Ivanchik: Encountering domains in ferroelectrics, *Ferroelectrics* **6**, 29–31 (1973)

[101] E. K. H. Salje & H. Zhang: Domain boundary engineering, *Phase Transitions* **82**, 452–469 (2009)

[102] E. K. H. Salje: Multiferroic domain boundaries as active memory devices: Trajectories towards domain boundary engineering, *ChemPhysChem* **11**, 940–950 (2010)

[103] P. Maksymovych *et al.*: Dynamic conductivity of ferroelectric domain walls in $BiFeO_3$, *Nano Letters* **11**, 1906–1912 (2011)

[104] L. Li *et al.*: Giant resistive switching via control of ferroelectric charged domain walls, *Advanced Materials* **28**, 6574–6580 (2016)

[105] R. K. Vasudevan *et al.*: Domain wall geometry controls conduction in ferroelectrics, *Nano Letters* **12**, 5524–5531 (2012)

[106] A. Crassous, T. Sluka, A. K. Tagantsev & N. Setter: Polarization charge as a reconfigurable quasi-dopant in ferroelectric thin films, *Nature Nanotechnology* **10**, 614–618 (2015)

[107] T. Rojac, H. Ursic, A. Bencan, B. Malic & D. Damjanovic: Mobile domain walls as a bridge between nanoscale conductivity and macroscopic electromechanical response, *Advanced Functional Materials* **25**, 2099–2108 (2015)

[108] A. Tselev *et al.*: Microwave AC conductivity of domain walls in ferroelectric thin films, *Nature Communications* **7**, 11630 (2016)

[109] I. Gaponenko, P. Tückmantel, J. Karthik, L. W. Martin & P. Paruch: Towards reversible control of domain wall conduction in $Pb(Zr_{0.2}Ti_{0.8})O_3$ thin films, *Applied Physics Letters* **106**, 162902 (2015)

[110] I. Stolichnov *et al.*: Bent ferroelectric domain walls as reconfigurable metallic-like channels, *Nano Letters* **15**, 8049–8055 (2015)

[111] T. Kämpfe *et al.*: Optical three-dimensional profiling of charged domain walls in ferroelectrics by Cherenkov second-harmonic generation, *Physical Review B* **89**, 035314 (2014)

[112] J. Gonnissen *et al.*: Direct observation of ferroelectric domain walls in $LiNbO_3$: Wall-meanders, kinks, and local electric charges, *Advanced Functional Materials* **26**, 7599–7604 (2016)

[113] Y. Kim, M. Alexe & E. K. H. Salje: Nanoscale properties of thin twin walls and surface layers in piezoelectric WO_{3-x}, *Applied Physics Letters* **96**, 032904 (2010)

[114] A. Aird & E. K. H. Salje: Sheet superconductivity in twin walls: experimental evidence of WO_{3-x}, *Journal of Physics: Condensed Matter* **10**, L377 (1998)

[115] E. Y. Ma *et al.*: Mobile metallic domain walls in an all-in-all-out magnetic insulator, *Science* **350**, 538–541 (2015)

[116] M. Fiebig, T. Lottermoser, D. Fröhlich, A. V. Goltsev & R. V. Pisarev: Observation of coupled magnetic and electric domains, *Nature* **419**, 818–820 (2002)

[117] B. Lorenz: Hexagonal manganites ($RMnO_3$): Class I multiferroics with strong coupling of magnetism and ferroelectricity, *ISRN Condensed Matter Physics* **2013**, 43 (2013)

[118] S. C. Chae *et al.*: Direct observation of the proliferation of ferroelectric loop domains and vortex-antivortex pairs, *Physical Review Letters* **108**, 167603 (2012)

[119] S. Remsen & B. Dabrowski: Synthesis and oxygen storage capacities of hexagonal $Dy_{1-x}Y_xMnO_{3+\delta}$, *Chemistry of Materials* **23**, 3818–3827 (2011)

[120] C. Abughayada, B. Dabrowski, S. Kolesnik, D. E. Brown & O. Chmaissem: Characterization of oxygen storage and structural properties of oxygen-loaded hexagonal $RMnO_{3-\delta}$ (R = Ho, Er, and Y), *Chemistry of Materials* **27**, 6259–6267 (2015)

[121] C. J. Fennie & K. M. Rabe: Ferroelectric transition in $YMnO_3$ from first principles, *Physical Review B* **72**, 100103 (2005)

[122] M. Lilienblum: *Ferroelectric order in multiferroic hexagonal manganites*, Ph.D. thesis, ETH Zürich (2016)

[123] A. S. Gibbs, K. S. Knight & P. Lightfoot: High-temperature phase transitions of hexagonal $YMnO_3$, *Physical Review B* **83**, 094111 (2011)

[124] M. Lilienblum *et al.*: Ferroelectricity in the multiferroic hexagonal manganites, *Nature Physics* **11**, 1070–1073 (2015)

[125] Y. Kumagai & N. A. Spaldin: Structural domain walls in polar hexagonal manganites, *Nature Communications* **4**, 1540 (2013)

[126] M. Lilienblum, E. Soergel & M. Fiebig: Manipulation of ferroelectric vortex domains in hexagonal manganites, *Journal of Applied Physics* **110**, 052007 (2011)

[127] S. C. Chae *et al.*: Self-organization, condensation, and annihilation of topological vortices and antivortices in a multiferroic, *Proceedings of the National Academy of Sciences* **107**, 21366–21370 (2010)

[128] S. M. Griffin *et al.*: Scaling behavior and beyond equilibrium in the hexagonal manganites, *Physical Review X* **2**, 041022 (2012)

[129] S.-Z. Lin *et al.*: Topological defects as relics of emergent continuous symmetry and higgs condensation of disorder in ferroelectrics, *Nature Physics* **10**, 970–977 (2014)

[130] Q. Zhang *et al.*: Direct observation of multiferroic vortex domains in $YMnO_3$, *Scientific Reports* **3**, 2741 (2013)

[131] Q.-H. Zhang *et al.*: Topology breaking of the vortex in multiferroic $Y_{0.67}Lu_{0.33}MnO_3$, *Applied Physics Letters* **105**, 012902 (2014)

[132] Q. H. Zhang *et al.*: Direct observation of interlocked domain walls in hexagonal $RMnO_3$ (R = Tm, Lu), *Physical Review B* **85**, 020102 (2012)

[133] M.-G. Han *et al.*: Ferroelectric switching dynamics of topological vortex domains in a hexagonal manganite, *Advanced Materials* **25**, 2415–2421 (2013)

[134] T. Matsumoto *et al.*: Multivariate statistical characterization of charged and uncharged domain walls in multiferroic hexagonal $YMnO_3$ single crystal visualized by a spherical aberration-corrected STEM, *Nano Letters* **13**, 4594–4601 (2013)

[135] L. Tian, Y. Wang, B. Ge, X. Zhang & Z. Zhang: Direct observation of interlocked domain walls and topological four-state vortex-like domain patterns in multiferroic $YMnO_3$ single crystal, *Applied Physics Letters* **106**, 112903 (2015)

[136] M. Fiebig *et al.*: Determination of the magnetic symmetry of hexagonal manganites by second harmonic generation, *Physical Review Letters* **84**, 5620–5623 (2000)

[137] G. Subba Rao, B. Wanklyn & C. Rao: Electrical transport in rare earth ortho-chromites, -manganites and -ferrites, *Journal of Physics and Chemistry of Solids* **32**, 345–358 (1971)

[138] S. H. Skjærvø *et al.*: Interstitial oxygen as a source of p-type conductivity in hexagonal manganites, *Nature Communications* **7**, 13745 (2016)

[139] A. M. Kalashnikova & R. V. Pisarev: Electronic structure of hexagonal rare-earth manganites $\mathrm{RMnO_3}$, *Journal of Experimental and Theoretical Physics Letters* **78**, 143–147 (2003)

[140] T. Katsufuji *et al.*: Dielectric and magnetic anomalies and spin frustration in hexagonal $\mathrm{RMnO_3}$ (R = Y, Yb, and Lu), *Physical Review B* **64**, 104419 (2001)

[141] D. Smyth: The role of impurities in insultating transition metal oxides, *Progress in Solid State Chemistry* **15**, 145–171 (1984)

[142] B. B. Van Aken, J.-W. G. Bos, R. A. de Groot & T. T. M. Palstra: Asymmetry of electron and hole doping in $\mathrm{YMnO_3}$, *Physical Review B* **63**, 125127 (2001)

[143] S. M. Selbach *et al.*: Crystal structure, chemical expansion and phase stability of $\mathrm{HoMnO_3}$ at high temperature, *Journal of Solid State Chemistry* **196**, 528–535 (2012)

[144] P. Ren, H. Fan & X. Wang: Bulk conduction and nonlinear behaviour in multiferroic $\mathrm{YMnO_3}$, *Applied Physics Letters* **103**, 152905 (2013)

[145] F. Kröger & H. Vink: Relations between the concentrations of imperfections in crystalline solids, in F. Seitz & D. Turnbull (eds.), *Solid State Physics*, volume 3, 307 – 435, Academic Press (1956)

[146] C. Moure, M. Villegas, J. Fernandez, J. Tartaj & P. Duran: Phase transition and electrical conductivity in the system $\mathrm{YMnO_3}$-$\mathrm{CaMnO_3}$, *Journal of Materials Science* **34**, 2565–2568 (1999)

[147] K. Kamata, T. Nakajima & T. Nakamura: Thermogravimetric study of rare earth manganites $\mathrm{AMnO_3}$ (A=Sm,Dy,Y,Er,Yb) at 1200 °C, *Materials Research Bulletin* **14**, 1007–1012 (1979)

[148] A. J. Overton, J. L. Best, I. Saratovsky & M. A. Hayward: Influence of topotactic reduction on the structure and magnetism of the multiferroic $\mathrm{YMnO_3}$, *Chemistry of Materials* **21**, 4940–4948 (2009)

[149] Y. Du *et al.*: Domain wall conductivity in oxygen deficient multiferroic $\mathrm{YMnO_3}$ single crystals, *Applied Physics Letters* **99**, 252107 (2011)

[150] Y. Du *et al.*: Manipulation of domain wall mobility by oxygen vacancy ordering in multiferroic $\mathrm{YMnO_3}$, *Physical Chemistry Chemical Physics* **15**, 20010–20015 (2013)

[151] G. Binnig, H. Rohrer, C. Gerber & E. Weibel: Surface studies by scanning tunneling microscopy, *Physical Review Letters* **49**, 57–61 (1982)

[152] G. Binnig, C. F. Quate & C. Gerber: Atomic force microscope, *Physical Review Letters* **56**, 930–933 (1986)

[153] E. Meyer, H. Hug & R. Bennewitz: *Scanning Probe Microscopy: The Lab on a Tip*, Advanced Texts in Physics, Springer Berlin Heidelberg (2003)

[154] E. Soergel: Visualization of ferroelectric domains in bulk single crystals, *Applied Physics B* **81**, 729–751 (2005)

[155] F. Saurenbach & B. D. Terris: Imaging of ferroelectric domain walls by force microscopy, *Applied Physics Letters* **56**, 1703–1705 (1990)

[156] R. Lüthi *et al.*: Surface and domain structures of ferroelectric crystals studied with scanning force microscopy, *Journal of Applied Physics* **74**, 7461–7471 (1993)

[157] R. Lühi *et al.*: Statics and dynamics of ferroelectric domains studied with scanning force microscopy, *Journal of Vacuum Science & Technology B* **12**, 2451–2455 (1994)

[158] K. Franke, J. Besold, W. Haessler & C. Seegebarth: Modification and detection of domains on ferroelectric PZT films by scanning force microscopy, *Surface Science* **302**, L283 – L288 (1994)

[159] A. Gruverman, O. Auciello & H. Tokumoto: Scanning force microscopy for the study of domain structure in ferroelectric thin films, *Journal of Vacuum Science & Technology B* **14**, 602–605 (1996)

[160] T. Hidaka *et al.*: Characteristics of PZT thin films as ultra-high density recording media, *Integrated Ferroelectrics* **17**, 319–327 (1997)

[161] A. Gruverman, O. Auciello & H. Tokumoto: Imaging and control of domain structures in ferroelectric thin films via scanning force microscopy, *Annual Review of Materials Science* **28**, 101–123 (1998)

[162] G. Meyer & N. M. Amer: Novel optical approach to atomic force microscopy, *Applied Physics Letters* **53**, 1045–1047 (1988)

[163] F. Johann, A. Hoffmann & E. Soergel: Impact of electrostatic forces in contact-mode scanning force microscopy, *Physical Review B* **81**, 094109 (2010)

[164] B. Cappella & G. Dietler: Force-distance curves by atomic force microscopy, *Surface Science Reports* **34**, 1–104 (1999)

[165] S. Rast, C. Wattinger, U. Gysin & E. Meyer: Dynamics of damped cantilevers, *Review of Scientific Instruments* **71**, 2772–2775 (2000)

[166] P. Eyben *et al.*: Scanning spreading resistance microscopy and spectroscopy for routine and quantitative two-dimensional carrier profiling, *Journal of Vacuum Science & Technology B* **20**, 471–478 (2002)

[167] E. Soergel: Piezoresponse force microscopy (PFM), *Journal of Physics D: Applied Physics* **44**, 464003 (2011)

[168] M. Molotskii: Generation of ferroelectric domains in atomic force microscope, *Journal of Applied Physics* **93**, 6234–6237 (2003)

[169] P. De Wolf, T. Clarysse & W. Vandervorst: Quantification of nanospreading resistance profiling data, *Journal of Vacuum Science & Technology B* **16**, 320–326 (1998)

[170] A. Kumar *et al.*: Nanometer-scale mapping of irreversible electrochemical nucleation processes on solid Li-ion electrolytes, *Scientific Reports* **3**, 1621 (2013)

[171] N. Domingo *et al.*: Giant reversible nanoscale piezoresistance at room temperature in Sr_2IrO_4 thin films, *Nanoscale* **7**, 3453–3459 (2015)

[172] D. Bonnell, S. Kalinin, A. Kholkin & A. Gruverman: Piezoresponse force microscopy: A window into electromechanical behavior at the nanoscale, *MRS Bulletin* **34**, 648–657 (2009)

[173] R. Birss: *Symmetry and magnetism*, Selected topics in solid state physics, North-Holland Pub. Co. (1964)

[174] T. Jungk: *Untersuchung der Abbildungsmechanismen ferroelektrischer Domänen mit dem Rasterkraftmikroskop*, Ph.D. thesis, Universität Bonn (2006)

[175] T. Limboeck & E. Soergel: Evolution of ferroelectric domain patterns in $BaTiO_3$ at the orthorhombic ↔ tetragonal phase transition, *Applied Physics Letters* **105**, 152901 (2014)

[176] P. Girard: Electrostatic force microscopy: Principles and some applications to semiconductors, *Nanotechnology* **12**, 485 (2001)

[177] S. Kalinin & A. Gruverman: *Scanning Probe Microscopy of Functional Materials: Nanoscale Imaging and Spectroscopy*, Springer New York (2010)

[178] S. Hudlet, M. Saint Jean, C. Guthmann & J. Berger: Evaluation of the capacitive force between an atomic force microscopy tip and a metallic surface, *European Physical Journal B: Condensed Matter Physics* **2**, 5–10 (1998)

[179] C. Barth *et al.*: AFM tip characterization by Kelvin probe force microscopy, *New Journal of Physics* **12**, 093024 (2010)

[180] E. Brüche: Elektronenmikroskopische Abbildung mit lichtelektrischen Elektronen, *Zeitschrift für Physik* **86**, 448–450 (1933)

[181] E. Brüche & W. Knecht: Bemerkung über die Erreichung hoher Auflösungen mit dem elektronenoptischen Immersionsobjektiv, *Zeitschrift für Physik* **92**, 462–466 (1934)

[182] W. Telieps & E. Bauer: An analytical reflection and emission UHV surface electron microscope, *Ultramicroscopy* **17**, 57 – 65 (1985)

[183] F. Nickel: *Aberrationskorrigierte Photoemissionsmikroskopie an magnetischen Systemen: Von statischer Charakterisierung zu zeitaufgelöster Abbildung*, Ph.D. thesis, Universität Duisburg-Essen (2013)

[184] S. Bügel, T. Brückel, R. Waser & C. M. Schneider: *Electronic Oxides – Correlation Phenomena, Exotic Phases and Novel Functionalities*, Forschungszentrum Jülich GmbH (2010)

[185] S. Tanuma, C. J. Powell & D. R. Penn: Calculations of electron inelastic mean free paths. III. Data for 15 inorganic compounds over the 50 - 2000 eV range, *Surface and Interface Analysis* **17**, 927–939 (1991)

[186] S. Tanuma *et al.*: Experimental determination of electron inelastic mean free paths in 13 elemental solids in the 50 to 5000 eV energy range by elastic-peak electron spectroscopy, *Surface and Interface Analysis* **37**, 833–845 (2005)

[187] I. P. Krug: *Magnetic proximity effects in highly-ordered transition metal oxide heterosystems studied by soft x-ray photoemission electron microscopy*, Ph.D. thesis, Universität Duisburg-Essen (2007)

[188] M. Escher *et al.*: NanoESCA: A novel energy filter for imaging x-ray photoemission spectroscopy, *Journal of Physics: Condensed Matter* **17**, S1329 (2005)

[189] N. Barrett *et al.*: Full field electron spectromicroscopy applied to ferroelectric materials, *Journal of Applied Physics* **113**, 187217 (2013)

[190] D. Gottlob: *Spin-reorientation transition in epitaxial* Ni_xPd_{1-x} *fims on Cu(001): a microscopic analysis*, Ph.D. thesis, Universität Duisburg-Essen (2015)

[191] R. M. Tromp *et al.*: A simple energy filter for low energy electron microscopy / photoelectron emission microscopy instruments, *Journal of Physics: Condensed Matter* **21**, 314007 (2009)

[192] R. Tromp *et al.*: A new aberration-corrected, energy-filtered LEEM / PEEM instrument. I. Principles and design, *Ultramicroscopy* **110**, 852–861 (2010)

[193] R. Tromp, J. Hannon, W. Wan, A. Berghaus & O. Schaff: A new aberration-corrected, energy-filtered LEEM / PEEM instrument II. Operation and results, *Ultramicroscopy* **127**, 25–39 (2013)

[194] Specs-GmbH: `http://www.specs.de/cms/front_content.php?idcat=281` (01-20-2017)

[195] C. M. Schneider & G. Schönhense: Investigating surface magnetism by means of photoexcitation electron emission microscopy, *Reports on Progress in Physics* **65**, 1785 (2002)

[196] E. Bauer: Low energy electron microscopy, *Reports on Progress in Physics* **57**, 895 (1994)

[197] E. Bauer: LEEM basics, *Surface Review and Letters* **05**, 1275–1286 (1998)

[198] G. F. Rempfer, D. M. Desloge, W. P. Skoczylas & O. H. Griffith: Simultaneous correction of spherical and chromatic aberrations with an electron mirror: An electron optical achromat, *Microscopy and Microanalysis* **3**, 14–27 (1997)

[199] D. Preikszas & H. Rose: Correction properties of electron mirrors, *Journal of Electron Microscopy* **46**, 1 (1997)

[200] S. Schramm, A. Pang, M. Altman & R. Tromp: A Contrast Transfer Function approach for image calculations in standard and aberration-corrected LEEM and PEEM, *Ultramicroscopy* **115**, 88–108 (2012)

[201] A. Einstein: Über einen die Erzeugung und Verwandlung des Lichtes betreffenden heuristischen Gesichtspunkt, *Annalen der Physik* **322**, 132–148 (1905)

[202] J. Hölzl, F. Schulte & H. Wagner: *Solid Surface Physics*, Springer-Verlag (1979)

[203] D. Attwood: *Soft X-Rays and Extreme Ultraviolet Radiation: Principles and Applications*, Cambridge University Press (2007)

[204] D. Harris & M. Bertolucci: *Symmetry and Spectroscopy: An Introduction to Vibrational and Electronic Spectroscopy*, Dover Publications (1978)

[205] A. C. Thompson *et al.*: *X-ray Data Booklet*, Lawrence Berkeley Laboratory (2001)

[206] R. Waser & M. Wuttig: *Memristive Phenomena – From Fundamental Physics to Neuromorphic Computing*, Forschungszentrum Jülich GmbH (2016)

[207] E. Bauer: *Surface Microscopy with Low Energy Electrons*, Springer Science+Business Media New York (2014)

[208] R. L. Bihan, J. L. Chartier & L. Jean: Measurement of surface potential between ferroelectric domains, *Ferroelectrics* **13**, 475–477 (1976)

[209] R. L. Bihan, J. L. Chartier & L. Jean: Measurement of surface potential between ferroelectric domains with a quantitative electron mirror microscope, *Ferroelectrics* **17**, 429–431 (1977)

[210] J. E. Rault *et al.*: Thickness-dependent polarization of strained $BiFeO_3$ films with constant tetragonality, *Physical Review Letters* **109**, 267601 (2012)

[211] G. F. Nataf *et al.*: Low energy electron imaging of domains and domain walls in magnesium-doped lithium niobate, *Scientific Reports* **6**, 33098 (2016)

[212] S. A. Nepijko, N. N. Sedov & G. Schönhense: Peculiarities of imaging one- and two-dimensional structures using an electron microscope in the mirror operation mode, *Journal of Microscopy* **203**, 269–276 (2001)

[213] S. A. Nepijko, A. Gloskovskii, N. N. Sedov & G. Schönhense: Measurement of the electric field distribution and potentials on the object surface in an emission electron microscope without restriction of the electron beams, *Journal of Microscopy* **211**, 89–94 (2003)

[214] S. A. Nepijko & G. Schönhense: Measurement of potential distribution function on object surface by using an electron microscope in the mirror operation mode, *Journal of Microscopy* **238**, 90–94 (2010)

[215] D. Hurle: *Handbook of crystal growth*, North-Holland (1993)

[216] Z. Yan *et al.*: Growth of high-quality hexagonal $ErMnO_3$ single crystals by the pressurized floating-zone method, *Journal of Crystal Growth* **409**, 75 – 79 (2015)

[217] O. J. Schumann: *Structural investigations on layered manganites and ruthenates*, Ph.D. thesis, University of Cologne (2010)

[218] B. B. Van Aken, A. Meetsma & T. T. M. Palstra: Hexagonal $ErMnO_3$, *Acta Crystallographica Section E: Structure Reports Online* **57**, i38–i40 (2001)

[219] E. Ruff *et al.*: Conductivity contrast and tunneling charge transport in the vortexlike ferroelectric domain patterns of multiferroic hexagonal $YMnO_3$, *Physical Review Letters* **118**, 036803 (2017)

[220] L. Diederich, O. Küttel, P. Aebi & L. Schlapbach: Electron affinity and work function of differently oriented and doped diamond surfaces determined by photoelectron spectroscopy, *Surface Science* **418**, 219–239 (1998)

[221] H. Han *et al.*: Switchable photovoltaic effects in hexagonal manganite thin films having narrow band gaps, *Chemistry of Materials* **27**, 7425–7432 (2015)

[222] Y. W. Xie *et al.*: Magnetically and electrically tunable transport property of the heterojunction composed of $La_{0.9}Ca_{0.1}MnO_{3+\delta}$ and Nb-doped $SrTiO_3$, *Journal of Physics: Condensed Matter* **19**, 196223 (2007)

[223] T. Choi, S. Lee, Y. J. Choi, V. Kiryukhin & S.-W. Cheong: Switchable ferroelectric diode and photovoltaic effect in $BiFeO_3$, *Science* **324**, 63–66 (2009)

[224] S. Bubel, N. Mechau, H. Hahn & R. Schmechel: Trap states and space charge limited current in dispersion processed zinc oxide thin films, *Journal of Applied Physics* **108**, 124502 (2010)

[225] E. Verrelli & D. Tsoukalas: Investigation of the gate oxide leakage current of low temperature formed hafnium oxide films, *Journal of Applied Physics* **113**, 114103 (2013)

[226] J. M. Montero, J. Bisquert, G. Garcia-Belmonte, E. M. Barea & H. J. Bolink: Trap-limited mobility in space-charge limited current in organic layers, *Organic Electronics* **10**, 305–312 (2009)

[227] D. Joung, A. Chunder, L. Zhai & S. I. Khondaker: Space charge limited conduction with exponential trap distribution in reduced graphene oxide sheets, *Applied Physics Letters* **97**, 093105 (2010)

[228] U. Adem *et al.*: Dielectric relaxation in $YMnO_3$ single crystals, *Journal of Alloys and Compounds* **638**, 228–232 (2015)

[229] E. Hassanpour *et al.*: Robustness of magnetic and electric domains against charge carrier doping in multiferroic hexagonal $ErMnO_3$, *New Journal of Physics* **18**, 043015 (2016)

[230] M. P. Campbell *et al.*: Hall effect in charged conducting ferroelectric domain walls, *Nature Communications* **7**, 13764 (2016)

[231] J. A. Mundy *et al.*: Functional electronic inversion layers at ferroelectric domain walls, *Nature Materials* **16**, 622–627 (2017)

[232] J. A. Mundy *et al.*: Visualizing the interfacial evolution from charge compensation to metallic screening across the manganite metal–insulator transition, *Nature Communications* **5**, 3464 (2014)

[233] P. Coeuré, F. Guinet, J. C. Peuzin, G. Buisson & E. F. Bertaut: Ferroelectric properties of hexagonal orthomanganites of yttrium and rare earths, *Proceedings of the International Meeting on Ferroelectricity Prague* **1** (1966)

[234] J. E. Medvedeva, V. I. Anisimov, M. A. Korotin, O. N. Mryasov & A. J. Freeman: The effect of Coulomb correlation and magnetic ordering on the electronic structure of two hexagonal phases of ferroelectromagnetic $YMnO_3$, *Journal of Physics: Condensed Matter* **12**, 4947 (2000)

[235] K. Rahmanizadeh, D. Wortmann, G. Bihlmayer & S. Blügel: Charge and orbital order at head-to-head domain walls in $PbTiO_3$, *Physical Review B* **90**, 115104 (2014)

[236] J. Crawford & L. Slifkin: *Point Defects in Solids: General and Ionic Crystals*, Point Defects in Solids, Springer Science & Business Media (2013)

[237] P. Lunkenheimer *et al.*: Colossal dielectric constants in transition-metal oxides, *The European Physical Journal Special Topics* **180**, 61–89 (2009)

[238] S. Emmert *et al.*: Electrode polarization effects in broadband dielectric spectroscopy, *The European Physical Journal B* **83**, 157 (2011)

[239] S. Hong: *Nanoscale Phenomena in Ferroelectric Thin Films*, Multifunctional Thin Film Series, Springer US (2013)

[240] I. Stolichnov *et al.*: Persistent conductive footprints of 109° domain walls in bismuth ferrite films, *Applied Physics Letters* **104**, 132902 (2014)

[241] M. Schröder *et al.*: Nanoscale and macroscopic electrical ac transport along conductive domain walls in lithium niobate single crystals, *Materials Research Express* **1**, 035012 (2014)

[242] T. Jungk, A. Hoffmann & E. Soergel: Impact of the tip radius on the lateral resolution in piezoresponse force microscopy, *New Journal of Physics* **10**, 013019 (2008)

[243] N. Barrett *et al.*: Influence of the ferroelectric polarization on the electronic structure of $BaTiO_3$ thin films, *Surface and Interface Analysis* **42**, 1690–1694 (2010)

[244] S. Cherifi *et al.*: Imaging ferroelectric domains in multiferroics using a low-energy electron microscope in the mirror operation mode, *physica status solidi (RRL) - Rapid Research Letters* **4**, 22–24 (2010)

[245] I. Krug *et al.*: Extrinsic screening of ferroelectric domains in $Pb(Zr_{0.48}Ti_{0.52})O_3$, *Applied Physics Letters* **97**, 222903 (2010)

[246] J. E. Rault, T. O. Menteş, A. Locatelli & N. Barrett: Reversible switching of in-plane polarized ferroelectric domains in $BaTiO_3$ (001) with very low energy electrons, *Scientific Reports* **4**, 6792 (2014)

[247] J. Schaab *et al.*: Imaging and characterization of conducting ferroelectric domain walls by photoemission electron microscopy, *Applied Physics Letters* **104**, 232904 (2014)

[248] P. W. Hawkes & J. C. Spence (eds.): *Science of Microscopy*, Springer Science+Business Media (2007)

[249] J. Schaab *et al.*: Contact-free mapping of electronic transport phenomena of polar domains in $SrMnO_3$ films, *Physical Review Applied* **5**, 054009 (2016)

[250] R. Erickson & D. Maksimovic: *Fundamentals of Power Electronics*, Power electronics, Springer US (2001)

[251] S. R. Burns, J. M. Gregg & V. Nagarajan: Nanostructuring ferroelectrics via focused ion beam methodologies, *Advanced Functional Materials* **26**, 8367–8381 (2016)

[252] F. Nickel *et al.*: Time-resolved magnetic imaging in an aberration-corrected, energy-filtered photoemission electron microscope, *Ultramicroscopy* **130**, 54–62 (2013)

[253] N. Barrett *et al.*: Operando x-ray photoelectron emission microscopy for studying forward and reverse biased silicon p-n junctions, *Review of Scientific Instruments* **87**, 053703 (2016)

Curriculum vitae

Jakob Schaab
Zurich, Switzerland

Education

05/2013 – 03/2017	**Doctorate in Materials Science** ETH Zurich (Switzerland) Multifunctional Ferroic Materials Department of Materials, Prof. M. Fiebig
10/2010 – 10/2012	**Engineer's Degree in Materials Science** University of Stuttgart (Germany) Thesis at the Max-Planck-Institute for Intelligent Systems *X-ray diffraction analysis of shape-memory transformations under load in Ni-Ti thin films*

Publications

Publications over the course of the doctorate:

- *Functional electronic inversion layers at ferroelectric domain walls.*
  J. A. Mundy, J. Schaab, Y. Kumagai, A. Cano, M. Stengel, I. P. Krug, D. M. Gottlob, H. Doğanay, M. E. Holtz, R. Held, Z. Yan, E. Bourret, C. M. Schneider, D. G. Schlom, D. A. Muller, R. Ramesh, N. A. Spaldin, D. Meier. *Nature Materials* **16**, 622 (2017)
  Contribution: Concept, execution, and evaluation of the cAFM-based domain-wall experiments. X-PEEM experiments and evaluation. Assisting in writing the manuscript.

- *Domain wall architecture in tetragonal ferroelectric thin films.*
  G. De Luca, M. D. Rossell, J. Schaab, N. Viart, M. Fiebig, M. Trassin. *Advanced Materials* **29**, 1605145 (2017)
  Contribution: Observation and imaging of conductive domain walls by scanning probe microscopy.

- *Contact-free mapping of electronic transport phenomena of polar domains in $SrMnO_3$ films.*

J. Schaab, I. P. Krug, H. Doğanay, J. Hackl, D. M. Gottlob, M. I. Khan, S. Nemšák, L. Maurel, E. Langenberg, P. A. Algarabel, J. A. Pardo, C. M. Schneider, D. Meier. *Physical Review Applied* **5**, 054009 (2016)
Contribution: LEEM and SPM measurements on $SrMnO_3$. Evaluation and interpretation of the data with Matlab and electronic transport models, respectively.

- *Robustness of magnetic and electric domains against charge carrier doping in multiferroic hexagonal* $ErMnO_3$*.*
  E. Hassanpour, V. Wegmayr, J. Schaab, Z. Yan, E. Bourret, Th. Lottermoser, M. Fiebig, D. Meier. *New Journal of Physics* **18**, 43015 (2016)
  Contribution: PFM measurements to reveal the ferroelectric domains of doped h-RMnO$_3$.

- *Optimization of electronic domain-wall properties by aliovalent cation substitution.*
  J. Schaab, A. Cano, M. Lilienblum, Z. Yan, E. Bourret,R. Ramesh, M. Fiebig, D. Meier. *Advanced Electronic Materials* **2**, 1500195 (2016)
  Contribution: Characterization of the microscopic electronic transport at domain walls of p-doped $ErMnO_3$ by SPM.

- *Ferroelectric domains in the multiferroic phase of* $ErMnO_3$ *imaged by low-temperature photoemission electron microscopy.*
  J. Schaab, M. Trassin, A. Scholl, A. Doran, Z. Yan, E. Bourret, R. Ramesh, D. Meier. *Journal of Physics: Conference Series* **592**, 012120 (2015)
  Contribution: Imaging of the ferroelectric domain structure by SPM at room temperature.

- *Growth of high-quality hexagonal* $ErMnO_3$ *single-crystals by the pressurized floating-zone method.*
  Z. Yan, D. Meier, J. Schaab, R. Ramesh, E. Samulon, E. Bourret. *Journal of Crystal Growth* **409**, 75-79 (2015)
  Contribution: PFM imaging of the ferroelectric domains in the as-grown state.

- *Imaging and characterization of conducting ferroelectric domain walls by photoemission electron microscopy.*
  J. Schaab, I. P. Krug, F. Nickel, D. M. Gottlob, H. Doğanay, A. Cano, M. Hentschel, Z. Yan, E. Bourret, C. M. Schneider, R. Ramesh, D. Meier. *Applied Physics Letters* **104**, 232904 (2014)
  Contribution: Identification of the domain-wall type that produces X-PEEM contrasts by SPM, i. e., the essential finding for interpretation of the underlying contrasts mechanism.

Publications prior to the doctorate:

- *X-ray diffraction study of the reverse martensitic transformation in NiTi shape memory thin films.*
  M. K. A. Koker, J. Schaab, N. Zotov, E. J. Mittemeijer. *Thin Solid Films* **545**, 71-80 (2013)

- *Tuning the emission colour by manipulating terbium-terbium interactions: Terbium doped aluminum nitride as an example system* F. Benz, H. P. Strunk, J. Schaab, U. Künecke, P. Wellmann. *Journal of Applied Physics* **114**, 073518 (2013)

Contributions

Talks:

- *Functional electronic inversion layers at ferroelectric domain walls*
  DPG Spring Meeting, Dresden, Germany (2017)
- *Electronic transport and contact-free conductance-mapping of polar domains in $SrMnO_3$ films*
  ISAF/ECAPD/PFM Conference, Darmstadt, Germany (2016)
- *Controlling electronic domain-wall conductance by charge-carrier doping*
  DPG Spring Meeting, Regensburg, Germany (2016)
- *Optimization of electronic DW properties by aliovalent cation substitution*
  Ferroelectrics Workshop of the Laboratory of Ceramics (EPFL), Leysin, Switzerland (2015)
  First prize in the Best Presentation Award
- *Advanced characterization of functional ferroelectric domain walls by X-ray photoemission electron microscopy*
  DPG Spring Meeting, Berlin, Germany (2015)
- *Imaging and characterization of conducting ferroelectric domain walls by photoemission electron microscopy*
  APS March Meeting, San Antonio, Texas, USA (2015)
- *Imaging and characterization of conducting ferroelectric domain walls by photoemission electron microscopy*
  MRS Fall Meeting, Boston, Massachusetts, USA (2014)

Posters:

- *Properties of domain topologies revealed by SPM*
  Evaluation of the Department of Materials at ETH Zürich, Zürich, Switzerland (2016)
- *Optimization of electronic domain-wall properties by aliovalent cation substitution*
  Theo Murphy meeting of the Royal Society, Buckinghamshire, England (2016)

- *Characterizing electronic transport properties of ferroic domains and domain walls by LEEM and X-PEEM*
  BESSY User Meeting, Berlin, Germany (2015)

- *Contact-free probing of electronic transport phenomena at the nanoscale*
  MaP Graduate Symposium, Zürich, Switzerland (2015)

- *Advanced characterization of functional ferroelectric domain walls by X-ray photoemission electron microscopy*
  DPG Spring Meeting, Berlin, Germany (2015)

- *Tuning the electronic transport behavior at functional ferroelectric domain walls*
  MaP Graduate Symposium, Zürich, Switzerland (2014)

Teaching and supervision

2015 **Master thesis**
Supervision and mentoring in annealing experiments and advanced SPM characterization, ETH Zurich (Switzerland), Department of Materials (Supervision and mentoring)

2015 **Research Lab II**
Tutoring of material science students, ETH Zurich (Switzerland), Department of Materials (Tutoring)

2015 **Schweizer Jugend forscht**
Tutoring of a high school student, ETH Zurich (Switzerland), Department of Materials (Supervision and mentoring)

2015 **Crystal Optics Lecture**
Organization and supervision of exercise classes and examination, ETH Zurich (Switzerland), Department of Materials (Organization, Tutoring)

2014 **Introduction to Materials Science Lecture**
Organization and supervision of exercise classes and examination, ETH Zurich (Switzerland), Department of Materials (Organization, Tutoring)

2013 **Crystal Optics Lecture**
Organization and supervision of exercise classes and examination, ETH Zurich (Switzerland), Department of Materials (Organization, Tutoring)